Nonlinear Dynamics of Double Beam Piezoelectric Energy Harvesters under Parametric, Magnetic and Galloping Excitation

A thesis submitted in partial fulfilment of the requirements

for the degree of

Doctor of Philosophy

By

Ranit Roy

Roll No: 196103024

DEPARTMENT OF MECHANICAL ENGINEERING

INDIAN INSTITUTE OF TECHNOLOGY GUWAHATI

Guwahati – 781039

INDIA

Dedicated to my parents, and to the service of humanity

Declaration

I declare that the thesis entitled “Nonlinear Dynamics of Double Beam Piezoelectric Energy Harvesters under Parametric, Magnetic and Galloping Excitation” submitted by me is a presentation of my original research work done under the supervision of Dr. Santosha Kumar Dwivedy, Professor, Department of Mechanical Engineering, Indian Institute of Technology Guwahati. This work has not been submitted elsewhere for the award of any degree, diploma, associateship, fellowship, titles in this institute or any other university or institution of higher education.

Ranit Roy

Department of Mechanical Engineering

Indian Institute of Technology Guwahati

Assam - 781039, India

Date: 30th April, 2026

Place: IIT Guwahati

Certificate

This is to certify that the thesis entitled "Nonlinear Dynamics of Double Beam Piezoelectric Energy Harvesters under Parametric, Magnetic and Galloping Excitation" submitted by "Ranit Roy" in partial fulfillment of the requirement for the award of the degree of Doctor of Philosophy, to the Indian Institute of Technology Guwahati, Assam, India is a record of the *bona fide* research work carried out by him under my supervision and guidance at the Department of Mechanical Engineering, Indian Institute of Technology Guwahati, Assam, India. To the best of my knowledge, no part of the work reported in this thesis has been presented for the award of any degree, diploma, associateship, fellowship, titles in this institute or any other university or institution of higher education.

Dr. Santosha Kumar Dwivedy

Professor

Department of Mechanical Engineering

Indian Institute of Technology Guwahati

Assam - 781039, India

Email: dwivedy@iitg.ac.in

Phone: +91-361-2582670

Date: 30th April, 2026

Place: IIT Guwahati

Acknowledgements

At the very beginning, I want to express my deepest gratitude to my advisor, Prof. Santosha Kumar Dwivedy, for his constant support, guidance, and encouragement throughout my PhD journey. His passion for research, clarity of thought, and commitment to excellence have always inspired me. I am especially thankful for his patience, kindness, and the freedom he gave me to think, explore, and grow on my own as a researcher. Working under his supervision has truly been a privilege.

I am sincerely thankful to Prof. Sashindra K. Kakoty, my doctoral committee chairman, for his thoughtful feedback and valuable suggestions that helped me improve my work at every stage. I would also like to thank Prof. Poonam Kumari and Prof. Arbind Kumar Singh, members of my doctoral committee, for their valuable comments, advice, and continued support.

I am grateful to Prof. V. Kulkarni for allowing me to carry out experiments at the institute's wind tunnel facility. My heartfelt thanks to Mr. Anand Verma for his generous help during the experiments, and to Mr. Monoranjan Duarah and Mr. Jiten Basumatary for their technical assistance and cooperation, which made the experimental work much smoother and more enjoyable.

I feel fortunate to have shared this journey with my lab-mates, whose friendship, discussions, and laughter made every day memorable. I owe special thanks to Dr. Anshul Garg for his thoughtful advice, Dr. Sibananda Mohanty for his insightful discussions, and Dr. Patel Bhavik Maheshkumar for his motivation and positive energy.

My sincere thanks also go to Mr. Arun Jyoti Borgohain and Mr. Ayushman Gogoi for their help in developing and refining the experimental setup. Their technical skills and willingness to assist with instruments and measurements were a great support.

Words cannot fully express my love and gratitude to my parents, Late Pradip Kumar Roy and Mrs. Indira Roy, whose sacrifices, unconditional love, and blessings have been my greatest source of strength. I am deeply thankful to my aunt, Ms. Kalpana Roy, for her affection and prayers. I would also like to thank my sister, Mrs. Udita Roy (Das), for her patience, understanding, and constant emotional support, and my brother-in-law, Mr. Ranodip Das, for his encouragement and meaningful conversations.

I would like to extend my appreciation to my friends, Dr. Anirban Bhowmik, Dr. Biswajit Manna, Mr. Rohan Pratihar, Mr. Lalit Kumar, Dr. Manmohan whose companionship, understanding, and moral support helped me to stay positive and focused during the challenging times.

I acknowledge the assistance of AI tool ChatGPT, which helped me with checking grammar, enhancing the language proficiency of the writings. For better readability, I have included the writing suggestions of ChatGPT in some portions of acknowledgement, summary, conclusion and scope of future work of the thesis. However, the the original research work doesnot contain any AI generated content.

I gratefully acknowledge all those, known and unknown, whose goodwill and silent contributions have supported me along the way. I also express my deep appreciation to the natural surroundings of the institute, the serene landscape, fresh air, and the majestic flow of the Brahmaputra, whose calm presence provided constant inspiration and inner peace. My thanks also go to the institute's staff, administrators, and maintenance personnel for their dedicated efforts in keeping the system running smoothly and efficiently.

Above all, I bow in reverence to the divine mother, whose grace, strength, and wisdom have guided me at every step. Finally, I offer my humble salutations to his holiness, whose blessings have filled my path with clarity, faith, and peace.

Ranit Roy

Department of Mechanical Engineering,

Indian Institute of Technology Guwahati,

Assam - 781039, India

Abstract

Energy harvesting from ambient vibrations is an emerging field of research in the era of rapidly developing microelectromechanical systems (MEMS) and the growing demand for autonomous, self-powered devices. These systems are widely being integrated in wireless sensor networks, structural health monitoring, and wearable electronics, where long-term maintenance-free operation is difficult. Initially, the linear vibrational energy harvesting techniques have been employed, which are constrained by their typically narrow operational bandwidth and sensitivity towards the excitation conditions. Later on, to overcome these challenges and enhance the performance of the energy harvesters, the vast dynamical behaviours of nonlinear vibrations are being explored.

Instabilities such as parametric and galloping excitations, which lead to high-amplitude oscillations, need to be avoided for structural stability. However, these two naturally occurring phenomena can be utilized for the purpose of vibrational energy harvesting by using piezoelectric energy harvesters (PEH). So, the present study aims to enhance the understanding and performance of energy harvesting systems operating under parametric, magnetic, and galloping instabilities, where geometric and inertial nonlinearities significantly influence the harvesting capability. Parametric instability is introduced through base excitation, while galloping is modelled via a quasi-steady aerodynamic force approach, and magnetic force is modelled using the dipole-dipole model.

In this research work, three nonlinear piezoelectric energy harvesting systems have been thoroughly investigated. In all cases, the energy harvesters consist of double cantilever beams to enhance the total power output of the systems. In the first problem, the nonlinear dynamic analysis of a spring-coupled double beam-based piezoelectric energy harvester under parametric base excitation is carried out. In the second work, a similar spring-coupled double beam-based energy harvester under parametric base excitation has been studied with the introduction of a magnetic repulsive force, which is induced by two NdFeB permanent magnets. In the first and second problems, comprehensive theoretical frameworks are developed by formulating coupled electro-mechanical models incorporating geometric and inertial nonlinearities, piezoelectric coupling, and parametric instability. In the third work, a

magnetically coupled double beam-based energy harvester under galloping excitation is investigated both theoretically and experimentally. The governing spatio-temporal second-order differential equations of motion of these systems have been formulated using the energy method. These equations are then reduced to their temporal forms by using generalized Galerkin's method.

In the first and second works, reduced temporal equations are further non-dimensionalized using non-dimensional parameters and transformed into a set of first-order differential equations. To obtain the steady state response and stability, the approximate analytical perturbation method (method of multiple scales) is applied. At steady state, the differential equations are transformed into a set of nonlinear algebraic equations, which are further solved using Newton's method. The approximate solutions are then verified with those obtained numerically by employing the 4^{th} order Runge-Kutta method-based MATLAB solver (ode45). Both time and frequency responses have been plotted to gain insight into the system dynamics.

In the third work, in addition to the theoretical work, an experimental setup of the proposed galloping-based piezoelectric energy harvester has been fabricated and tested in a wind tunnel setup. Experimental findings show good agreement with the theoretical results, which are obtained numerically. Voltage-time responses are plotted for different load resistances and wind speed conditions. Study reveals some rich nonlinear phenomena such as periodicity, quasi-periodicity, and chaos, which play a critical role in determining the energy harvester performance.

The thesis is organized into six chapters. Substantial parametric studies have been conducted, and the results have been presented in three major chapters, and in addition to that, a literature review chapter where more than 230 articles have been critically reviewed and correspondingly, the major research gaps have been highlighted. All the findings from the present work are presented in the last chapter. In addition, the scope for future work, which may be extended from the present study, is pointed out.

Keywords: piezoelectric energy harvester, cantilever beam, parametric excitation, galloping, nonlinear dynamics, magnetic repulsive force, the method of multiple scales, bifurcation, periodic, quasi-periodic, chaotic, parametric instability, bluff body, electromechanical

Content

List of Figures

List of Tables

List of Abbreviations

AC	Alternating Current
AFC	Active Fiber Composites
DC	Direct Current
DOF	Degree of Freedom
FEM	Finite Element Modelling
FIV	Flow Induced Vibration
GPEH	Galloping Piezoelectric Energy Harvester
HB	Hopf Bifurcation
HBM	Harmonic Balance Method
IC	Integrated Circuit
IHBM	Incremental Harmonic Balance Method
MEMS	Micro Electro Mechanical System
MFC	Macro Fiber Composite
NdFeB	Neodymium Iron Boron
PEH	Piezoelectric Energy Harvester
PFB	Pitchfork Bifurcation
PLZT	Lead Lanthanum Zirconate Titanate
PT	Lead Titanate
PVDF	Polyvinylidene Difluoride
PZT	Lead Zirconate Titanate
QP	Quasi-periodic
RMS	Root Mean Square
S	Stable

SECE	Synchronous Electric Charge Extraction
SNB	Saddle Node Bifurcation
SSHI	Synchronised Switch Harvesting on Inductor
TUR	Trivial Unstable Region
UAV	Unmanned Aerial Vehicles
US	Unstable
VEH	Vibration Energy Harvester
VIPEC	Vortex Induced Piezoelectric Energy Converter
VIV	Vortex Induced Vibration
WSN	Wireless Sensor Network

List of Symbols

A	Cross-sectional area of the beam
$A_1(T_1),\ A_2(T_1)$	Displacement amplitudes as complex function
A_1	Linear aerodynamic force coefficient
A_3	Nonlinear cubic aerodynamic coefficient
$a_1,\ a_2$	Amplitude of complex function $A_1(T_1),\ A_2(T_1)$
$b_{bb1},\ b_{bb2}$	Width of the 1st and 2nd bluff body
b_i	Width of the *I*-th beam
b_{Pi}	Width of the piezoelectric patch attached to the *i*-th beam
C_i	Effective damping coefficient of the *i*-th beam
C_P	Capacitance of piezoelectric patch
CC	Complex conjugate
D	Gap distance between the magnets
d_{31}	Piezoelectric charge coefficient
E	Young's modulus of beam material
E_P	Young's modulus of piezoelectric material
$F(t)$	External forcing
$F_{g1}(t),\ F_{g2}(t)$	Galloping force on 1st and 2nd bluff body
$f_1,\ f_2$	Nondimensional external forcing coefficient
g	Acceleration due to gravity

h_i	Thickness of the *i*-th beam
h_{Pi}	Thickness of the piezoelectric patch attached to the *i*-th beam
I_{bb1}, I_{bb2}	Mass moment of inertia of 1st and 2nd bluff body
I_i	Area moment of inertia of the *i*-th beam
I_{m_i}	Mass moment of inertia of the tip mass attached to the *i*-th beam
$I_{m_{m1}}$, $I_{m_{m2}}$	Mass moment of inertia of the magnet 1 and magnet 2
$\{J\}$	Jacobian matrix
K	Stiffness of the coupled spring
l_{bb1}, l_{bb2}	Length of the 1st and 2nd bluff body
l_i	Length of the *i*-th beam
l_K	Length from the base of the beam to the point where spring is attached
l_{Pi}	Length of the piezoelectric patch attached to the *i*-th beam
$\vec{M}_A$	Magnetic moment vector of magnet A
$\vec{M}_B$	Magnetic moment vector of magnet B
$M_i(s_i,t)$	Moment produced by voltage across the neutral axis of *i*-th beam
$\vec{M}_{mag1}$, $\vec{M}_{mag2}$	Magnetic moment vector of magnet 1 and magnet 2
$\vec{m}_A$	Magnetization vector of magnet A
$\vec{m}_B$	Magnetization vector of magnet B
m_{bb1}, m_{bb2}	Mass of the 1st and 2nd bluff body
$\vec{m}_{mag1}$, $\vec{m}_{mag2}$	Magnetization vector of magnet 1 and magnet 2

m_i	Tip mass attached to the *i*-th beam
m_{m1}, m_{m2}	Mass of the magnet 1 and magnet 2
P_i	Output power of the *i*-th beam patch system
$\vec{R}$	Distance vector between two NdFeB magnets
R_L	Load resistance
s_i	Distance of an arbitrary point *O* along the neutral axis of the beam
T	Total kinetic Energy
T_n	*n*-th nondimensional time scale
t	Time
U	Total potential energy
U_g	Potential energy due to gravity
U_m	Magnetic potential energy
U_s	Strain energy or elastic potential energy
U_w	Wind speed
$u_{Oi}(s_i,t)$	Axial displacement of an arbitrary point *O* along the neutral axis of the *i*-th beam
$w_i(t)$	Transverse displacement of the tip of *i*-th beam
$\bar{w}_i$	Nondimensional transverse displacement of tip of the *i*-th beam
$w_{Oi}(s_i,t)$	Transverse displacement of an arbitrary point *O* along the neutral axis of the *i*-th beam
$V_i(t)$	Output voltage of the *i*-th beam patch system
V_i^{RMS}	RMS output voltage of the *i*-th beam patch system

$\bar{V}_i$	Nondimensional output voltage of the *i*-th beam patch system
V_{magA}, V_{magB}	Volume of magnet A and magnet B
V_{mag1}, V_{mag2}	Volume of magnet 1 and magnet 2
W_d	Dissipation function for damping
W_e	Work done by electric moment
W_g	Work done by galloping force
x-y-z	Co-ordinates in Cartesian system
$Z_1(T_1)$, $Z_2(T_1)$	Voltage amplitudes as complex function
$z(t)$	External displacement at the base
z_0	External excitation amplitude

Greek symbols

α_{10}, α_{20}	Nondimensional damping coefficients
α_{11}, α_{21}	Nondimensional stiffness coefficients
α_{12}, α_{22}	Nondimensional inertial nonlinear coefficients
α_{13}, α_{23}	Nondimensional cubic nonlinear coefficients
α_{14}, α_{24}	Nondimensional coupling coefficients for coupled spring
α_{15}, α_{25}	Nondimensional electromechanical coupling coefficients
α_2	Inertial nonlinear coefficient
α_3	Cubic nonlinear coefficient

$\beta_1,\ \beta_2$	Phase of complex function $A_1(T_1), A_2(T_1)$
ε	Book keeping parameter
γ_P	Piezo constant
Φ	Nondimensional external excitation frequency
$\phi_{Oi}(s_i,t)$	Angular displacement of an arbitrary point O along the neutral axis of the i-th beam
$\kappa_{Oi}(s_i,t)$	Curvature of the i-th beam
ρ	Density of the beam material
ρ_a	Density of the air
τ	Non-dimensional time
ω_i	Natural frequency of the i-th beam system
ω	External excitation frequency
ω_n	Natural frequency of a system
θ_1	Linear electromechanical coupling coefficient
θ_2	Nonlinear electromechanical coupling coefficient
θ_{i1}	Linear electromechanical coupling coefficient of the i-th beam
μ_0	Permeability of free space
$\sigma,\ \sigma_1$	Nondimensional frequency detuning parameters
ζ	Damping ratio
$\psi_i(s_i)$	Shape function of the i-th beam

Chapter 1

Introduction

1.1 Overview

Microelectronic devices are widely used as sensors, actuators and data transmitters. Mostly, these devices are battery-powered. Traditional batteries need recharging or replacement over a certain period of time, which is sometimes difficult in a remote environment. Recent technological advancements have significantly reduced the power requirement of these devices [1]. Considering these aspects, worldwide researchers focus on harvesting energy from the ambient sources to power up these microelectronic devices. The self-powered devices may be capable of sustaining even in remote environments.

Applications of PEH systems involve condition monitoring of many structures such as bridges, buildings, aircraft, and railways. In data transmission of micro-electromechanical systems (MEMS), wireless sensor networks (WSN), PEH systems can be integrated to power them up. Energy involved in human or animal motion can be utilized to power wearable devices (smart watches, bands, earphones, GPS trackers, animal tags) and biomedical monitoring devices (pacemakers, pressure, tissue stimulators). Extracting energy from ambient sources like solar, wind and water is common around the globe, which can generate macro-scale power in the range of a few kW to GW. However, the power consumption of these micro-electronic devices may vary in a range of μW or mW, and to address this objective, micro-scale energy harvesting comes into the picture.

Vibrational energy is available almost everywhere in nature and our surroundings, e.g., human and other animal motion, vibration of machinery, vibration of vehicles and locomotives, vibration of bridges, wind-induced vibrations (galloping, flutter and vortex-induced vibration), ocean waves. To convert the vibrational energy into useful electrical energy, various transduction mechanisms [2] such as electromagnetic [3], electrostatic [4], piezoelectric [5], triboelectric [6] or a combination of them [7-9] have been explored. Among them, the piezoelectric-based transduction mechanism has advantages over the others due to its high

energy density [10], power extraction capability over a wide range of available frequencies, easy fabrication and structural integration, which make it suitable for micro-scale energy harvesting and applications.

Due to the atomic configuration of the piezoelectric crystals, they can generate electricity under the application of mechanical stress. Apart from traditional PZT (Lead Zirconate Titanate) material, which is brittle in nature, various other flexible piezoelectric materials are used for high-amplitude oscillations. Vibrational energy can be converted into useful electrical energy by embedding the piezoelectric patches with structural elements, e.g., beams, plates, shells, etc., which are further excited through vibration. Mostly, the beam-based structures are used for the purpose of energy harvesting because of their simple configuration.

Figure 1.1 shows a traditional piezoelectric energy harvester, which consists of a slender cantilever beam attached with a tip mass and piezoelectric patches. The beam is fixed with a movable base. When the base gets externally excited, the PEH system starts to oscillate in the transverse direction. As maximum strain is developed near the fixed end, the piezoelectric patches are bonded to the beam surface close to the fixed end to generate maximum voltage.

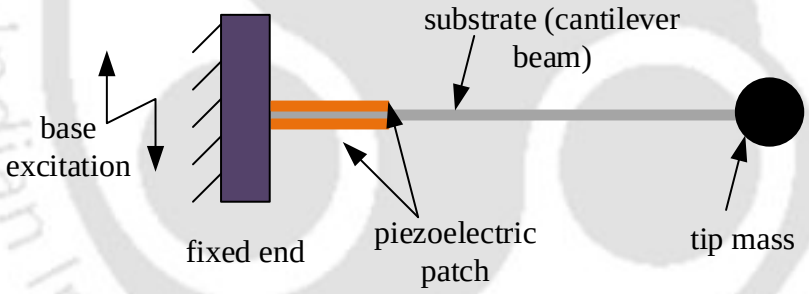

Figure 1.1: Conventional cantilever beam-based piezoelectric energy harvester (PEH) [7]

At the initial stages of research, linear vibrations of PEHs have been investigated. These linear systems can be operational for a narrow range of bandwidth near the resonance frequency. As a result, a sharp reduction in energy generation occurs whenever the excitation frequency is mistuned (away from the resonance frequency). To overcome this issue, researchers are focusing on introducing nonlinearity into the PEH systems [11]. Nonlinear systems can portray interesting behaviour such as bifurcation, quasi-periodicity, chaos, and internal resonance. Depending on the nonlinearity, the responses of the PEH can be periodic, quasi-periodic or chaotic [12]. Energy harvesters based on nonlinear vibration may obtain energy for a wide range of available excitation frequencies. In most of the systems, nonlinearity arises from

geometry or material behaviour of the components, though it can also be induced through external excitation or constraints such as impact, friction, backlash, etc.

Geometric nonlinearity appears due to the large curvature of the beams, while the inertial nonlinearity comes from the concentrated or distributed mass [13]. Material nonlinearity arises from the nonlinear stress-strain relationship; geometric nonlinearity occurs from the nonlinear strain-displacement relationship. Other sources of nonlinearity are due to the external forces applied to the system. These forces may be in the form of gravitational, magnetic or fluid forces. The performance associated with PEHs can be enhanced by exploiting various characteristics of the nonlinear dynamics [14].

The governing equations of motion of nonlinear PEHs are expressed by coupled electro-mechanical partial differential equations of space and time [15]. Discretization through Galerkin's method reduces these equations to the temporal form. Apart from numerical methods, some analytical methods are also employed to solve these nonlinear equations. The analytical methods include the harmonic balance method and perturbation methods such as the Linstedt-Poincaré method, the method of averaging and the method of multiple scales. The method of multiple scales is a commonly used technique that gives transient and steady-state responses. The steady-state reduced equations obtained through this method are used to study responses and their stability and bifurcation under various amplitudes and frequencies of excitations [16].

Depending on the source of excitation, most of the existing PEH systems can be categorized as base-excited systems [17-19], fluid flow-excited systems [20-22] or combined base and flow-excited systems [23-25]. Commonly used base-excited energy harvesters receive the vibrational energy in the form of direct [26] and parametric excitation [27] or a combination of both [28, 29]. In case of directly excited systems, the simple, sub-harmonic and super-harmonic resonances may occur. For a simple resonance condition, the ratio of external excitation frequency (ω) and the system's natural frequency is nearly 1:1. The sub-harmonic and super-harmonic resonance conditions arise when the ratio of the above-mentioned is a rational number. The parametric resonance occurs when the external excitation frequency is nearly equal to the sum of the modal frequencies of the system, i.e., $\omega = \omega_m + \omega_n$. When $\omega_m = \omega_n$, the excitation frequency is twice the modal frequency, and the resonance condition is known as principal parametric resonance. In the case of $\omega_m \neq \omega_n$, the excitation frequency appears to be a combination (sum or difference) of the modal frequencies, and the resonance is combinational

parametric resonance. Parametric resonance may lead to large amplitude oscillations compared to the simple resonance condition.

In the context of flow-induced vibration (FIV), the interaction between fluid flow and flexible solid structures may give rise to self-excited oscillations, such as galloping, flutter, and lock-in through vortex shedding in vortex-induced vibration (VIV). Among these, galloping is widely employed for the purpose of piezoelectric energy harvesting due to its large amplitude transverse oscillation and low frequency. The flow energy transfers to the flexible solid structures in the form of a negative type damping force. Usually, a bluff body is mounted on the beam with piezo patches to harvest the flow energy.

With significant studies on simple single cantilever beam-based systems, researchers investigated two or multiple beam-based systems to improve the energy harvesting capability of the PEH systems. The beams are coupled with different coupling conditions, such as spring coupling [30, 31] and magnetic coupling [32, 33]. As the outcomes of coupled systems, the bandwidth of operating frequency may be enhanced, and energy transfer may take place between the beams, which can amplify the overall power generation of the system. Nonlinearity may arise from the coupling condition, which can further bring many critical phenomena. The dynamic response can be fixed point, periodic, quasi-periodic or chaotic.

There exists huge potential in the field of smart and self-sustained PEH systems. Recent advancements in PEHs suggest that there is strong commercial credibility apart from the common usage of these devices [34, 35]. Due to the above-mentioned versatile advantages of the piezoelectric-based energy harvesters, in the present work, an attempt has been made to study and investigate the nonlinear dynamics of such systems to enhance the operational frequency bandwidth as well as the energy harvesting capability. A spring-coupled double cantilever-based PEH is explored under parametric instability. Also, the effect of the magnetic force on such a system is examined thoroughly. A magnetically coupled double beam-based piezoelectric energy harvester is investigated under galloping excitation. The structure of the thesis is outlined in the following section.

1.2 Thesis organization

The present thesis consists of 6 chapters, which are described below.

Chapter 1 starts with a brief introduction and overview of piezoelectric energy harvesting. In Chapter 2, a thorough literature review has been presented, comprising the use case of

piezoelectric energy harvesting, its prospective applications and limitations. Some technical research gaps are also pointed out, which provide the motivation to conduct the present work. Through several studies and investigations, the objective of this work is fulfilled.

Chapter 3 presents the nonlinear dynamic analysis of a spring-coupled double cantilever beam-based piezoelectric energy harvester under parametric excitation. Cubic and inertial nonlinearities are considered while formulating the governing coupled electro-mechanical equations of motion of the proposed system. The effects of coupled spring stiffness, tip masses attached to the beams, load resistance and external excitation parameters on the output voltage and power are studied.

Chapter 4 depicts the nonlinear dynamic study of a similar PEH as described in Chapter 3 with minor geometric changes in the system configuration. The major contribution of this chapter includes the effect of externally applied magnetic repulsive force on the system dynamics. The parametric instability regions, time and frequency response curves, voltage and power output for different parameters have been examined. Bifurcation and stability analysis have also been performed.

Chapter 5 contains the dynamic analysis of a double cantilever beam-based piezoelectric energy harvester subjected to galloping excitation. The beams are coupled with a magnetic force, which brings rich nonlinear phenomena such as periodic, quasi-periodic and chaotic oscillations. A detailed investigation is carried out on the influence of magnet spacing, revealing its critical role in system dynamics. Considering the Beaufort wind scale, the maximum obtainable output power of the PEH system is investigated with varying load resistance. Theoretical predictions are supported by corresponding experimental studies.

Chapter 6 outlines the general and specific conclusions, along with a discussion on the scope for future research.

Chapter 2

Literature Review

2.1 Introduction

The interdisciplinary nature of piezoelectric energy harvesting showcases situations where researchers and industrialists all over the globe approach towards its potential benefits. Consequently, this chapter aims to cover the state-of-the-art research in the areas of fundamentals of piezoelectricity, piezoelectric materials, potential applications of piezoelectric energy harvesting, various sources of vibration for piezoelectric energy harvesting, mathematical modelling, miscellaneous PEH systems and electrical circuits behind piezoelectric power generation, which are discussed in consecutive sections. The technical gaps for the motivation to carry out this research are also described in this chapter.

2.2 Fundamentals of piezoelectricity

2.2.1 Brief Historical Remarks

In the late 19th century, Pierre and Jacques Curie first experimentally observed an interesting property in certain crystals, like quartz and tourmaline, that they generate surface-bound electrons when deformed mechanically. This effect was later referred to as the direct piezoelectric effect. In 1881, the converse piezoelectric effect was mathematically predicted by French physicist Gabriel Lippmann. This converse effect was experimentally confirmed by the Curie brothers once again. In 1950, the first piezoelectric material was synthesized, which had higher electromechanical coupling than any other naturally available piezoelectric material. Later, the breakthrough happened with the development of Lead Zirconate Titanate (PZT) type material. Variations of the originally developed PZT are still widely used.

2.2.2 Basic Principles and Constitutive Equations

A commercially available piezoceramic comprises a piezoelectric material sandwiched between two surface electrodes, as shown in Figure 2.1. When the ceramic is subjected to

mechanical stress, strain is developed, and correspondingly, electric polarization is produced on the surface of the material due to the direct piezoelectric effect. The generated electric polarization is proportional to the strength of the applied mechanical strain. Synthetic piezoceramics such as PZT-5 are manufactured and artificially poled using a poling process, which involves subjecting the ceramic to a strong direct current (DC) field at a certain temperature. The result of the poling process induces permanent polarization of the ceramic, even after the DC source is removed.

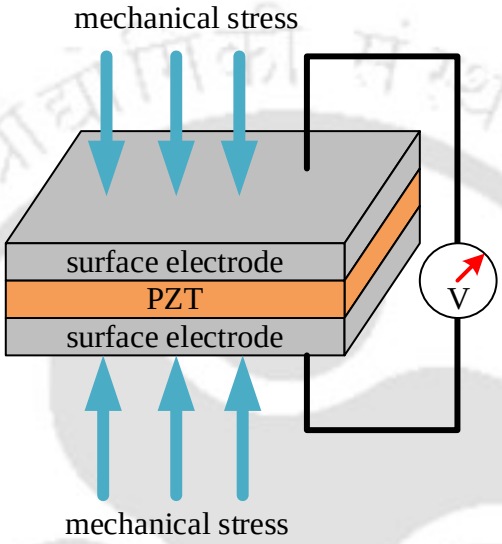

Figure 2.1: Schematic diagram of a piezoelectric transducer under mechanical stress

The IEEE standard on piezoelectricity [36] provides the linear piezoelectric constitutive equations. These equations describe the relationship between mechanical properties (stress and strain) and electrical properties (electrical field and displacement). Four field variables need to be considered for expressing the relation, which are mechanical stress (T_{kl}), mechanical strain (S_{ij}), electric field (E_k) and electric displacement (D_i).

$$S_{ij} = s^E_{ijkl} T_{kl} + d_{kij} E_k \tag{2.1}$$

$$D_i = d_{ikl} T_{kl} + \varepsilon^T_{ik} E_k \tag{2.2}$$

Here d_{kij}, s^E_{ijkl} and ε^T_{ik} denote piezoelectric constant, elastic compliance and permittivity constant, respectively. The details of the above-mentioned Eq. (2.1) and Eq. (2.2) can be found in the book of [37]. There are three piezoelectric modes, i.e., d_{31}, d_{33} and d_{15} which are used for energy harvesting [38]. These modes are different with respect torespect to the direction of the stress and field polarization. The direction of the generated electric field and the input strain

is perpendicular in d_{31} mode [39] and parallel in d_{33} mode [40]. In the following section, various types of piezoelectric materials have been discussed.

2.3 Piezoelectric materials

Naturally available piezoelectric crystals include quartz (SiO_2), tourmaline, topaz, Rochelle salt, and cane sugar. Some organic materials, such as bone, silk, wood, dentin, etc., also exhibit piezoelectric properties. Human-made piezoelectric materials can be classified into three types: polymer, ceramics and composite-based materials [41, 42]. Ceramic-based piezoelectric materials can be classified as Lead-based and Lead-free materials. Lead-based materials are Lead Titanate (PT), Lead Zirconate Titanate (PZT), Lead Lanthanum Zirconate Titanate (PLZT), Lead Magnesium Niobate ($MgNb_2O_9Pb_3$) and Lead-free materials are Barium Titanate (BT), Cadmium Sulphide (CdS), Potassium Niobate ($KNbO_3$), Lithium Niobate ($LiNbO_3$), Zinc Stannate ($ZnSnO_3$), Zinc Oxide (ZnO), Iron Oxide (Fe_3O_2), Aluminium Nitride (AlN) etc. Polymer-based piezoelectric materials are Polyvinylidene Difluoride (PVDF), Urea, Polylactic Acid, Cellulose Acetate, and Polyacrylonitrile. Examples of some piezoelectric composites are PVDF-PZT, Macro Fibre Composite (MFC), PZT-TiO_2 composite, etc. Another flexible type of piezo-ceramic AlN is used in a low-frequency ring-type energy harvester [43]. Nowadays, flexible piezoelectric materials are widely manufactured for the purpose of biomedical applications [44]. MFC piezoelectric patches are highly flexible and durable for field application and are commonly used for energy harvesting. In the next section, potential applications of PEH systems have been reviewed.

2.4 Applications of PEH

PEH devices are commonly used in structural health monitoring of bridges [45-47], buildings [48], aircraft [49, 50] and railways [51, 52], small-scale machine components like tire pressure monitoring devices [53], rolling bearings [54]. In electro-mechanical systems, wireless sensor networks [55, 56] are used for data transmission, which can be powered by integrated PEH systems. Energy harvesting from human activities [57, 58] to power up smart wearable devices [59, 60] and implantable biomedical equipment [61-63], such as a pacemaker [64], pressure and tissue stimulation [65], is another potential application. In the present day, PEH systems are employed in agricultural fields as well for powering smart sensors and monitoring plant growth and soil quality. In military and defence sectors [69-72], PEH systems are getting

employed for powering sensitive devices, unmanned aerial vehicles (UAVs). The next section portrays the basic PEH systems.

2.5 Conventional PEH systems

Figure 2.2 shows different types of conventional PEH systems. These PEHs consist of elastic structures (substrate or beam) with piezoelectric patches bonded to the substrate either in unimorph [17, 73] (on one side, Figure 2.2 (a), (c)) or bimorph [15, 19, 73] (on both sides, Figure 2.2 (b), (d)) condition. External excitation in the form of base excitation [15, 17-19] (Figure 2.2 (a), (b), (c)) or wind excitation [20, 22] (Figure 2.2 (d)) is induced on the system to start oscillation and further harvest energy. A tip mass is attached at the free end to reduce the natural frequency of the system and increase the deflection. In the case of wind-excited systems, a bluff body is attached at the tip position of the beam.

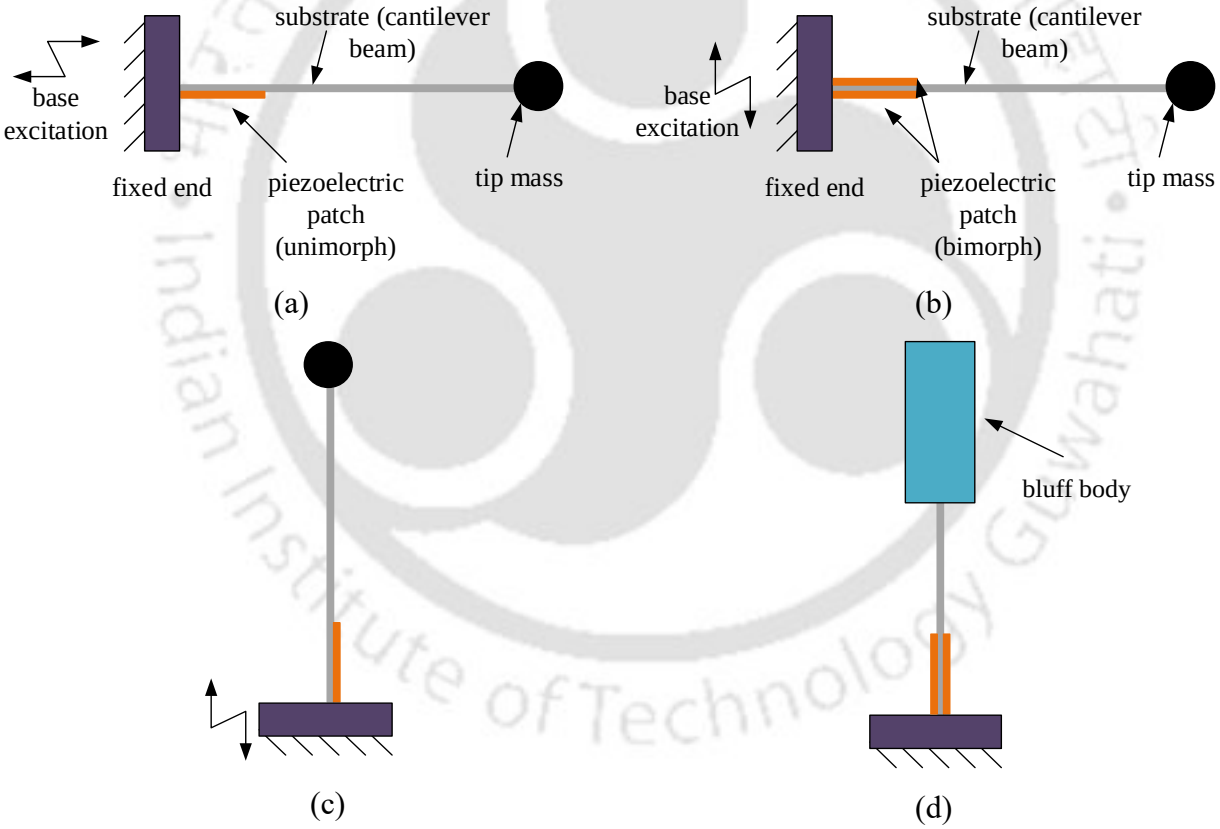

Figure 2.2: Different configurations of conventional PEH systems (a, b) horizontal PEH with base excitation, (c) vertical PEH with base excitation, (d) wind-excited vertical PEH

The electricity generated across the piezoelectric patch is in alternating current (AC) form, which needs to be converted into DC for storage in a battery. Some energy storage devices are a capacitor, a super-capacitor or a combination of a battery with a capacitor. In case of multiple piezoelectric components, a series or parallel connection is adopted between them. The detailed

procedure can be found in the book of Erturk and Inman [73]. Based on the types of external excitation, the next section discusses the base-excited PEHs.

2.6 Base excited PEH systems

Generally, the cantilever beam-based PEH systems are subjected to external excitation from the ambient vibration. External excitations can be broadly classified into deterministic and stochastic forms. Among them, deterministic cases are studied extensively. For the PEH systems with deterministic excitations, harmonic forces are mostly studied. Harmonic base excitation can be categorized as direct or parametric excitation. The nature of vibration in the PEH is linear when the excitation amplitude is small. With high excitation amplitude and under certain resonance conditions, the vibration response can be nonlinear. Based on the type of base excitations, the following subsections represent directly and parametrically excited PEHs, and PEHs with stochastic excitation.

2.6.1 PEH systems with direct base excitation

In the case of a directly excited PEH, the direction of external excitation and the direction of oscillation of the system are same. This is the most explored excitation condition for piezoelectric energy harvesting so far (Erturk and Inman [74, 75], Roundy et al. [76], Friswell et al. [77]). For directly excited linear PEH systems, the excitation frequency must be calibrated nearly equal to the natural frequency of the system. A simple resonance condition arises, which leads to high-amplitude oscillation and further voltage generation. Whereas, for nonlinear PEHs with direct excitation, subharmonic and superharmonic resonance conditions also may occur depending on the excitation frequency.

2.6.2 PEH systems with parametric excitation

Parametric instability arises due to periodic variation of a system parameter (typically stiffness), which enables energy transfer directly into the system. When the external excitation frequency satisfies the parametric resonance condition (nearly twice the natural frequency), the system absorbs energy efficiently, leading to exponential growth of oscillation amplitude within the instability region.

In the context of piezoelectric energy harvesting, larger oscillation amplitudes result in higher strain in the piezoelectric material, which directly enhances the generated voltage and power output. Therefore, operation within or near the parametric instability region significantly

improves energy harvesting performance compared to conventional direct excitation. The governing equation of a parametrically excited system resembles the Mathieu type equation [78]. When the excitation frequency is twice the natural frequency of the system, principal parametric resonance [79, 80] takes place. However, if the external excitation frequency is equal to the sum or difference of the two fundamental frequencies, then a combinational parametric resonance condition arises [81]. In recent years, there have been several studies of directly excited PEH systems; in parallel, the number of research articles on parametrically excited PEHs is comparatively less. Xia et al. [82] have investigated the performance comparison between directly and parametrically excited PEH systems. With suitable tuning, parametric excitation leads to larger amplitude oscillation of the system, which is capable of more energy harvesting compared to directly excited systems. However, due to large oscillations, there may be the possibility of system failure. There are several such systems where parametric resonance occurs and causes damage to these systems [83]. Mechanical amplification is another phenomenon of such systems [84, 85]. Existence of such behaviour brings instabilities which can be observed in ship rolling [86], rail corrugation [87], rail vibration and noise [88], fluid conveying pipes [89].

Daqaq et al. [90] investigated the parametrically excited nonlinear PEH using a lumped parameter approach. The system configuration is horizontal. The effects of load resistance and electro-mechanical coupling on generated voltage and power are analyzed. Alevras et al. [91] analyzed a cubic nonlinear Mathieu-type PEH and proposed that the system can be very robust for broadband operation. Time-varying damping causes parametric excitation, and such systems enhance the bandwidth and harvesting capability of the PEH, compared to directly excited systems [92]. Yildirim et al. [93] designed an array of cantilever-based PEH under parametric excitation. Here, a significant improvement in frequency bandwidth has been reported. Each of the beams produces power in the mW range.

Jia and Seshia [94] developed an autoparametric PEH system, where parametric and autoparametric base excitation show superiority over direct excitation. Yan and Hajj [95] have studied an autoparametric vibration energy harvester-absorber system. Similarly, Kecik and Borowiec [96] also studied a combined harvester-absorber system with autoparametric excitation. The chaotic motion of the pendulum generated the highest output voltage. Tan et al. [97] have investigated an autoparametric PEH system with a chaos control feature. The system features internal resonance and enhanced bandwidth.

Bobryk and Yurchenko [98] reported a PEH system under random parametric excitation, and results reveal significantly enhanced performance. Ramakrishnan and Edlund [99] studied stochastic stability and noise reduction of a parametrically excited PEH. Li et al. [100] explored the coherence resonance of a buckled PEH under stochastic parametric excitation. A robust parametrically excited PEH system with resonant attachment has been reported by Fan et al. [101]. The system experiences a broadband frequency range.

2.6.3 Stochastic excitation

As the majority of the ambient excitations are random, several studies have focused on investigating the dynamics of PEH systems under stochastic excitations. Daqaq [102] studied a PEH with cubic and inertial nonlinearity, considering Gaussian white and coloured noise. Results show that nonlinearities can enhance the performance of the harvester. Adhikari et al. [103] investigated an energy harvester under Gaussian white noise. Exact closed-form solutions have been obtained. Paula et al. [104] demonstrated a piezomagnetoelastic beam subjected to random excitation. Performance is enhanced when the response oscillates around the stable equilibrium points. Ali et al. [105] also studied a piezomagnetoelastic energy harvester under broadband random excitation. The excitation is in the form of zero-mean white noise. Mean harvested power can be maximized with an optimized design. A nonlinear magnetoelastic energy harvester with white Poisson noise has been investigated by Khovanova and Khovanov [106]. Improved performance is observed under random impulsive excitation for monostable and bistable systems. Litak et al. [107] examined a bistable piezomagnetoelastic energy harvester with Gaussian white noise excitation. A similar type of system has been studied by Kumar et al. [108] also. Here, the solution approach using the Fokker-Planck (FP) equation reduces the time of computation.

A cantilever beam-based PEH has been studied by Lan et al. [109] under vertical stochastic excitation. Improved efficiency has been reported from this study. Bobryk and Yurchenko [98] studied the effect of ambient random excitation and telegraphic noise as parametric excitation on the performance of a linear energy harvester. A hybrid piezoelectric and electromagnetic energy harvester under broadband random vibration has been explored by Li et al. [110]. Study shows that a stronger coupling strength widens the frequency bandwidth. Cottone et al. [111] investigated a buckled beam-based PEH under random excitation. The system exhibits superior power generation for a wide range of resistors. In the following section, flow-induced PEH have been reviewed.

2.7 Flow induced PEH systems

Flow induced vibration (FIV) in elastic structures is a common phenomenon when subjected to fluid flow. FIV-based instability can be majorly classified into three types, i.e., galloping, vortex-induced vibration (VIV) and flutter. Galloping is a low-frequency, high-amplitude oscillation of structures in housing with bluff bodies. When the aerodynamic lift increases with displacement, the motion is fed with more energy, leading to larger oscillation amplitude. The aerodynamic forcing of galloping is accounted for as the negative type of damping in the equation of motion of the energy harvesters. VIV is caused by vortex shedding of bluff bodies, and further frequency lock-in with the natural frequency of the system causes oscillation. The amplitude of oscillation in VIV is less compared to galloping. Flutter is another type of dynamic instability caused by the coupling of aerodynamic force and structural elasticity. Based on the three types of aerodynamic instabilities, the PEH systems under FIV have been discussed in the following subsections.

2.7.1 Galloping based PEH systems

Galloping is an aerodynamic instability which is commonly observed in electrical transmission cables and tall structures when they are subjected to continuous wind flow. It is generally a self-excited vibration [112]. Hartog and Pieter [113] explained the criteria for this instability. A critical wind speed (onset of galloping) is required to start the oscillation. Before exploring galloping-based energy harvesting, researchers used to study the effect of galloping on structural stability. Novak [114] studied the galloping of structures having a prismatic shape. Nayfeh and Abdel-Rohman [115] analyzed a cantilever beam system subjected to galloping force. The study considers higher-order lift force. Alonso et al. [116] studied the effect of cross-section and shape of the bluff bodies on galloping instability. Mukhopadhay and Dugundji [117] investigated the nonlinear dynamics of a slender cantilever beam under galloping.

In the last two decades, galloping instability has been utilized for piezoelectric energy harvesting. Ewere and Wang [118], Zhao and Yang [119], Zhao et al. [120], Abdelkefi et al. [121], Barrero-Gil et al. [122] further inspired the research on galloping-based piezoelectric energy harvester. Sirohi and Mahadik [123] developed a GPEH for low-power sensors. Truitt and Mahmoodi [124] critically reviewed various designs and methodologies of wind-excited energy harvesters. Ewere et al. [125] studied a GPEH with a bio-inspired square-shaped bluff body. Roohi et al. [126] investigated the effect of an elliptical bluff body on the performance

of the GPEH. Dash et el. [127] explored higher-order aerodynamic force representation of the GPEH system and studied the dynamic stability. Transverse galloping of a rhombic-shaped bluff body has been investigated by Ibarra et al. [128]. Javed and Abdelkefi [129] found that the geometry of the bluff body and angle of attack affect the performance of the energy harvester. A nonlinear restoring force has been introduced by Bibo et al. [130] to enhance the output of the GPEH. In most of the literature on GPEH, aerodynamic force is modelled using quasi-steady approximation, while Yan and Abdelkefi [131] introduced nonlinear quasi-steady approximation.

Abdel-Rohman [132] examined the impact of galloping on tall prismatic structures with a square cross-section. The structure was modelled with two degrees of freedom (DOF) movement, both along and across the direction of the wind. His findings showed that the motion along the wind direction was relatively small compared to the motion across it. While many studies use steady wind for simplicity, actual wind conditions are often unsteady and turbulent. To address this, Abdel-Rohman [133] extended his work by analyzing a similar system under unsteady wind, using a single harmonic component to represent wind fluctuations in a simplified way. Later, Zulli and Luongo [134], as well as Luongo and Zulli [135], considered wind with two frequency components to better capture the variability. Additionally, a study by Kwuimy et al. [136] explored how piezoelectric energy harvesters (PEHs) perform in turbulent airflow. To aid in designing such systems, realistic wind data maps [137] can be helpful in estimating average wind speeds at specific locations.

2.7.2 VIV based PEH systems

VIV is a phenomenon where a bluff body placed in a fluid flow starts to oscillate due to the alternating shedding of vortices. These oscillations, especially when the vortex shedding frequency matches the natural frequency of the structure (known as lock-in), can be used to generate electricity if piezoelectric materials are attached to the vibrating structure.

The idea of using VIV for energy generation was notably advanced by Bernitsas et al. [138]. Since then, researchers have developed various models, particularly based on wake oscillator theory, to better understand and predict the behaviour of VIV energy harvesters [139, 140]. Dai et al. [141] formulated a nonlinear electromechanical model for VIV-PEH, analyzing how electrical load and coupling parameters influence performance. Chen et al. [142] studied an array of VIV harvesters, showing that interactions among harvesters significantly boost voltage output—up to 168% improvement compared to a single device. An et al. [143] investigated the

performance evaluation of a vortex-induced piezoelectric energy converter (VIPEC) with a computational fluid dynamics approach. Adhikari et al. [144] studied a VIV-based PEH under a random flow field. For the cases without the inductor, the average harvested power monotonically decreases with an increase in the damping ratio and a decrease in the coupling factor. Naseer and Abdelkefi [145] have investigated the efficacy and nonlinear modelling of a VIV-based energy harvester. Here, monostable and bistable configurations have been considered. Quenching phenomenon is observed in the system. A bi-directional VIV-based PEH system has been explored by Su and Lin [146]. A U-shaped model is designed in this study, and the aspect ratio of the model can be adjusted to change the lock-in wind speed. A circular cylinder with two splitter plates for VIV-based energy harvesting can be found in the study of Wang et al. [147]. The installation angle of the splitter plates affects the harvesting efficiency of the PEH system. A comprehensive experimental investigation on the shape of a bluff body for VIV-based PEH has been done by Mehdipour et al. [148]. Study shows that bluff bodies with higher drag coefficients can harvest more energy. Lu et al. [149] examined a two DOF system for VIV-based piezoelectric energy harvesting. Study reveals that by tuning the masses and stiffnesses, the lock-in region can be adjusted. Franzini and Bunzel [150] numerically investigated single and two DOF PEH systems under VIV. Results show that 50% harvesting efficiency can be increased with a particular reduced velocity. Jia et al. [151] modelled an equivalent circuit and analyzed a VIV-based PEH system. The proposed system can harvest an output power of 81.71 μW with a capacitor filter and 114.64 μW with an alternating circuit interface. In the next subsection, Flutter-based PEH systems are discussed.

2.7.3 Flutter based PEH systems

Flutter, a type of self-excited aeroelastic instability, has gained attention in recent years as a viable mechanism for broadband and high-efficiency piezoelectric energy harvesting. Unlike vortex-induced vibration (VIV) or galloping, flutter occurs due to the coupling of aerodynamic forces with structural modes, typically in lifting surfaces like plates, beams, or aerofoils.

McCarthy et al. [152] explored the downstream flow behaviour of a flutter-based PEH system. They have found 40% increment in power output from the downstream harvester. For this study, a smoke wire flow visualization with a novel bi-lighting technique has been used. Bryant and Garcia [153] proposed a novel PEH device driven by aeroelastic flutter. A simple flag and beam-based system has been studied, which is subjected to modal convergence flutter response above a critical wind speed and a limit cycle oscillation at higher wind speeds. Abdelkefi et al.

[154] have designed a piezo-aeroelastic harvester with a pitching and plunging airfoil, using springs and piezoelectric coupling on the plunge motion. Linear velocity feedback is used to reduce the flutter speed and generate limit-cycle oscillations at low wind speeds. Zakaria et al. [155] experimentally investigated a composite beam-based energy harvester under self-induced flutter. The influence of angle of attack, wind speed, and load resistance on harvested power has been analyzed. The findings reveal a complex relationship between aerodynamic loading and the resulting static deflection. A piezo-aeroelastic energy harvester based on nonlinear aeroelastic behaviour can be found in the work of Bae and Inman [156]. The system is modelled using a two-dimensional typical section airfoil. With nondimensional parameters, the governing piezo-aeroelastic equations are formulated accordingly. Abdelkefi and Nuhait [157] reported a cambered-wing based PEH system under aeroelastic flutter. The results show that with an increase in the camber, the level of the harvested power decreases.

With numerous studies on individual base-excited and wind-excited PEH systems, researchers have investigated PEH systems with combined wind and base excitations, which are presented in the next section.

2.8 Combined flow induced and base excited PEHs

While flow-induced and base-excited PEHs have been extensively studied as separate systems, recent research has focused on PEH systems that incorporate both flow-induced and base excitations to enhance energy output, bandwidth, and robustness under varying ambient conditions. Bibo and Daqaq [158] have investigated a PEH system that consists of a rigid airfoil and a torsional spring, which is subjected to combined flutter-induced instability and harmonic base excitation. Study shows that beyond the flutter speed, two distinct regions of response exist depending on the frequency of base excitation. Dai et al. [159] explored a PEH system under concurrent base excitation and VIV. The nonlinear model of the proposed system is based on the Van der Pol oscillator. An increment of 150% in power output can be observed in the lock-in region. Base acceleration can suppress vortex effects due to quenching. Stamatellou and Kalfas [160] have experimentally examined film-type piezoelectric harvesters under combined aerodynamic flutter and base excitation. Output voltage, tip deflection, and power have been analyzed to evaluate performance and identify optimal bandwidth for energy harvesting.

Zhao and Yang [161] have studied a cantilever-type PEH model under concurrent galloping and sinusoidal base excitation. The impact force is induced into the vibrating structure through

a mechanical stopper. Broadened frequency bandwidth has been achieved. A maximum power output of 3.8 mW can be harvested at a wind speed of 5.5 m/s and 0.5 g of base acceleration. A hybrid piezoelectric-electromagnetic energy harvester has been explored by Iqbal and Khan [162]. The system can harvest energy from the vibration of traffic-induced bridges and pulsating wind flow. Adding a secondary beam enhances the power output of the system by adding an extra resonance peak. Hu et al. [163] theoretically investigated a 2-DOF PEH system excited with concurrent aeroelastic and base excitation. Several interesting nonlinear phenomena, such as quasi-periodic oscillation and peak-to-valley transition, can be observed in their system. Hou et al. [164] have proposed a novel piezoelectric-electromagnetic energy harvester under combined VIV and base excitation. The dual transduction mechanism significantly improves the power output of the system. Chen et al. [165] have designed a PEH system with nonlinear softening behaviour. The system is excited with combined galloping and base excitation. Experimentally, the proposed device enhances the effective bandwidth by 300% than its linear counterpart. Kuang et al. [166] studied a magnetic transfer piezoelectric wind energy harvester using dual-mode conversion by combining vortex-induced vibration and galloping. It achieved a wide operating wind range and a peak power output of 0.78 mW, successfully lighting 10 LEDs. Xu and Zhao [167] have proposed a novel 2-DOF energy harvester with 2:1 internal resonance. The system can harness energy from combined wind and base vibrations. Using magnetic nonlinear stiffness, the system shows a 211.1% bandwidth increase and 50% higher peak voltage at 3 m/s wind and 0.9 m/s² base acceleration.

The next section deals with mathematical modelling and solution strategies for coupled electromechanical equations of motion of PEH systems.

2.9 Mathematical modelling and solution strategies

Generally, single or multiple beam-based structures are used for piezoelectric energy harvesting. The Euler-Bernoulli beam theory is commonly employed for deriving the equation of motion of these slender types of beams. Theoretical modelling of the entire PEH system includes the substrate (beam, plate, etc.), piezoelectric components (unimorph or bimorph) and their electrical characteristics, external forcing mechanisms. The piezoelectric element of the system correlates the mechanical and electrical domains; a set of coupled electromechanical equations of motion is usually obtained. For unimorph configuration, the neutral axis shifts and for bimorph configuration, the neutral axis may (asymmetric piezoelectric patches) or may not (symmetric piezoelectric patches) shift. The moment balance method or the energy principles

can be incorporated to derive the equations of motion of the system. In the cases of force or moment balance method, either Newton's second law of motion or D'Alembert's principle may be used. For the energy method, one may use the Lagrange principle or the extended Hamilton's principle. In case of complex designs of PEHs, finite element modelling (FEM) [168, 169] can be used for this purpose. Gauss's law is used to obtain the circuit equations. The equations of motion of PEHs can be linear or nonlinear depending on the system's geometry, forcing conditions and other parameters. Examples of typical linear (Eqs. (2.3), (2.4)) and nonlinear (Eqs. (2.5), (2.6)) governing equations of motion are given below. Here, $w(t)$ and $V(t)$ represent the transverse displacement of the beam and the generated voltage of the PEH, respectively. Other coefficients, ζ, ω_n, α_2, α_3, θ_1, θ_2, F, C_P and R_L denote the mechanical damping ratio, natural frequency, inertial nonlinearity, cubic nonlinearity, linear electromechanical coupling term, nonlinear electromechanical coupling term, forcing, capacitance of the piezoelectric element and load resistance, respectively.

$$\ddot{w}+2\zeta\omega_n\dot{w}+\omega_n^2 w-\theta_1 V=F(t) \tag{2.3}$$

$$C_P\dot{V}+\frac{V}{R_L}+\theta_1\dot{w}=0 \tag{2.4}$$

$$\ddot{w}+2\zeta\omega_n\dot{w}+\omega_n^2 w+\alpha_2\left(w\dot{w}^2+w^2\ddot{w}\right)+\alpha_3 w^3-\theta_1 V-\theta_2 w^2 V=F(t) \tag{2.5}$$

$$C_P\dot{V}+\frac{V}{R_L}+\theta_1\dot{w}+\theta_2 w^2\dot{w}=0 \tag{2.6}$$

It may be noted that the equations of motion can be formulated using either a lumped parameter model (discrete) [39, 90, 170, 171] or a distributed parameter model (continuous) [15, 17, 27, 77, 81]. In nonlinear equations of motion, the inertial nonlinear terms arise from the beam mass and the tip mass attached to the beam [77, 79 - 81]. Cubic nonlinearity comes into the picture when the beam is subjected to large transverse displacement [13, 17, 77, 81], which leads to a nonlinear curvature-displacement relation. Nonlinearity can arise from different types of ambient excitation, such as galloping force, which introduces cubic damping [118 - 122]. Magnetic force induces hardening and softening effects through cubic or fifth-order nonlinear terms [30, 32, 172, 173].

To solve these nonlinear coupled electromechanical equations of motion, a different analytical approach is required.The harmonic balance method (HBM), the incremental harmonic balance

method (IHBM), perturbation methods such as the method of multiple scales, the Linstedt-Poincaré method, and the method of averaging are commonly used methods for solving the coupled nonlinear differential equations. Based on the modelling approach, PEH systems can be categorized as linear and nonlinear PEH systems, which are discussed in the next sections.

2.10 Linear PEH systems

In the initial works, linear vibration-based PEH systems have been explored, where a near-resonance condition is necessary for efficient energy harvesting. Roundy et al. [170] presented a linear electromechanical model for conventional PEH with tip mass. They have fabricated a prototype of size 1 cm^3 which can generate 70 $\mu W/cm^3$ power density. Sodano et al. [174] investigated a linear PEH model theoretically and experimentally. Many researchers have investigated to enhance the power output and increase the operational bandwidth of the linear PEH systems by geometric alteration [175, 176], strain magnification [177]. One may find the details of earlier developed linear PEH systems in the review works of Anton and Sodano [178] and Cook-Chennault et al. [179]. In the next section, nonlinear PEH systems are reviewed.

2.11 Nonlinear PEH systems

The drawbacks of linear PEH systems are their limited, narrow frequency bandwidth and resonance conditions, which shift the focus towards introducing nonlinear vibration in energy harvesters. In nonlinear PEHs, usually a wider bandwidth can be found, which means a higher range of ambient energy can be harvested. As discussed earlier, nonlinearity may arise from the material behaviour or geometry of the system, which leads to cubic, inertial nonlinearities. Different forcing conditions also may induce nonlinearity into the system. Multiple resonance conditions can be observed in nonlinear PEHs depending on different types of external excitations. In these types of systems, one may find both stable and unstable fixed points, periodic responses with multiple solutions and many bifurcation points. Quasi-periodic and chaotic responses may also exist in such nonlinear systems with variation of system parameters.

In the work of Wang et al. [32], a nonlinear jump down phenomenon can be found along with periodic and chaotic inter-well motion. Friswell et al. [77] modelled a nonlinear PEH system with a cantilever beam and a tip mass. Chaotic oscillation may occur in the system depending on the excitation level and tip mass value. Karličić et al. [78] investigated a nonlinear Mathieu-Duffing type PEH system. Combined fundamental and parametric resonances can be observed. Kecik and Borowiec [96] studied an autoparametric energy harvester, which consists of a

pendulum and a nonlinear oscillator. The chaotic motion of the pendulum generates the highest power compared to the swinging motion of the pendulum. Yan and Abdelkefi [131] investigated the nonlinear characterization of a PEH system under concurrent aerodynamic and base excitation.

Several other types of nonlinear systems are also present in the field of piezoelectric energy harvesting. Critical review of such systems can be found in the work of Ahmed and Khan [7], Daqaq et al. [11], Zelenika et al. [49], Truitt and Mahmoodi [124]. The following section deals with two or multi-DOF energy harvesters with mechanical and magnetic coupling.

2.12 Coupled PEH systems with two or multiple beams

Two or multiple-beam-based piezoelectric energy harvesters are increasingly being explored due to their potential to boost power output, expand operating frequency ranges, and enhance dynamic performance under different types of excitation. Mechanical or magnetic coupling between the beams allows these systems to take advantage of internal resonances, leading to more efficient energy harvesting.

Chen et al. [30] studied a spring-coupled dual-beam-based PEH device. The magnetic force induces bistability into the system. The disturbance of the coupling spring provides additional energy. Wang et al. [32] investigated a magnetically coupled double vertical cantilever beam-based GPEH. The coupled bistable system significantly reduces the cut-in wind speed for the onset of galloping. Parametric study reveals the influences of the stiffness ratio of the beams, the effective mass ratio and the width of the bluff body. Lan et al. [173] examined a base-excited double cantilever beam-based PEH system under magnetic interaction. The benefits and trade-offs are highlighted in this study. The operation frequency bandwidth increases significantly while the overall harvested power from both the beams is restricted. Fan et al. [180] studied a magnetically coupled double-beam piezoelectric energy harvester under parametric excitation. Study shows that the bistable interwell periodic motion and threshold amplitude for parametric resonance depend on the base excitation level. Malaji and Ali [181] studied a magneto-mechanically coupled double pendulum-type energy harvester, showing that the coupled system can be operated in a broader frequency bandwidth with increasing power output.

Song et al. [182] proposed a double cantilever beam-based PEH that considered both bending and torsional modes, experimentally validating the model and demonstrating performance

improvements over single beam PEHs. Ramalingam et al. [183] investigated a double-beam-based PEH with a tapered cavity, highlighting its enhanced operating frequency bandwidth and output response. Machado et al. [184] studied a double cantilever beam PEH with a spring stop under rotational excitation, observing that the contact force was maximized at the lowest rotational frequency, leading to an 80% energy conversion rate. Lu et al. [185] examined a spring-coupled double cantilever beam PEH under rotational excitation and magnetic repulsive force, revealing a wide operating frequency range (10-35 rad/s). Eshtehardiha et al. [186] have studied a directly excited PEH consisting of a double cantilever beam that is connected by a spring. Externally applied magnetic force results in a wide operational frequency bandwidth, which precisely depends upon the selection of magnetic parameters and the distance between the permanent magnets. A spring-coupled double-beam-based PEH system can be found in the work of Xiang et al. [187]. An additional magnetic force introduces a double potential well. Numerical and experimental results verify enhanced power output compared to traditional bistable PEH systems. Shao et al. [188] investigated a magnetically coupled dual cantilever-based PEH system with an annular potential well. The beams are placed orthogonal to each other. The response oscillates around the potential barrier rather than jumping over it, leading to high output voltage.

Over the last two decades, many researchers have presented literature reviews on energy harvesting systems. In the following section, published review articles on energy harvesting are discussed briefly.

2.13 Review works on PEH systems

This section presents a concise overview of key developments in the field of piezoelectric energy harvesting, focusing on review papers published since 2003.

One of the earliest and most influential reviews in this area was conducted by Roundy et al. [76], who compared various power scavenging methods and traditional energy sources. They discussed three primary energy conversion mechanisms: electromagnetic, electrostatic, and piezoelectric. A more focused review was later offered by Sodano et al. [189], who concentrated on vibration-based PEH systems. They recommended using rechargeable batteries over capacitors and highlighted several critical aspects, including the design of harvesting circuits, optimal placement of harvesters, tuning mechanisms, and identifying practical applications such as wireless sensors and self-powered damage detection systems.

DuToit et al. [190] introduced a coupled electromechanical model to examine the dynamic behaviour of PEH systems and validated it with experimental results. Anton and Sodano [178] provided a detailed review of piezoelectric energy harvesters from 2003 to 2006, emphasizing the need to develop complete systems with practical applicability. Their work addressed advancements in piezoelectric configurations, power circuitry, and storage, and discussed energy sources from biomedical, fluid flow, and MEMS applications. They also explored materials beyond traditional piezoceramics, such as PVDF, Active Fibre Composites (AFC), and Macro Fibre Composites (MFC), for use in energy harvesting. A more detailed discussion of PVDF can be found in the work by Kawai [191].

Wei and Jing [192] reviewed the fundamentals of vibration energy harvesters (VEHs), including conversion mechanisms, theoretical models, and potential applications. Priya [193] offered insights into material selection and modelling techniques for evaluating system efficiency and output power. Alireza et al. [194] presented a comprehensive review of kinetic energy harvesting via piezoelectric and electromagnetic transduction methods.

Cook-Chennault et al. [179] acknowledged the potential growth of VEHs in powering sensors, condition monitoring devices, biomedical devices, and wearable electronics. Similarly, Bogue [195] discussed commercially available harvesters based on electrodynamic, piezoelectric, and thermoelectric transductions, suggesting their use in automotive applications—such as tire pressure monitoring using vehicle-induced vibrations. Shaikh and Zeadally [196] provided an extensive overview of energy harvesting strategies for wireless sensor networks, covering various ambient sources including mechanical and human motion.

Kim et al. [197] focused on the integration of piezoceramics and piezopolymers in VEHs. Their review included critical system components such as power electronics, storage elements, and structural substrates (e.g., cantilever, cymbal, stack, and shell). They highlighted key challenges in developing flexible piezoelectric materials with high coupling efficiency and the need for more efficient circuitry. The application of these materials in wearable biomedical devices was also discussed. Further advancements in flexible piezoelectric materials used for energy harvesting and actuation were reviewed by Dagdeviren et al. [198].

Twiefel and Westermann [199] surveyed both linear and nonlinear harvesting systems, including bistable/multistable configurations, amplitude limiters, and resonance tuning techniques. Harne and Wang [200] delved deeper into nonlinear bistable systems, covering

modelling strategies and key challenges. Xiao and Wang [201] provided a broad review that included linear and nonlinear systems, materials, circuitry, and large-scale applications.

Tuning the resonant frequency of harvesters has been a major focus for enhancing performance. Zhu et al. [202] reviewed mechanical and electrical tuning strategies, while Yildirim et al. [203] explored amplification, resonance tuning, and the use of nonlinear oscillations. Ibrahim and Ali [204] offered a detailed survey of both manual and autonomous frequency tuning methods, stressing the importance of self-tuneable systems and MEMS-based PEHs. Li et al. [205] focused on optimizing system configuration, material choice, and circuitry for overall performance enhancement.

Hybrid energy harvesting, especially systems utilizing both aerodynamic and elastic forces were reviewed by Abdelkefi [206], whereas Tan et al. [207] concentrated on MEMS-based electromagnetic harvesters. Uchino [208] reviewed general strategies for improving harvesting efficiency, and Wong et al. [209] specifically looked at raindrop energy harvesting. Their experiments indicated that bridge-type structures outperform cantilevers in voltage generation due to structural advantages.

In recent years, attention has increasingly shifted from linear to nonlinear vibration systems, which offer the potential for broader frequency bandwidth and improved energy capture. Daqaq et al. [11] provided an in-depth review of how nonlinearity can benefit VEH performance. They also emphasized the importance of internal resonance mechanisms, where modal energy exchange enables efficient harvesting at low frequencies. Panda et al. [62] reviewed piezoelectric energy harvesting in the field of biomedical applications. Sezer and Koç [210] published a comprehensive review of PEHs, covering their principles, operational modes, and advancements in various material types, including inorganic, organic, composite, and bio-inspired materials. It also highlights applications across multiple fields such as transportation, biomedicine, and smart systems. In the next section, the electrical circuit study related to the explored PEH systems is discussed.

2.14 Electrical circuits

Electrical circuits play a crucial role in the efficient operation of PEH systems. A typical electrical interface comprises an AC-DC rectifier, voltage regulator, and energy storage component, such as a capacitor, supercapacitor, or rechargeable battery (Li et al. [205]). In

some configurations, DC-DC converters (such as buck or boost converters) are also employed to regulate the output voltage as per load requirements.

Over the years, several efforts have been made to enhance the performance of electrical circuits used in PEH systems. Ramadass and Chandrakasan [211] proposed the use of a bias-flip rectifier with a shared inductor, replacing the conventional full-bridge rectifier, which can improve power extraction while reducing the number of passive components. An asynchronous full-wave rectifier was explored by Guilar et al. [212] to reduce the voltage drop across diode bridges, especially for systems involving multiple piezo-generators.

To get even better performance, more advanced circuits like synchronized switch harvesting on inductor (SSHI) were created. SSHI circuits use an inductor and switch to reverse the voltage across the piezoelectric element, improving energy capture. Both parallel (P-SSHI) and series (S-SSHI) types exist. P-SSHI designs by Hsieh et al. [213] and Sanchez et al. [214] showed 3 to 6 times more energy than a regular full-wave rectifier. Another type, synchronous electric charge extraction (SECE), doesn't need impedance matching and works well under varying loads. New versions like bidirectional SECE [215] and unipolar SECE [216] improved performance, especially at low voltages.

The design and optimization of interfacing circuits have also been widely explored in the literature to improve energy conversion efficiency and overall system performance [119, 151, 217]. Various energy storage components have been employed, including capacitors, supercapacitors [218, 219], and rechargeable batteries [220, 221]. Among these, supercapacitors and rechargeable batteries are generally preferred due to their better suitability for continuous energy supply [222, 223]. Although capacitors can deliver quick bursts of energy, they are limited in providing a sustained power supply [224]. Additionally, leakage resistance and the characteristics of the piezoelectric element significantly influence the efficiency of the storage system [219]. Commercially available energy harvesting integrated circuits (ICs) are also commonly used for power management in PEH systems [225, 226]. For deeper insights into electrical circuits tailored for energy harvesting applications, the works of Ottman et al. [227, 228] provide a comprehensive understanding.

2.15 Summary and identification of research gaps

The literature review gives a detailed understanding of how PEH has developed over the years. It covers the basics of piezoelectricity, different materials used, how these systems are designed

and modelled, their practical uses, and what types of vibrations are used to generate energy. Different types of piezoelectric materials are used in energy harvesters, which include ceramic-based materials like PZT and flexible materials like PVDF. Composites like PVDF-PZT or MFC are also common. These materials are chosen based on where and how the energy harvester will be used. For example, flexible materials are better for wearable devices, while strong ceramics work well in industrial applications.

In early studies, linear cantilever beam-based systems were popular due to their simple structure and ease of design. However, these systems only work well at or near their natural frequency. This means that if the vibration frequency changes, the system becomes less efficient. Because real-world vibrations are not always steady or predictable, researchers began exploring nonlinear systems to overcome this limitation. While in most linear systems, small curvature of the beam is considered, in some cases, moderately large curvatures are considered, which gives rise to geometric nonlinearity. In some studies, tip mass is considered to enhance the bending and, correspondingly, higher output voltage and power. Commonly explored base excitation condition accounts direct harmonic excitation, whereas some literature focuses on parametric and stochastic random excitations. Various resonance conditions have also been investigated, such as simple resonance, subharmonic, and superharmonic resonance. Further, one may opt for principal and combinational parametric resonances to enhance the frequency bandwidth of operation. While a single-mode approximation is taken for analysis in most of the literature, a few studies account for a larger number of modes. In some cases, these modes are in integer relations, which may give rise to 1:1, 1:2 or 1:3 internal resonance conditions. Such internal resonances can be achieved by attaching a mass at a specific position of the cantilever beam. Mostly, in nonlinear PEHs, rich phenomena like modal interaction, bifurcations, quasiperiodicity, chaos, intra- and inter-well motion can be observed.

Another area of review focuses on multi DOF systems. Instead of a single cantilever beam, these systems use two or more beams coupled together using springs or magnets. These setups can transfer energy between beams, add more resonance modes, and improve the total power output. Magnetic coupling also introduces bistable or multistable behaviour, which adds complexity but also enhances performance. Most of the multi DOF systems are studied under direct base excitation, rotational motion or FIV. However, these systems under parametric excitation are yet to be explored.

The review then discusses electrical circuits, which are just as important as the mechanical design. The voltage generated by piezoelectric materials is usually AC and needs to be converted into DC before it can be stored or used. Circuits like full-bridge rectifiers, SSHI and SECE are used to do this more efficiently. Some circuits are specially designed to extract more power under variable loads or at low voltages. Storage devices like supercapacitors, rechargeable batteries, or hybrid systems are also discussed. Based on the review of nearly 230 studies, the following section presents some research gaps.

2.15.1 Research gaps

The field of piezoelectric energy harvesting (PEH) has seen substantial progress over the past two decades, particularly in systems subjected to base and wind excitations. However, several key gaps remain unaddressed, especially for complex structural configurations. The following research gaps are identified based on a critical review of existing literature:

- **Limited studies on parametrically excited two DOF systems:**

  Most existing studies on base-excited PEHs focus on single-beam systems and typically employ either direct or parametric excitation. Although some research has extended to two DOF double beam systems, these are primarily analyzed under direct excitation scenarios. In contrast, detailed investigations of two DOF PEHs under parametric excitation are limited**.**

- **Lack of analysis on spring-coupled beam systems:**

  Several two or multi DOF PEHs use spring-coupled piezo beams [31, 186] or special cantilever geometries to study dynamic coupling. These models are mostly driven by direct base excitation, which typically leads to primary and internal resonance responses**.** However, the potential of energy harvesting from spring-coupled two DOF systems, especially under parametric excitation conditions, remains underexplored.

- **Under-explored magnetic coupling in two DOF PEHs under parametric excitation:**

  Single DOF PEHs influenced by magnetic forces [145, 172, 180, 200] have been extensively investigated. Variations in magnet position, strength, and orientation have enabled the bi-stable, tri-stable, and quad-stable systems**,** each showing rich nonlinear dynamics. However, in the case of two DOF systems with magnetic coupling**,** only a

handful of studies exist, mainly under direct base excitation [30, 33, 173, 182, 188] or rotational motion [184, 185, 229-231]. To date, there is a lack of work examining the effect of magnetic forces in such configurations under parametric excitation conditions.

- **Insufficient integration of galloping and magnetic nonlinearities in two DOF PEHs:**

  Wind-induced vibrations, particularly galloping, have been widely explored for energy harvesting using bluff bodies in single DOF configurations. A few studies have extended these concepts to two DOF systems. There exists a significant opportunity to explore how magnetic coupling affects the energy harvesting performance in double-beam or multi DOF PEHs subjected to wind-induced galloping excitations.

With the above-mentioned research gap, the following section addresses the objective of the present research work.

2.16 Objectives of the present work

Considering the research gaps from the current state-of-the-art literature, the objectives of the present work are as follows.

- To study the nonlinear dynamics of a spring-coupled double cantilever beam-based piezoelectric energy harvester under parametric base excitation.
- To investigate the effect of magnetic force-induced nonlinearity in the spring-coupled double-beam-based PEH for the parametric resonance condition.
- Analyze the effect of magnetic coupling in a two DOF galloping-based PEH in detail for different wind speed conditions.

The studies to achieve these objectives are discussed in Chapter 3, Chapter 4 and Chapter 5.

Chapter 3

Spring Coupled Double Beam Piezoelectric Energy Harvester under Parametric Excitation

3.1 Introduction

As discussed in the previous chapter, most of the piezoelectric energy harvester (PEH) systems comprise a base-excited cantilever beam with piezoelectric patches, and with or without a tip mass. The systems are mostly modelled as directly or parametrically excited systems. In the case of directly excited systems, the direction of external excitation and the direction of oscillation of the beam are in the same direction. Whereas, for parametrically excited systems, the direction of excitation is orthogonal to the direction of oscillation of the beam. The studies on parametrically excited single cantilever beam-based PEH systems by Garg and Dwivedy [17], Abdelkefi et al. [27], and Xia et al. [82] investigated that; large amplitude oscillation due to parametric instability is beneficial for more power generation. The work of Chen et al. [30], Lan et al. [173] and Lu et al. [185] has incorporated more than one beam to enhance the performance of base-excited PEHs. These three systems are modelled considering direct excitation. Inspired by the above-mentioned research works, the present study explores the nonlinear dynamic behaviour and energy harvesting performance of a spring-coupled double cantilever beam-based PEH system under harmonic base excitation. Parametric instability is focused on in this study as it leads to higher power generation compared to a directly excited system. In the next section 3.2, detailed mathematical modelling of the governing equations of motion is carried out. Section 3.3 formulates the solution using the method of multiple scales, followed by section 3.4 with results and discussion and finally section 3.5 with a summary.

3.2 Mathematical modelling

The presently studied PEH system consists of two inverted slender cantilever beams with uniform cross-sectional area having masses attached at their tip positions and are coupled by a linear spring, as shown in Figure 3.1. The Macro Fibre Composite (MFC) piezoelectric patches

are bonded to both surfaces of the beams. The system is excited harmonically at the base with $z(t) = z_0 \sin(\omega t)$, where z_0 and ω are the amplitude and frequency of external excitation. The length, width and thickness of the beams are denoted by l_i, b_i and h_i, respectively, where $i = 1$ and 2 for the 1st and 2nd beam, respectively. The tip mass attached to the *i*-th beam and the coupled spring stiffness are denoted by m_i and *K*, respectively. The length, width and thickness of the piezoelectric MFC patch bonded to the *i*-th beam are denoted as h_{Pi}, respectively. The Euler-Bernoulli beam theory is used for mathematical modelling of beams. Along the neutral axis of the *i*-th beam, considering an arbitrary point *O* at a distance s_i from the base, the transverse displacement (in y - direction), the axial displacement (in z - direction), and the angular or rotational displacement (about x - axis) can be given by $w_{Oi}(s_i,t), u_{Oi}(s_i,t)$ and $\phi_{Oi}(s_i,t)$, respectively. The displacement-curvature relation of the beam is nonlinear due to the large amplitude oscillation of the beam.

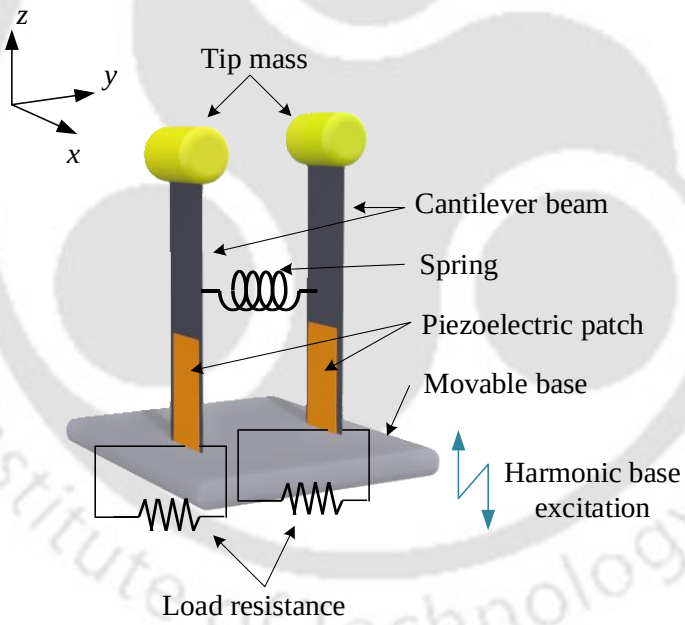

Figure 3.1: Schematic representation of the energy harvester

The axial displacement (u_{Oi}), angular displacement (ϕ_{Oi}) and curvature (κ_{Oi}) of the beams can be written in terms of the transverse displacement (v_{Oi}) as follows [13, 77].

$$u_{Oi}(s_i,t) = \frac{1}{2}\int_0^{s_i}\left(\frac{\partial w_{Oi}}{\partial \xi_i}\right)^2 d\xi,\ \phi_{Oi}(s_i,t) = \frac{\partial w_{Oi}}{\partial s_i} \text{ and } \kappa_{Oi}(s_i,t) = \frac{\partial \phi_{Oi}}{\partial s_i} \tag{3.1}$$

It is considered that the beam material is homogeneous and isotropic in nature. The transverse displacement (w_{Oi}) of the beams can be represented as a function of the generalized temporal

displacement (w_i) of the tip position of the beam and a shape function for beam elastic deformation, $\psi_i(s_i)$.

$$w_{Oi}(s_i,t) = w_{Oi}(l_i,t)\psi_i(s_i) = w_i(t)\psi_i(s_i) \tag{3.2}$$

The PEH system is assumed to be operated at a low frequency of external excitation. To bring the first mode natural frequency of the system near half of the external excitation frequency, the tip masses are substantially larger compared to the beam masses. As the first mode of vibration dominates for the present excitation condition, the single-mode approximation is sufficient to capture the dynamic behaviour of the cantilever beam. The shape function for single-mode approximation can be defined as follows [77].

$$\psi_i(s_i) = \left[1 - \cos\left(\frac{\pi s_i}{2l_i}\right)\right] \tag{3.3}$$

The total kinetic energy (T) of the proposed system can be expressed as follows,

$$T = \sum_{i=1,2}\left[\begin{array}{l}\frac{1}{2}\rho A\int_0^{l_i}\left[\left(\dot{w}_{Oi}(s_i,t)\right)^2 + \left(\dot{u}_{Oi}(s_i,t) + \dot{z}(t)\right)^2\right]ds_i \\ + \frac{1}{2}m_i\left[\left(\dot{w}_{Oi}(l_i,t)\right)^2 + \left(\dot{u}_{Oi}(l_i,t) + \dot{z}(t)\right)^2\right] + \frac{1}{2}I_{m_i}\left(\dot{\phi}_{Oi}(l_i,t)\right)^2\end{array}\right] \tag{3.4}$$

where ρ is the density of the beam material, A is the cross-sectional area of the beams, I_{m_i} and is the mass moment of inertia of the i-th tip mass. Here, a dot over the displacements denotes differentiation with respect to time (t). The total potential energy of the system consists of the strain energy of the beams, potential energy due to the gravity, and potential energy due to the coupled spring, and can be written as follows.

$$\begin{aligned}U = \sum_{i=1,2}\left[\frac{1}{2}EI_i\int_0^{l_i}\left[\kappa_{Oi}(s_i,t)\right]^2 ds_i - \rho Ag\int_0^{l_i}\left[u_{Oi}(s_i,t) + z(t)\right]ds_i - m_i g\left[u_{Oi}(l_i,t) + z(t)\right]\right] \\ + \frac{1}{2}K\left[w_{O1}(l_K,t) - w_{O2}(l_K,t)\right]^2\end{aligned} \tag{3.5}$$

Here, E is the Young's modulus of the beam material, g is the acceleration due to gravity and l_K is the distance from the base of the beam to the point where the spring is connected. The work done by internal material damping and viscous force can be expressed by a dissipation function (W_d), which can be written as follows.

$$W_d = \sum_{i=1,2}\left[\int_0^{l_i} C_i \dot{w}_{Oi}(s_i,t)\,\delta w_{Oi}\,ds_i\right] \tag{3.6}$$

where C_i is the effective damping coefficient of the *i*-th beam system. The MFC patches are bonded to the beam surface in a bimorph configuration. The beam-patch systems are considered to be symmetric and subjected to the bending strain only. The derivation of strain-induced actuation using Euler-Bernoulli beam theory has been given by Crawley and Anderson [232]. Erturk and Inman [73] have given detailed modelling procedures for piezoelectric sensors and actuators integrated with beam structures. During the oscillations of the beams, a voltage (V_i) generates across the piezoelectric layers. The generated voltage induces moments across the neutral axis of the beam-patch systems, which can be expressed as follows [77].

$$M(s_i,t) = \sum_{i=1,2} M_i(s_i,t) = \sum_{i=1,2} \gamma_P V_i(t) \tag{3.7}$$

Where γ_p is a constant which depends on the geometry of the system and the configuration of the piezoelectric transducers. In the case of bimorph piezoelectric layers in 31 configurations, the constant γ_p can be defined as

$$\gamma_P = E_P d_{31} b_{Pi}\left(h_i + h_{Pi}\right) \tag{3.8}$$

where, E_P and d_{31} denote the Young's modulus and piezoelectric charge coefficient of the MFC patch. The work done by the moment produced by the voltage about the neutral axis of the beam can be written as follows.

$$W_e = \sum_{i=1,2}\left[\int_0^{l_P} M_i(s_i,t)\,\kappa_{Oi}(s_i,t)\,ds_i\right] \tag{3.9}$$

By using Lagrange's principle and generalized Galerkin's method, the governing nonlinear coupled electromechanical equations of motion of the proposed system can be derived in terms of transverse displacement of the beam tip and are expressed as follows.

$$\ddot{w}_i + \alpha_{i0}\dot{w}_i + \alpha_{i1}w_i + \alpha_{i2}\left(\ddot{w}_i w_i^2 + \dot{w}_i^2 w_i\right) + \alpha_{i3}w_i^3 - \alpha_{i4}w_j - \alpha_{i5}V_i + f_i \sin(\omega t)\,w_i = 0 \tag{3.10}$$

$$C_P\dot{V}_i + \frac{V_i}{R_L} + \theta_i \dot{w}_i = 0 \tag{3.11}$$

Here, C_P is the capacitance of the piezoelectric (MFC) patches R_L is the resistive load connected to the electrical circuit at the MFC patch ends. It is to be noted that when $i = 1$, then $j = 2$ or vice versa. The coefficients N_{i1} to N_{i11} and θ_i used in Eq. (3.11) and (3.12) are given below. From Eq. (3.10), it can be stated that $\alpha_{11} = \omega_1^2$ and $\alpha_{21} = \omega_2^2$.

$$N_{i1} = \int_0^{l_i} \left(\psi_i(s_i)\right)^2 ds_i = \left(1.5 - \frac{4}{\pi}\right) l_i, \quad N_{i2} = \int_0^{l_i} \left[\int_0^{s_i} \left(\frac{\partial \psi_i(\xi_i)}{\partial \xi_i} \right) d\xi_i \right] ds_i = \left(\frac{\pi^2}{16} - 0.25 \right),$$

$$N_{i3} = \int_0^{l_i} \left[\int_0^{s_i} \left(\frac{\partial \psi_i(\xi_i)}{\partial \xi_i} \right) d\xi_i \right]^2 ds_i = \left(\frac{2\pi^4 - 9\pi^2}{384} \right) \frac{1}{l_i}, \quad N_{i4} = \int_0^{l_i} \left(\frac{\partial \psi_i(s_i)}{\partial s_i} \right)^2 ds_i = \left(\frac{\pi^2}{8} \right) \frac{1}{l_i},$$

$$N_{i5} = \left. \frac{\partial \psi_i(s_i)}{\partial s_i} \right|_{l_i} = \left(\frac{\pi}{2} \right) \frac{1}{l_i}, \quad N_{i6} = \int_0^{l_i} \left(\frac{\partial^2 \psi_i(s_i)}{\partial s_i^2} \right)^2 ds_i = \left(\frac{\pi^4}{32} \right) \frac{1}{l_i^3},$$

$$N_{i7} = \int_0^{l_i} \left(\left(\frac{\partial \psi_i(s_i)}{\partial s_i} \right) \left(\frac{\partial^2 \psi_i(s_i)}{\partial s_i^2} \right) \right)^2 ds_i = \left(\frac{\pi^6}{512} \right) \frac{1}{l_i^5},$$

$$N_{i8} = \int_0^{l_i} \left(\frac{\partial \psi_i(s_i)}{\partial s_i} \right)^4 \left(\frac{\partial^2 \psi_i(s_i)}{\partial s_i^2} \right)^2 ds_i = \left(\frac{\pi^8}{4096} \right) \frac{1}{l_i^7}, \quad N_{i9} = \left(\frac{\pi^2}{16} - 0.25 \right)$$

$$N_{i10} = K\left(\psi_i(l_K)\right)^2, \quad N_{i11} = K\psi_i(l_K)\psi_j(l_K), \quad \theta_i = \gamma_P \frac{\pi}{2l_i} \sin\left(\frac{\pi l_P}{2l_i} \right)$$

In the absence of piezoelectric patches and considering a single beam, the equation of motion of the system reduces to that of the model investigated theoretically and experimentally by Zavodney and Nayfeh [233]. If one considers a single beam and the forcing is direct instead of parametric, then Eq. (3.10) reduces to a similar governing equation of motion obtained by Friswell et al. [77]. The undamped natural frequency of the *i*-th beam is ω_i. For the ease of numerical study, Eq. (3.10) and (3.11) are nondimensionalized using the nondimensional time ($\tau = \omega_1 t$), tip displacement ($\bar{w}_i = w_i / l_g$) and voltage ($\bar{V}_i = \left(C_P / \left(\theta_i l_g\right)\right) V_i$). The transformed equations of motion for both beams are expressed as follows.

$$\ddot{\bar{w}}_1 + \varepsilon\bar{\alpha}_{10}\dot{\bar{w}}_1 + \bar{\alpha}_{11}\bar{w}_1 + \varepsilon\bar{\alpha}_{12}\left(\ddot{\bar{w}}_1\bar{w}_1^2 + \dot{\bar{w}}_1^2\bar{w}_1\right) + \varepsilon\bar{\alpha}_{13}\bar{w}_1^3 - \varepsilon\bar{\alpha}_{14}\bar{w}_2 - \varepsilon\bar{\alpha}_{15}\bar{V}_1 = \varepsilon\bar{f}_1 \sin\left(\Phi\tau\right)\bar{w}_1 \tag{3.12}$$

$$\dot{\bar{V}}_1 + r_{11}\bar{V}_1 + \dot{\bar{w}}_1 = 0 \tag{3.13}$$

$$\ddot{\bar{w}}_2 + \varepsilon\bar{\alpha}_{20}\dot{\bar{w}}_2 + \bar{\alpha}_{21}\bar{w}_2 + \varepsilon\bar{\alpha}_{22}\left(\ddot{\bar{w}}_2\bar{w}_2^2 + \dot{\bar{w}}_2^2\bar{w}_2\right) + \varepsilon\bar{\alpha}_{23}\bar{w}_2^3 - \varepsilon\bar{\alpha}_{24}\bar{w}_1 - \varepsilon\bar{\alpha}_{25}\bar{V}_2 = \varepsilon\bar{f}_2 \sin\left(\Phi\tau\right)\bar{w}_2 \tag{3.14}$$

$$\dot{\bar{V}}_2 + r_{21}\bar{V}_2 + \dot{\bar{w}}_2 = 0 \tag{3.15}$$

Here, the external excitation frequency $\Phi = \omega / \omega_1$ is given in nondimensionalized form. The coefficients of these equations of motion are given in Appendix A. The bookkeeping parameter ε is introduced to adjust the coefficients in the same order of $\bar{\alpha}_{11}$ and $\bar{\alpha}_{21}$. The value of ε considered to be 0.1 in this study. In the next section, the solutions of Eqs. (3.12 – 3.15) are obtained using the method of multiple scales (MMS).

3.3 Solution of the temporal equations

The above equations of motion of the system are coupled equations with weak nonlinearity, as the coefficients of the nonlinear terms come with ε order. To solve this type of equation, the method of harmonic balance, perturbation-based methods like the method of multiple scales, the method of averaging, Linstedt-Poincaré method are widely used. In case of the harmonic balance method, it is required to have prior knowledge about the solution of these nonlinear equations, or to consider enough number of terms in the assumed solutions and check for order of all the coefficients of the neglected harmonics. Otherwise, one may obtain an inaccurate approximation of the solutions. This makes the solution approach more critical. The method of multiple scales, which uses the fast and slow time scales to obtain the solutions. This method is well established to solve weakly nonlinear coupled multi-degrees of freedom equations with a systematic approach without complications of multiple harmonics.

To obtain uniform approximate solutions of Eqs. (3.12 – 3.15), the standard method of multiple scales is used [13, 17, 27, 81, 233]. The nondimensional time (τ) can be expressed in multiple time scales as $T_n = \varepsilon^n \tau$. The time derivatives can be expressed as follows.

$$\frac{d}{d\tau} = D_0 + \varepsilon D_1 + O\left(\varepsilon^2\right), \quad \frac{d^2}{d\tau^2} = D_0^2 + 2\varepsilon D_0 D_1 + O\left(\varepsilon^2\right), \quad D_n = \frac{\partial}{\partial T_n} \tag{3.16}$$

The nondimensional tip displacements ($\bar{w}_1, \bar{w}_2$) and voltages ($\bar{V}_1, \bar{V}_2$) generated across the piezoelectric patches can be expanded in the following form.

$$\bar{w}_1(\tau) = \bar{w}_{10}(T_0, T_1) + \varepsilon \bar{w}_{11}(T_0, T_1) + O\left(\varepsilon^2\right) \tag{3.17}$$

$$\bar{w}_2(\tau) = \bar{w}_{20}(T_0, T_1) + \varepsilon \bar{w}_{21}(T_0, T_1) + O\left(\varepsilon^2\right) \tag{3.18}$$

$$\bar{V}_1(\tau) = \bar{V}_{10}(T_0, T_1) + \varepsilon \bar{V}_{11}(T_0, T_1) + O\left(\varepsilon^2\right) \tag{3.19}$$

$$\bar{V}_2(\tau) = \bar{V}_{20}(T_0, T_1) + \varepsilon \bar{V}_{21}(T_0, T_1) + O\left(\varepsilon^2\right) \tag{3.20}$$

By substituting Eqs. (3.16 – 3.20) in Eqs. (3.12 – 3.15) and further equating the terms associated with ε^0 and ε^1 equal to zero, yields the following set of equations.

ε^0 order terms:

$$D_0^2\bar{w}_{10}+\bar{\alpha}_{11}\bar{w}_{10}=0 \tag{3.21}$$

$$D_0\bar{V}_{10}+r_{11}\bar{V}_{10}=-D_0\bar{w}_{10} \tag{3.22}$$

$$D_0^2\bar{w}_{20}+\bar{\alpha}_{21}\bar{w}_{20}=0 \tag{3.23}$$

$$D_0\bar{V}_{20}+r_{21}\bar{V}_{20}=-D_0\bar{w}_{20} \tag{3.24}$$

ε^1 order terms:

$$D_0^2\bar{w}_{11}+\bar{\alpha}_{11}\bar{w}_{11}=\begin{bmatrix}-2D_0D_1\bar{w}_{10}-\bar{\alpha}_{10}D_0\bar{w}_{10}-\bar{\alpha}_{12}\left\{\bar{w}_{10}^2D_0^2\bar{w}_{10}+\bar{w}_{10}\left(D_0\bar{w}_{10}\right)^2\right\}\\ -\bar{\alpha}_{13}\bar{w}_{10}^3+\bar{\alpha}_{14}\bar{w}_{20}+\bar{\alpha}_{15}\bar{V}_{10}+\bar{f}_1\left(\dfrac{e^{i\Phi T_0}-e^{-i\Phi T_0}}{2i}\right)\bar{w}_{10}\end{bmatrix} \tag{3.25}$$

$$D_0\bar{V}_{11}+r_{11}\bar{V}_{11}=-D_1\bar{V}_{10}-D_0\bar{w}_{11}-D_1\bar{w}_{10} \tag{3.26}$$

$$D_0^2\bar{w}_{21}+\bar{\alpha}_{21}\bar{w}_{21}=\begin{bmatrix}-2D_0D_1\bar{w}_{20}-\bar{\alpha}_{20}D_0\bar{w}_{20}-\bar{\alpha}_{22}\left\{\bar{v}_{20}^2D_0^2\bar{w}_{20}+\bar{w}_{20}\left(D_0\bar{w}_{20}\right)^2\right\}\\ -\bar{\alpha}_{23}\bar{w}_{20}^3+\bar{\alpha}_{24}\bar{w}_{10}+\bar{\alpha}_{25}\bar{V}_{20}+\bar{f}_2\left(\dfrac{e^{i\Phi T_0}-e^{-i\Phi T_0}}{2i}\right)\bar{w}_{20}\end{bmatrix} \tag{3.27}$$

$$D_0\bar{V}_{21}+r_{21}\bar{V}_{21}=-D_1\bar{V}_{20}-D_0\bar{w}_{21}-D_1\bar{w}_{20} \tag{3.28}$$

The general solutions of the differential equations of ε^0 order are obtained as follows.

$$\bar{w}_{10}=A_1\left(T_1\right)e^{i\sqrt{\bar{\alpha}_{11}}T_0}+CC \tag{3.29}$$

$$\bar{V}_{10}=-Z_1\left(T_1\right)e^{i\sqrt{\bar{\alpha}_{11}}T_0}+CC \tag{3.30}$$

$$\bar{w}_{20}=A_2\left(T_1\right)e^{i\sqrt{\bar{\alpha}_{21}}T_0}+CC \tag{3.31}$$

$$\bar{V}_{20}=-Z_2\left(T_1\right)e^{i\sqrt{\bar{\alpha}_{21}}T_0}+CC \tag{3.32}$$

Here, $Z_1=\left[\left(\bar{\alpha}_{11}+i\sqrt{\bar{\alpha}_{11}}r_{11}\right)/\left(\bar{\alpha}_{11}+r_{11}^2\right)\right]A_1$ and $Z_2=\left[\left(\bar{\alpha}_{21}+i\sqrt{\bar{\alpha}_{21}}r_{21}\right)/\left(\bar{\alpha}_{21}+r_{21}^2\right)\right]A_2$.

CC denotes the complex conjugates. Resonance may occur in the system when $\Phi = 2\sqrt{\bar{\alpha}_{11}}$, i.e., at the principal parametric resonance condition, and the responses may become unbounded. For tuning the excitation frequency and finding the nearness of it to $2\sqrt{\bar{\alpha}_{11}}$, a detuning parameter σ_1 is introduced, and hence one may write $\Phi = 2\sqrt{\bar{\alpha}_{11}} + \varepsilon\sigma_1$. Considering nearly 1:1 internal resonance between the two beam systems, it is assumed that $\sqrt{\bar{\alpha}_{21}} = \sqrt{\bar{\alpha}_{11}} + \varepsilon\sigma_2$, where σ_2 is another detuning parameter. Now, the Eqs. (3.29 – 3.32) are substituted in the Eqs. (3.25) and (3.27). Afterwards, for obtaining the bounded solutions from this set of equations, one must eliminate the secular terms, i.e., the terms containing $e^{i\sqrt{\bar{\alpha}_{11}}T_0}$ which are expressed as follows.

$$\left[\begin{array}{l} -2i\sqrt{\bar{\alpha}_{11}}D_1A_1 - \bar{\alpha}_{10}i\sqrt{\bar{\alpha}_{11}}A_1 + \left(2\bar{\alpha}_{11}\bar{\alpha}_{12} - 3\bar{\alpha}_{13}\right)A_1^2\bar{A}_1 \\ +\bar{\alpha}_{14}A_2\exp\left(i\sigma_2T_1\right) - \bar{\alpha}_{15}\left(\dfrac{\bar{\alpha}_{11} + i\sqrt{\bar{\alpha}_{11}}r_{11}}{\bar{\alpha}_{11} + r_{11}^2}\right)A_1 + \dfrac{\bar{f}_1}{2i}\bar{A}_1e^{i\sigma_1T_1} \end{array}\right] = 0 \tag{3.33}$$

$$\left[\begin{array}{l} -2i\sqrt{\bar{\alpha}_{21}}D_1A_2 - \bar{\alpha}_{20}i\sqrt{\bar{\alpha}_{21}}A_2 + \left(2\bar{\alpha}_{21}\bar{\alpha}_{22} - 3\bar{\alpha}_{23}\right)A_2^2\bar{A}_2 \\ +\bar{\alpha}_{24}A_1\exp\left(-i\sigma_2T_1\right) - \bar{\alpha}_{25}\left(\dfrac{\bar{\alpha}_{21} + i\sqrt{\bar{\alpha}_{21}}r_{21}}{\bar{\alpha}_{21} + r_{21}^2}\right)A_2 + \dfrac{\bar{f}_2}{2i}\bar{A}_2e^{i(\sigma_1 - 2\sigma_2)T_1} \end{array}\right] = 0 \tag{3.34}$$

After eliminating the secular terms, the particular integral parts of the solutions of the Eqs. (3.25 – 3.28) can be written as follows.

$$\bar{w}_{11} = -\left[\frac{\left(2\bar{\alpha}_{11}\bar{\alpha}_{12} - \bar{\alpha}_{13}\right)A_1^3 - i\dfrac{\bar{f}_1}{2}A_1e^{i\sigma_1T_1}}{8\bar{\alpha}_{11}}\right]e^{3i\sqrt{\bar{\alpha}_{11}}T_0} + CC \tag{3.35}$$

$$\bar{V}_{11} = \left(\frac{9\bar{\alpha}_{11} + 3i\sqrt{\bar{\alpha}_{11}}r_{11}}{9\bar{\alpha}_{11} + r_{11}^2}\right)\left\{\frac{\left(2\bar{\alpha}_{12}\bar{\alpha}_{11} - \bar{\alpha}_{13}\right)A_1^3 - i\dfrac{\bar{f}_1}{2}A_1e^{i\sigma_1T_1}}{8\bar{\alpha}_{11}}\right\}e^{3i\sqrt{\bar{\alpha}_{11}}T_0} + CC \tag{3.36}$$

$$\bar{w}_{21} = -\left[\frac{\left(2\bar{\alpha}_{21}\bar{\alpha}_{22} - \bar{\alpha}_{23}\right)A_2^3 - i\dfrac{\bar{f}_2}{2}A_2e^{i\sigma_1T_1}}{8\bar{\alpha}_{21}}\right]e^{3i\sqrt{\bar{\alpha}_{21}}T_0} + CC \tag{3.37}$$

$$\bar{V}_{21} = \left(\frac{9\bar{\alpha}_{21} + 3i\sqrt{\bar{\alpha}_{21}}r_{21}}{9\bar{\alpha}_{21} + r_{21}^2}\right)\left\{\frac{\left(2\bar{\alpha}_{22}\bar{\alpha}_{21} - \bar{\alpha}_{23}\right)A_2^3 - i\dfrac{\bar{f}_2}{2}A_2e^{i\sigma_1T_1}}{8\bar{\alpha}_{21}}\right\}e^{3i\sqrt{\bar{\alpha}_{21}}T_0} + CC \tag{3.38}$$

The amplitudes $A_1(T_1)$ and $A_2(T_2)$ are complex functions, which can be written in polar form as follows.

$$A_1 = \frac{a_1}{2}e^{i\beta_1},\ A_2 = \frac{a_2}{2}e^{i\beta_2} \tag{3.39}$$

Now, the Eqs. (3.39) is substituted in the Eqs. (3.33) and (3.34). To convert these equations into a set of autonomous equations, it can be assumed that $\sigma_1 T_1 - 2\beta_1 = 2\gamma_1$ and $(\sigma_1 - \sigma_2)T_1 - 2\beta_2 = 2\gamma_2$. By separating the real and imaginary parts, the following reduced first-order differential equations are further obtained.

Real parts:

$$a_1\gamma_1' = \begin{bmatrix} \sigma_1\frac{a_1}{2} + \left(2\sqrt{\bar{\alpha}_{11}}\bar{\alpha}_{12} - \frac{3\bar{\alpha}_{13}}{\sqrt{\bar{\alpha}_{11}}}\right)\frac{a_1^3}{8} + \frac{\bar{\alpha}_{14}}{\sqrt{\bar{\alpha}_{11}}}\frac{a_2}{2}\cos(\gamma_1-\gamma_2) \\ -\frac{\sqrt{\bar{\alpha}_{11}}\bar{\alpha}_{15}}{(\bar{\alpha}_{11}+r_{11}^2)}\frac{a_1}{2} + \frac{\bar{f}_1}{2\sqrt{\bar{\alpha}_{11}}}\frac{a_1}{2}\sin(2\gamma_1) \end{bmatrix} \tag{3.40}$$

$$a_2\gamma_2' = \begin{bmatrix} \sigma_1\frac{a_2}{2} + \left(2\sqrt{\bar{\alpha}_{21}}\bar{\alpha}_{22} - \frac{3\bar{\alpha}_{23}}{\sqrt{\bar{\alpha}_{21}}}\right)\frac{a_2^3}{8} + \frac{\bar{\alpha}_{24}}{\sqrt{\bar{\alpha}_{21}}}\frac{a_1}{2}\cos(\gamma_2-\gamma_1) \\ -\frac{\sqrt{\bar{\alpha}_{21}}\bar{\alpha}_{25}}{(\bar{\alpha}_{21}+r_{21}^2)}\frac{a_2}{2} + \frac{\bar{f}_2}{2\sqrt{\bar{\alpha}_{21}}}\frac{a_2}{2}\sin(2\gamma_2) \end{bmatrix} \tag{3.41}$$

Imaginary parts:

$$a_1' = -\frac{\bar{\alpha}_{10}}{2}a_1 + \frac{\bar{\alpha}_{14}}{2\sqrt{\bar{\alpha}_{11}}}a_2\sin(\gamma_1-\gamma_2) - \frac{\bar{\alpha}_{15}r_{11}}{2(\bar{\alpha}_{11}+r_{11}^2)}a_1 + \frac{\bar{f}_1}{4\sqrt{\bar{\alpha}_{11}}}a_1\cos(2\gamma_1) \tag{3.42}$$

$$a_2' = -\frac{\bar{\alpha}_{20}}{2}a_2 + \frac{\bar{\alpha}_{24}}{2\sqrt{\bar{\alpha}_{21}}}a_1\sin(\gamma_2-\gamma_1) - \frac{\bar{\alpha}_{25}r_{21}}{2(\bar{\alpha}_{21}+r_{21}^2)}a_2 + \frac{\bar{f}_2}{4\sqrt{\bar{\alpha}_{21}}}a_2\cos(2\gamma_2) \tag{3.43}$$

Due to the presence of multiple harmonic terms and coupling between the phase differences of the responses, i.e., $\cos(\gamma_1-\gamma_2)$ and $\sin(\gamma_1-\gamma_2)$), the resulting equations are coupled nonlinear and not easily solvable in closed form using trigonometric manipulations. However, considering a special case, where both the beams oscillate with the same phase, i.e., $\gamma_1 = \gamma_2$, it is possible to obtain the closed form solutions in terms of frequency and amplitude.

3.3.1 Stability of steady state response

To study the stability of the steady state response, the above reduced equations need to be perturbed. However, the perturbed equations will not contain the perturbations $\Delta\gamma_1'$ and $\Delta\gamma_2'$ for the trivial solutions (i.e., when $a_1 = \gamma_1 = a_2 = \gamma_2 = 0$). So, the stability of trivial solutions cannot be obtained by perturbing the above reduced equations. Hence, to overcome this difficulty, the Eqs. (3.40 – 3.43) are transformed into a Cartesian coordinate system by introducing the coordinate transformations $p_1 = a_1\cos\gamma_1$, $q_1 = a_1\sin\gamma_1$, $p_2 = a_2\cos\gamma_2$ and $q_2 = a_2\sin\gamma_2$. Further, by carrying out trigonometric manipulations, the following set of equations is obtained from the Eqs. (3.40 – 3.43).

$$p_1' = \begin{bmatrix} -\frac{\sigma_1}{2}q_1 - \frac{\bar{\alpha}_{10}}{2}p_1 - \left(2\sqrt{\bar{\alpha}_{11}}\bar{\alpha}_{12} - \frac{3\bar{\alpha}_{13}}{\sqrt{\bar{\alpha}_{11}}}\right)\left(\frac{p_1^2 q_1 + q_1^3}{8}\right) - \frac{\bar{\alpha}_{14}}{2\sqrt{\bar{\alpha}_{11}}}q_2 \\ + \frac{\bar{\alpha}_{15}}{2\left(\bar{\alpha}_{11} + r_{11}^2\right)}\left(\sqrt{\bar{\alpha}_{11}}q_1 - r_{11}p_1\right) - \frac{\bar{f}_1}{4\sqrt{\bar{\alpha}_{11}}}p_1 \end{bmatrix} \tag{3.44}$$

$$q_1' = \begin{bmatrix} \frac{\sigma_1}{2}p_1 - \frac{\bar{\alpha}_{10}}{2}q_1 + \left(2\sqrt{\bar{\alpha}_{11}}\bar{\alpha}_{12} - \frac{3\bar{\alpha}_{13}}{\sqrt{\bar{\alpha}_{11}}}\right)\left(\frac{p_1^3 + p_1 q_1^2}{8}\right) \\ + \frac{\bar{\alpha}_{14}}{2\sqrt{\bar{\alpha}_{11}}}p_2 - \frac{\bar{\alpha}_{15}}{2\left(\bar{\alpha}_{11} + r_{11}^2\right)}\left(r_{11}q_1 + \sqrt{\bar{\alpha}_{11}}p_1\right) + \frac{\bar{f}_1}{4\sqrt{\bar{\alpha}_{11}}}q_1 \end{bmatrix} \tag{3.45}$$

$$p_2' = \begin{bmatrix} -\left(\frac{\sigma_1}{2} - \sigma_2\right)q_2 - \frac{\bar{\alpha}_{20}}{2}p_2 - \left(2\sqrt{\bar{\alpha}_{21}}\bar{\alpha}_{22} - \frac{3\bar{\alpha}_{23}}{\sqrt{\bar{\alpha}_{21}}}\right)\left(\frac{p_2^2 q_2 + q_2^3}{8}\right) - \frac{\bar{\alpha}_{24}}{2\sqrt{\bar{\alpha}_{21}}}q_1 \\ + \frac{\bar{\alpha}_{25}}{2\left(\bar{\alpha}_{11} + r_{11}^2\right)}\left(\sqrt{\bar{\alpha}_{21}}q_2 - r_{21}p_2\right) - \frac{\bar{f}_2}{4\sqrt{\bar{\alpha}_{21}}}p_2 \end{bmatrix} \tag{3.46}$$

$$q_2' = \begin{bmatrix} \left(\frac{\sigma_1}{2} - \sigma_2\right)p_2 - \frac{\bar{\alpha}_{20}}{2}q_2 + \left(2\sqrt{\bar{\alpha}_{21}}\bar{\alpha}_{22} - \frac{3\bar{\alpha}_{23}}{\sqrt{\bar{\alpha}_{21}}}\right)\left(\frac{p_2^3 + p_2 q_2^2}{8}\right) \\ + \frac{\bar{\alpha}_{24}}{2\sqrt{\bar{\alpha}_{21}}}p_1 - \frac{\bar{\alpha}_{25}}{2\left(\bar{\alpha}_{21} + r_{21}^2\right)}\left(r_{21}q_2 + \sqrt{\bar{\alpha}_{21}}p_2\right) + \frac{\bar{f}_2}{4\sqrt{\bar{\alpha}_{21}}}q_2 \end{bmatrix} \tag{3.47}$$

Now perturbing the Eqs. (3.44 – 3.47), one gets,

$$\left\{\Delta p_1',\ \Delta q_1',\ \Delta p_2',\ \Delta q_2'\right\}^T = \left\{J\right\}\left\{\Delta p_1,\ \Delta q_1,\ \Delta p_2,\ \Delta q_2\right\}^T \tag{3.48}$$

where superscript T is the transpose and $\{J\}$ is the Jacobian matrix whose eigenvalues will determine the stability of the solutions. Those eigenvalues having negative real parts signify the asymptotically stable solutions and vice versa. For the steady state, i.e., when $p_1' = q_1' = p_2' = q_2' = 0$ the above equations are transformed into a set of nonlinear algebraic equations, which are then solved using Newton's method. The obtained solutions are verified with those obtained using the 4th order Runge-Kutta method (ode45 solver). The output power (P_i) of the i-th beam of the harvester can be calculated from the root mean square (RMS) value of the output voltage (V_i), which can be expressed as $P_i = \left(V_i^{RMS}\right)^2 / R_L$.

3.4 Results and discussion

In this section, the results of the proposed PEH system, which are obtained through the MMS and the Runge-Kutta method, are discussed using the frequency responses, time responses and plots with varying system parameters. Physical dimensions and material properties of the components of the system are given in Table 3.1. Properties of the 1st beam and the MFC patches are similar to the theoretical and experimental work of Friswell et al. [77]. Keeping the material properties the same as those of the 1st beam, the length and the tip mass of the 2nd beam are so chosen that the natural frequencies (ω_1, ω_2) of both the beams are nearly the same, leading to the 1:1 internal resonance. The system is externally excited with a frequency twice the natural frequencies of the beams and hence exhibits the principal parametric resonance condition.

Table 3.1: Physical dimensions and material properties of the PEH system

Parameters	**Values (unit)**	**Parameters**	**Values (unit)**
Young's modulus, E	210 GPa	Damping co-eff, C_2	0.002 N-s/m
Density, ρ	7850 kg/m^3	Spring stiffness, K	1 – 2 N/m
1st beam length, l_1	0.3 m	l_K	0.1 m
2nd beam length, l_2	0.15 m	MFC length, l_P	0.028 m
Beam width, $b_1 = b_2$	0.016 m	MFC width, b_P	0.014 m
Beam thickness, $h_1 = h_2$	0.254 mm	MFC thickness, h_P	0.3×10^{-3} m
1st beam tip mass, m_1	0.001 – 0.016kg	Piezo charge co-eff, d_{31}	-170 pC/N
2nd beam tip mass, m_2	0.04 – 0.065 kg	γ_P	-4×10^{-5} N-m/V
Mass MOI, I_{m_i}	$m_i \times 40.87$ kg-mm^2	Capacitance, C_P	51.4 nF
Damping co-eff, C_1	0.001 N-s/m	Load resistance, R_L	0 – 30 MΩ

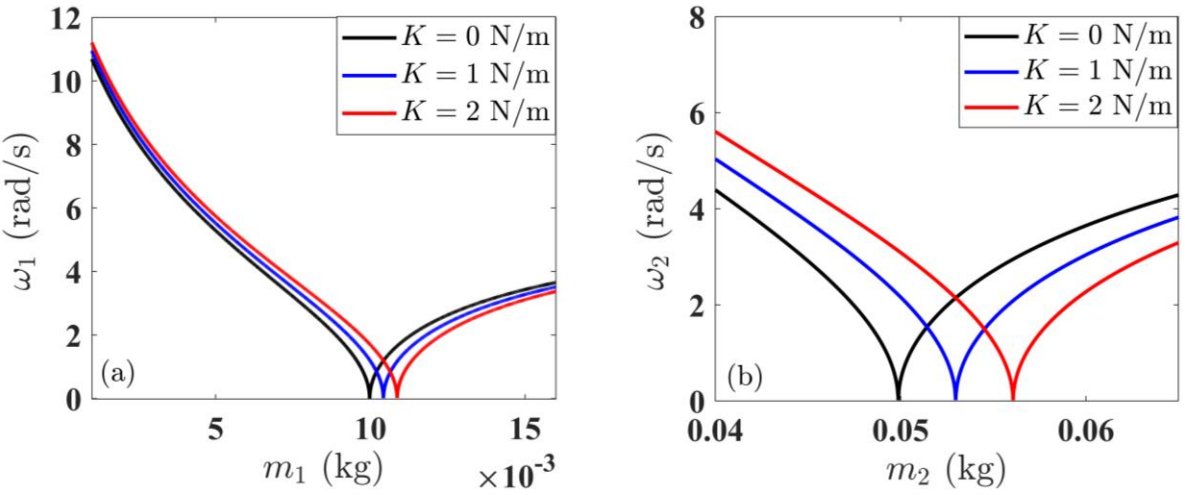

Figure 3.2: Variation of natural frequencies with change in tip mass and different spring stiffness for (a) 1st beam and (b) 2nd beam

Table 3.2: Critical value of tip masses corresponding to buckling of the beams

Stiffness of the spring (K)	**Tip mass of 1st beam** (m_1)	**Tip mass of 2nd beam** (m_2)
0 N/m	0.01 kg	0.0499 kg
1 N/m	0.0104 kg	0.053 kg
2 N/m	0.0109 kg	0.0561 kg

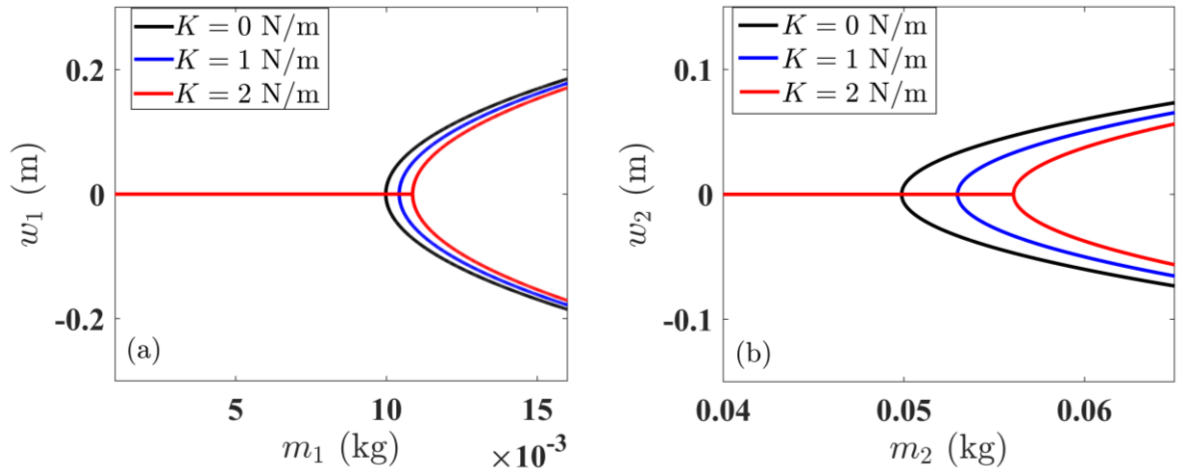

Figure 3.3: Static equilibrium positions of the (a) 1st and (b) 2nd beam for the pre- and post-buckling condition with change in tip mass values

Figure 3.2 illustrates the change in the natural frequencies of the beams with varying the tip masses and the coupled spring stiffness (K). As the tip mass value increases, the natural frequencies of the system decrease and become zero at the critical values. Beyond these critical values of tip masses, the beams start to buckle. For $K = 0$ N/m i.e., in case of the uncoupled condition, buckling of the 1st beam occurs when $m_1 = 0.01$ kg , which can be found in the work

of Friswell et al. [77]. Similarly, the uncoupled 2nd beam starts to buckle when $m_2 = 0.0499$ kg. Table 3.2 represents the critical tip mass values for buckling of the beams for different *K* values.

Figure 3.3 shows the static equilibrium positions of the beams for pre and post-buckling conditions. After reaching the critical value of the tip masses, the initial stable trivial state becomes unstable (dashed lines) and bifurcates with pitchfork bifurcation (PFB), giving rise to two nontrivial stable (solid lines) branches. As the coupled spring stiffness increases, the bifurcation points shift towards the right. In the following results, the pre-buckled condition is mainly considered.

Table 3.3: Natural frequencies of the system for different values of coupled spring stiffness

Spring stiffness (K)	**1st natural frequency** (ω_1)	**2nd natural frequency** (ω_2)
0 N/m	3.6174 rad/s	3.5379 rad/s
1 N/m	3.8783 rad/s	4.2618 rad/s
2 N/m	4.1227 rad/s	4.8794 rad/s

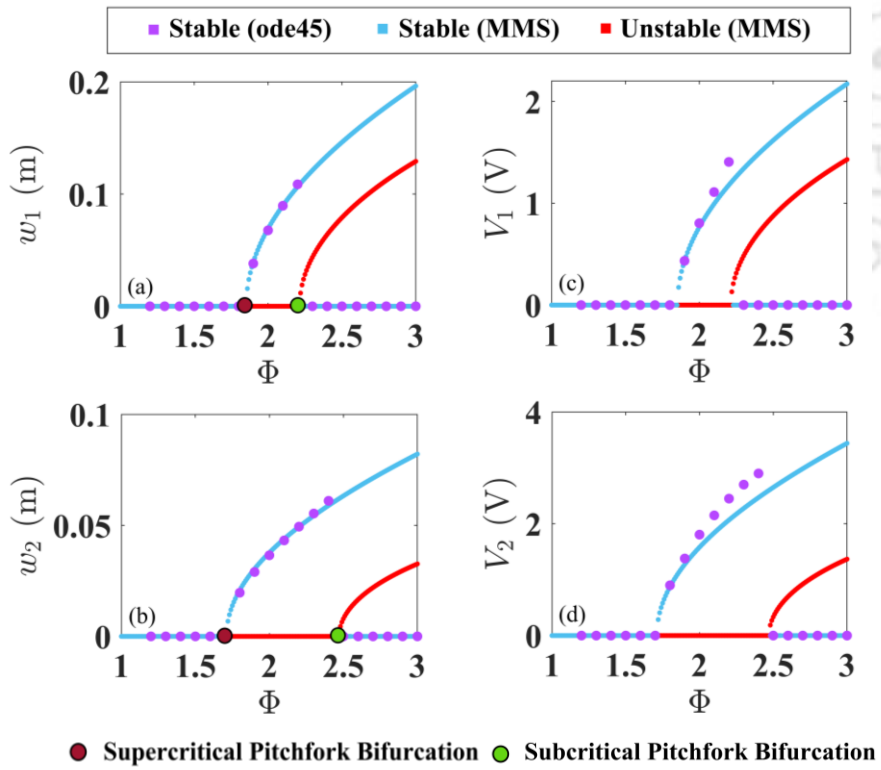

Figure 3.4: Frequency responses of the uncoupled PEH showing tip displacement of (a) 1st and (b) 2nd beam, output peak voltage from MFC patches of (c) 1st and (d) 2nd beam

Considering $m_1 = 0.007$ kg and $m_2 = 0.043$ kg, the natural frequencies of the 1st and 2nd beam are tabulated in Table 3.3 for different values of spring stiffness. The above-mentioned tip mass

values are used for obtaining the following frequency responses. In Figure 3.4, the tip displacements of the beams and the peak output voltages are shown with respect to the variation of excitation frequency, considering the beams are at uncoupled condition and $R_L = 100\ \text{k}\Omega$. The approximated stable (cyan dots) and unstable (red dots) solutions obtained by solving the Eqs. (3.45 – 3.48) which are derived using MMS, are compared with the solutions obtained from the governing equations of motion, i.e., Eqs. (3.13 – 3.16) using ode45 (violet dots). Solutions obtained by both methods are found to be in good agreement near the principal parametric resonance condition.

Initially, the system is at a stable trivial state; until the external excitation frequency reaches a value near the principal parametric resonance frequency, where the trivial state bifurcates with supercritical pitchfork bifurcation (PFB_{sup}) and becomes unstable, giving rise to nontrivial stable solutions. For the 1st and 2nd beam, PFB_{sup} it occurs at $\Phi = 1.86$ and $\Phi = 1.72$, respectively. The unstable trivial state again bifurcates with a subcritical pitchfork bifurcation (PFB_{sup}) and becomes stable. For the 1st and 2nd beam, PFB_{sup} occurs at $\Phi = 2.16$ and $\Phi = 2.4$, respectively. In the trivial unstable region (TUR), voltage generation takes place. After the PFB_{sup}, the system has two stable states, viz., the trivial state in which no voltage is produced and a non-trivial state in which one may get maximum voltage generation. The frequency bandwidths of the trivial unstable region of the 1st and 2nd beams are 0.3 and 0.68, respectively. The peak output voltages obtained in the TUR are $V_1 = 1.4\ \text{V}$ at $\Phi = 2.16$ for the 1st beam and $V_2 = 2.9\ \text{V}$ at $\Phi = 2.4$ for the 2nd beam.

Figure 3.5 represents the time responses and phase portraits of the uncoupled beams for the external excitation frequency of $\Phi = 1.5,\ 2$ and 2.5. It can be observed from the time responses of the tip displacements that before reaching the principal parametric resonance condition, at $\Phi = 1.5$ the beams do not vibrate. After initial perturbation, the oscillations decay out to the trivial state. The corresponding phase portraits show that the response moves to the sink. For $\Phi = 2$ i.e., at the principal parametric resonance condition, the time responses exhibit periodic motion. In the corresponding phase portraits, a closed loop can be observed, which signifies the limit cycle oscillation. The primary focus of the present study is to enhance the frequency bandwidth of the TUR. To achieve this, the individual beams are coupled by a linear spring and the investigation is carried out.

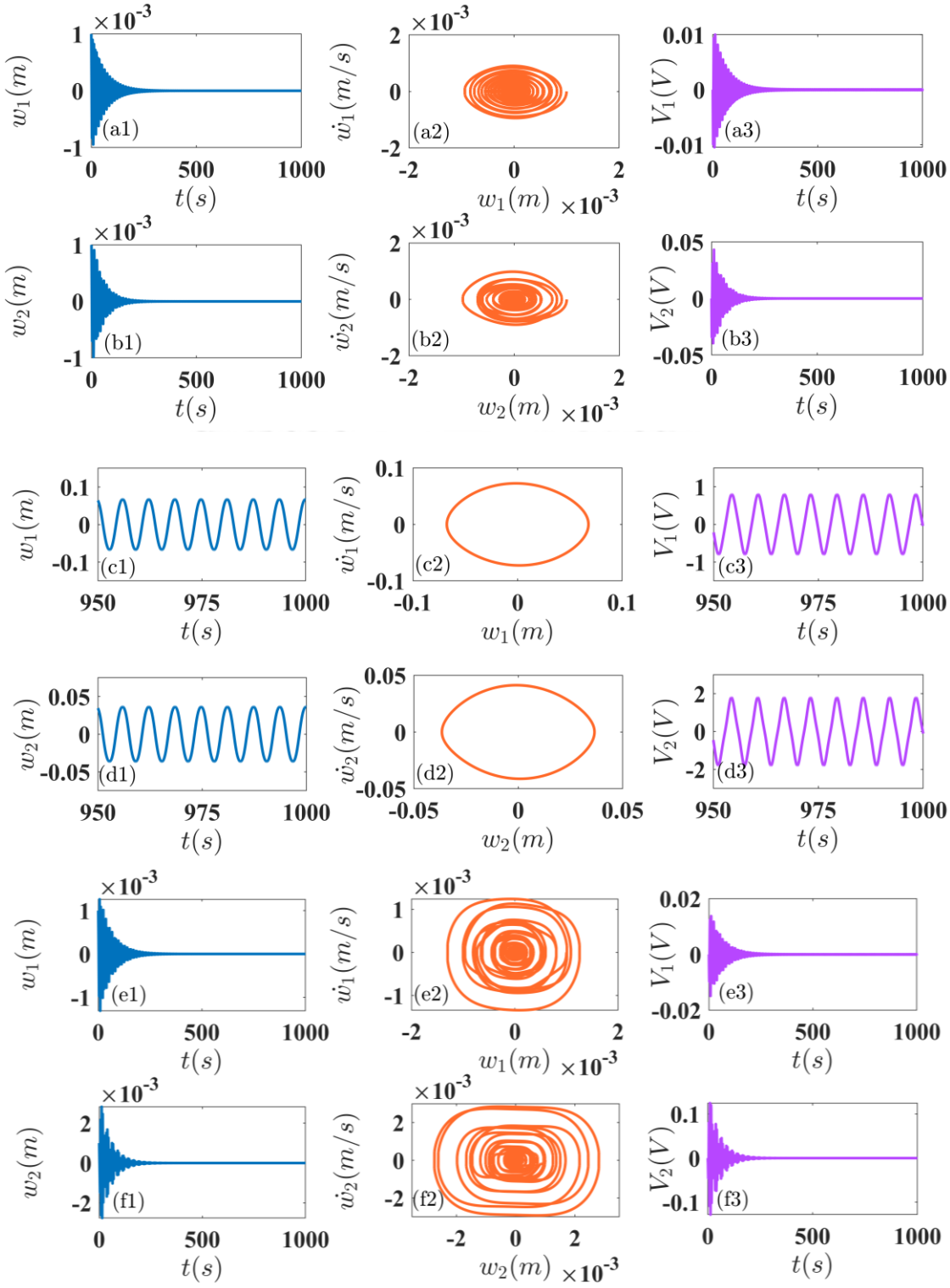

Figure 3.5: Time responses and phase portraits of the uncoupled system. For $\Phi = 1.5$, (a1, b1) tip displacements; (a2, b2) phase portraits; (a3, b3) peak output voltages. For $\Phi = 2$, (c1, d1) tip displacements; (c2, d2) phase portraits; (c3, d3) peak output voltages. For $\Phi = 2.5$, (e1, f1) tip displacements; (e2, f2) phase portraits; (e3, f3) peak output voltages. 1 and 2 refers to 1st and 2nd beam.

For the coupled spring stiffness (K) of 1 N/m and $R_L = 100\ \text{k}\Omega$, the frequency responses of the system are illustrated in Figure 3.6. As the system is coupled, PFB_{sup} occurs at $\Phi = 1.7$ and PFB_{sub} occurs at $\Phi = 2.9$. The frequency bandwidth of the TUR is 1.2. Compared to the uncoupled system, the frequency bandwidth of the coupled system is enhanced by 300% and 76.47% for the 1st and 2nd beam, respectively. Apart from the pitchfork bifurcations, the saddle node bifurcations (SNB) or turning point bifurcations are also evident at $\Phi = 2.3, 2.34$ and 2.87. Beyond $\Phi = 2.3$, multiple stable and unstable solutions can be observed, which typically depend on the initial conditions of the system provided.

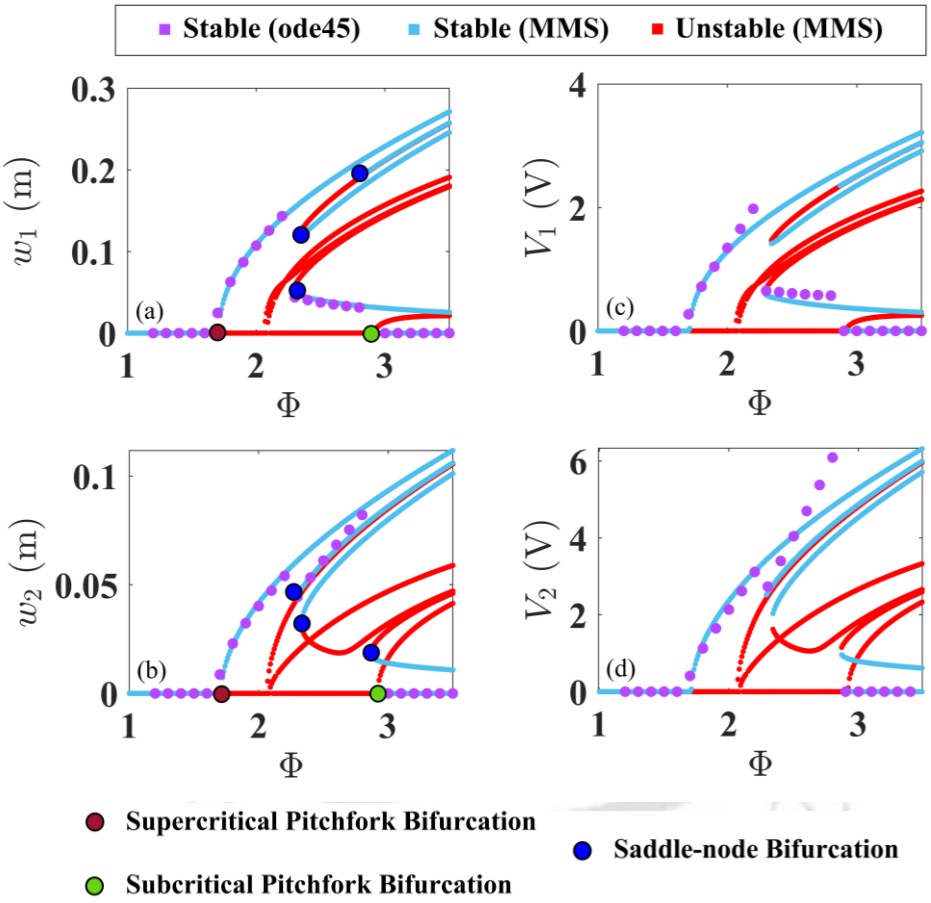

Figure 3.6: Frequency responses of the spring coupled (K = 1 N/m) PEH showing tip displacement of (a) 1st and (b) 2nd beam, output peak voltage from MFC patches of (c) 1st and (d) 2nd beam

Figure 3.7 and Figure 3.8 show the time responses and the phase portraits of the coupled PEH system with K = 1 N/m while considering two different sets of initial conditions. Comparing these two figures, it can be observed that at $\Phi = 2.4$, the system exhibits multiple solutions which solely depend on the given initial conditions. With the initial condition of

$w_1 = 0.001, \dot{w}_1 = 0, V_1 = 0, w_2 = 0.001, \dot{w}_2 = 0, V_2 = 0$, the peak output voltages of the 1st and 2nd beam are 0.63 V and 3.39 V, respectively. Now, by switching the initial condition to $w_1 = 0.166, \dot{w}_1 = 0, V_1 = 0, w_2 = 0.066, \dot{w}_2 = 0, V_2 = 0$, peak output voltages are 2.7 V and 4.17 V for the 1st and 2nd beam, respectively.

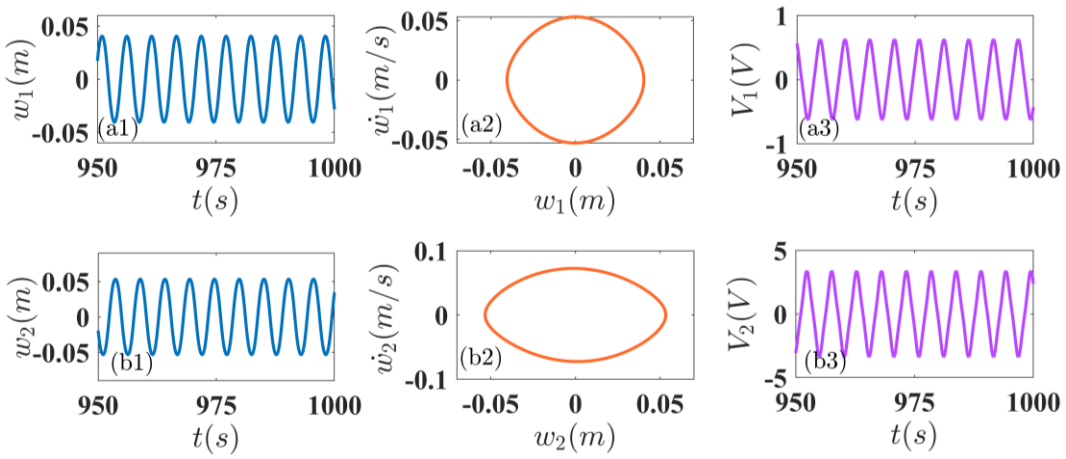

Figure 3.7: Time responses and phase portraits of the coupled PEH (with K = 1 N/m) for $\Phi = 2.4$, (a1, b1) tip displacements; (a2, b2) phase portraits; (a3, b3) peak output voltages with initial conditions, $w_1 = 0.001, \dot{w}_1 = 0, V_1 = 0, w_2 = 0.001, \dot{w}_2 = 0, V_2 = 0$

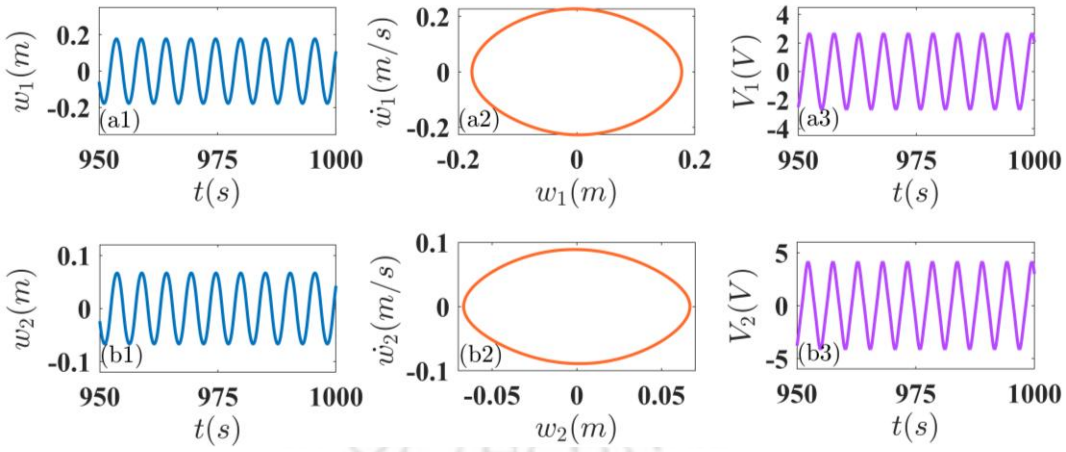

Figure 3.8: Time responses and phase portraits of the coupled PEH (with K = 1 N/m) for $\Phi = 2.4$, (a1, b1) tip displacements; (a2, b2) phase portraits; (a3, b3) peak output voltages with initial conditions, $w_1 = 0.166, \dot{w}_1 = 0, V_1 = 0, w_2 = 0.066, \dot{w}_2 = 0, V_2 = 0$

By increasing the spring stiffness to 2 N/m, the responses of the coupled system are portrayed in Figure 3.9 considering $R_L = 100\ \text{k}\Omega$. Here one can observe two distinct frequency bandwidths of TUR at $\Phi = 1.6 - 2$ and $\Phi = 2.27 - 3.1$. In the second bandwidth of the TUR, the solutions obtained using the MMS show that PFB_{sub} occurs at $\Phi = 3.27$; which slightly

deviates from the solutions obtained through ode45. In between these two TURs, the stable trivial state bifurcates with hopf bifurcation (HB) and becomes unstable. The HB region has a frequency bandwidth of $\Phi = 2.13 - 2.21$. The total frequency bandwidth of the TUR is 1.31. Compared to the uncoupled system, the frequency bandwidth of the coupled system (with $K = 2$ N/m) is enhanced by 336.66% and 92.64% for the 1st and 2nd beam, respectively. The above-mentioned figures and their analysis focus on the behaviour of the PEH on the basis of the external excitation frequency, and it is evident that the frequency bandwidth significantly enhances with the introduction of the coupled spring.

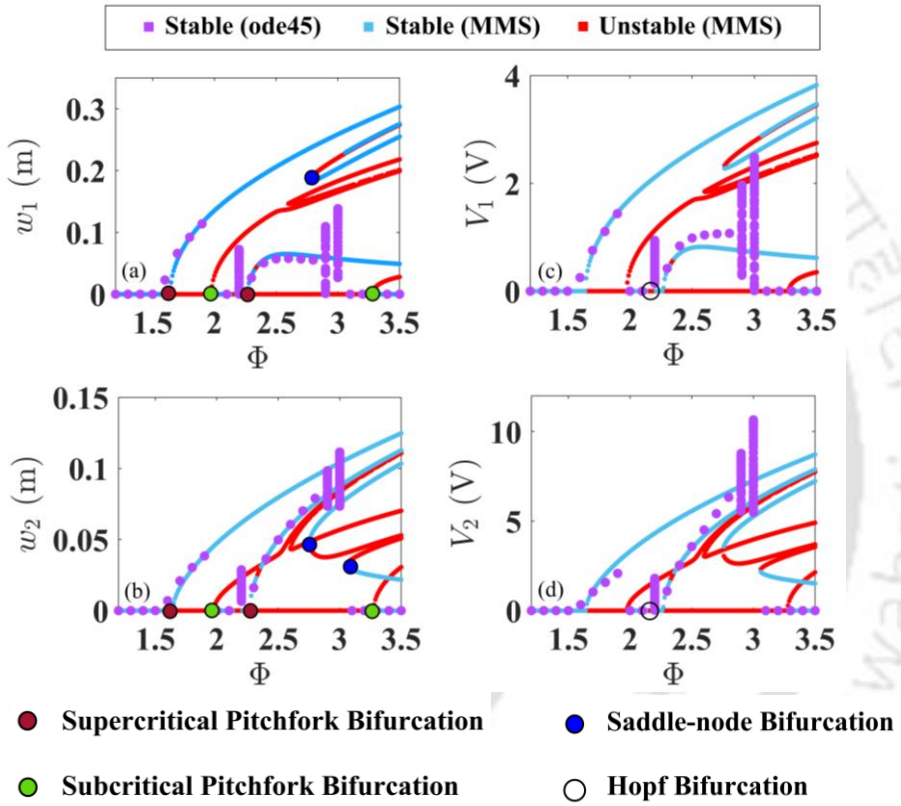

Figure 3.9: Frequency responses of the coupled PEH (with $K = 2$ N/m) showing tip displacement of (a) 1st and (b) 2nd beam, output peak voltages of (c) 1st and (d) 2nd beam

Quasi-periodic oscillations, which are commonly evident in the dynamic response of coupled nonlinear oscillators, can be observed in this region. The rise of quasi-periodic oscillation from the stable trivial equilibrium through HB is illustrated by the time responses and phase portraits shown in Figure 3.10, Figure 3.11 and Figure 3.12 for the excitation frequency of $\Phi = 2.1$, $\Phi = 2.2$ and $\Phi = 2.25$, respectively. In QP oscillation, two or more frequencies are dominant, which are irrational in nature. As a result, a beating type of response can be observed in quasi-periodic oscillation.

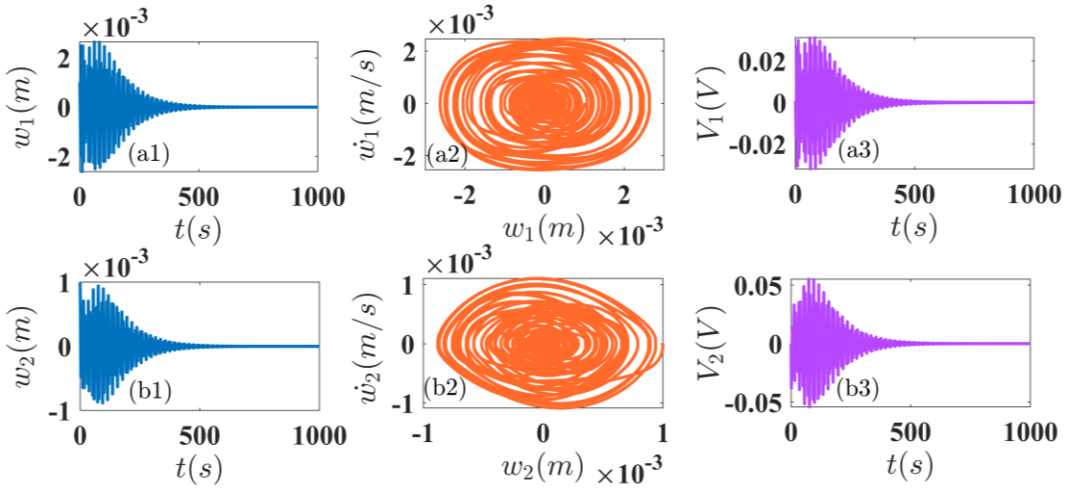

Figure 3.10: Time responses and phase portraits of the coupled PEH (with $K = 2$ N/m) for $\Phi = 2.1$; (a1, b1) tip displacements; (a2, b2) phase portraits; (a3, b3) peak output voltages

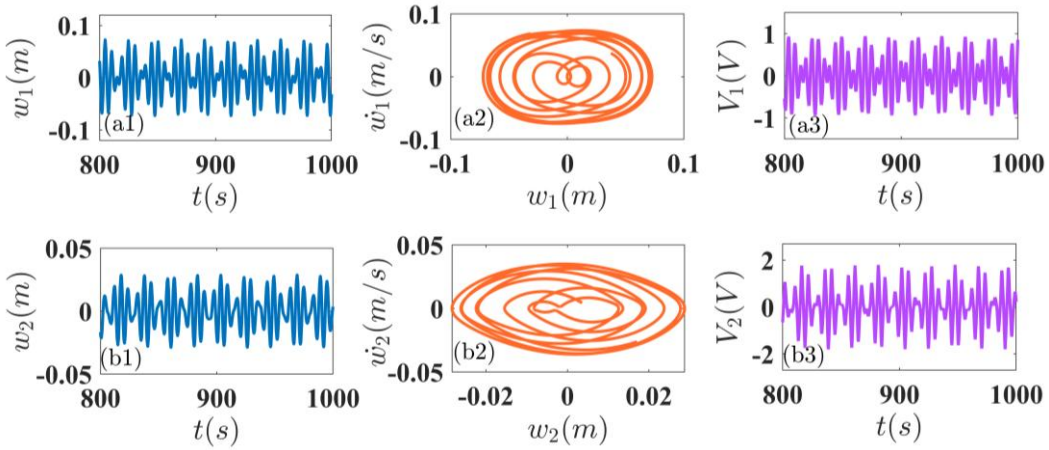

Figure 3.11: Time responses and phase portraits of the coupled PEH (with $K = 2$ N/m) for $\Phi = 2.2$; (a1, b1) tip displacements; (a2, b2) phase portraits; (a3, b3) peak output voltages

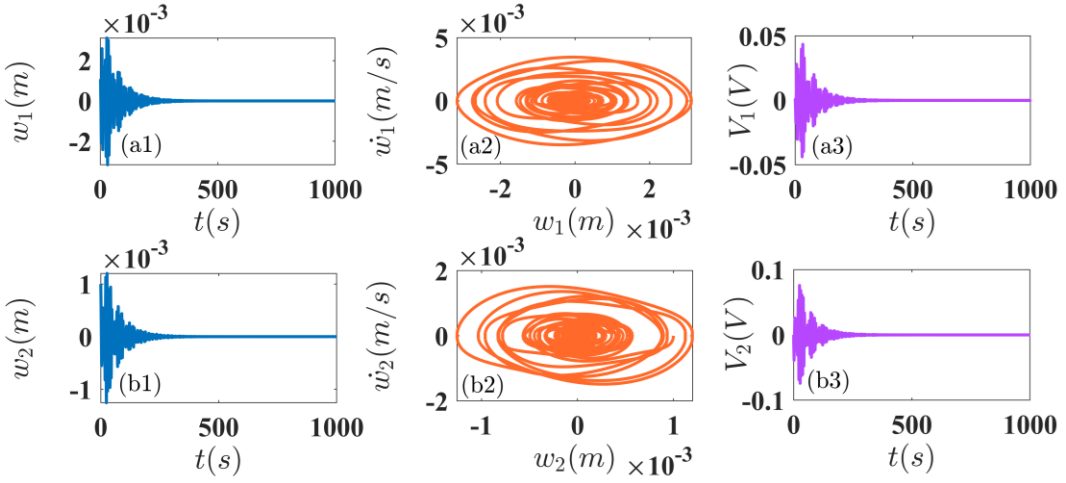

Figure 3.12: Time responses and phase portraits of the coupled PEH (with $K = 2$ N/m) for $\Phi = 2.25$; (a1, b1) tip displacements; (a2, b2) phase portraits; (a3, b3) peak output voltages

Figure 3.13 shows the comparison of tip displacements and the corresponding output voltages of the uncoupled and the spring-coupled systems. As discussed earlier, it is from this figure that under coupled conditions, the operational frequency bandwidths of both beams enhance significantly compared to uncoupled individual beams. The maximum output voltage of the energy harvester also improves in the coupled configuration, mainly due to energy transfer between the beams.

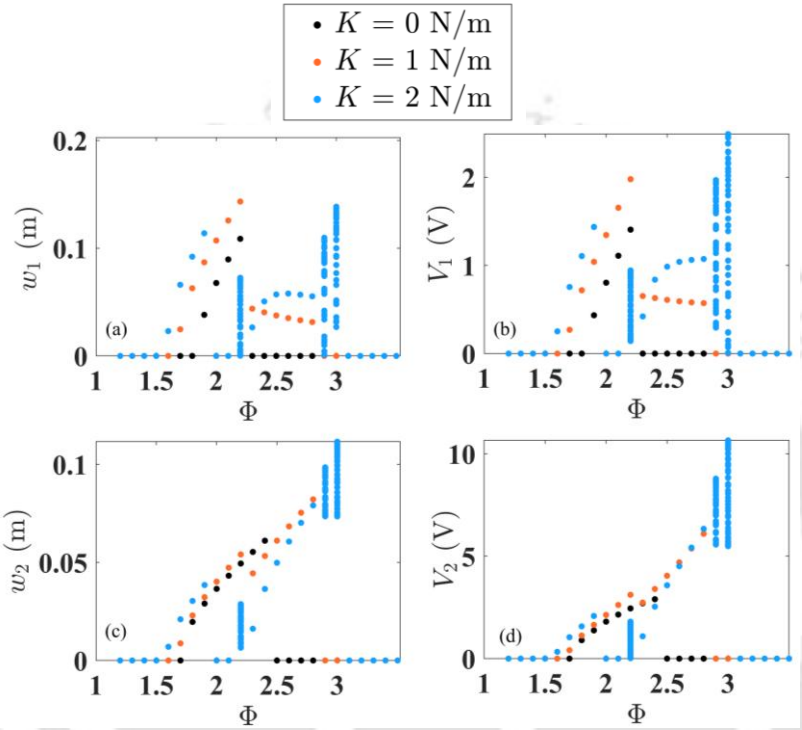

Figure 3.13: Comparison of (a, c) tip displacements and (b. d) output voltages of the uncoupled and spring-coupled PEH system; (a, b) for the 1st beam, (c, d) for the 2nd beam

However, when the coupled spring stiffness is higher (K = 2 N/m), the operational frequency bandwidth splits into two separate bands. Near $\Phi \approx 2$, the response suddenly jumps down to the trivial stable state and continues up to $\Phi \approx 2.13$. As a result, the system with K = 2 N/m is unable to harvest any energy in this frequency band. In comparison, the coupled PEH system with K = 1 N/m, exhibits a continuous operational frequency band without such interruptions. Qualitatively, it can be stated that with a higher value of spring stiffness, the oscillation may be restricted at certain excitation conditions.

Therefore, depending on the excitation conditions, careful selection of the spring stiffness is necessary. While the present study primarily focuses on understanding the changes in the nonlinear dynamic behaviour when the system shifts from uncoupled to coupled state, optimizing the coupling stiffness for enhanced energy harvesting remains an important direction for future work.

Tip masses attached to beams are important system parameters to tune the natural frequencies of the system. In the static condition without any external disturbance, the pre-buckled and post-buckled states of the beams depend on the tip mass values. Hence, the dynamics of the proposed PEH system need to be studied by tuning the tip masses. Figure 3.14 shows the bifurcation diagram of the tip displacements of the beams for coupled spring stiffness of $K = 1$ and 2 N/m. It is to be noted that the excitation frequency is considered to be twice of ω_2. While, the 2nd beam tip mass value is fixed at 0.043 kg, the 1st beam tip mass is tuned from 0.001 kg to 0.016 kg, and the responses are obtained.

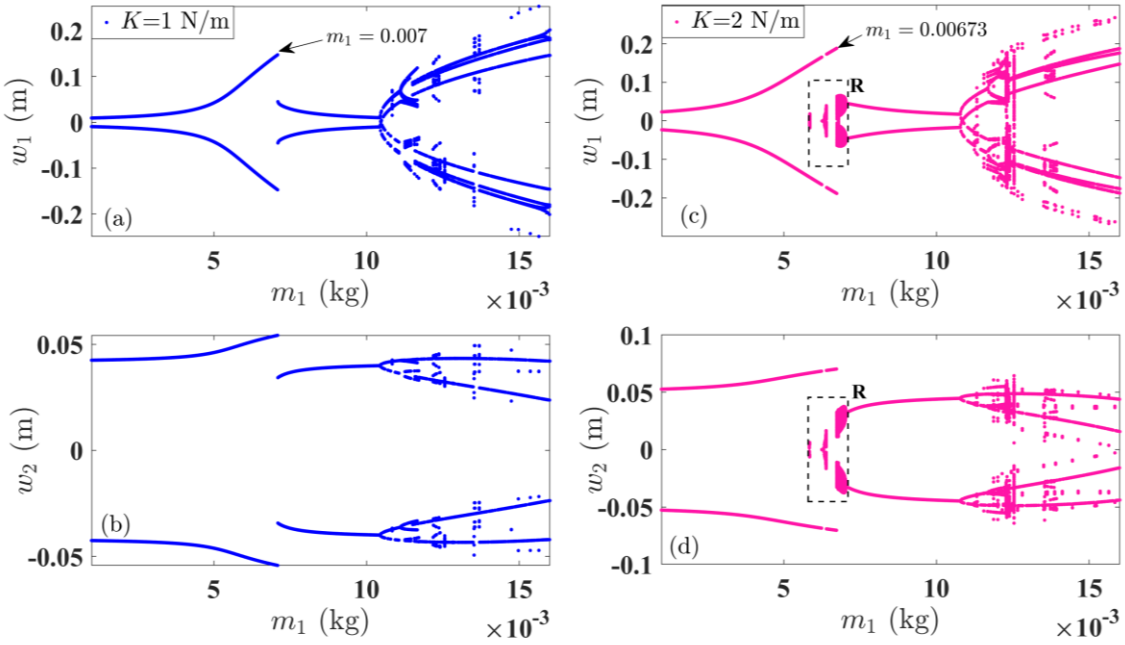

Figure 3.14: Bifurcation diagram of the tip displacements of the beams with varying m_1 and fixed $m_2 = 0.043$ kg. For K = 1 N/m, tip displacements of (a) 1st and (b) 2nd beam; for $K = 2$ N/m, tip displacements of (c) 1st and (d) 2nd beam.

As the tip mass value increases, the tip displacements also increase, single periodic responses can be observed. Up to $m_1 = 0.007$ kg, the amplitude of tip displacements increases and then suddenly drops. This jump down occurs as further increasing the m_1 value leads the system out of resonance. Beyond $m_1 = 0.0104$ kg, the 1st beam shifts from pre-buckled to post-buckled state, which can be verified from Figure 3.2 and Figure 3.3. Here, mostly the quasi-periodic or chaotic motions are dominant. For $K = 2$ N/m, the **R** marked regions in Figure 3.14 (c) and (d) exhibit quasi-periodic motion, which is shown in Figure 3.15. The FFT plots show that there are three dominant frequencies which are incommensurable.

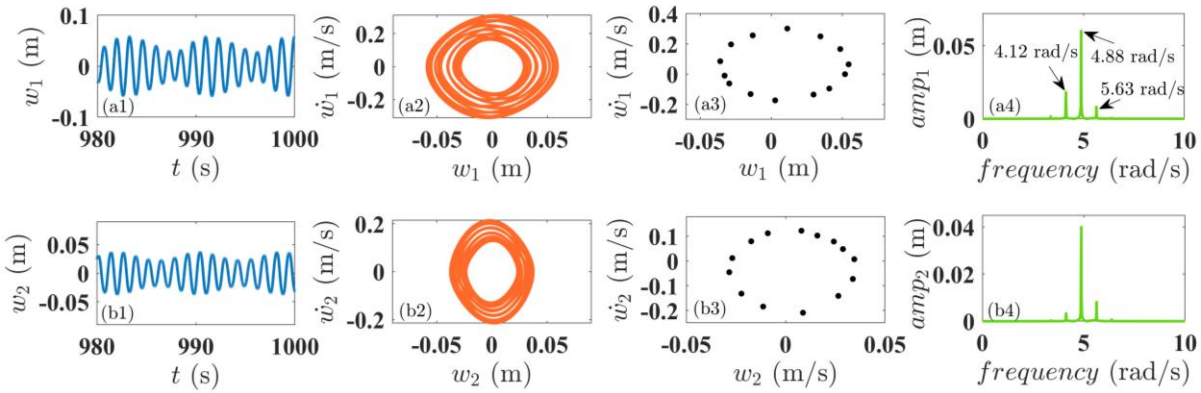

Figure 3.15: For the region marked **R** in Figure 3.14, (a1) time response, (a2) phase portrait, (a3) Poincaré section (a4) FFT plot for the 1st beam; (b1) time response, (b2) phase portrait, (b3) Poincaré section (b4) FFT plot for the 2nd beam

In Figure 3.16, the RMS values of output voltages from the 1st and 2nd beam are plotted by varying the tip mass of the 1st beam and keeping the value of the 2nd beam tip mass fixed. From Figure 3.14, it can be observed that the output voltage increases up to 0.007 kg and then drops as a result of moving out of resonance. The output voltage increases with K = 2 N/m as compared to K = 1 N/m, because increasing the spring stiffness leads to a higher natural frequency of the system and correspondingly higher excitation frequency. In the post-buckled region i.e., beyond $m_1 = 0.0104$ kg, output of the 1st patch is mostly less than 0.5 V; however, that of the 2nd patch is between 1 and 2 V. As the output voltage is higher in the pre-buckled regime than that of the post-buckled regime, one may not tune the tip mass of the 1st beam beyond the critical buckling point in case of a parametrically excited system.

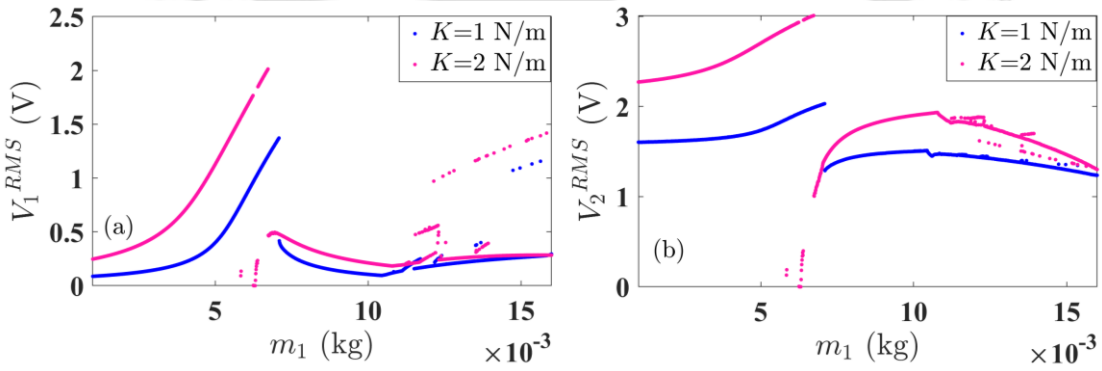

Figure 3.16: By varying m_1, RMS output voltages from MFC patches of (a) 1st beam and (b) 2nd beam

Similarly, by keeping the 1st beam tip mass fixed at $m_1 = 0.007$ kg and tuning the 2nd beam tip mass in between 0.04 kg and 0.065 kg, the beam tip displacement and output RMS voltage

responses are plotted in Figure 3.17 and Figure 3.18, respectively. Here, it can be observed that the system responses with coupled spring stiffness, $K = 2$ N/m is higher compared to those with $K = 1$ N/m. While tuning the tip mass, as the natural frequency changes and gets mistuned from the principal parametric resonance state with the external excitation frequency, the response jumps down to a lower energy orbit. At this out of resonance state, higher coupled spring stiffness i.e., $K = 2$ N/m restricts the oscillation more compared to that with $K = 1$ N/m. As a result, when $K = 2$ N/m; the range of tip mass for which very low amplitude oscillations persist, is wider compared to that when $K = 1$ N/m.

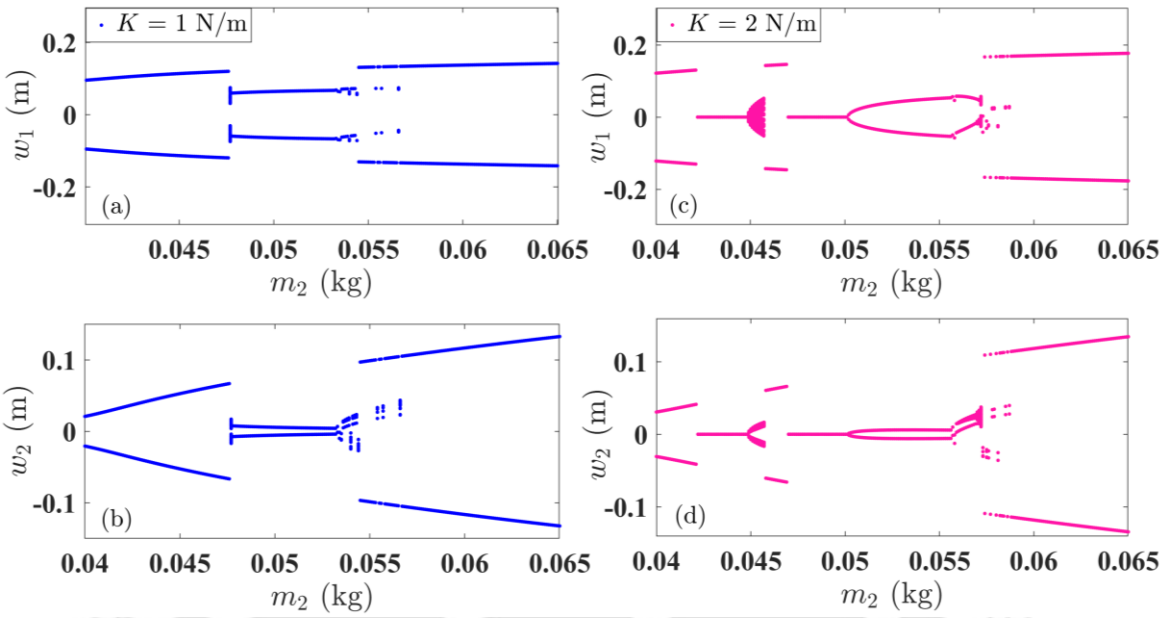

Figure 3.17: Bifurcation diagram of the tip displacements of the beams with varying m_2 and fixed $m_1 = 0.007$ kg. For $K = 1$ N/m, tip displacements of (a) 1st and (b) 2nd beam; for $K = 2$ N/m, tip displacements of (c) 1st and (d) 2nd beam.

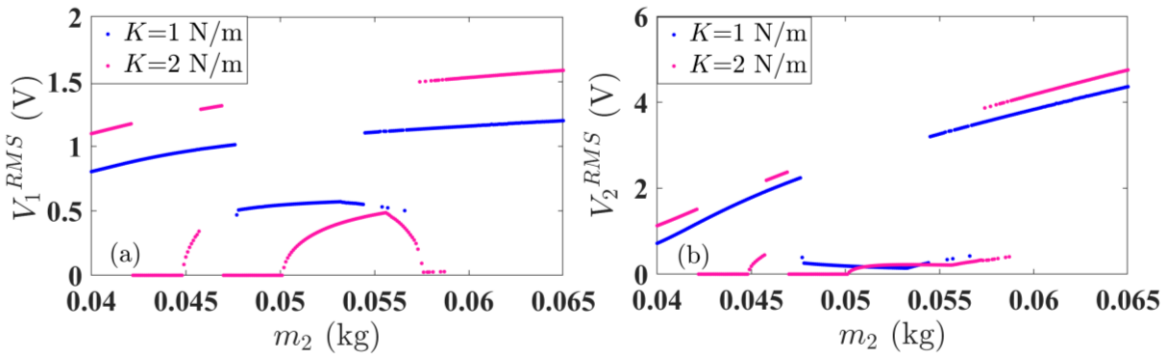

Figure 3.18: By varying m_2, (a) RMS output voltages from MFC patches of (a) 1st beam and (b) 2nd beam

Load resistance (R_L) is another important system parameter and needs to be chosen wisely for obtaining the optimum output power from the PEH system. To study the effect of R_L on harvested power, Figure 3.19 is illustrated with RMS output power vs. load resistance of the uncoupled (K = 0 N/m) and the coupled (K = 1 N/m) PEH system. The optimum value of R_L is quite high due to the small value of capacitance of the MFC patches and low excitation frequency. For the uncoupled 1st beam, optimum load resistance is 3.5 MΩ when the excitation frequency is $\Phi = 2.2$, and the corresponding maximum obtainable power output is 0.157 mW. For the uncoupled 2nd beam, the optimum value of load resistance is 3 MΩ and the corresponding maximum output power is 0.963 mW when $\Phi = 2.4$. For the coupled system (K = 2 N/m) externally excited at $\Phi = 2.8$, the maximum harvestable power from the 1st beam MFC patch is 0.76 mW at a load resistance of 0.35 MΩ and that from the 2nd beam MFC patch is 3.91 mW at a load resistance of 2.5 MΩ. For both uncoupled and coupled cases, the output power increases with increase in load resistance, reaches a maximum and then gradually decreases.

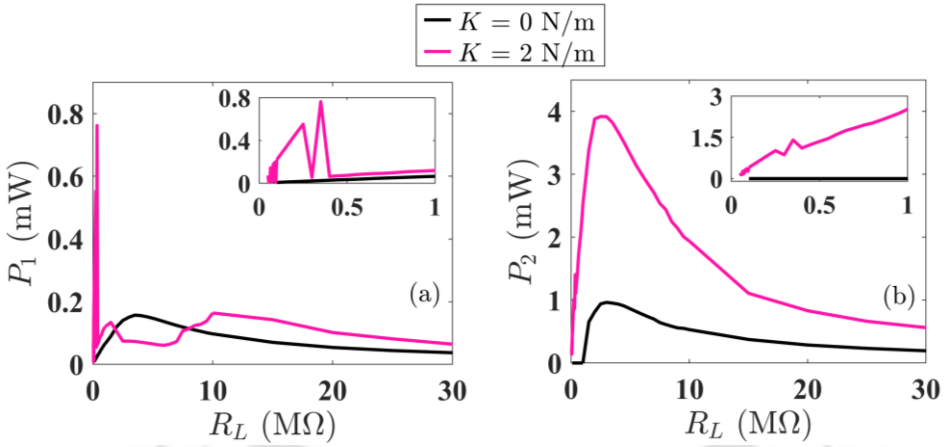

Figure 3.19: RMS output power vs. load resistance for (a) 1st beam, (b) 2nd beam

Table 3.4: Input power requirement for various electronic devices and sensors

Electronic devices and sensors	Input power requirement
PPG sensor	1.47 mW
Humidity sensor	1 mW
Pressure sensor	0.5 mW
3D accelerometer	0.32 mW
Temperature	27 µW
A/D conversion	1 µW
R/F transmission	Sub µW
ECG/Heart rate sensor	~61.1 µW
Nanojunction gas sensor	< 6 µW

Figure 3.20 shows the parametric instability region or trivial unstable region (TUR) of the proposed PEH system that is obtained by solving the Eqs. (3.10) and (3.11) using ode45. The black and white coloured regions in the diagram signify the unstable (US) and the stable (S) region. As the coupled spring stiffness increases, the 'w' shaped US region splits into two distinct 'v' shaped US regions. In between these two 'v' shaped regions, there exists a small US region nearby $\Phi = 2.2$, which verifies the HB and occurrence of quasi-periodic oscillations. The same can be found in the frequency and time response shown in Figure 3.9 and Figure 3.11, respectively. As mentioned earlier, for a parametrically excited system, an initial threshold amplitude of external excitation is necessary to obtain the resonance state. For the presently studied PEH, the threshold amplitude (z_0) of excitation is 0.002 m.

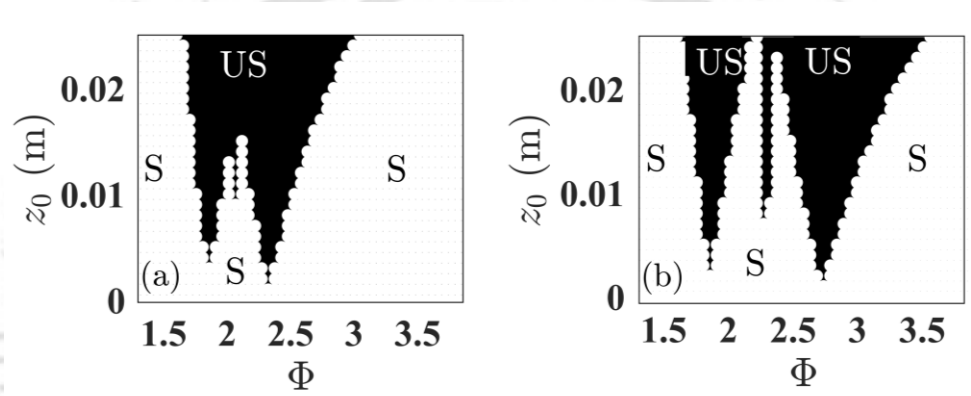

Figure 3.20: Parametric instability regions or trivial unstable region (TUR) of the coupled PEH for (a) K = 1 N/m and (b) K = 2 N/m

3.5 Summary

This chapter presents a detailed study on the nonlinear dynamics and energy harvesting performance of a spring-coupled double cantilever beam-based PEH under parametric excitation. The system consists of two inverted cantilever beams with tip masses, coupled by a linear spring. The beams are equipped with MFC piezoelectric patches. Using Euler–Bernoulli beam theory, the model incorporates geometric and inertial nonlinearities. The governing electromechanical spatio-temporal equations of motion are derived using the Lagrange principle and discretized to their temporal form using the generalized Galerkin's method.

For the principal parametric resonance condition, frequency responses are obtained using the MMS and further verified with the results obtained by the Runge-Kutta method. Stability of the system is analyzed using the eigenvalues of the Jacobian matrix, which identify the key

bifurcations such as supercritical and subcritical pitchfork, saddle node, and Hopf bifurcations, portraying the transitions between stable and unstable vibration states.

Results show that the coupling spring significantly increases the frequency bandwidth of the trivial unstable region (TUR), enabling higher energy harvesting. For example, at spring stiffnesses of 1 N/m and 2 N/m, the bandwidth enhances significantly compared to the uncoupled system. Time responses and phase portraits confirm multiple steady states and quasi-periodic oscillations depending on initial conditions, highlighting strong nonlinear interactions.

Parametric studies reveal that tip mass and spring stiffness critically affect system performance. Increasing tip mass reduces natural frequencies and may induce buckling, while operating in the pre-buckled state ensures higher voltage output. Optimal load resistance maximizes output power, with a peak RMS power of 3.91 mW achieved for $K = 2$ N/m, sufficient to power low-energy devices like sensors and microelectronic systems.

The chapter concludes that parametric excitation combined with spring coupling broadens the operational frequency range and enhances power output. The observed nonlinear behaviour, including internal resonance and bifurcations, demonstrates that the proposed configuration offers a robust and efficient method for wideband piezoelectric energy harvesting suitable for real-world applications.

Chapter 4

Spring Coupled Double Beam Piezoelectric Energy Harvester with Magnetic and Parametric Instabilities

4.1 Introduction

The nonlinear dynamic study of a spring-coupled double cantilever-based piezoelectric energy harvester under the principal parametric resonance condition is discussed in Chapter 3. It is observed that the coupled system exhibits a broader operational frequency bandwidth as compared to its uncoupled counterpart. To further improve the performance of the energy harvester, following the work of Eshtehardiha et al. [31, 186], in this chapter, magnetic force is introduced to a similar PEH system investigated in the previous work. In section 4.2, the mathematical modelling is carried out for deriving the governing equations of motion of the proposed system. The equations are solved using the method of multiple scales as presented in section 4.3. The results are discussed in section 4.4, followed by section 4.5 summarizing the present study.

4.2 Mathematical modelling

Figure 4.1 schematically represents the proposed PEH system. Here, the beam attached with bimorph piezoelectric patches acts as the primary beam (1st beam) for energy harvesting, while the 2nd beam is under the influence of a magnetic force. MFC patches are the active piezo material. Tip masses are placed at the free end positions of both the beams. The tip mass of the 2nd beam is considered to be a Neodymium Iron Boron (NdFeB) permanent magnet (magnet B), which introduces the magnetic force into the PEH system while repulsing with another NdFeB magnet (magnet A) attached to the movable base. The magnet B can be adjusted (in the x-direction) to vary the gap between the magnets. The system is base-excited in the vertical direction (z - direction) with $z(t) = z_0 \sin(\omega t)$, which induces large amplitude oscillations to the beams in transverse direction, leading to a parametrically excited system. The beams are modelled as an Euler-Bernoulli beam with fixed at one end and attached mass at the free end.

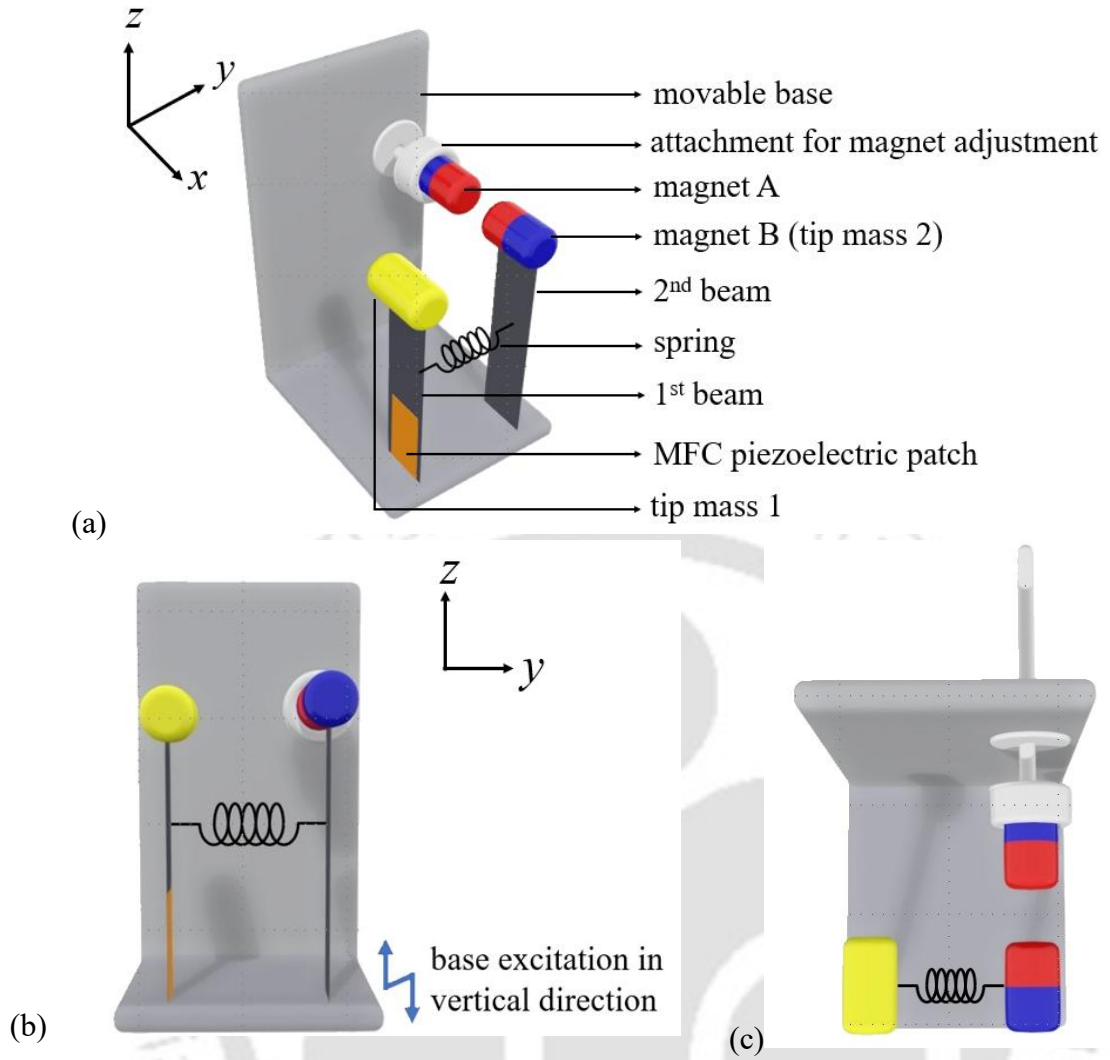

Figure 4.1: Schematic representation of the proposed piezoelectric energy harvester; (a) isometric view, (b) front view and (c) top view

The length, width and thickness of the beams are denoted by l_i, b_i and h_i, respectively, where $i = 1$ and 2 represent the 1st and 2nd beam. The tip mass attached to the i-th beam and the coupled spring stiffness are denoted by m_i and K, respectively. The length, width and thickness of the MFC patches are l_{Pi}, b_{Pi} and h_{Pi}, respectively. Along the neutral axis of the i-th beam, considering an arbitrary point O at a distance s_i from the base, the transverse displacement (in y - direction), axial displacement (in z - direction) and angular or rotational displacement (about x - axis) of the point O can be given by $w_{Oi}(s_i,t), u_{Oi}(s_i,t)$ and $\phi_{Oi}(s_i,t)$, respectively. The detailed expressions for these displacements, curvature and assumed first mode shape function are the same as given in section 3.2 of Chapter 3. The kinetic energy (T) of the proposed energy harvester can be expressed as follows.

$$T=\sum_{i=1,2}\left[\begin{array}{l}\frac{1}{2}\rho A\int_0^{l_i}\left[\left(\dot{w}_{Oi}\left(s_i,t\right)\right)^2+\left(\dot{u}_{Oi}\left(s_i,t\right)+\dot{z}\left(t\right)\right)^2\right]ds_i \\ +\frac{1}{2}m_i\left[\left(\dot{w}_{Oi}\left(l_i,t\right)\right)^2+\left(\dot{u}_{Oi}\left(l_i,t\right)+\dot{z}\left(t\right)\right)^2\right]+\frac{1}{2}I_{m_i}\left(\dot{\phi}_{Oi}\left(l_i,t\right)\right)^2\end{array}\right] \tag{4.1}$$

Here, ρ and A denote the density of the beam material and cross-sectional area of the beam, respectively. The mass of the piezoelectric patches (MFC) attached to beam surface are very less compared to the beam and hence its effect on the total kinetic energy of the system is considered to be negligible. The strain energy or the elastic potential energy of the beams, and the potential energy of the attached linear spring can be expressed as

$$U_s=\sum_{i=1,2}\left[\frac{1}{2}EI_i\int_0^{l_i}\left(\kappa_{Oi}\left(s_i,t\right)\right)^2 ds_i\right]+\frac{1}{2}K\left(w_{O1}\left(l_K,t\right)-w_{O2}\left(l_K,t\right)\right)^2 \tag{4.2}$$

where, the notations E, I_i and l_K represent the modulus of elasticity of the beam material, area moment of inertia of the *i*-th beam, and distance from the base to the position where the spring is connected with the beams, respectively. The potential energy of the system due to the effect of gravity can be defined as follows.

$$U_g=\sum_{i=1,2}\left[-\left\{\rho Ag\int_0^{l_i}\left(u_{Oi}\left(s_i,t\right)+z\left(t\right)\right)ds_i\right\}-m_i g\left(u_{Oi}\left(l_i,t\right)+z\left(t\right)\right)\right] \tag{4.3}$$

The interaction between two magnets induces magnetic repulsive force into the system and its strength depends on the gap between two same facing poles of these magnets. The distance vector ($\vec{R}$) between magnet A and magnet B can be written as follows,

$$\vec{R}=\begin{bmatrix}w_2\left(l_2,t\right)\\ D\end{bmatrix} \tag{4.5}$$

where, D is the gap between the permanent magnets. the work done by the repulsive magnetic force can also be expressed in terms of magnetic potential energy (U_m) and can be derived considering the dipole-dipole model [173, 236].

$$U_m=\frac{\mu_0}{4\pi}\left[\frac{\vec{M}_B}{\left\|\vec{R}\right\|_2^3}-\frac{3\left(\vec{M}_B\cdot\vec{R}\right)}{\left\|\vec{R}\right\|_2^5}\vec{R}_{AB}\right]\cdot\vec{M}_A \tag{4.6}$$

Where, the notations $\mu_0, \vec{M}_A, \vec{M}_B$ represent the permeability of free space, magnetic moment vector of the magnet A and magnet B, respectively. The magnetic moment vectors are defined as the product of the magnitude of the magnetization vector ($\vec{m}_A$ and $\vec{m}_B$) and the volume of the magnets (V_{magA} and V_{magB}).

$$\vec{M}_A = \begin{bmatrix} 0 \\ m_A \mathrm{V}_{magA} \end{bmatrix} \text{ and } \vec{M}_B = \begin{bmatrix} 0 \\ m_B \mathrm{V}_{magB} \end{bmatrix} \tag{4.7}$$

By substituting Eq. (4.5) and (4.7) in Eq. (4.6), magnetic potential energy can further be written as follows.

$$U_m = \frac{\mu_0 m_A \mathrm{V}_{magA} m_B \mathrm{V}_{magB}}{4\pi} \left[\frac{1}{\left\{ \left(w_2(t) \right)^2 + D^2 \right\}^{\frac{3}{2}}} - \frac{3D^2}{\left\{ \left(w_2(t) \right)^2 + D^2 \right\}^{\frac{5}{2}}} \right] \tag{4.8}$$

The total potential energy of the PEH system can be expressed as follows.

$$U = U_s + U_g + U_m \tag{4.9}$$

The dissipated energy due to internal material damping of the proposed system and air resistance can be expressed by a dissipation function (W_d) and can be written as follows,

$$W_d = \sum_{i=1,2} \left[\int_0^{l_i} C_i \dot{w}_{Oi}(s_i, t) \delta w_{Oi} ds_i \right] \tag{4.10}$$

where, C_i is the effective damping co-efficient of the *i*-th beam system. The piezoelectric patches (MFC) are bonded to the beam surface in bimorph configuration. Assuming the uniformity of the piezoelectric patches attached to the beam, the beam-patch system is considered to be symmetric and subjected to the bending strain only. Erturk and Inman [73] have presented detailed modelling procedures for piezoelectric sensors and actuators integrated with beam structures. During the oscillations of the beam, voltage is generated across the piezoelectric layers. The generated voltage induces moment across the neutral axis of the beam-patch system, which can be expressed as follows [77].

$$M_1(s_1, t) = \gamma_P V_1(t) \tag{4.11}$$

where, γ_p is a constant which depends on the geometry of the system and the configuration of the piezoelectric transducers. In case of bimorph piezoelectric layers in 31 configurations; the constant γ_p can be defined as

$$\gamma_p = E_p d_{31} b_p \left(h_1 + h_p\right) \tag{4.12}$$

where, E_P, d_{31}, b_P, h_1, h_P denote Young's modulus of the piezoelectric MFC patch, piezoelectric constant, width of the piezoelectric patch, thickness of the 1st beam and thickness of the piezoelectric patch, respectively. The work done by the moment produced by the voltage about the neutral axis can be written as follows.

$$W = \int_0^{l_p} M_1\left(s_1, t\right) \kappa_{Q1}\left(s_1\right) ds_1 \tag{4.13}$$

By using Lagrange's principle, the governing electro mechanical equations of motion of the proposed system can be found and further discretized to temporal forms using generalized Galerkin's method.

$$\ddot{w}_1 + \alpha_{10}\dot{w}_1 + \alpha_{11}w_1 + \alpha_{12}\left(\ddot{w}_1 w_1^2 + \dot{w}_1^2 w_1\right) + \alpha_{13}w_1^3 - \alpha_{14}w_2 + \alpha_{15}V_1 = f_1 \sin\left(\omega t\right) w_1 \tag{4.14}$$

$$C_p \dot{V}_1 + \frac{V_1}{R_L} + \theta_1 \dot{w}_1 = 0 \tag{4.15}$$

$$\ddot{w}_2 + \alpha_{20}\dot{w}_2 + \alpha_{21}w_2 + \alpha_{22}\left(\ddot{w}_2 w_2^2 + \dot{w}_2^2 w_2\right) + \alpha_{23}w_2^3 - \alpha_{24}w_1 = f_2 \sin\left(\omega t\right) w_2 \tag{4.16}$$

Here, C_P and R_L represent the capacitance of the piezoelectric (MFC) patches and load resistance connected to the electrical circuit of the piezo transducers, respectively. The coefficients used in the equations of motion are given in Appendix B1. It is to be noted that $\alpha_{11} = \omega_1^2$ and $\alpha_{21} = \omega_2^2$. The power output (P_1) of the system is calculated using the RMS value of the output AC voltage and is given as follows.

$$P_1 = \frac{\left(V_1^{RMS}\right)^2}{R_L} \tag{4.17}$$

The Eqs. (4.14 – 4.16) can further be reduced to the non-dimensionalized forms by assuming the non-dimensional time scale ($\tau = \sqrt{\alpha_{11}}t$), the non-dimensional transverse displacements of

the tip ($\bar{w}_i = \left(w_i / l_g\right)$; here $l_g = 0.1$ m), non-dimensional voltage ($\bar{V}_i = l_g\left(\theta_1 / C_p\right)V_i$), and can be written as follows.

$$\ddot{\bar{w}}_1 + \varepsilon\bar{\alpha}_{10}\dot{\bar{w}}_1 + \bar{\alpha}_{11}\bar{w}_1 + \varepsilon\bar{\alpha}_{12}\left(\ddot{\bar{w}}_1\bar{w}_1^2 + \dot{\bar{w}}_1^2\bar{w}_1\right) + \varepsilon\bar{\alpha}_{13}\bar{w}_1^3 - \varepsilon\bar{\alpha}_{14}\bar{w}_2 - \varepsilon\bar{\alpha}_{15}\bar{V}_1 = \varepsilon f_1 \sin\left(\Phi\tau\right)\bar{w}_1 \tag{4.18}$$

$$\dot{\bar{V}}_1 + r_{11}\bar{V}_1 + \dot{\bar{w}}_1 = 0 \tag{4.19}$$

$$\ddot{\bar{w}}_2 + \varepsilon\bar{\alpha}_{20}\dot{\bar{w}}_2 + \bar{\alpha}_{21}\bar{w}_2 + \varepsilon\bar{\alpha}_{22}\left(\ddot{\bar{w}}_2\bar{w}_2^2 + \dot{\bar{w}}_2^2\bar{w}_2\right) + \varepsilon\bar{\alpha}_{23}\bar{w}_2^3 - \varepsilon\bar{\alpha}_{24}\bar{w}_1 = \varepsilon f_2 \sin\left(\Phi\tau\right)\bar{w}_2 \tag{4.20}$$

Here, $\varepsilon \ll 1$ is a book keeping parameter. The nondimensional coefficients of the Eqs. (4.18 – 4.20) are given in Appendix B2. The static equilibrium positions of the system and their stability can be found by equating the linear and cubic nonlinear stiffness terms of the Eqs. (4.18) and (4.20) to zero; which can be written as follows.

$$\bar{\alpha}_{11}\bar{w}_1 + \varepsilon\bar{\alpha}_{13}\bar{w}_1^3 - \bar{\alpha}_{14}\bar{w}_2 = 0 \tag{4.21}$$

$$\bar{\alpha}_{21}\bar{w}_2 + \varepsilon\bar{\alpha}_{23}\bar{w}_2^3 - \bar{\alpha}_{24}\bar{w}_1 = 0 \tag{4.22}$$

The solutions of $\bar{w}_1$ and $\bar{w}_2$ obtained from the Eqs. (4.21 and 4.22) give the static equilibrium positions of the 1st and 2nd beam, respectively.

4.3 Solution of the temporal equations

Uniform first order approximate solutions of Eqs. (4.18 – 4.20) are obtained using the standard method of multiple scales (MMS) as similar to the section 3.3 in Chapter 3. It is to be noted that the present study considers the magnetic repulsive force induced in the double beam based PEH system which is not studied in the previous chapter. Following the similar procedure of MMS, the non-dimensional displacements ($\bar{w}_1, \bar{w}_2$) and voltage ($\bar{V}_1$) can be expressed as follows.

$$\bar{w}_1 = \bar{w}_{10}\left(T_0, T_1\right) + \varepsilon\bar{w}_{11}\left(T_0, T_1\right) \tag{4.23}$$

$$\bar{V}_1 = \bar{V}_{10}\left(T_0, T_1\right) + \varepsilon\bar{V}_{11}\left(T_0, T_1\right) \tag{4.24}$$

$$\bar{v}_2 = \bar{w}_{20}\left(T_0, T_1\right) + \varepsilon\bar{w}_{21}\left(T_0, T_1\right) \tag{4.25}$$

Substituting Eqs. (4.23 – 4.25) in Eqs. (4.18 – 4.20) and collecting the terms of ε^0 and ε^1 order, one may obtain the following sets of equations.

Terms associated with ε^0 order:

$$D_0^2\bar{w}_{10}+\alpha_{11}\bar{w}_{10}=0 \tag{4.26}$$

$$D_0\bar{V}_0+r_{11}\bar{V}_0=-D_0\bar{w}_{10} \tag{4.27}$$

$$D_0^2\bar{w}_{20}+\alpha_{21}\bar{w}_{20}=0 \tag{4.28}$$

Terms associated with ε^1 order:

$$D_0^2\bar{w}_{11}+\bar{\alpha}_{11}\bar{w}_{11}=\begin{bmatrix}-2D_0D_1\bar{w}_{10}-\bar{\alpha}_{10}D_0\bar{w}_{10}-\bar{\alpha}_{12}\left\{\bar{w}_{10}^2D_0^2\bar{w}_{10}+\bar{w}_{10}\left(D_0\bar{w}_{10}\right)^2\right\}\\ -\bar{\alpha}_{13}\bar{w}_{10}^3+\bar{\alpha}_{14}\bar{w}_{20}+\bar{\alpha}_{15}\bar{V}_0+\bar{\alpha}_{16}\dfrac{e^{i\Phi T_0}-e^{-i\Phi T_0}}{2i}\bar{w}_{10}\end{bmatrix} \tag{4.29}$$

$$D_0\bar{V}_1+r_{11}\bar{V}_1=-D_1\bar{V}_0-D_0\bar{w}_{11}-D_1\bar{w}_{10} \tag{4.30}$$

$$D_0^2\bar{w}_{21}+\bar{\alpha}_{21}\bar{w}_{21}=\begin{bmatrix}-2D_0D_1\bar{w}_{20}-\bar{\alpha}_{20}D_0\bar{w}_{20}-\bar{\alpha}_{22}\left\{\bar{w}_{20}^2D_0^2\bar{w}_{20}+\bar{w}_{20}\left(D_0\bar{w}_{20}\right)^2\right\}\\ -\bar{\alpha}_{23}\bar{w}_{20}^3+\bar{\alpha}_{24}\bar{w}_{10}+\bar{\alpha}_{26}\dfrac{e^{i\Phi T_0}-e^{-i\Phi T_0}}{2i}\bar{w}_{20}\end{bmatrix} \tag{4.31}$$

General solutions of Eqs. (4.26 – 4.28) are

$$\bar{w}_{10}=A_1\left(T_1\right)e^{\left(i\sqrt{\bar{\alpha}_{11}}T_0\right)}+CC \tag{4.32}$$

$$\bar{V}_{10}=-Z\left(T_1\right)e^{\left(i\sqrt{\bar{\alpha}_{11}}T_0\right)}+CC \tag{4.33}$$

$$\bar{w}_{20}=A_2\left(T_1\right)e^{\left(i\sqrt{\bar{\alpha}_{21}}T_0\right)}+CC \tag{4.34}$$

where, $Z\left(T_1\right)=\dfrac{\left(\bar{\alpha}_{11}+i\sqrt{\bar{\alpha}_{11}}r_{11}\right)}{\left(\bar{\alpha}_{11}+r_{11}^2\right)}A_1\left(T_1\right)$.

Now, by substituting the solutions obtained in Eqs. (4.32 – 4.34) into the Eqs. (4.29) and (4.31) and setting the secular terms to zero, one can obtain the following expressions. In case of the principal parametric resonance condition, the external excitation frequency is equal to twice of the natural frequencies of the system, i.e., $\Phi=2\sqrt{\bar{\alpha}_{11}}+\varepsilon\sigma_1$ .he non-dimensional natural

frequencies of the system are considered to be in a relation of $\sqrt{\bar{\alpha}_{21}} = \sqrt{\bar{\alpha}_{11}} + \varepsilon\sigma_2$. Here, σ_1 and σ_2 are the detuning parameters.

$$\left[\begin{array}{l} -2i\sqrt{\bar{\alpha}_{11}}D_1A_1 - \bar{\alpha}_{10}i\sqrt{\bar{\alpha}_{11}}A_1 + \left(2\bar{\alpha}_{11}\bar{\alpha}_{12} - 3\bar{\alpha}_{13}\right)A_1^2\bar{A}_1 \\ +\bar{\alpha}_{14}A_2\exp\left(i\sigma_2T_1\right) - \bar{\alpha}_{15}\left(\dfrac{\bar{\alpha}_{11} + i\sqrt{\bar{\alpha}_{11}}r_{11}}{\bar{\alpha}_{11} + r_{11}^2}\right)A_1 + \dfrac{\bar{\alpha}_{16}}{2i}\bar{A}_1\exp\left(i\sigma_1T_1\right) \end{array}\right] = 0 \tag{4.35}$$

$$\left[\begin{array}{l} -2i\sqrt{\bar{\alpha}_{21}}D_1A_2 - \bar{\alpha}_{20}i\sqrt{\bar{\alpha}_{21}}A_2 + \left(2\bar{\alpha}_{21}\bar{\alpha}_{22} - 3\bar{\alpha}_{23}\right)A_2^2\bar{A}_2 \\ +\bar{\alpha}_{24}A_1\exp\left(-i\sigma_2T_1\right) + \dfrac{\bar{\alpha}_{26}}{2i}\bar{A}_2\exp\left\{i\left(\sigma_1 - 2\sigma_2\right)T_1\right\} \end{array}\right] = 0 \tag{4.36}$$

After elimination of the secular terms, the particular solutions of the Eqs. (4.29 – 4.32) can be written as follows.

$$\bar{w}_{11} = -\left[\frac{\left(2\bar{\alpha}_{11}\bar{\alpha}_{12} - \bar{\alpha}_{13}\right)A_1^3 - i\dfrac{\bar{\alpha}_{16}}{2}A_1e^{i\sigma_1T_1}}{8\bar{\alpha}_{11}}\right]e^{3i\sqrt{\bar{\alpha}_{11}}T_0} + CC \tag{4.37}$$

$$\bar{V}_1 = \left(\frac{9\bar{\alpha}_{11} + 3i\sqrt{\bar{\alpha}_{11}}r_{11}}{9\bar{\alpha}_{11} + r_{11}^2}\right)\left\{\frac{\left(2\bar{\alpha}_{12}\bar{\alpha}_{11} - \bar{\alpha}_{13}\right)A_1^3 - i\dfrac{\bar{\alpha}_{16}}{2}A_1e^{i\sigma_1T_1}}{8\bar{\alpha}_{11}}\right\}e^{3i\sqrt{\bar{\alpha}_{11}}T_0} + CC \tag{4.38}$$

$$\bar{w}_{21} = -\left[\frac{\left(2\bar{\alpha}_{21}\bar{\alpha}_{22} - \bar{\alpha}_{23}\right)A_2^3 - i\dfrac{\bar{\alpha}_{26}}{2}A_2e^{i\sigma_1T_1}}{8\bar{\alpha}_{21}}\right]e^{3i\sqrt{\bar{\alpha}_{21}}T_0} + CC \tag{4.39}$$

Introducing $A_1 = \frac{a_1}{2}e^{i\beta_1}$, $\bar{A}_1 = \frac{a_1}{2}e^{-i\beta_1}$, $A_2 = \frac{a_2}{2}e^{i\beta_2}$ and $\bar{A}_2 = \frac{a_2}{2}e^{-i\beta_2}$ where a_1, a_2, β_1, β_2 are real numbers along with $\sigma_1T_1 - 2\beta_1 = 2\gamma_1$ and $\left(\sigma_1 - 2\sigma_2\right)T_1 - 2\beta_2 = 2\gamma_2$ in Eqs. (4.35) and (4.36), the following reduced equations can be obtained by separating the real and imaginary parts. The following equations are first order nonlinear differential equations of amplitude and phase and are further used to obtain the solutions of the system. These equations are first order nonlinear differential equations which are function of amplitudes and phases.

Real parts:

$$a_1\gamma_1' = \left[\begin{array}{l} \sigma_1\frac{a_1}{2} + \left(2\sqrt{\bar{\alpha}_{11}}\bar{\alpha}_{12} - \frac{3\bar{\alpha}_{13}}{\sqrt{\bar{\alpha}_{11}}}\right)\frac{a_1^3}{8} + \frac{\bar{\alpha}_{14}}{\sqrt{\bar{\alpha}_{11}}}\frac{a_2}{2}\cos(\gamma_1-\gamma_2) - \frac{\sqrt{\bar{\alpha}_{11}}\bar{\alpha}_{15}}{\left(\bar{\alpha}_{11}+r_{11}^2\right)}\frac{a_1}{2} \\ + \frac{\bar{\alpha}_{16}}{2\sqrt{\bar{\alpha}_{11}}}\frac{a_1}{2}\sin(2\gamma_1) \end{array}\right] \tag{4.40}$$

$$a_2\gamma_2' = \left[\left(\sigma_1 - 2\sigma_2\right)\frac{a_2}{2} + \left(2\sqrt{\bar{\alpha}_{21}}\bar{\alpha}_{22} - \frac{3\bar{\alpha}_{23}}{\sqrt{\bar{\alpha}_{21}}}\right)\frac{a_2^3}{8} + \frac{\bar{\alpha}_{24}}{\sqrt{\bar{\alpha}_{21}}}\frac{a_1}{2}\cos(\gamma_2-\gamma_1) + \frac{\bar{\alpha}_{26}}{2\sqrt{\bar{\alpha}_{21}}}\frac{a_2}{2}\sin(2\gamma_2)\right] \tag{4.41}$$

Imaginary parts:

$$a_1' = -\frac{\bar{\alpha}_{10}}{2}a_1 + \frac{\bar{\alpha}_{14}}{2\sqrt{\bar{\alpha}_{11}}}a_2\sin(\gamma_1-\gamma_2) - \frac{\bar{\alpha}_{15}r_{11}}{2\left(\bar{\alpha}_{11}+r_{11}^2\right)}a_1 - \frac{\bar{\alpha}_{16}}{4\sqrt{\bar{\alpha}_{11}}}a_1\cos(2\gamma_1) \tag{4.42}$$

$$a_2' = -\frac{\bar{\alpha}_{20}}{2}a_2 + \frac{\bar{\alpha}_{24}}{2\sqrt{\bar{\alpha}_{21}}}a_1\sin(\gamma_2-\gamma_1) - \frac{\bar{\alpha}_{26}}{4\sqrt{\bar{\alpha}_{21}}}a_2\cos(2\gamma_2) \tag{4.43}$$

To study the stability and bifurcations of trivial as well as non-trivial solutions, the Eqs. (4.40 – 4.43) are transformed into Cartesian co-ordinate system by introducing $p_1 = a_1\cos\gamma_1$, $q_1 = a_1\sin\gamma_1$, $p_2 = a_2\cos\gamma_2$, $q_2 = a_2\sin\gamma_2$ and one may obtain the following set of equations.

$$p_1' = \left[\begin{array}{l} -\frac{\sigma_1}{2}q_1 - \frac{\bar{\alpha}_{10}}{2}p_1 - \left(2\sqrt{\bar{\alpha}_{11}}\bar{\alpha}_{12} - \frac{3\bar{\alpha}_{13}}{\sqrt{\bar{\alpha}_{11}}}\right)\left(\frac{p_1^2q_1+q_1^3}{8}\right) - \frac{\bar{\alpha}_{14}}{2\sqrt{\bar{\alpha}_{11}}}q_2 \\ + \frac{\bar{\alpha}_{15}}{2\left(\bar{\alpha}_{11}+r_{11}^2\right)}\left(\sqrt{\bar{\alpha}_{11}}q_1 - r_{11}p_1\right) - \frac{\bar{\alpha}_{16}}{4\sqrt{\bar{\alpha}_{11}}}p_1 \end{array}\right] \tag{4.44}$$

$$q_1' = \left[\begin{array}{l} \frac{\sigma_1}{2}p_1 - \frac{\bar{\alpha}_{10}}{2}q_1 + \left(2\sqrt{\bar{\alpha}_{11}}\bar{\alpha}_{12} - \frac{3\bar{\alpha}_{13}}{\sqrt{\bar{\alpha}_{11}}}\right)\left(\frac{p_1^3+p_1q_1^2}{8}\right) \\ + \frac{\bar{\alpha}_{14}}{2\sqrt{\bar{\alpha}_{11}}}p_2 - \frac{\bar{\alpha}_{15}}{2\left(\bar{\alpha}_{11}+r_{11}^2\right)}\left(r_{11}q_1 + \sqrt{\bar{\alpha}_{11}}p_1\right) + \frac{\bar{\alpha}_{16}}{4\sqrt{\bar{\alpha}_{11}}}q_1 \end{array}\right] \tag{4.45}$$

$$p_2' = \left[\begin{array}{l} -\left(\frac{\sigma_1}{2}-\sigma_2\right)q_2 - \frac{\bar{\alpha}_{20}}{2}p_2 - \left(2\sqrt{\bar{\alpha}_{21}}\bar{\alpha}_{22} - \frac{3\bar{\alpha}_{23}}{\sqrt{\bar{\alpha}_{21}}}\right)\left(\frac{p_2^2q_2+q_2^3}{8}\right) \\ - \frac{\bar{\alpha}_{24}}{2\sqrt{\bar{\alpha}_{21}}}q_1 - \frac{\bar{\alpha}_{26}}{4\sqrt{\bar{\alpha}_{21}}}p_2 \end{array}\right] \tag{4.46}$$

$$q_2' = \left[\begin{array}{l} \left(\frac{\sigma_1}{2} - \sigma_2 \right) p_2 - \frac{\bar{\alpha}_{20}}{2} q_2 + \left(2\sqrt{\bar{\alpha}_{21}}\bar{\alpha}_{22} - \frac{3\bar{\alpha}_{23}}{\sqrt{\bar{\alpha}_{21}}} \right) \left(\frac{p_2^3 + p_2 q_2^2}{8} \right) \\ + \frac{\bar{\alpha}_{24}}{2\sqrt{\bar{\alpha}_{21}}} p_1 + \frac{\bar{\alpha}_{26}}{4\sqrt{\bar{\alpha}_{21}}} q_2 \end{array} \right] \tag{4.47}$$

The Eqs. (4.44 – 4.47) are solved using Newton's method and solutions are obtained for the steady state ($p_1' = q_1' = p_2' = q_2' = 0$). To study the stability of the trivial and non-trivial solutions, one may find the eigenvalues of the Jacobian matrix obtained using the right-hand side of the nonlinear algebraic Eqs. (4.44 – 4.47). The Jacobian matrix can be written as follows.

$$\{J\} = \begin{Bmatrix} j_{11} & j_{13} & j_{13} & j_{14} \\ j_{21} & j_{22} & j_{23} & j_{24} \\ j_{31} & j_{32} & j_{33} & j_{34} \\ j_{41} & j_{42} & j_{43} & j_{44} \end{Bmatrix} \tag{4.48}$$

The elements of the Jacobian matrix are given in Appendix B2.

4.4 Results and discussion

This section deals with the parametric study of the energy harvester under the influence of magnetic force. Results obtained by both MMS and ode45 are verified. Physical dimensions and material properties of the components of the system are given in Table 4.1, where most of the parameters are same as that in Chapter 3. The length and tip masses of the beams are modified so that their modal frequencies are nearly in 1:1 ratio.

Figure 4.2 represents the static equilibrium positions of the beams obtained by solving the Eqs. (4.21) and (4.22). Here, equilibrium positions are plotted in the dimensionalized form. With decreasing the gap (D) between the magnets, the static system changes from monostable to bi-stable state. Due to the system configuration, the 2nd beam is under magnetic interaction and hence when both the beams are not coupled with a linear spring, static bifurcation occurs in the 2nd beam only and 1st beam remains in trivial state. In the coupled condition with K = 1 N/m, one can observe that the trivial state of both the beams bifurcate with pitchfork bifurcation; become unstable and two non-trivial stable branches appear when the gap (D) between the two permanent magnets decreases. In Figure 4.2 (b), it can also be noted that with the coupled spring, the bifurcation point shifts from right to left and the non-trivial equilibrium points reduce to lesser value. It is because of stiffness hardening of the system.

Table 4.1: Physical dimensions and material properties of the PEH system

Parameters	**Values (unit)**	**Parameters**	**Values (unit)**
Young's modulus, E	210 GPa	Spring stiffness, K	1 N/m
Density, ρ	7850 kg/m^2	l_K	0.1 m
1st beam length, l_1	0.15 m	MFC length, l_P	0.028 m
2nd beam length, l_2	0.155 m	MFC width, b_P	0.014 m
Beam width, $b_1 = b_2$	0.016 m	MFC thickness, h_P	0.3×10^{-3} m
Beam thickness, $h_1 = h_2$	0.254×10^{-3} m	Piezo constant, d_{31}	-170 pC/N
1st beam tip mass, m_1	0.03 kg	γ_P	-4×10^{-5} N-m/v
2nd beam tip mass, m_2	0.027 kg	Capacitance, C_P	51.4 nF
Mass MOI, I_{m_i}	$m_i \times 40.87$ kg-mm^2	Load resistance, R_{Li}	100 kΩ
Coeff. of damping, C_1	0.001 N-s/m	Magnet height, $h_A = 2h_B$	0.006 m
Coeff. of damping, C_2	0.002 N-s/m	Magnet dia., $d_A = d_B$	0.01 m
Free space permeability, μ_0	1×10^6 A/m	$\lvert\vec{m}_A\rvert$, $\lvert\vec{m}_B\rvert$	$4\pi\times10^{-7}$ H/m

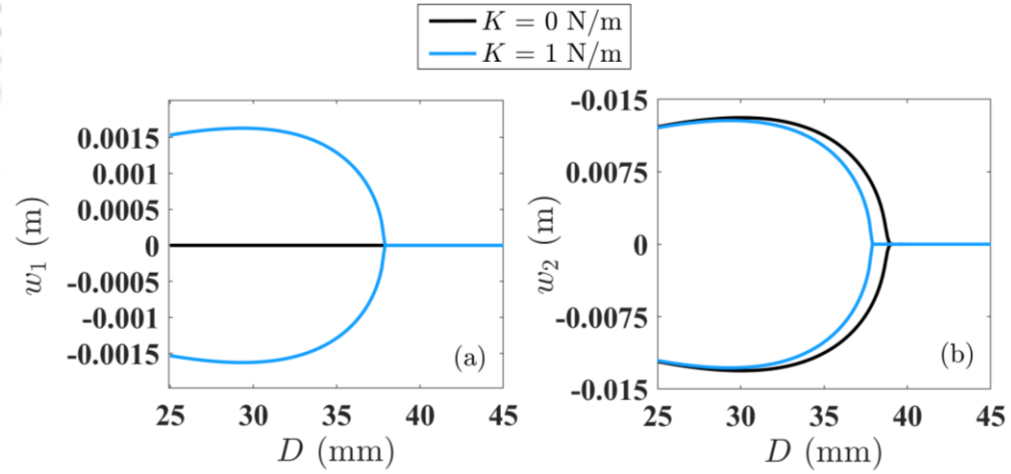

Figure 4.2: Static bifurcation and equilibrium positions of (a) 1st beam and (b) 2nd beam with varying distance (D) between two NdFeB magnets

To show the enhanced operability of the proposed PEH at different excitation condition, the parametric instability curves are plotted for five different cases as shown in Figure 4.3. Phenomenally, the 'v' or 'w' shaped curves represent the transitions or the boundaries between the stable (S) and unstable (US) trivial states. For $p_1 = q_1 = p_2 = q_2 = 0$, these instability curves have been obtained by finding the points where the real part of the eigenvalues of the Jacobian

matrix $\{J\}$ change sign from negative to positive or vice-versa. If all the real parts of the eigenvalues are negative, the fixed point is asymptotically stable, else if even one of real part of the eigenvalues become positive, the fixed point becomes unstable. In this figure, Φ is the non-dimensional excitation frequency and $\bar{z}$ is the non-dimensional excitation amplitude (where $\bar{z} = (z_0 / z_r)$ and $z_r = 1$ mm).

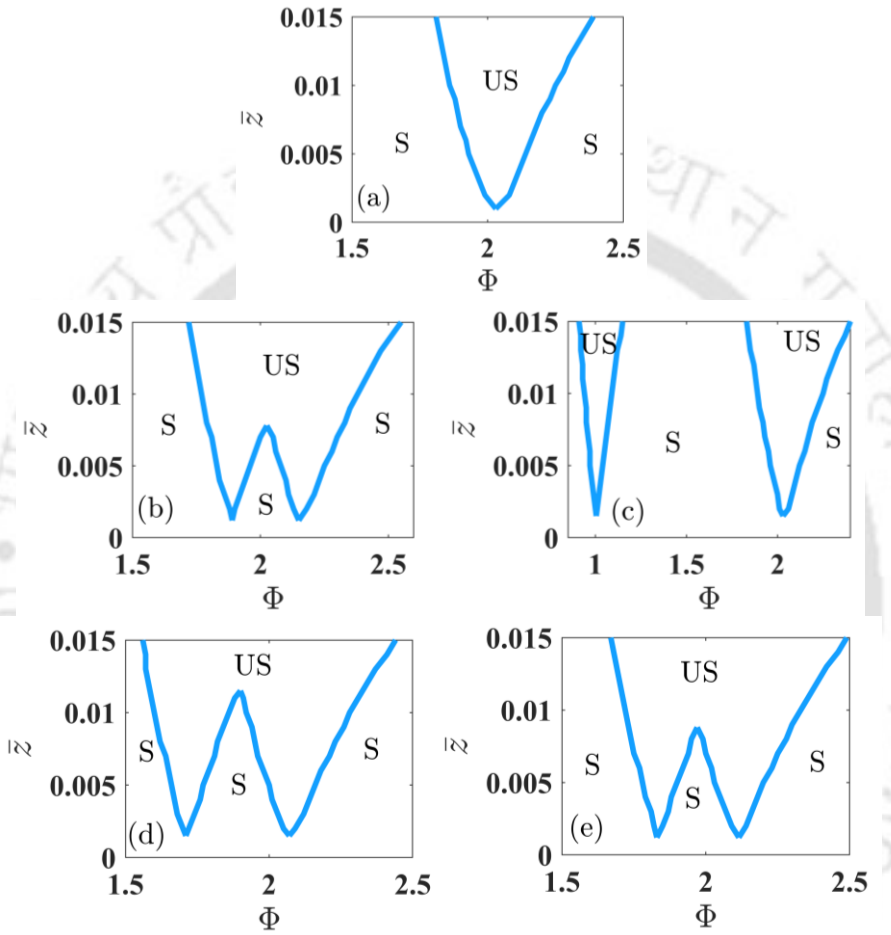

Figure 4.3: Parametric instability regions of the energy harvester for (a) K = 0 N/m and no magnet; for K = 1 N/m (b) no magnet, (c) D = 40 mm, (d) D = 50 mm and (e) D = 60 mm

It may be observed that as the excitation amplitude increases, the instability region also widens. Initially for the uncoupled system without any magnetic interaction, a single 'v' shaped instability curve appears. Whereas, for the coupled system with K = 1 N/m, the system exhibits 'w' shaped curves with or without magnetic interactions except for the case of D = 40 mm. Here, one can observe that the 'w' shaped instability region separates into two distinct 'v' shaped instability regions. This separation of the instability region occurs because when the distance between the permanent magnets decreases, the natural frequency of the system also decreases. Correspondingly, at a lesser excitation frequency, the system becomes unstable,

which may further lead the system to harvest energy nearby $\Phi = 1$. It can also be observed that at lower values of $\bar{z}$, when the system is under magnetic interaction, the region of parametric instability is narrower compared to the case without magnetic interaction. For example, with $K = 1$ N/m and $\bar{z} = 0.005$, the system without magnetic force exhibits an instability range of $\Phi = 1.83$ to 1.96 and $\Phi = 2.08$ to 2.25. However, when the system is under magnetic force (with D = 50 mm), the instability range appears to be $\Phi = 1.66$ to 1.77 and $\Phi = 2$ to 2.16. As the energy harvester can be operated in the unstable trivial state, one should properly choose the stiffness of the spring and the distance between the magnets to get a wide range of frequencies for the harvester.

Table 4.2: Natural frequencies of the uncoupled and coupled system

Distance between the magnets (*D*)	**Natural frequencies (rad/s)**
Uncoupled (*K* = 0 N/m)	
no magnet	7.16 rad/s and 7.37 rad/s
Coupled (*K* = 1 N/m)	
no magnet	7.26 rad/s and 8.29 rad/s
D = 40 mm	7.79 rad/s and 3.81 rad/s
D = 45 mm	7.86 rad/s and 5.83 rad/s
D = 50 mm	7.95 rad/s and 6.56 rad/s
D = 55 mm	8.04 rad/s and 6.89 rad/s
D = 60 mm	8.11 rad/s and 7.04 rad/s

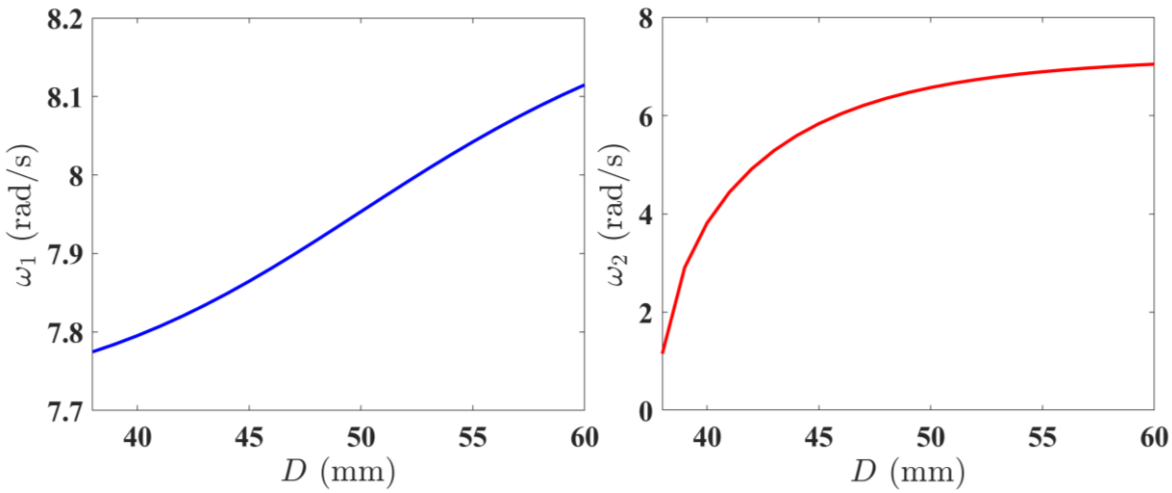

Figure 4.4: For K = 1 N/m, natural frequencies of the PEH with varying gap distance between the magnets

Case 1: MFC patches on 1st beam

Table 4.2 represents the natural frequencies of the system. Figure 4.4 shows the change in the modal frequencies of the coupled system with variation in the gap between the magnets. This gap significantly influences the modal frequencies. It can be observed that with decrease in the D value, ω_2 decreases sharply. Figure 4.5 represents the frequency responses of tip displacements and output voltage of the system without coupled spring and magnetic force. Here, it can be observed that the stable trivial state bifurcates with PFB_{sup} (at $\Phi = 1.93$) and unstable trivial state bifurcates with PFB_{sub} (at $\Phi = 2.07$). Hence, for energy harvesting the operational frequency bandwidth is $\Phi = 1.93$ to 2.07 i.e., 0.14. The corresponding maximum RMS voltage output is 2.66 V for a load resistance of 100 kΩ.

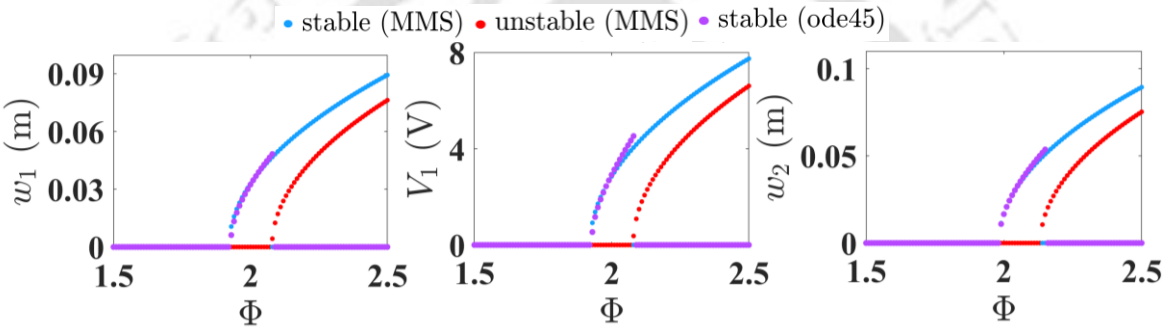

Figure 4.5: Frequency responses of the uncoupled PEH system

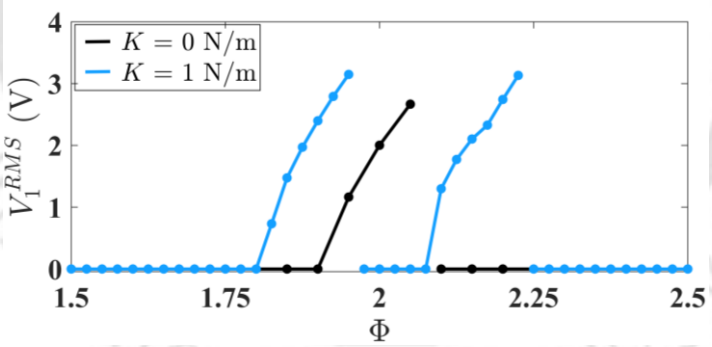

Figure 4.6: RMS output voltage of the system in absence of magnetic interaction

Figure 4.6 shows the RMS output voltage of the system for uncoupled ($K = 0$ N/m) and coupled condition ($K = 1$ N/m) with a load resistance of 100 kΩ. For $K = 1$ N/m, the maximum RMS output voltage is 3.14 V and the operational frequency range is $\Phi = 1.81$ to 1.95 and $\Phi = 2.075$ to 2.225. The RMS voltage increases by 18.04% and the bandwidth is doubled than the uncoupled condition. Hence, it is observed that the system performance in terms of output voltage, power and operational frequency range enhances with addition of the spring between the two beams.

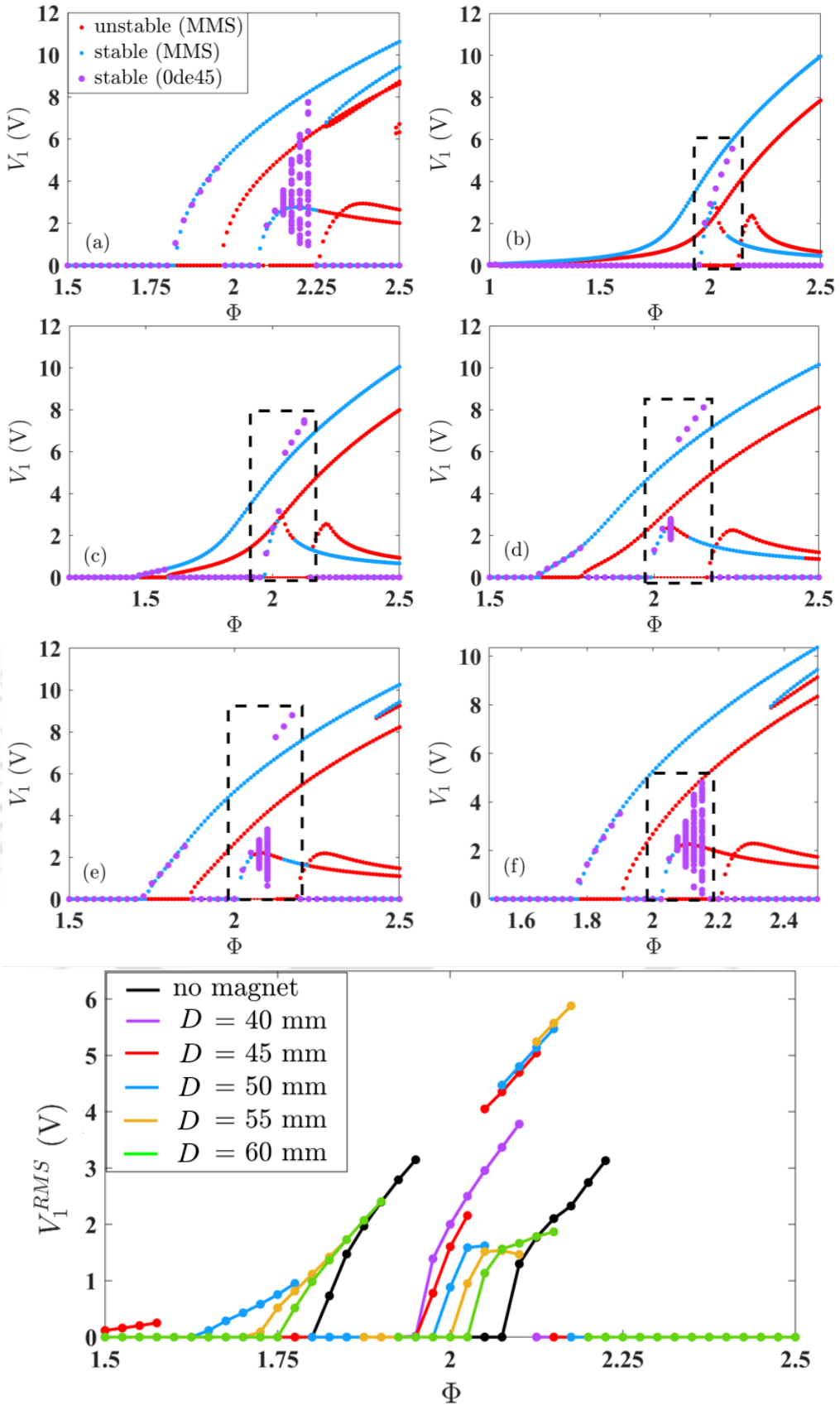

Figure 4.7: At K = 1 N/m, frequency vs. voltage responses for (a) no magnet, (b) D = 40 mm, (c) D = 45 mm, (d) D = 50 mm, (e) D = 55 mm, (f) D = 60 mm and (g) RMS voltage of all

Figure 4.7 shows the frequency responses when the coupled spring stiffness is 1 N/m and the load resistance is 100 kΩ. The solutions obtained through MMS show the stable and unstable responses which are important for interpretation of the bifurcation points. In Figure 4.7 (a - f), one can observe that when the excitation frequency is approximately near two or more, the non-trivial stable branch bifurcates with hopf bifurcation and becomes unstable. For some specific values of D, periodic to quasi-periodic or chaotic responses can also be observed as the excitation frequency increases, which can further be verified from the time responses plotted in Figure 4.8 and Figure 4.9. The dash-marked regions in Figure 4.7 (b - f) show that, when the excitation frequency is nearby the principal parametric resonance frequency, due to the dominance of two nearby unstable orbits; the low amplitude stable responses jump towards the higher amplitude stable orbits. As a result, the voltage output increases in this region as compared to the case of without magnetic force. Figure 4.7 (g) obtained from solving Eqs. (4.18 – 4.20) using ode45, shows that the RMS voltage output is maximum at $\Phi = 2.15$ when D = 55 mm. The highest peak denotes the value of 5.96 V, which is 89.8% more compared to that of without magnetic force ($V_1^{RMS} = 3.14$ V). Hence, by setting the gap (D) between the permanent magnets properly, the performance of the system can be enhanced.

Figure 4.8 and Figure 4.9 show the time responses, phase portraits, Poincaré sections (red dots) and FFT plots of the proposed piezoelectric energy harvester with coupled spring stiffness of K = 1 N/m and without any magnetic interaction. While tuning the external excitation frequency from $\Phi = 2.1$ to $\Phi = 2.2$, it can be observed that the dynamic response of the energy harvester changes its behavior from period-1 to quasi-periodic. The phase portraits change from single stable limit cycle to torus through torus bifurcation or secondary hopf bifurcation. Torus bifurcations in coupled mechanical systems have been studied extensively by Bakri et al. [237]. The Poincaré sections of the torus show closed invariant curves. Also, the FFT plots for both periodic and quasi-periodic responses justify the above-mentioned. Figure 4.10 and Figure 4.11 illustrate the time responses, phase portraits, Poincaré sections and FFT plots for K = 1 N/m, D = 60 mm. Here, one can find chaotic responses for $\Phi = 2.15$. Periodic to quasi-periodic to chaotic behavior is evident depending on the external excitation frequency which is also mentioned earlier and represented in Figure 4.7. Again at $\Phi = 2.175$, the responses become periodic with a stable limit cycle.

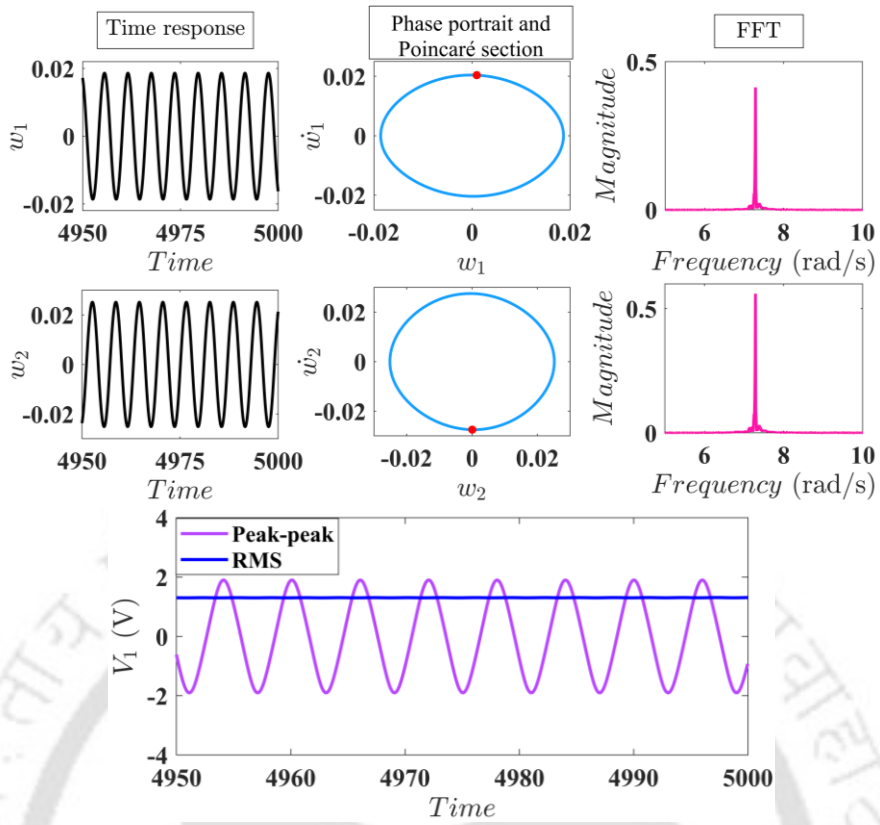

Figure 4.8: Time responses, phase portraits, Poincaré sections and output voltage of the PEH for $K = 1$ N/m and no magnet condition, at $\Phi = 2.1$

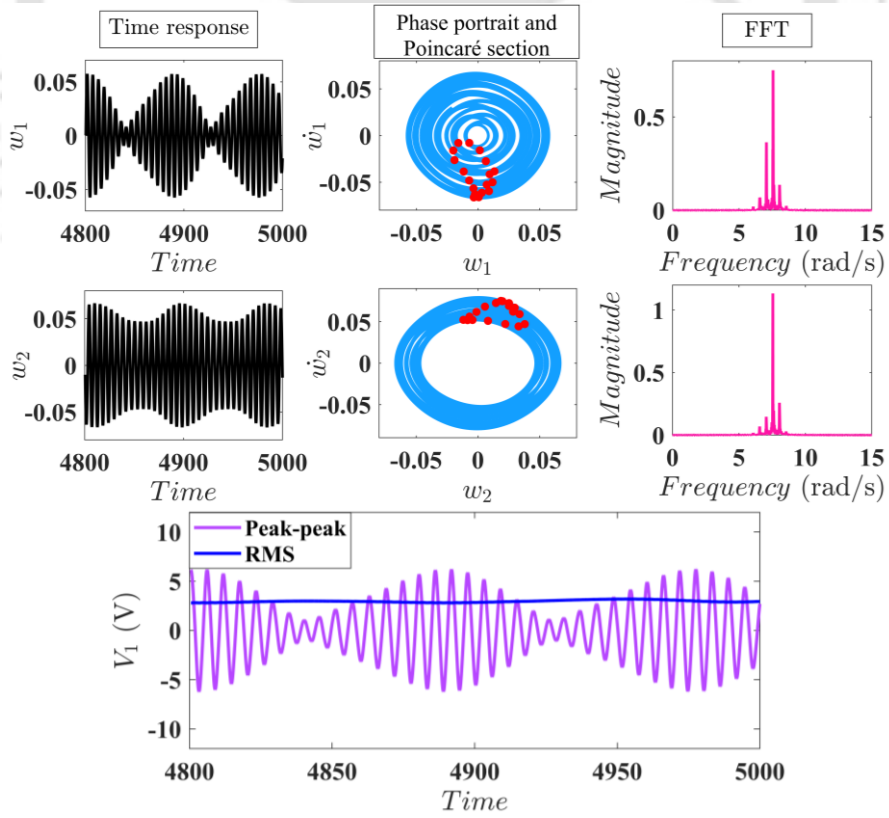

Figure 4.9: Time responses, phase portraits, Poincaré sections and output voltage of the PEH for $K = 1$ N/m and no magnet condition, at $\Phi = 2.2$

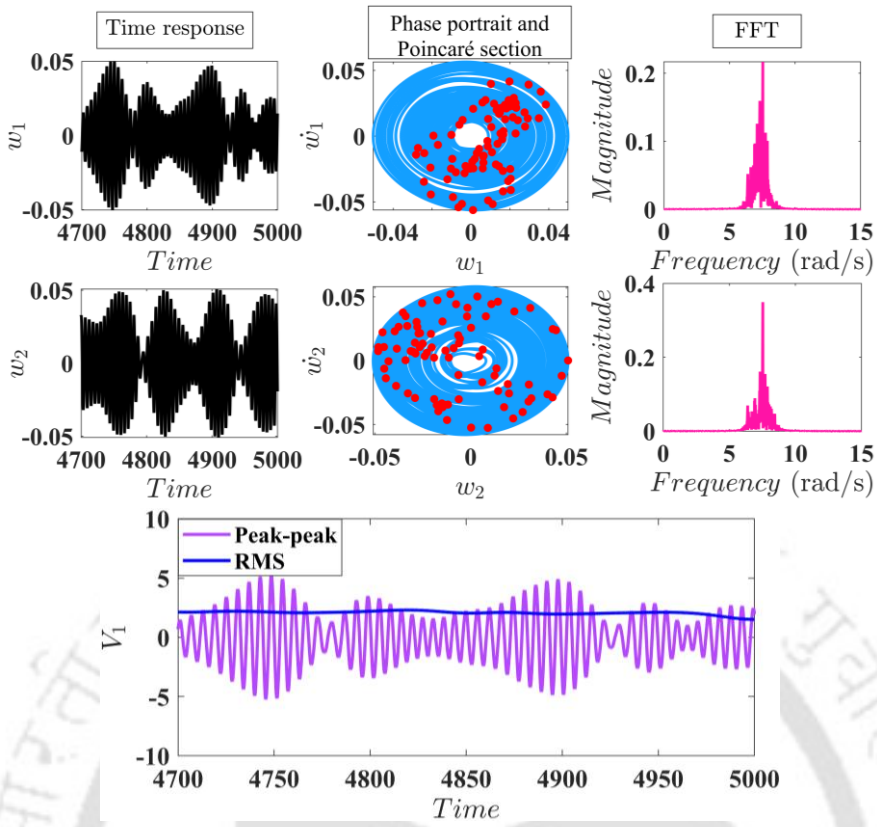

Figure 4.10: Time responses, phase portraits, Poincaré sections and output voltage of the PEH for K = 1 N/m and D = 60 mm, at $\Phi = 2.15$

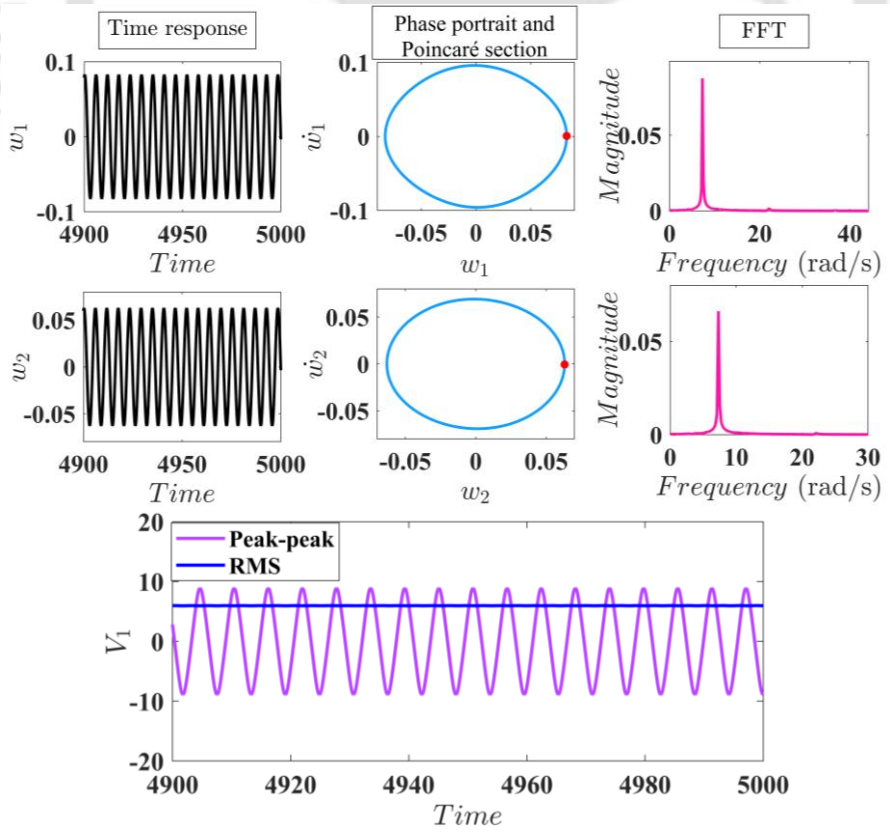

Figure 4.11: Time responses, phase portraits, Poincaré sections and output voltage of the PEH for K = 1 N/m and D = 60 mm, at $\Phi = 2.175$

Figure 4.12 represents the output voltage and power of the proposed PEH for a range of load resistance (R_L) of $50-2600$ kΩ. At $D = 45$ mm, the maximum RMS voltage of 29.06 V can be observed at $R_L = 1300$ kΩ and corresponding power output is 0.65 mW. However, the maximum power output of 1.134 mW and corresponding voltage output of 27 V can be harvested at $R_L = 590$ kΩ. In Table 4.3, the maximum RMS output voltage and power corresponds to specific load resistance are given, which critically shows the energy harvester performance.

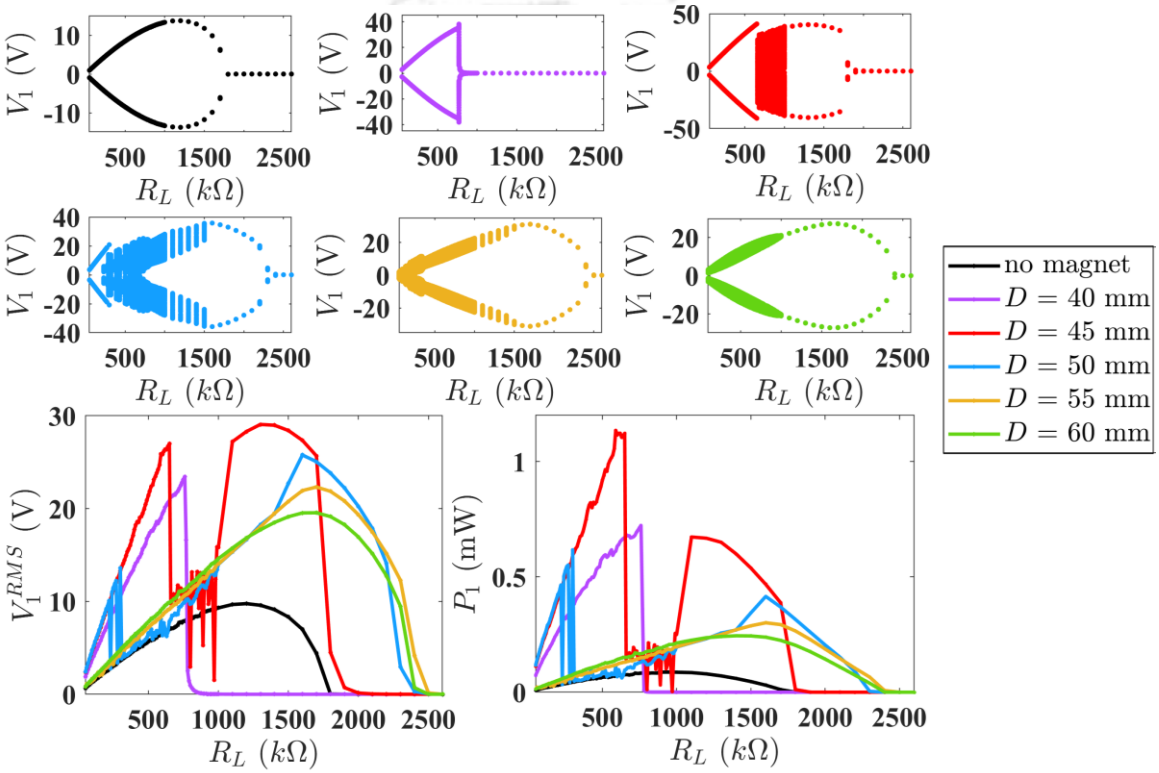

Figure 4.12: Output voltage and power of the PEH for $\Phi = 2.1$ when the system configuration is mono-stable in static condition

Table 4.3: Maximum RMS output voltage and power from different configurations

Configuration	Maximum RMS voltage output	Maximum RMS power output
no magnet	9.76 V at 1200 kΩ	0.087 mW at 960 kΩ
$D = 40$ mm	23.42 V at 760 kΩ	0.722 mW at 760 kΩ
$D = 45$ mm	29.06 V at 1300 kΩ	1.134 mW at 590 kΩ
$D = 50$ mm	25.77 V at 1600 kΩ	0.616 mW at 300 kΩ
$D = 55$ mm	22.32 V at 1700 kΩ	0.3 mW at 1600 kΩ
$D = 60$ mm	19.54 V at 1700 kΩ	0.24 mW at 1400 kΩ

In comparison to the no magnet case; where the maximum RMS power output is 0.087 mW at load resistance of 960 kΩ, the coupled system with D = 45 mm can generate 12 times more power, which is a significant improvement. Hence from these analyses, one can also observe that the load resistance plays an important role on modulating the system dynamics. The response can be periodic, quasi-periodic and chaotic for different values of load resistances. Here, the gap distance between the NdFeB magnets is also a key system parameter to obtain these periodic, quasi-periodic and chaotic oscillations. Beyond a critical value of gap between the permanent magnets of the proposed PEH, the trivial stable equilibria of the beams become unstable through pitchfork bifurcation, resulting in two non-trivial stable branches. In the bi-stable region, the performance of the energy harvester is investigated in this section.

Figure 4.13 shows the RMS output voltage of the energy harvester when the static system is in bi-stable state. The load resistance considered for the simulation is 100 kΩ. The maximum RMS output voltage is 4.84 V which can be generated by keeping D = 35 mm and $\Phi = 2.125$. The maximum output voltage increases by 54.14% as compared to the case of without magnetic interaction. However, in this case, the operational frequency range shrinks down in comparison to the above-mentioned. Far away from the principal parametric resonance frequency ($\Phi = 2$), one can observe that the proposed PEH generate some voltage at nearby $\Phi = 1$, though the value is insignificant in comparison to that of the parametric resonance amplitudes.

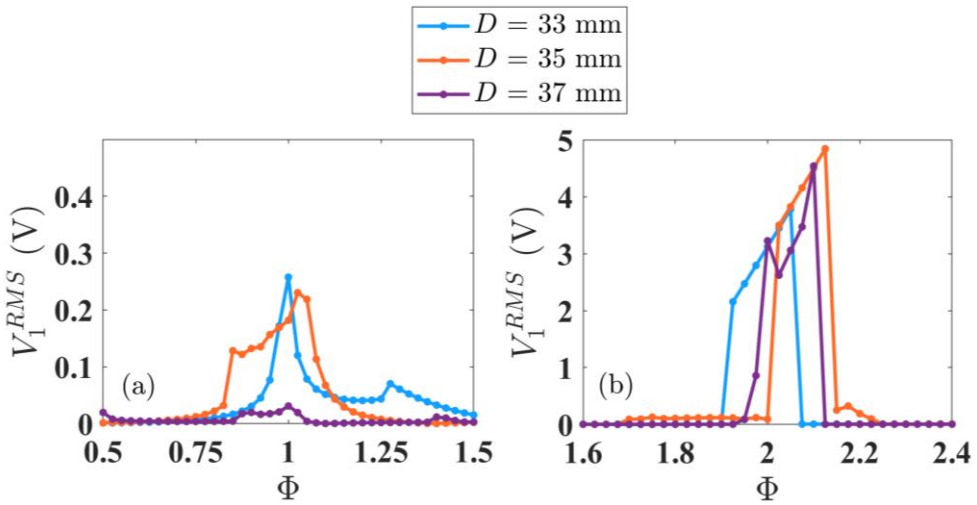

Figure 4.13: RMS output voltage of the PEH system while in the bi-stable state, nearby (a) $\Phi = 1$ and (b) $\Phi = 2$

Figure 4.14 represents the output peak to peak voltage, RMS voltage and RMS power of the proposed PEH when the system is initially bi-stable at static condition. It can be found that the maximum RMS output voltage and power corresponds to the gap of 35 mm when the excitation

frequency is $\Phi = 2.05$. Here, one can observe that at higher values of load resistance, the system response becomes chaotic resulting in further drop in output voltage and power. With reference to Figure 4.14, Table 4.4 gives the maximum RMS output voltage and power.

Table 4.4: Maximum RMS output voltage and power of the PEH in bistable state

Configuration	Maximum RMS output voltage	Maximum RMS output power
D = 33 mm	24.56 V at 830 kΩ	0.727 mW at 830 kΩ
D = 35 mm	28.43 V at 980 kΩ	0.825 mW at 980 kΩ
D = 37 mm	24.29 V at 760 kΩ	0.776 mW at 760 kΩ

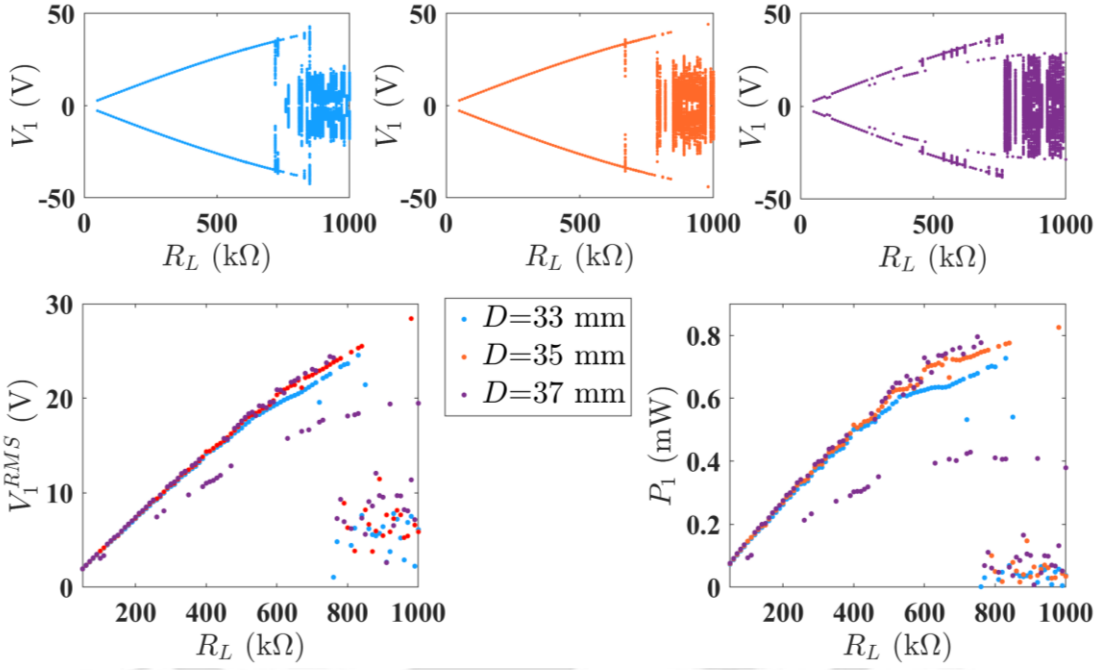

Figure 4.14: Output voltage and power with varying load resistance of the PEH for $\Phi = 2.05$ when the system is bi-stable in static condition

Case 2: MFC patches on both beams

In the previous case, the 1st beam is considered to be the primary beam for energy harvesting and attached with MFC patches. In the present case both beams are attached with bimorph MFC patches and harvest energy. Without any magnetic interaction, at $\Phi = 2.1$ the RMS output voltages of the coupled system are $V_1^{RMS} = 1.28$ V and $V_2^{RMS} = 1.59$ V. By introducing the magnetic repulsive force with D = 50 mm, the RMS output voltages are $V_1^{RMS} = 4.75$ V and $V_2^{RMS} = 2.73$ V at $\Phi = 2.1$. The output of the 1st and 2nd beam with magnets (D = 50 mm) enhances by 271.09% and 71.69% compared to that of without magnets.

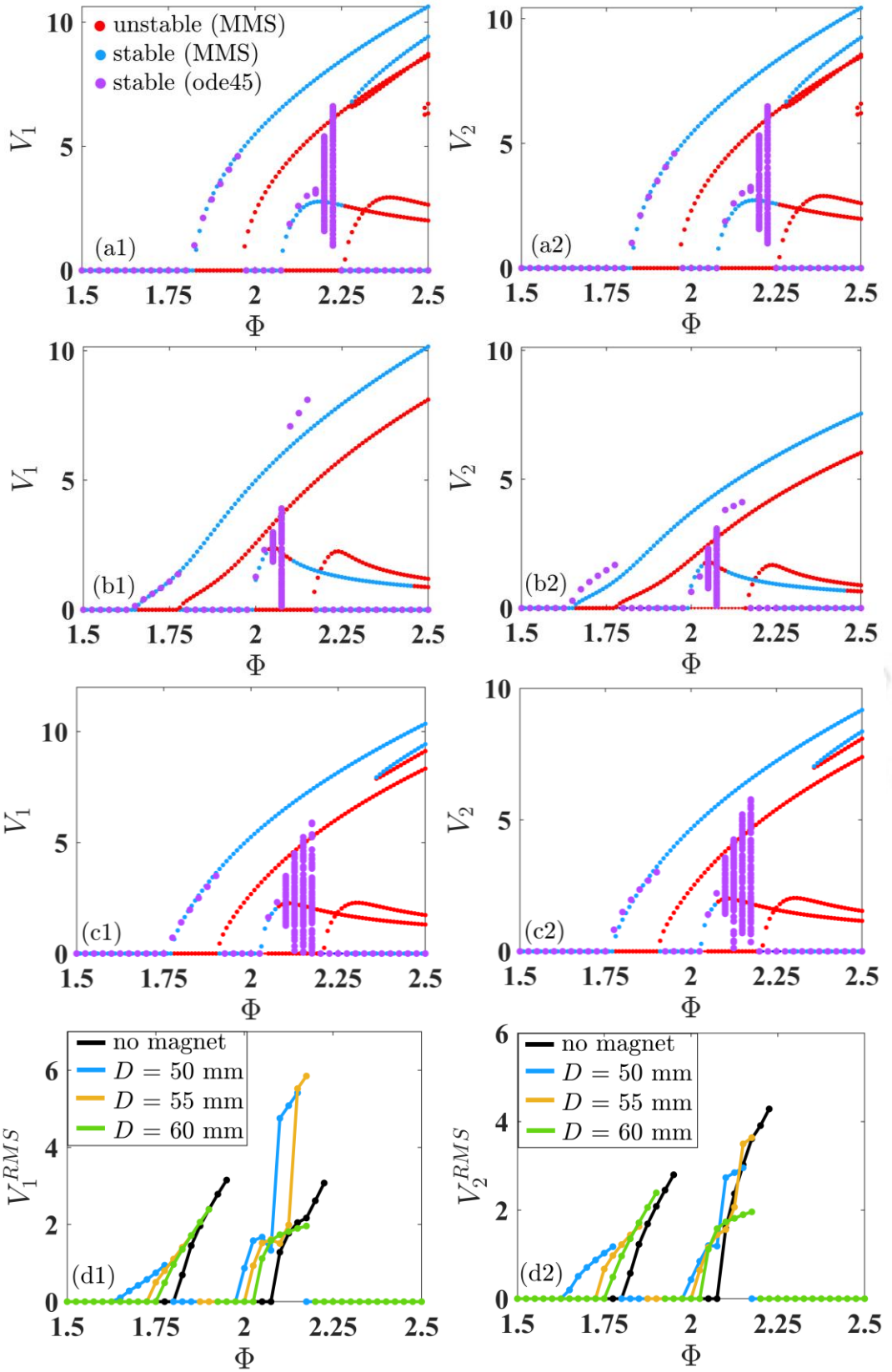

Figure 4.15: At K = 1 N/m, frequency vs. voltage responses of the coupled PEH; for (a1, a2) no magnet, (b1, b2) D = 50 mm, (c1, c2) D = 60 mm, and (d1, d2) RMS voltages

The frequency responses shown in Figure 4.7 (a – f) and Figure 4.15 (a1 – c2), illustrate the stable and unstable solutions obtained by the method of multiple scales (MMS) and the stable solutions obtained using ode45. MMS is a perturbation method that approximately predicts the solutions and vastly incorporated for weakly nonlinear systems. Nearby the resonance conditions, the solutions using this method show good agreement with those obtained by 4th order Runge-Kutta method. However, far away from the resonance condition, the dynamics of the system can become strongly nonlinear. In such cases, the perturbation analysis may not accurately predict the solutions.

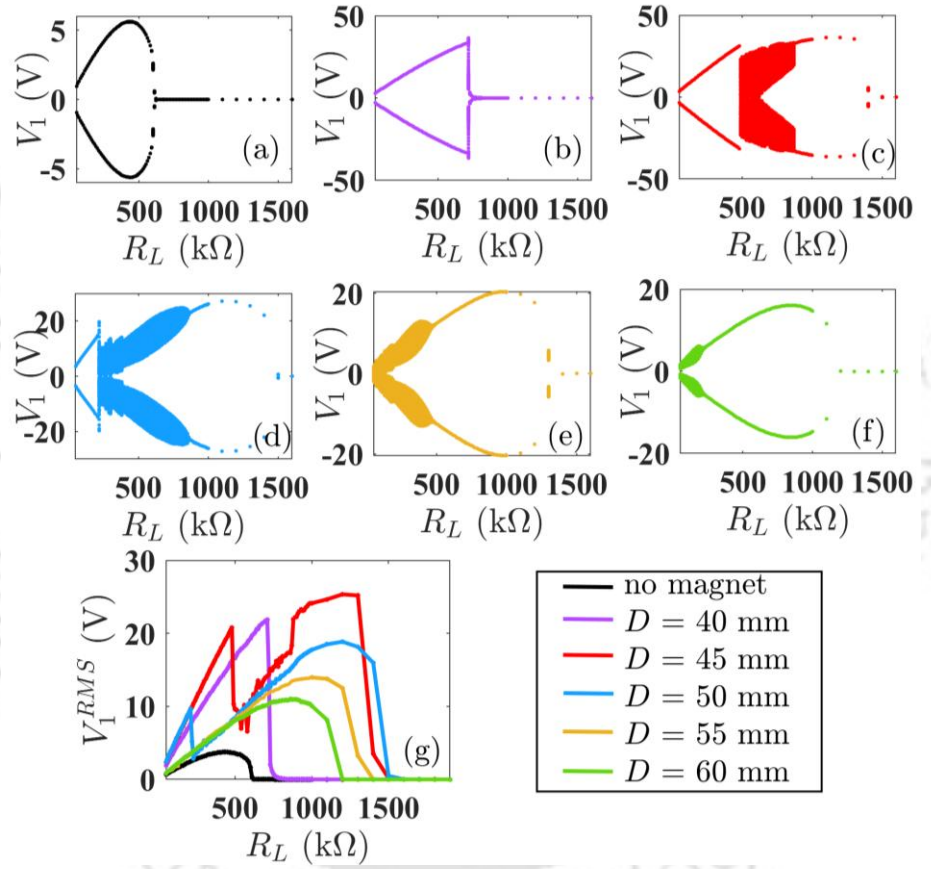

Figure 4.16: At $\Phi = 2.1$, output voltage of the 1st beam for (a) no magnet, (b) $D = 40$ mm, (c) $D = 45$ mm, (d) $D = 50$ mm, (e) $D = 55$ mm, (f) $D = 60$ mm and (g) RMS voltage of all

Figure 4.16 and Figure 4.17 portray the output voltage of the MFC patches of 1st and 2nd beam, respectively with variation of load resistance, while the excitation frequency is $\Phi = 2.1$. For system configuration without magnetic force and with magnetic force, responses are plotted. In case of the system without magnetic force, the maximum RMS output voltages are $V_1^{RMS} = 3.76$ V and $V_2^{RMS} = 4.55$ V with $R_L = 420$ kΩ. Upon introducing the magnetic force and setting the gap between the magnets, $D = 45$ mm, the maximum RMS output voltages of

the PEH system are $V_1^{RMS} = 25.34$ V at $R_L = 1200$ kΩ and $V_2^{RMS} = 10.41$ V at $R_L = 480$ kΩ. RMS output voltage increases by 573.93% and 128.79% as compared to without magnetic force case. With the maximum RMS output voltages of the energy harvester are $V_1^{RMS} = 18.85$ V at $R_L = 1200$ kΩ and $V_2^{RMS} = 11.50$ V at $R_L = 930$ kΩ.

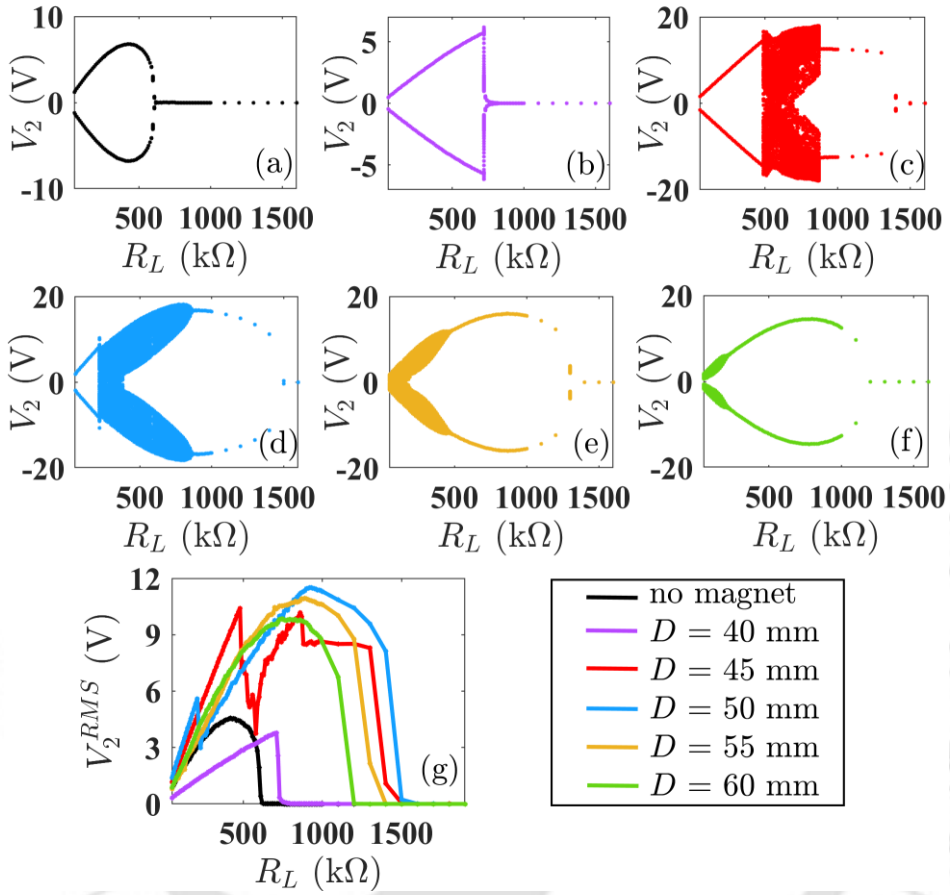

Figure 4.17: At $\Phi = 2.1$, output voltage of the 2nd beam for (a) no magnet, (b) $D = 40$ mm, (c) $D = 45$ mm, (d) $D = 50$ mm, (e) $D = 55$ mm, (f) $D = 60$ mm and (g) RMS voltage of all

The RMS output power of the energy harvester with variation of load resistance is shown in Figure 4.18. The maximum output power of the PEH without magnetic force is $P_1 = 0.035$ mW and $P_2 = 0.053$ mW at $R_L = 330$ kΩ, having total output of 0.088 mW. While, the PEH with magnetic force (D = 45 mm) can generate maximum output power of $P_1 = 0.897$ mW and $P_2 = 0.225$ mW at $R_L = 330$ kΩ, having total output of 1.132 mW. The output power of 1st and 2nd beam enhances by 24.42 times and 3.15 times compared to the case of without magnetic force. While, the total output power enhances by 11.86 times.

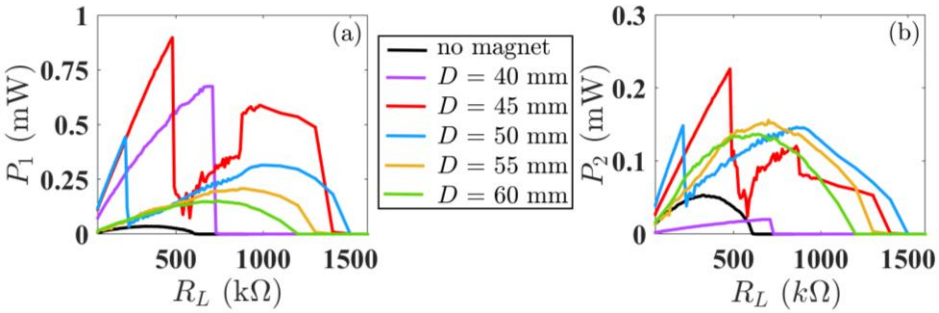

Figure 4.18: At $\Phi = 2.1$, output power from the MFC patches of (a) 1st and (b) 2nd beam for with and without magnetic force

4.5 Summary

This chapter presents a detailed investigation of the nonlinear dynamics and performance enhancement of a double beam based piezoelectric energy harvester subjected to parametric excitation and magnetic repulsive force. The system consists of two cantilever beams coupled by a linear spring, where the primary beam is bonded with MFC patches for energy generation, and the secondary beam interacts with a repulsive magnetic field created by two NdFeB permanent magnets. By adjusting the gap distance between the magnets, the system can switch between the monostable and bistable states, which significantly influences its dynamic characteristics.

Mathematical modelling is carried out using the Euler–Bernoulli beam theory and Lagrange's principle. To derive the electromechanical governing equations of motion; kinetic, potential, magnetic, dissipative energies, work done by the external excitation and work done by the moment produced by the generated voltage are considered. The method of multiple scales (MMS) is applied to obtain the solutions under principal parametric resonance condition. Stability and bifurcation of solutions are studied using eigenvalue analysis of the Jacobian matrix.

Results reveal that spring coupling and magnetic interaction greatly improve energy harvesting efficiency. As the distance between the magnets decreases, the static trivial state of the system undergoes a pitchfork bifurcation, leading to bistability with two non-trivial stable states. The proposed PEH system with coupled spring achieves a broader frequency bandwidth and higher RMS output voltage than the uncoupled one. For example, with a coupled spring stiffness of 1 N/m, the RMS output voltage increases by about 18%, and the operational bandwidth doubles. Under optimal magnetic spacing ($D = 45-55$ mm), the system exhibits up to 90% improvement in voltage output, reaching 5.96 V.

Nonlinear dynamic analysis identifies various bifurcations such as pitchfork, hopf, and torus bifurcations, showing transitions from periodic to quasi-periodic and chaotic oscillations as external excitation frequency varies. The influence of load resistance is also significant on the output of the energy harvester. The maximum output power of 1.134 mW can be obtained with $R_L = 590\ \text{k}\Omega$ for $D = 45$ mm, which is around 12 times higher compared to the no magnetic interaction case. In the bistable regime, a maximum voltage of 28.43 V and 0.825 mW power are achieved at $D = 35$ mm.

When both beams are attached with MFC and act as the energy harvester, the maximum total output power increases by 11.86 times, showing how effective the dual-beam setup is when magnetic force is used. Overall, the study shows that introducing magnetic force and connecting the beams through a spring helps the harvester work over a wider range of frequencies and produce energy more efficiently.

Chapter 5

Magnetically Coupled Double Beam Piezoelectric Energy Harvester under Galloping Excitation

5.1 Introduction

While, studies in the previous chapters focus on harmonically base excited spring coupled double cantilever beam based piezoelectric energy harvesters (PEH) under parametric and magnetic repulsive force induced instabilities, the present chapter investigates a detailed nonlinear dynamic study of a magnetically coupled double beam based PEH under wind-induced galloping instability. The proposed configuration consists of two cantilever beams; one horizontal and one vertical. Two square-shaped bluff bodies are attached to the tip of the beams to induce galloping-based oscillation in the proposed harvester. Two NdFeB permanent magnets are used to introduce a nonlinear magnetic repulsive force between the beam-bluff body system. This force couples the two beam systems magnetically. A prototype of the system is developed and experimented in a wind tunnel to support the theoretical findings. In section 5.2, mathematical modelling of the galloping based PEH is carried out. In section 5.3, theoretical results are discussed in detail, followed by section 5.4 which includes experimental investigations. The summary of this study is presented in section 5.5.

5.2 Mathematical modelling

Figure 5.1 shows the schematic diagram of the proposed galloping based PEH. The system consists of two cantilever beams that are placed orthogonally, one in horizontal and one in vertical direction. Square cross-section bluff bodies are attached to the tip of the beams. The beams are made of stainless steel and the bluff bodies are made of foam material. Wind flow is considered to be in x-direction and incident on the front y-z plane of the bluff bodies. MFC piezoelectric patches are bonded to the beam surface near the fixed ends, where maximum strain is induced during oscillation. Two permanent magnets are attached, one at the bottom surface of 1st bluff body and another on the top surface of the 2nd bluff body as shown in the

figure. The gap (D) between the magnets can be adjusted by moving the horizontal beam up and down using a movable fixture that holds the beam with the frame.

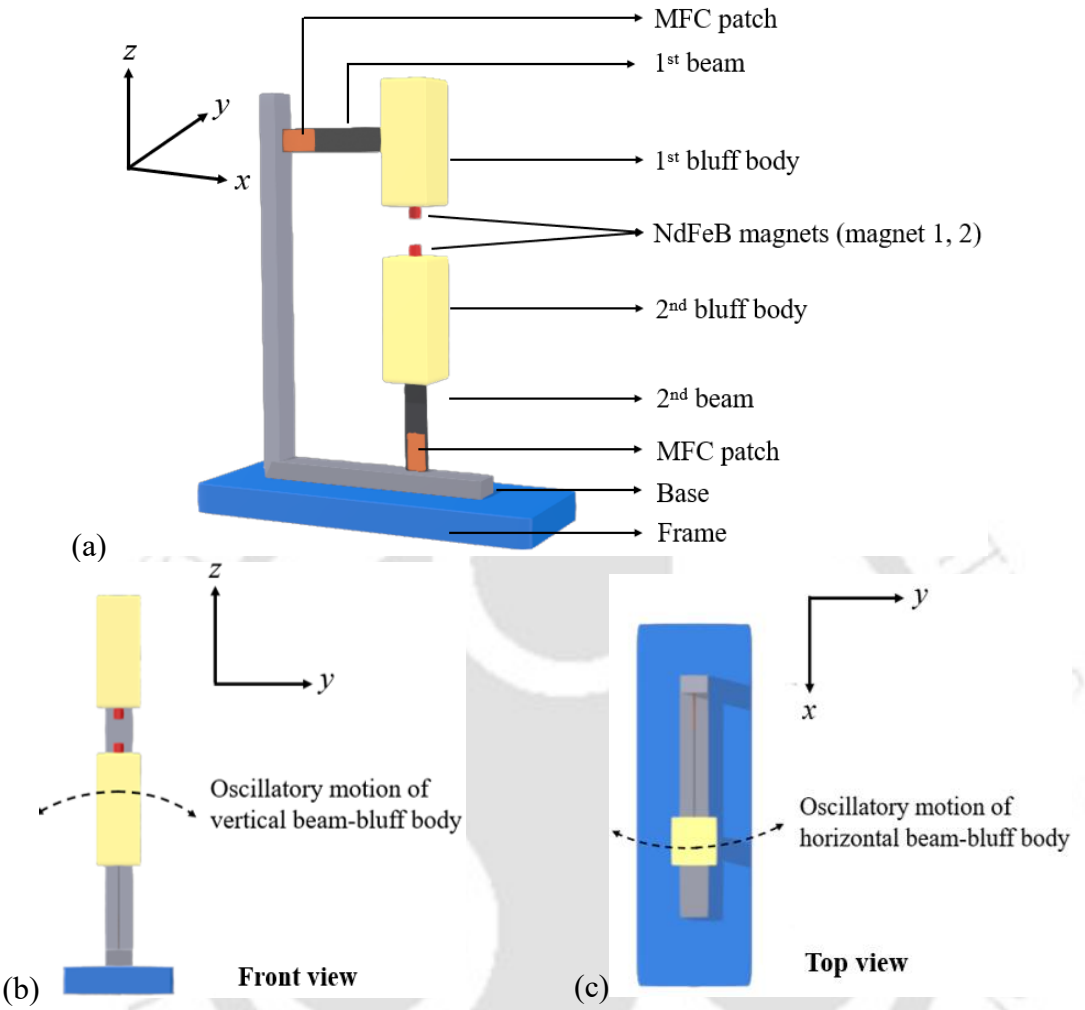

Figure 5.1: Schematic representation of the proposed galloping based energy harvester; (a) 3D view, (b) front view (view from the direction of the wind flow), and (c) top view

Considering the 1st beam oscillates in x-y plane, the transverse, axial and angular displacement are $w_{O1}(s_1,t), u_{O1}(s_1,t)$ and $\phi_{O1}(s_1,t)$. Similarly, for the 2nd beam which oscillates in the y-z plane, the transverse, axial and angular displacements are $w_{O2}(s_2,t), u_{O2}(s_2,t)$ and $\phi_{O2}(s_2,t)$. Here, s_1 and s_2 denote the distance of an arbitrary point O from the fixed end of the 1st and 2nd beam, respectively along the neutral axis. The detailed expressions for these displacements, curvature and assumed first mode shape function are same as given in section 3.2 of Chapter 3. Under the influence of wind induced galloping when the energy harvester starts to oscillate, the kinetic energy (T) of the system can be expressed as follows.

$$T = \sum_{i=1,2} T_i \tag{5.1}$$

Where, T_i denotes the kinetic energy of each beam system and i = 1,2 represents the 1st and 2nd beam, respectively. Kinetic energy of the 1st beam can be written as follows.

$$T_1 = \begin{bmatrix} \frac{1}{2}\rho A\int_0^{l_1}\left[\left\{\dot{w}_{O1}(s_1,t)\right\}^2+\left\{\dot{u}_{O1}(s_1,t)\right\}^2\right]ds_1 \\ +\frac{1}{2}m_{bb1}\left[\left\{\dot{w}_{O1}(l_1,t)+\frac{b_{bb1}\cos\left(\phi_{O1}(l_1,t)\right)}{2}\dot{\phi}_{O1}(l_1,t)\right\}^2+\left\{\dot{u}_{O1}(l_1,t)\right\}^2\right] \\ +\frac{1}{2}m_{m1}\left[\left\{\dot{w}_{O1}(l_1,t)+\frac{b_{bb1}\cos\left(\phi_{O1}(l_1,t)\right)}{2}\dot{\phi}_{O1}(l_1,t)\right\}^2+\left\{\dot{u}_{O1}(l_1,t)\right\}^2\right] \\ +\frac{1}{2}I_{bb1}\left\{\dot{\phi}_{O1}(l_1,t)\right\}^2+\frac{1}{2}I_{m_{m1}}\left\{\dot{\phi}_{O1}(l_1,t)\right\}^2 \end{bmatrix} \tag{5.2}$$

The kinetic energy of the 2nd beam can be written as,

$$T_2 = \begin{bmatrix} \frac{1}{2}\rho A\int_0^{l_2}\left[\left\{\dot{w}_{O2}(s_2,t)\right\}^2+\left\{\dot{u}_{O2}(s_2,t)\right\}^2\right]ds_2+\frac{1}{2}I_{bb2}\left\{\dot{\phi}_{O2}(l_2,t)\right\}^2+\frac{1}{2}I_{m_{m2}}\left\{\dot{\phi}_{O2}(l_2,t)\right\}^2 \\ +\frac{1}{2}m_{bb2}\left[\left\{\dot{w}_{O2}(l_2,t)+\frac{l_{bb2}}{2}\cos\left(\phi_{O2}(l_2,t)\right)\dot{\phi}_{O2}(l_2,t)\right\}^2+\left\{\dot{u}_{O2}(l_2,t)\right\}^2\right] \\ +\frac{1}{2}m_{m2}\left[\left\{\dot{w}_{O2}(l_2,t)+l_{bb2}\cos\left(\phi_{O2}(l_2,t)\right)\dot{\phi}_{O2}(l_2,t)\right\}^2+\left\{\dot{u}_{O2}(l_2,t)\right\}^2\right] \end{bmatrix} \tag{5.3}$$

where, ρ, A, l_1, m_{bb1}, b_{bb1}, I_{bb1}, m_{m1}, $I_{m_{m1}}$, l_2, m_{bb2}, b_{bb2}, I_{bb2}, m_{m2} and $I_{m_{m2}}$ denote density of the beam material, area of cross-section of the beams, length of 1st beam, mass of the 1st bluff body, width of the 1st bluff body, mass moment of inertia of 1st bluff body, mass of magnet 1, mass moment of inertia of magnet 1, cross-sectional area of 2nd beam, length of 2nd beam, mass of 2nd bluff body, length of 2nd bluff body, mass moment of inertia of 2nd bluff body, mass of magnet 2 and mass moment of inertia of magnet 2, respectively. The strain energy or elastic potential energy (U_e) of the system can be written as follows.

$$U_e = \sum_{i=1,2} U_{ei} = \frac{1}{2}EI_1\int_0^{l_1}\left(\kappa_{O1}(s_1,t)\right)^2 ds_1 + \frac{1}{2}EI_2\int_0^{l_2}\left(\kappa_{O2}(s_2,t)\right)^2 ds_2 \tag{5.4}$$

where, U_{ei} is the elastic potential energy of the individual beam, E, I_1 and I_2 are the modulus of elasticity of beam material, area moment of inertia of the 1st beam, and area moment of inertia of the 2nd beam, respectively. The work done on the vertical beam system by the

gravitational field can be stated as negative of potential energy due to gravity (U_g) and can be expressed as given below.

$$U_g = \begin{bmatrix} -\rho Ag\left\{\int_0^{l_2}\left(u_2(s_2,t)\right)ds_2\right\} - m_{bb2}g\left\{u_2(l_2,t) - \frac{l_{bb2}}{2}\sin\left(\phi_2(l_2,t)\right)\phi_2(l_2,t)\right\} \\ -m_{m2}g\left\{u_2(l_2,t) - l_{bb2}\sin\left(\phi_2(l_2,t)\right)\phi_2(l_2,t)\right\} \end{bmatrix} \quad (5.5)$$

where, g is the acceleration due to gravity. Two NdFeB permanent magnets which are attached to the bluff bodies are facing each other with the same poles resulting in a net magnetic repulsive force that tends to change the stability of the initial stable position of both the beam systems. Initially, the distance between the two facing magnets is considered to be D. After repulsion, the magnet attached to 1st beam gets displaced in the x-y plane and that attached to beam 2 gets displaced in the y-z plane and correspondingly, the distance vector ($\vec{R}$) between two permanent magnets can be written as follows by referring to Figure 5.2.

$$\vec{R} = \left[u_1, \left\{\left(w_1 + \frac{b_{bb1}}{2}\sin\phi_1\right) - \left(w_2 + l_{bb2}\sin\phi_2\right)\right\}, \left(D + u_2\right)\right] \quad (5.6)$$

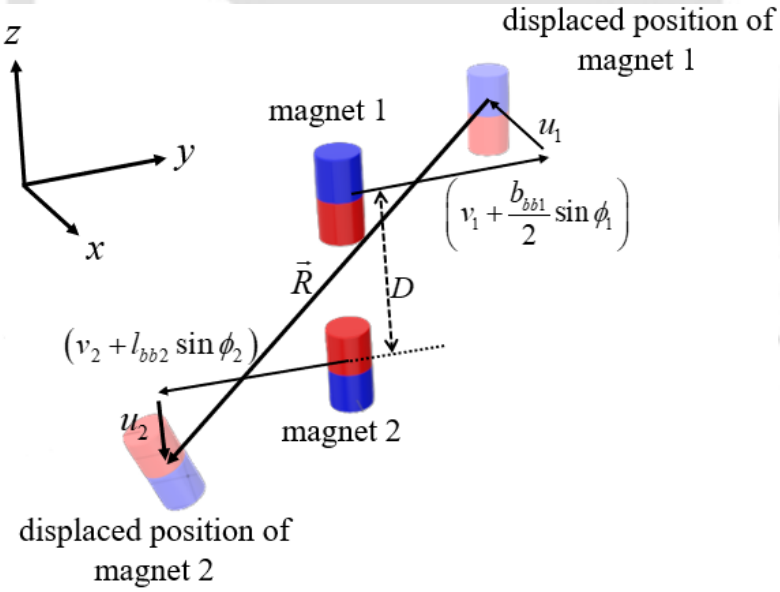

Figure 5.2: Schematic representation of the magnets with their displaced conditions under repulsion between same facing poles

Work done by the magnetic repulsive force on the system can also be stated as negative of magnetic potential energy (U_m) and written by following the dipole-dipole model [173, 236].

$$U_m = \frac{\mu_0}{4\pi}\left[\frac{\vec{M}_{mag1}}{\left\|\vec{R}\right\|_2^3} - \frac{3\left(\vec{M}_{mag1}\cdot\vec{R}\right)}{\left\|\vec{R}\right\|_2^5}\vec{R}\right]\cdot\vec{M}_{mag2} \tag{5.7}$$

where, the notations μ_0, $\vec{M}_{mag1}$, $\vec{M}_{mag2}$ represent the permeability of free space, magnetic moment vector of the magnet 1 and magnet 2, respectively. The magnetic moment vectors are defined as the product of the magnitude of the magnetization vector ($\vec{m}_{mag1}$ and $\vec{m}_{mag2}$) and the volume of the magnets (V_{mag1} and V_{mag2}), and can be expressed as follows.

$$\begin{aligned}\vec{M}_{mag1} &= \left[\vec{m}_{mag1}\mathrm{V}_{mag1}\sin\phi_1, \vec{m}_{mag1}\mathrm{V}_{mag1}\cos\phi_1, 0\right]\\ \vec{M}_{mag2} &= \left[0, \vec{m}_{mag2}\mathrm{V}_{mag2}\cos\phi_2, \vec{m}_{mag2}\mathrm{V}_{mag2}\sin\phi_2\right]\end{aligned} \tag{5.8}$$

The total potential energy of the system can be calculated as $U = U_e + U_g + U_m$. The energy dissipated from the system due to internal damping and air resistance can be expressed by a dissipation function (W_d) and can be written as follows.

$$W_d = \sum_{i=1,2}\left[\int_0^{l_i} C_i \dot{w}_{Oi}\left(s_i,t\right)\delta w_{Oi} ds_i\right] \tag{5.9}$$

Here, C_i is the effective damping co-efficient of the *i*-th beam system. Galloping is considered to be a self-excited oscillation, which mathematically takes the form of negative damping. Based on the quasi-steady hypothesis, the applied aerodynamic (galloping) force on a non-streamline cross-sectional body can be approximated. Detailed derivation of exerted galloping force on a bluff body with horizontal beam, can be found in the work of Abdelkefi et al. [239], Sagar et al. [240], Abdelmoula and Abdelkefi [241]. The galloping force (F_{g1}) exerted on the horizontally placed 1st beam and bluff body system can be expressed as follows.

$$F_{g1}(t) = \frac{1}{2}\rho_a b_{bb1} l_{bb1} U_w^2 \left[\begin{array}{l}\mathrm{A}_1\left\{\left(1+\frac{\pi b_{bb1}}{2l_1}\right)\left(\frac{\dot{w}_1}{U_w}\right)+\left(\frac{\pi}{2l_1}\right)\left(w_1\right)\right\}\\ +\mathrm{A}_3\left\{\left(1+\frac{\pi b_{bb1}}{2l_1}\right)\left(\frac{\dot{w}_1}{U_w}\right)+\left(\frac{\pi}{2l_1}\right)\left(w_1\right)\right\}^3\end{array}\right] \tag{5.10}$$

The Galloping force exerted on the bluff body attached to a vertically placed cantilever beam has been derived in the work of Abdollahzadeh Jamalabadi [242], Zhao et al. [243]. The 2nd beam and bluff body is configured vertically as similar to the systems considered in the above-

mentioned studies. For horizontal and vertical configuration, the derivation of galloping force is not exactly same. In the present system, induced galloping force on the vertical configuration can be written as follows.

$$F_{g2}(t)=\frac{1}{2}\rho_a b_{bb2} U_w^2 \left[\begin{array}{l} \mathrm{A}_1 \left\{ l_{bb2}+\dfrac{\pi l_{bb2}^2}{2l_2}+\dfrac{\pi^2 l_{bb2}^3}{12 l_2^2} \right\} \left(\dfrac{\dot{w}_2}{U_w} \right) \\ +\mathrm{A}_3 \left\{ \begin{array}{l} l_{bb2}\left(1+\dfrac{\pi^3 l_{bb2}^3}{32 l_2^3}+\dfrac{3\pi l_{bb2}}{4 l_2}+\dfrac{\pi^2 l_{bb2}^2}{4 l_2^2} \right) \\ +\dfrac{\pi l_{bb2}^2}{2 l_2}\left(\dfrac{1}{2}+\dfrac{\pi^3 l_{bb2}^3}{40 l_2^3}+\dfrac{\pi l_{bb2}}{2 l_2}+\dfrac{3\pi^2 l_{bb2}^2}{16 l_2^2} \right) \end{array} \right\} \left(\dfrac{\dot{w}_2}{U_w} \right)^3 \end{array} \right] \tag{5.11}$$

where, $\rho_a, U_w, \mathrm{A}_1$ and A_3 are density of air, speed of the wind flow, linear aerodynamic force co-efficient and nonlinear cubic aerodynamic force coefficient, respectively. These aerodynamic coefficients depend on the shape and geometry of the bluff body. For a square shaped bluff body, $\mathrm{A}_1 = 2.3$ and $\mathrm{A}_3 = -18$ [121, 122]. Work done by these external galloping forces can be written as follows.

$$\delta W_g = \sum_{i=1,2} F_{gi}\delta w_i(l_i,t) \tag{5.12}$$

As the beams start to oscillate, the MFC patches attached to the beams generate voltage (V_i) and the generated voltage produces a moment (M_i) across the neutral axis of the beam-patch system [77]. The total moment due to the voltage generated in both the beams can be expressed as follows.

$$M(s_i,t)=\sum_{i=1,2} M_i = \sum_{i=1,2} \gamma_P V_i(t) \tag{5.13}$$

Here, γ_p is a constant which depends on the configuration and geometry of the beam and piezoelectric patch. The work done by these electrical moments produced by the voltage about the neutral axis of the beams can be written as follows.

$$W_e = \sum_{i=1,2}\left[\int_0^{l_{Pi}} M_i(s_i,t)\kappa(s_i,t)\,ds_i \right] \tag{5.14}$$

Here, l_{Pi} is the active length of the piezoelectric component in the MFC patch. Considering the mass of the bluff body is larger than the mass of the beam, shape function with single mode

approximation is chosen to address the elastic deformation of the beam which satisfies the boundary conditions of a cantilever beam at $s_1 = 0, s_2 = 0$. Using Lagrange principle, the spatio-temporal equations of motion are derived and further discretized to their temporal forms using generalized Galerkin's method, which are written as follows.

$$\ddot{w}_1 + \alpha_{10}\dot{w}_1 + \alpha_{11}w_1 + \alpha_{12}\left(\ddot{w}_1 w_1^2 + \dot{w}_1^2 w_1\right) + \alpha_{13}w_1^3 + \frac{\partial U_m}{\partial w_1} - \theta_{11}V_1 = F_{g1} \tag{5.15}$$

$$C_p\dot{V}_1 + \frac{V_1}{R_L} + \theta_{11}\dot{w}_1 + = 0 \tag{5.16}$$

$$\alpha_{20}\ddot{w}_2 + \alpha_{21}\dot{w}_2 + \alpha_{22}w_2 + \alpha_{23}\left(\ddot{w}_2 w_2^2 + \dot{w}_2^2 w_2\right) + \alpha_{24}w_2^3 + \frac{\partial U_m}{\partial w_2} - \theta_{21}V_2 = F_{g2} \tag{5.17}$$

$$C_p\dot{V}_2 + \frac{V_2}{R_L} + \theta_{21}\dot{w}_2 = 0 \tag{5.18}$$

Here, C_p and R_L are the capacitance of the MFC patch and load resistance connected to the MFC output ends, respectively. The coefficients of the equations of motion are given in Appendix C. The natural frequencies of the beams can be calculated as, $\omega_1 = \sqrt{\alpha_{11}}$ and $\omega_2 = \sqrt{\alpha_{21}}$. Considering the previously obtained equations of motion in Chapter 3 and Chapter 4, the equations of motion derived in the present study additionally include complex nonlinear terms from the magnetic force, linear and nonlinear (cubic) damping terms from galloping excitation. These nonlinear differential equations are solved in MATLAB using 4th order Runge-Kutta method (ode45). It is to be noted that the power output of the system is calculated using the RMS value of the output AC voltage and is given as follows.

$$P_{total} = \sum_{i=1,2} P_i = \sum_{i=1,2} \frac{\left(V_i^{RMS}\right)^2}{R_L} \tag{5.19}$$

5.3 Results and discussion

In this section, the detailed numerical investigations of the proposed galloping based PEH are carried out. The parametric study of the system reveals interesting nonlinear phenomena. The dimensions and physical properties of the components of the energy harvester considered in the present study are given in Table 5.1. The system parameter values are chosen wisely to bring the modal frequencies closer to each other ($\omega_1 = 24.34$ rad/s and $\omega_2 = 26.17$ rad/s).

Table 5.1: Physical dimensions and material properties of components of the energy harvester

Parameters	**Values (unit)**	**Parameters**	**Values (unit)**
Young's modulus, E	210 GPa	Height of magnet, $h_{m1} = h_{m2}$	0.005 m
Density, ρ	7850 kg/m^3	Dia. of magnet, $d_{m1} = d_{m2}$	0.01 m
1st beam length, l_1	0.1 m	MFC length, l_{Pi}	0.028 m
2nd beam length, l_2	0.065 m	MFC width, b_{Pi}	0.014 m
Beam width, $b_1 = b_2$	0.018 m	MFC thickness, h_{Pi}	0.3 mm
Beam thickness, $h_1 = h_2$	0.4 mm	Piezo constant, d_{31}	-170 pC/N
1st bluff body mass, m_{bb1}	35 gm	γ_P	-4×10^{-5} N-m/V
2nd bluff body mass, m_{bb2}	13 gm	MFC Young's modulus, E_P	33.369 GPa
Bluff body length, $l_{bb1} = l_{bb2}$	0.15 m	Capacitance, C_P	51.4 nF
Bluff body width, $b_{bb1} = b_{bb2}$	0.065 m	Load resistance, R_L	0 – 10 MΩ
$\lvert\vec{m}_{mag1}\rvert$, $\lvert\vec{m}_{mag2}\rvert$	1×10^6 A/m	Free space permeability, μ_0	4π×10^{-7} H/m
Magnet mass, $m_{m1} = m_{m2}$	0.003 kg		

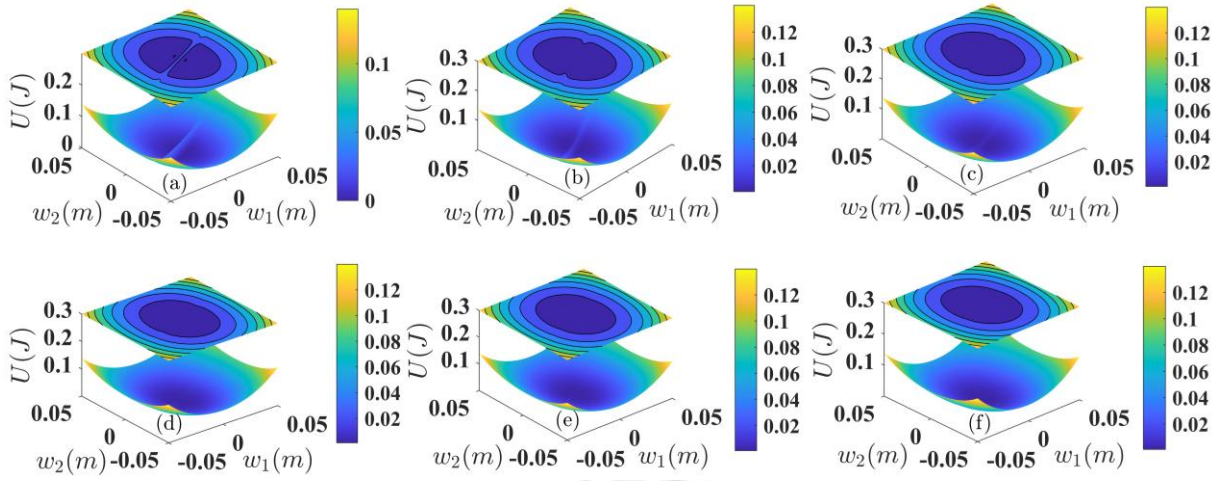

Figure 5.3: Potential energy of the PEH for (a) D = 5 mm, (b) D = 10 mm, (c) D = 15 mm, (d) D = 20 mm, (e) D = 25 mm, and (f) D = 30 mm

Figure 5.3 shows the potential energy (as a function of tip displacements, w_1 and w_2) of the system with change in gap (D) between the magnets. At D = 5 mm, one can observe two potential wells. As the gap is quite low, the magnetic force is very high, which introduces potential barrier. The trivial equilibrium states of both of the beams bifurcate with pitchfork bifurcation and become unstable and two non-trivial stable states come into existence. As D

increases, the bi-stability disappears leading towards single potential well at D = 25 mm. In Figure 5.4, one can find the change in magnetic repulsive force with variation of D. As D increases, the magnitude of magnetic force decreases. When the magnets are nearby the trivial equilibrium, the intensity of the force is maximum. As the magnets moves away from each other, the intensity of the force decreases.

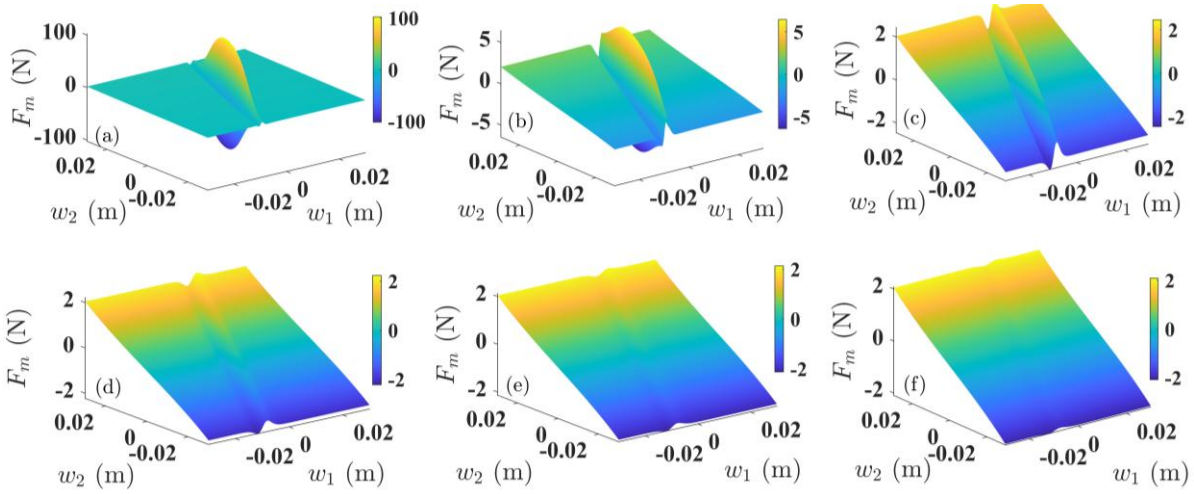

Figure 5.4: Magnetic repulsive force between two NdFeB magnets for (a) D = 5 mm, (b) D = 10 mm, (c) D = 15 mm, (d) D = 20 mm, (e) D = 25 mm, and (f) D = 30 mm

Based on the Beaufort wind force scale, performance of the energy harvester is studied and analyzed for three wind speed regions, namely light air (0 - 1.5 m/s), light breeze (1.5 - 3.3 m/s), and gentle breeze (3.3 - 5.5 m/s) [238]. In each of the wind speed regions, the integer values of wind speed (1, 2, 3, 4, and 5 m/s) are chosen and accordingly, the load resistances are varied to find the optimum value for maximum power harvest. In the light air region at 1 m/s wind speed, optimum load resistances are found for different D values and are given in Table 5.2. Figure 5.5 shows the same in a graphical form.

In the light breeze region, wind speed of 2 m/s and 3 m/s are considered to optimize the load resistances corresponding to maximum output power of the energy harvester and tabulated in Table 5.3 and Table 5.4, respectively. The same can also be found in Figure 5.6 and Figure 5.7. It can be observed that the total output power of the uncoupled system is higher than that of the coupled system in this wind speed region. For example, with D = 10 mm; the 1st beam generates maximum power among all configurations. However, due to energy transfer taking place in between the beams in coupled condition, the output power of the 2nd beam decreases significantly as a tradeoff.

Table 5.2: Load resistances corresponding to maximum output power for $U_w = 1$ m/s

D(mm)	R_L(kΩ)	P_1(mW)	R_L(kΩ)	P_2(mW)
uncoupled	2250	0.0267	3000	0.0266
10	275	0.0061	275	0.0351
15	150	0.0077	150	0.0458
20	200	0.0081	725	0.0294
25	250	0.022	125	0.0341
30	2500	0.0273	2500	0.0202

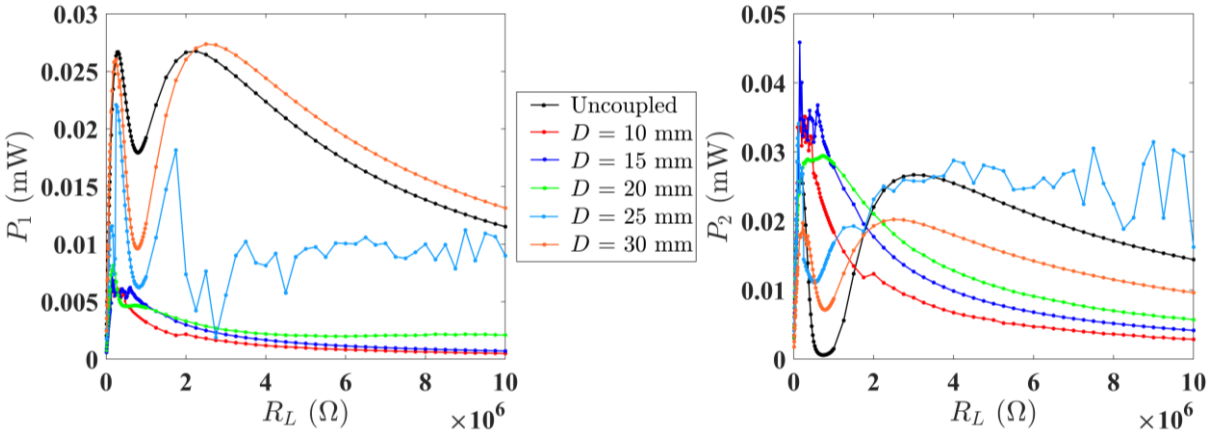

Figure 5.5: Load resistance vs. power output at wind speed of 1 m/s

Table 5.3: Load resistances corresponding to maximum output power for $U_w = 2$ m/s

D(mm)	R_L(kΩ)	P_1(mW)	R_L(kΩ)	P_2(mW)
uncoupled	800	0.3179	725	0.6646
10	325	0.0617	350	0.3655
15	2500	0.245	425	0.4474
20	875	0.0081	800	0.0294
25	775	0.2713	675	0.5234
30	775	0.4129	535	0.364

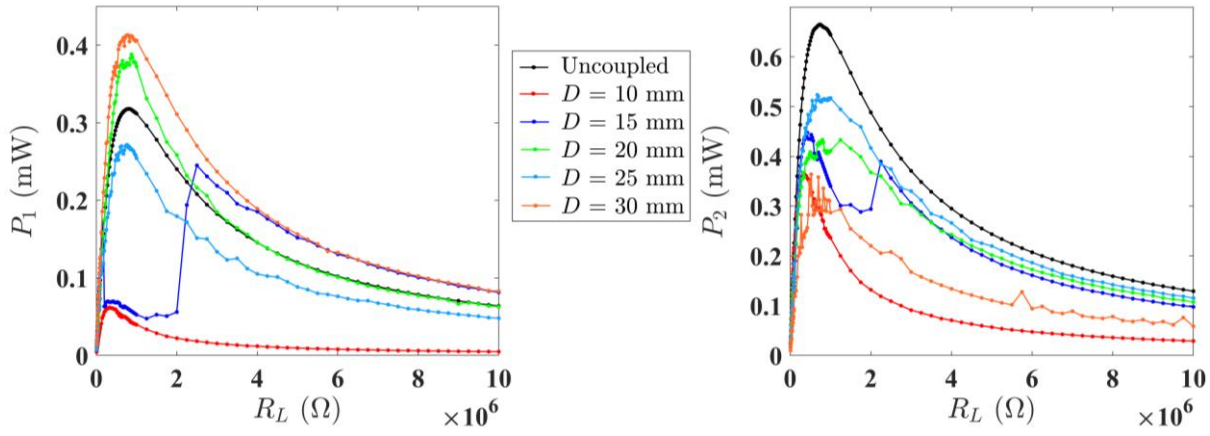

Figure 5.6: Load resistance vs. output power at wind speed of 2 m/s

Table 5.4: Load resistances corresponding to maximum output power for $U_w = 3$ m/s

D(mm)	R_L (kΩ)	P_1 (mW)	R_L (kΩ)	P_2 (mW)
uncoupled	800	0.6686	725	2.022
10	350	0.1679	350	1.015
15	750	0.5105	750	2.038
20	725	0.6741	850	2.039
25	800	0.7377	750	1.79
30	700	0.9498	625	1.7532

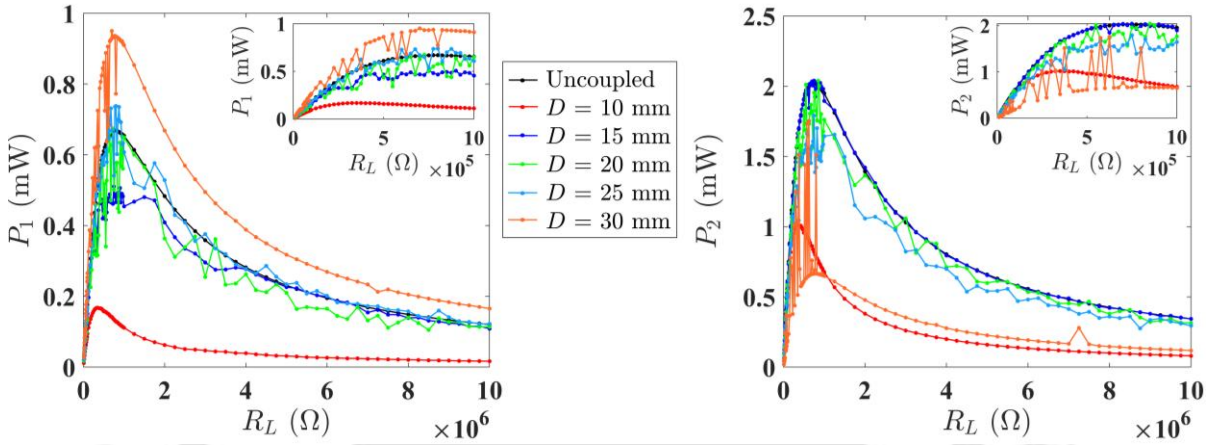

Figure 5.7: Load resistance vs. output power at wind speed of 3 m/s

In the gentle breeze region, the proposed energy harvester exploits more benefits than the other two wind speed regions explored in the present study. The optimum load resistances are found for wind speed of 4 m/s and 5 m/s and are given in Table 5.5 and Table 5.6. The same can also be found in Figure 5.8 and Figure 5.9. At wind speed of 4 m/s, the power output of the coupled system (for $D = 25 - 30$ mm) is more compared to the uncoupled system. At $D = 30$ mm, 5.02% increment in output power can be observed for the 1st beam system and that for the 2nd beam system is 4.48%. At wind speed of 5 m/s, the total output power of the system increases by 1.59%, 4.16%, 4.33%, and 3.38% for D = 15 mm, 20 mm, 25 mm and 30 mm, respectively.

Table 5.5: Load resistances corresponding to maximum output power for $U_w = 4$ m/s

D(mm)	R_L (kΩ)	P_1 (mW)	R_L (kΩ)	P_2 (mW)
uncoupled	800	0.9552	725	4.067
10	750	0.961	475	1.057
15	825	1.1561	625	3.3948
20	925	1.185	800	3.68
25	900	0.9854	725	4.1813
30	775	1.003	775	4.249

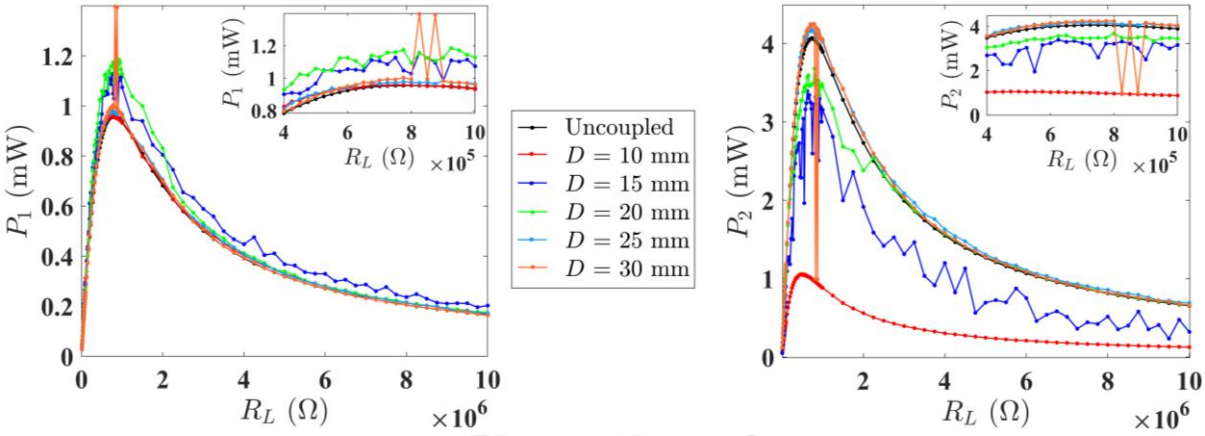

Figure 5.8: Load resistance vs. output power at wind speed of 4 m/s

Table 5.6: Load resistances corresponding to maximum output power for $U_w = 5$ m/s

D(mm)	R_L (kΩ)	P_1(mW)	R_L (kΩ)	P_2(mW)
uncoupled	800	1.171	750	6.771
0	825	1.584	650	1.212
15	825	1.229	825	6.84
20	925	1.208	825	7.065
25	825	1.192	825	7.094
30	825	1.203	675	7.008

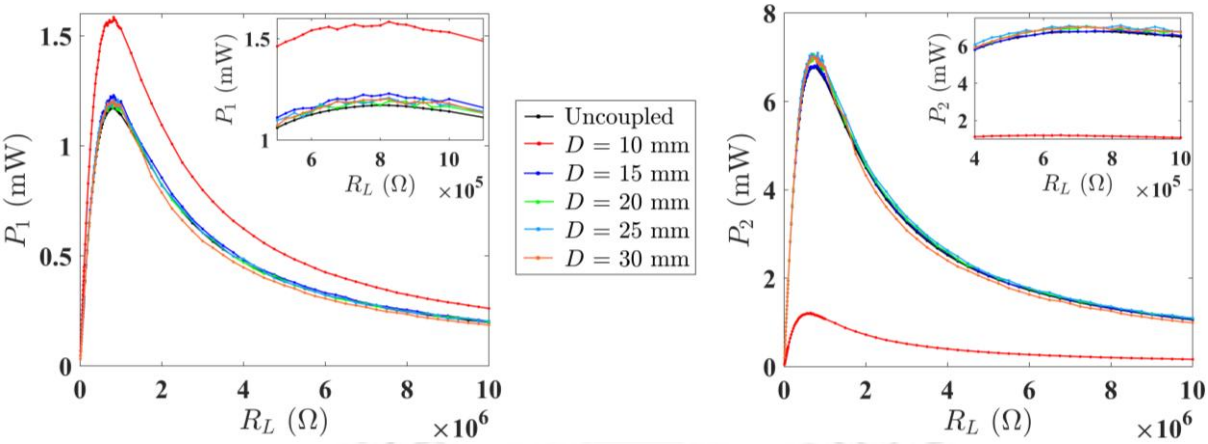

Figure 5.9: Load resistance vs. output power at wind speed of 5 m/s

From Figure 5.5 to Figure 5.9, an important observation can be made that in coupled conditions, when D is less than 20 mm, the power output of one beam gets increased and that of another beam gets suppressed. It is because there is energy transfer between the two beams. As a result, one beam oscillates with higher energy and another one with lesser energy. A similar phenomenon has been observed by Lan et al [173], in the case of a magnetically coupled double beam-based energy harvester. Also, when the gap distance between the magnets is small, the magnetic field is quite strong and the beams oscillation gets resistance while crossing the magnetic potential barrier.

In Figure 5.10, bifurcation diagrams of tip displacements are shown with respect to the variation of wind speed. As the wind speed increases, the beam-bluff body systems start oscillating from the static trivial state through hopf bifurcation. Limit cycles take birth from fixed points. The magnetically coupled system experiences pitchfork bifurcation at the static condition due to magnetic repulsive force. Non-trivial stable branches then bifurcate with hopf bifurcation when the wind speed reaches critical value for the occurrence of galloping.

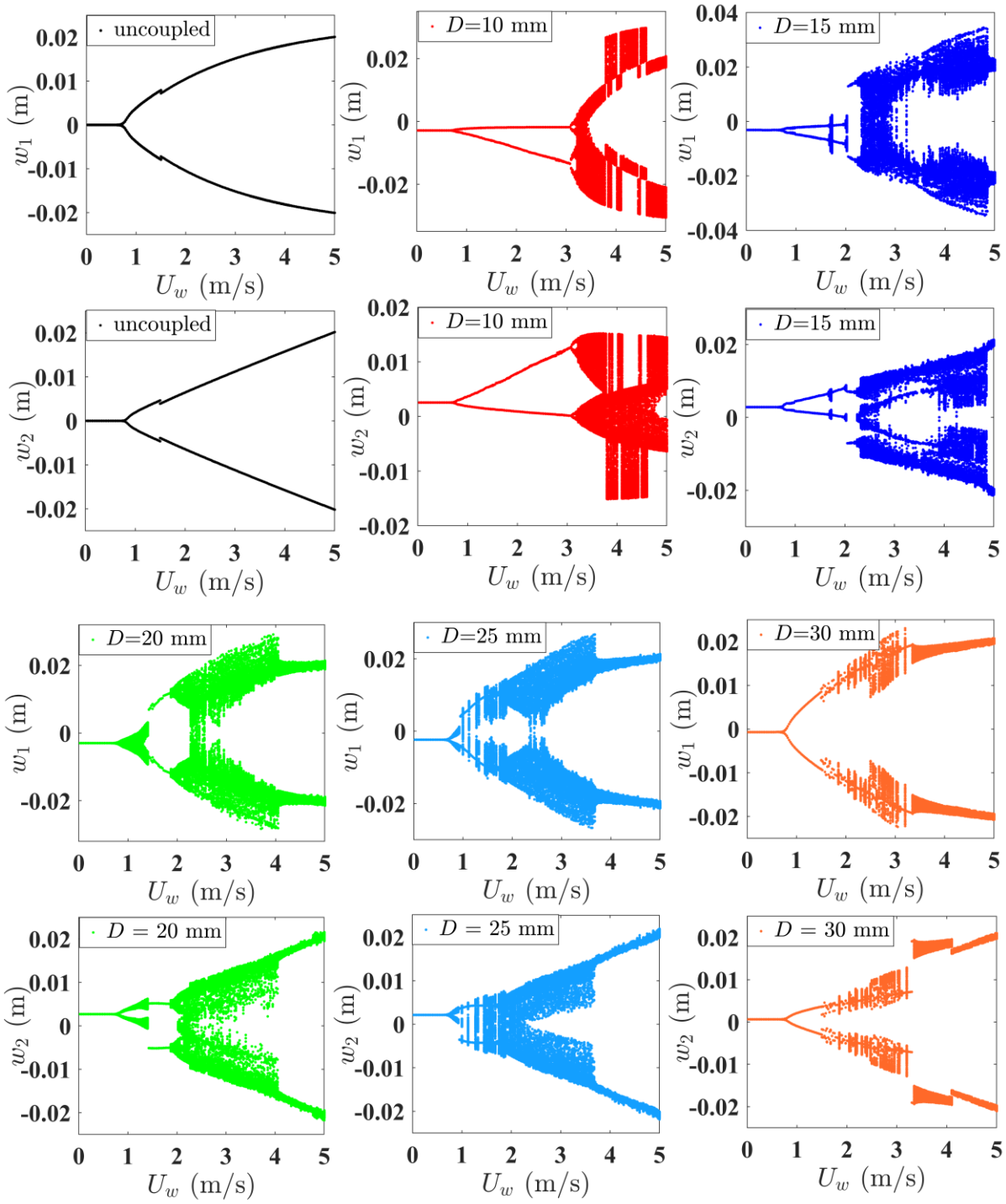

Figure 5.10: Bifurcation diagram of tip displacements for uncoupled and coupled conditions

Both of the beams exhibit intra-well periodic oscillations mostly throughout the light air wind speed region for D = 10 – 15 mm. In Figure 5.11, one can observe intra-well quasi periodic motion up to a wind speed of 1.4 m/s for D = 20 mm. Further increase in wind speed leads the system to move from intra-well quasi-periodic to inter-well periodic oscillation, which can be verified from Figure 5.12. At D = 25 mm, the system oscillates with intra-well quasi-periodic motion up to a wind speed of 0.9 m/s. Beyond that, inter-well chaotic motion occurs through the quasi-periodic route to chaos. Time responses, phase portraits, Poincaré sections, and FFT plots in Figure 5.13 and Figure 5.14, show the quasi-periodic and chaotic responses for 0.9 m/s and 1.125 m/s, respectively when D = 25 mm. Three irrational frequencies are present in the quasi periodic responses. Torus breakdown occurs with a slight change in the wind speed. It is to be noted that in all voltage vs. time response plots throughout this chapter, cyan and red colored lines represent peak output voltages and RMS value of the corresponding peak voltages, respectively.

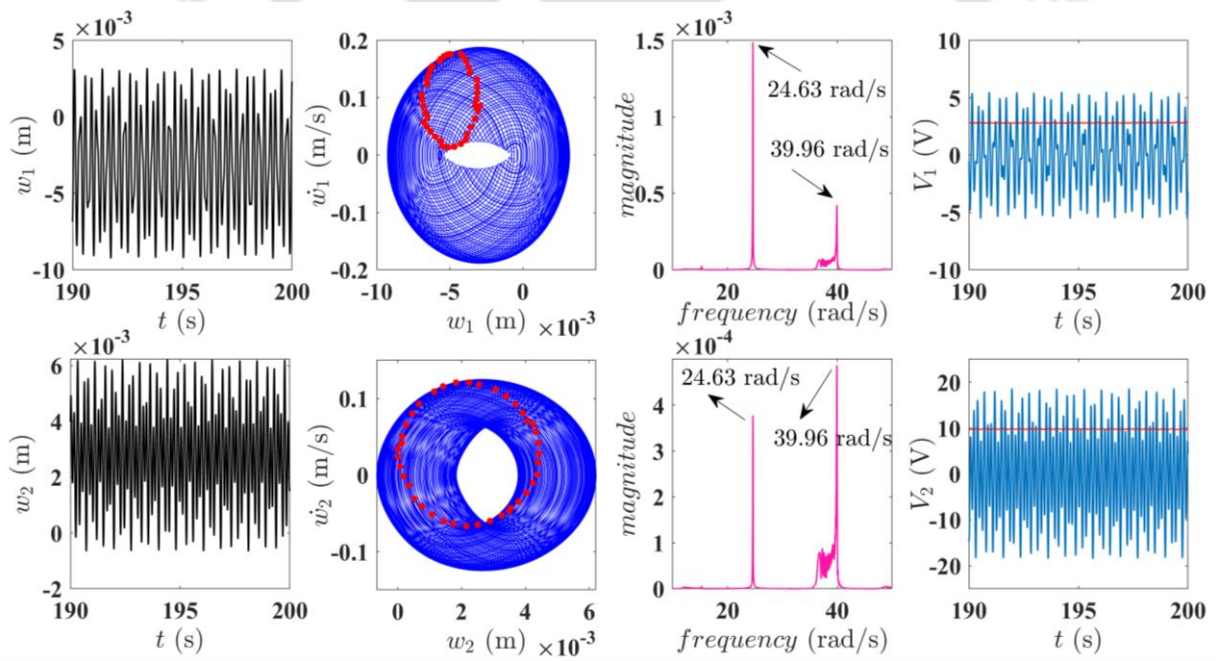

Figure 5.11: Time response, phase portrait, Poincaré sections, and FFT plot for D = 20 mm at a wind speed of 1.4 m/s

Further, chaos occurs through a finite sequence of hopf bifurcations. which qualitatively predicts the Torus 3 (T^3) bifurcation. Due to the significant distance between the magnets, inter-well periodic oscillations also co-exist in between chaotic windows. Similar quasi-periodic routes to chaos have been studied in coupled Duffing-Van der Pol oscillator with Coulomb damping under harmonic excitation [244], in two DOF nonlinear oscillator with cubic nonlinearity [245], and also in self-excited autonomous square prisms [246].

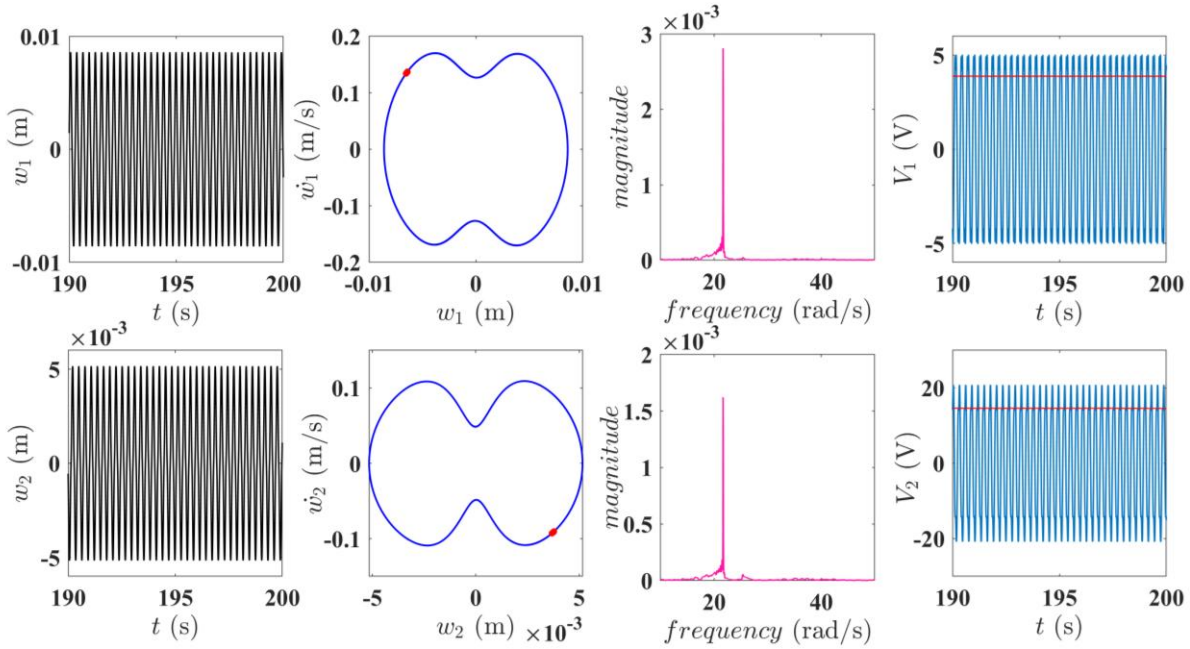

Figure 5.12: Time response, phase portrait, Poincaré sections, and FFT plot for D = 20 mm at wind speed of 1.5 m/s

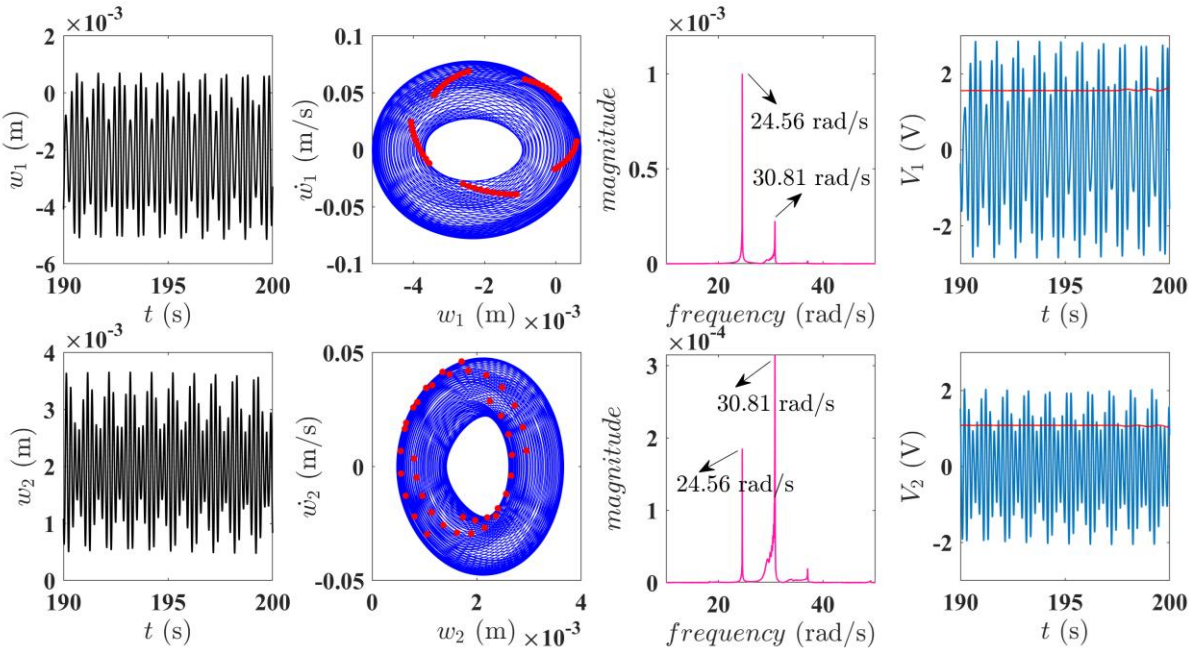

Figure 5.13: Time response, phase portrait, Poincaré sections, and FFT plot for D = 25 mm at wind speed of 0.9 m/s

From Figure 5.10, it can also be observed that in the light breeze region, for the uncoupled system and the coupled system with D = 10 mm; periodic motions exist throughout. One can observe periodic to quasi periodic or weakly chaotic transition at wind speed of 3.1 m/s when D = 10 mm. For D = 15 – 25 mm, periodic, quasi-periodic and chaotic responses occur as the

wind speed increases. At D = 30 mm, mostly quasi-periodic responses exist. Quasi-periodicity is a quite common phenomenon in coupled oscillatory systems.

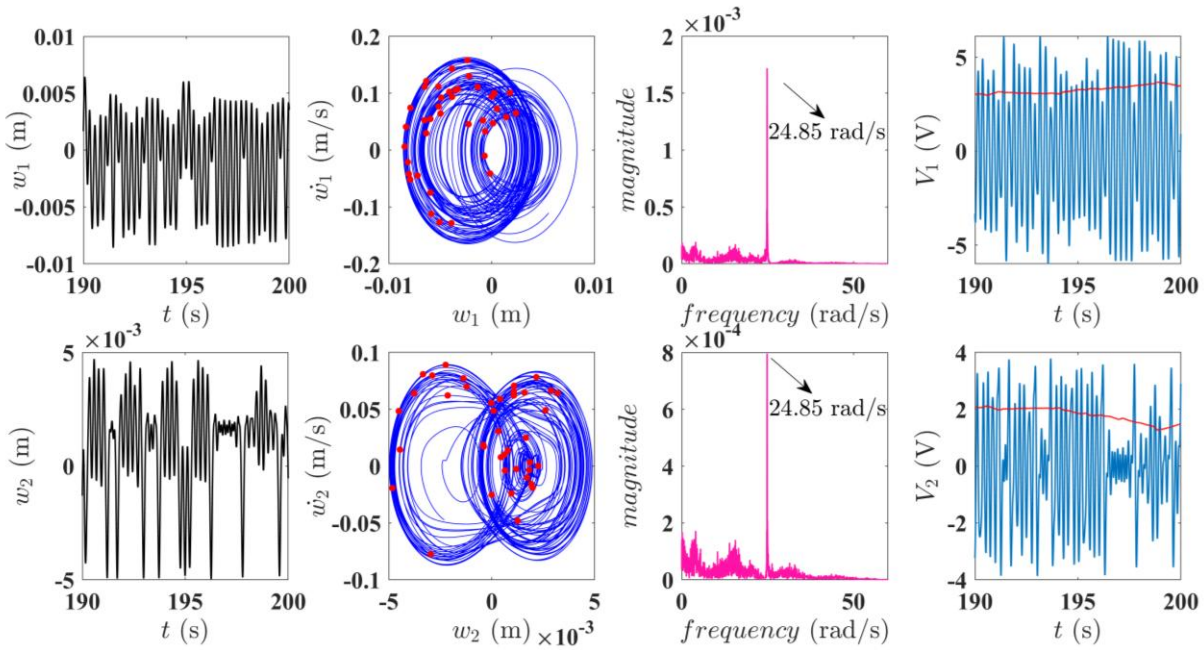

Figure 5.14: Time response, phase portrait, Poincaré sections, and FFT plot for D = 25 mm at wind speed of 1.125 m/s (initial conditions: $w_1 = 0.001, \dot{w}_1 = 0, V_1 = 0, w_2 = 0.001, \dot{w}_2 = 0, V_2 = 0$)

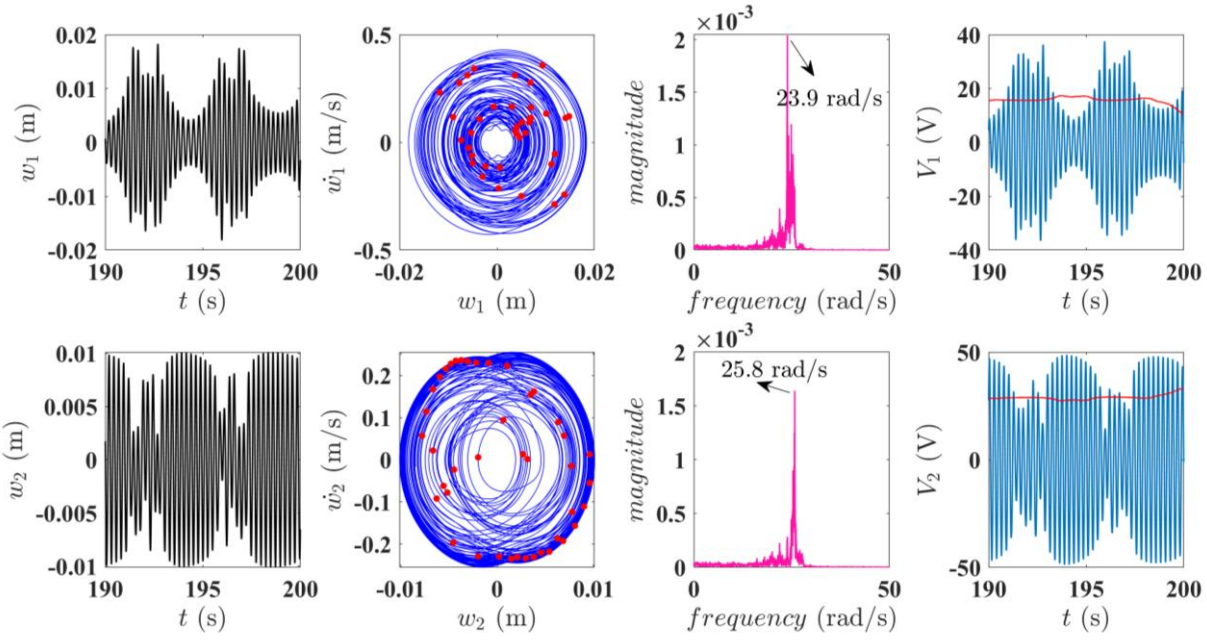

Figure 5.15: Time response, phase portrait, Poincaré section, and FFT plot at U_w = 2.5 m/s and D = 25 mm (initial conditions: $w_1 = 0.001, \dot{w}_1 = 0, V_1 = 0, w_2 = 0.001, \dot{w}_2 = 0, V_2 = 0$)

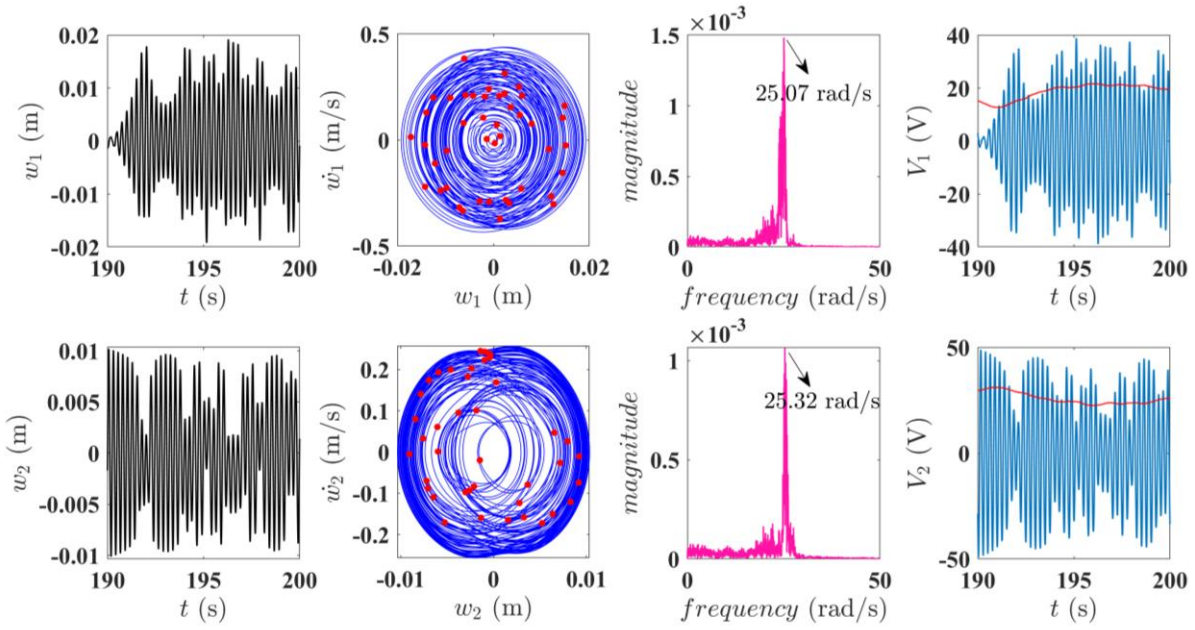

Figure 5.16: Time response, phase portrait, Poincaré section, and FFT plot for $U_w = 2.5$ m/s and $D = 25$ mm (initial conditions: $w_1 = 0.002, \dot{w}_1 = 0, V_1 = 0, w_2 = -0.001, \dot{w}_2 = 0, V_2 = 0$)

Figure 5.15 and Figure 5.16 shows the sensitive dependence of chaotic motion on initial conditions. From the discussions mentioned above, it can be stated that mostly quasi-periodic routes to chaos can be observed in cases of coupled system responses. At higher values of D, chaos again vanishes when the wind speed is significantly high (nearly 4 m/s). It can be noted that the system is sensitively dependent on the system parameters. A small change in parameter values can introduce periodic, quasi-periodic, and/or chaotic responses into the system. As the system is coupled, hence it is difficult to conduct parametric studies simultaneously considering the load resistances, wind speed, distance between the magnets, etc.

Figure 5.17 shows the total power output of the system for uncoupled and coupled conditions for different wind speed regions. It can be observed from Figure 5.17 (a) that at low wind speed (below 0.9 m/s), by setting D = 15 mm; the coupled system performs better than the uncoupled system in terms of power output. At wind speed of 0.825 m/s, the total power output of the uncoupled system is 0.005 mW and that of the coupled system (with D = 15 mm) is 0.024 mW which is 380% increment. Beyond the wind speed of 0.9 m/s, the uncoupled system exhibits better performance. Again, at wind speed of 1.425 m/s; the coupled system (with D = 20 mm) generates more power compared to the uncoupled system. At wind speed of 1.5 m/s, the coupled system can generate 0.37 mW power which is 34.54% higher than that of the uncoupled system.

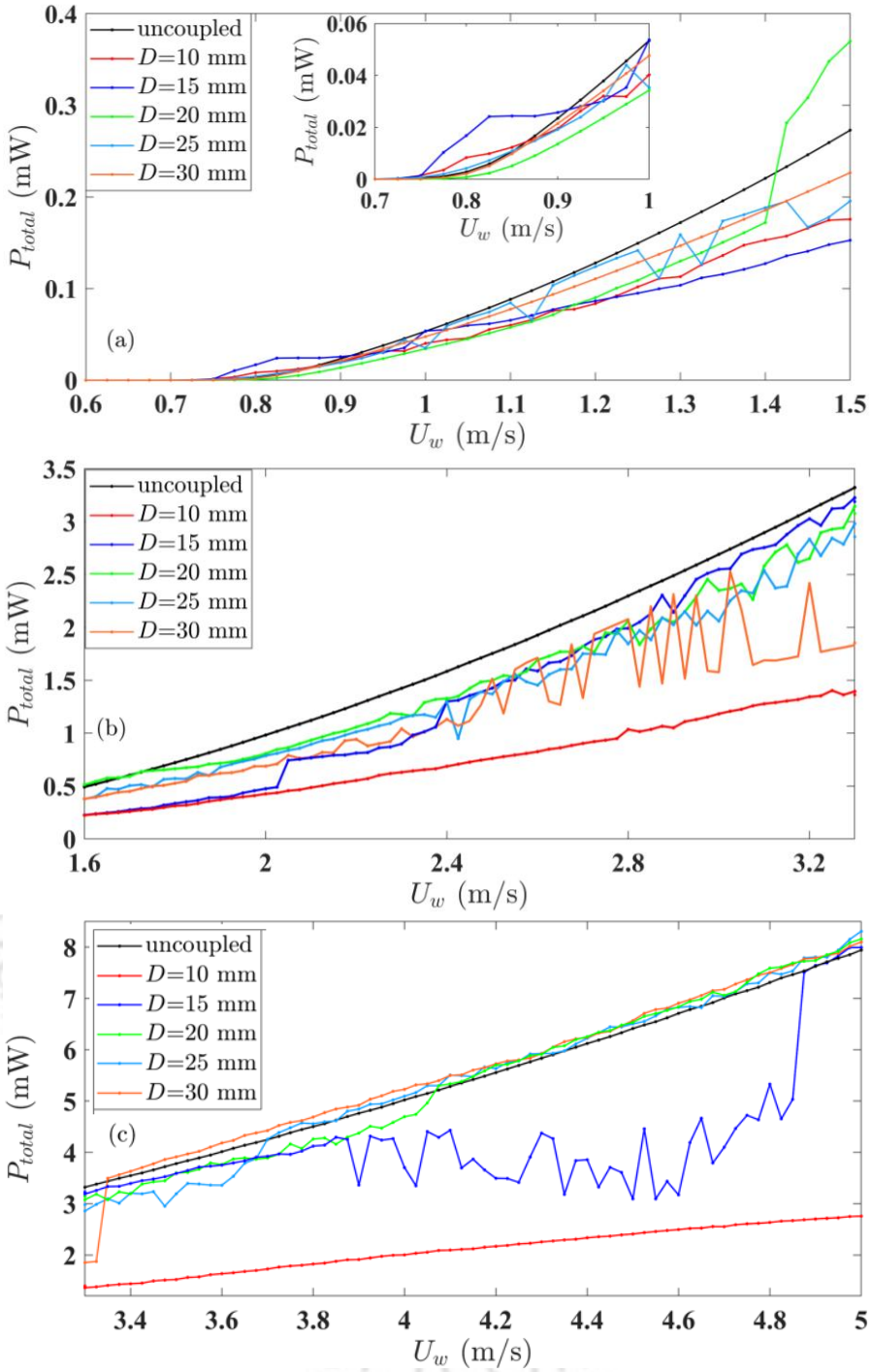

Figure 5.17: Wind speed vs. total output power of the system; for (a) light air, (b) light breeze, and (c) gentle breeze region

Referring to Figure 5.17 (b), In the light breeze wind speed region; the uncoupled system output is higher than that of the coupled system (for all of the *D* values). In this region, mostly quasi-periodic and chaotic oscillations dominate for the coupled system; as a result, many jump ups and downs can be observed which leads towards more fluctuation in harvested power. Hence, operating the system in uncoupled condition is preferable. In Figure 5.17 (c), one can observe that the total power output of the coupled system (with $D = 30$ mm) increases and exceeds that

of the uncoupled system when the wind speed reaches nearly 3.4 m/s. The power outputs of the coupled system with D = 20 mm and D = 25 mm also exceed that of the uncoupled system when the wind speed is beyond 3.7 m/s and 4.1 m/s, respectively.

In the light air region, a sudden appearance of chaotic window can be observed in Figure 5.10 for D = 25 mm. As a result, some jump ups and downs can also be observed in Figure 5.17 (a) for D = 25 mm. These phenomena occur due to phase un-synchronization of both of the beams under magnetic interaction which is wisely explained by Wang et al. [32]. For the light breeze wind speed condition, more frequent ups and downs can be observed in Figure 5.17 (b) for $D = 15$ mm, 20 mm, 25 mm and 30 mm, as one can find mostly chaotic responses for the mentioned D values in Figure 5.10. Similarly, Figure 5.17 (c) shows that in the gentle breeze region with increase in D values from 15 to 30 mm, jump ups and downs start to vanish with increase in wind speed. Correspondingly, in Figure 5.10 one can observe that chaotic responses try to approach towards inter-well periodic oscillations for higher wind speed values.

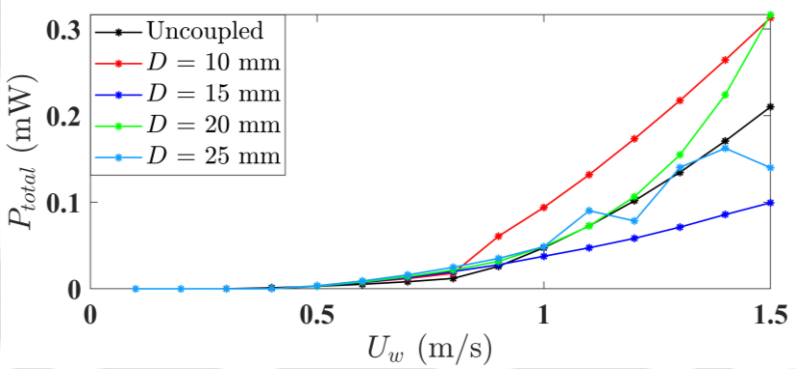

Figure 5.18: For modified mass of 1st bluff body ($m_{bb1} = 5$ gm), total output power of the PEH with varying wind speed

Mass of the bluff bodies plays a major role in computing the natural frequencies as well as studying the dynamic behavior of the system. Performance of the system is investigated considering the mass of bluff bodies. Assuming the mass of the 1st bluff body (m_{bb1}) to be 5 gm and keeping the mass of the 2nd bluff body unchanged ($m_{bb2} = 13$ gm), ω_1 increases to 52.69 rad/s and ω_2 remains constant at 26.17 rad/s, which leads to the ratio of the two natural frequencies be approximately 2:1. Considering the above mentioned modification, Figure 5.18 represents the output power of the uncoupled and coupled system for different D values and different wind speeds. Here, it can be observed that in the light air region, the power output of the coupled system increases significantly than that of the uncoupled system. At a wind speed

of 1 m/s, the coupled system (with D = 10 mm) generates 0.093 mW power which is nearly 97% more compared to that of the uncoupled system which is found to be 0.047 mW. From Figure 5.17 (a) and Figure 5.18, it can be observed that the overall performance of the system in the light air region enhances for the present case. Whereas, in other two wind speed regions, no significant improvement could be found with this new mass modification.

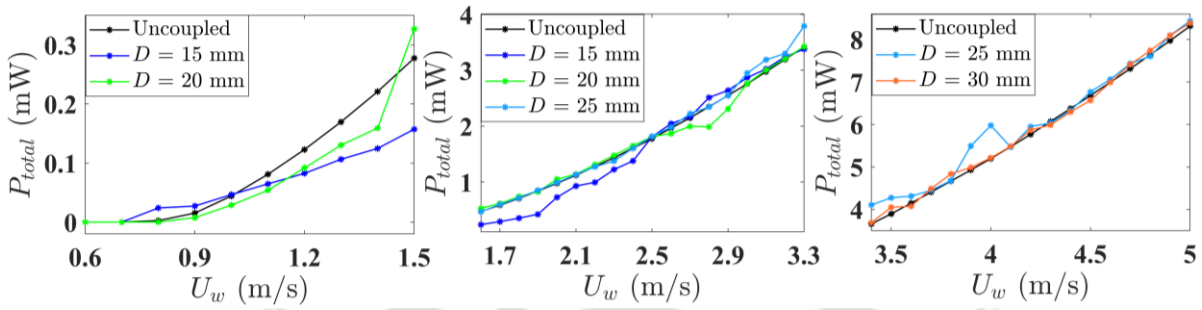

Figure 5.19: For modified mass of 2nd bluff body (m_{bb2} =16 gm), total output power of the PEH with varying wind speed; (a) light air, (b) light breeze, and (c) gentle breeze

Considering the mass of the 1st bluff body (m_{bb1}) fixed at 35 gm (as mentioned in Table 5.1) and the mass of the 2nd bluff body (m_{bb2}) to be 16 gm, ω_2 reduces to 24.27 rad/s and ω_1 remains unchanged with 24.34 rad/s. In this case, the ratio of the two natural frequencies becomes approximately 1:1. For this case, the output power of the energy harvester for different coupling conditions and wind speed regions are presented in Figure 5.19. In light air region at wind speed of 0.8 m/s, the power output of the coupled system (with D = 15 mm) is 0.023 mW which is 8.2 times than that of the uncoupled system (0.002 mW). In the range of 1 m/s to 1.4 m/s, the uncoupled system performs better. In the light breeze region, performance of the coupled system (with D = 20 mm and 25 mm) improves slightly compared to uncoupled system. It is to be noted that in the present case, one can observe better performance of the coupled system compared to that of the previous case shown in Figure 5.17 (b). At wind speed of 2 m/s, the power output of the coupled system (with D = 20 mm) is 1.05 mW which is nearly 8.24% more compared to that of the uncoupled system (0.97 mW). At wind speed of 3.3 m/s, the power output of the coupled system (with D = 25 mm) is 3.79 mW and that of the uncoupled system is 3.42 mW, which is 10.81% increase in power. In the gentle breeze region, the coupled system (with D = 25 mm and 30 mm) shows better performance than the uncoupled case for wind speed of 3.4 m/s to 4.2 m/s. For higher wind speeds beyond 4.2 m/s, minor variations can be observed. At wind speed of 4 m/s, power output of the coupled system (with D = 25 mm)

enhances by 15.02% than the uncoupled case. Hence, one can find that the masses of the bluff bodies play an important role in controlling the system dynamics.

The galloping-based piezoelectric energy harvester model proposed in this study can be adjusted in vertical and horizontal directions by using the sliding mechanisms (at the fixed ends of the cantilever beams) guided along the Aluminum fixture, hence by observing the ambient wind speed condition; the system can easily be converted from uncoupled to coupled or vice versa. A detailed description of the physical model is given in the next section.

5.4 Experimental investigations

A prototype of the proposed energy harvester has been developed to investigate the effect of magnetic coupling, the existence of periodic; quasi-periodic, and chaotic responses, the influence of wind speed, etc. The dimensions of the prototype are the same as considered in Table 5.1. The oscillatory beam-bluff body parts of the prototype are fixed at their base which can be guided along the Aluminum frame. A simple resistor-based electrical circuit (which is connected at the piezo-ends) is configured on a breadboard and attached to the Aluminum frame.

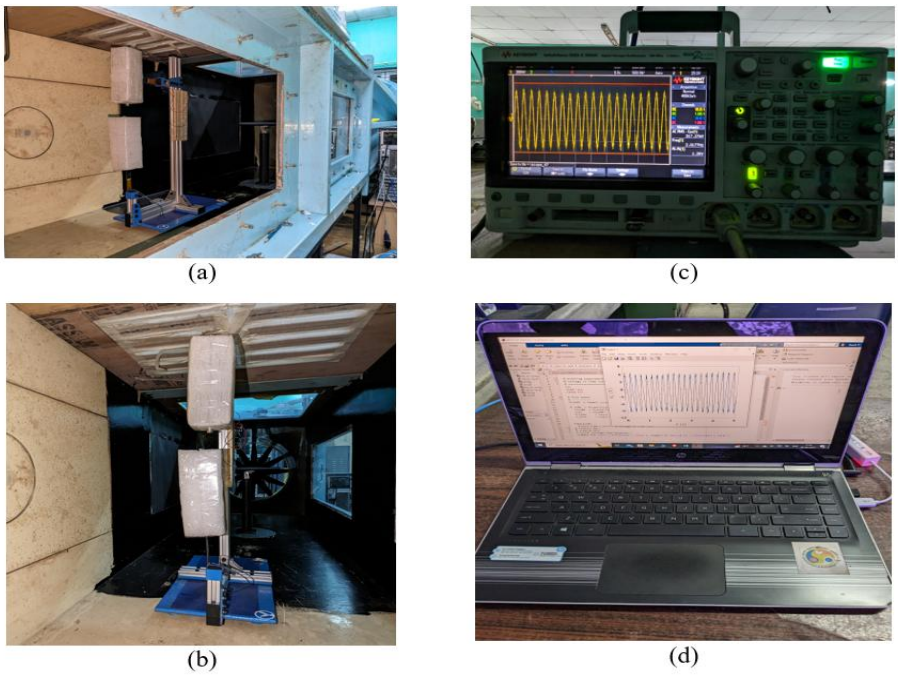

Figure 5.20: Experimental setup: (a) the proposed PEH inside the wind tunnel, (b) the static displaced state of the system under magnetic repulsion, (c) digital oscilloscope, (d) computer

Figure 5.20 shows the prototype of the proposed energy harvester inside the wind tunnel, digital oscilloscope, and computer which are used in measuring and processing the data of output

voltage from the energy harvester. All the experiments have been performed in wind tunnel test setup (Sunshine Measurements Pvt. Ltd.) at Wind Tunnel Laboratory, IIT Guwahati. Cross-sectional dimensions of the test section of the tunnel are 600 mm×600 mm and the length is 2000 mm. Maximum operating speed is 50 m/s. The tunnel is calibrated to provide uniform flow velocity from 3 m/s onwards and is considered to have a turbulence intensity of 0.4%. Wind speed inside the tunnel is measured by a pitot tube setup. All experimental data are recorded by KEYSIGHT InfiniiVision DSO-X 3024A digital storage oscilloscope and processed in a computer.

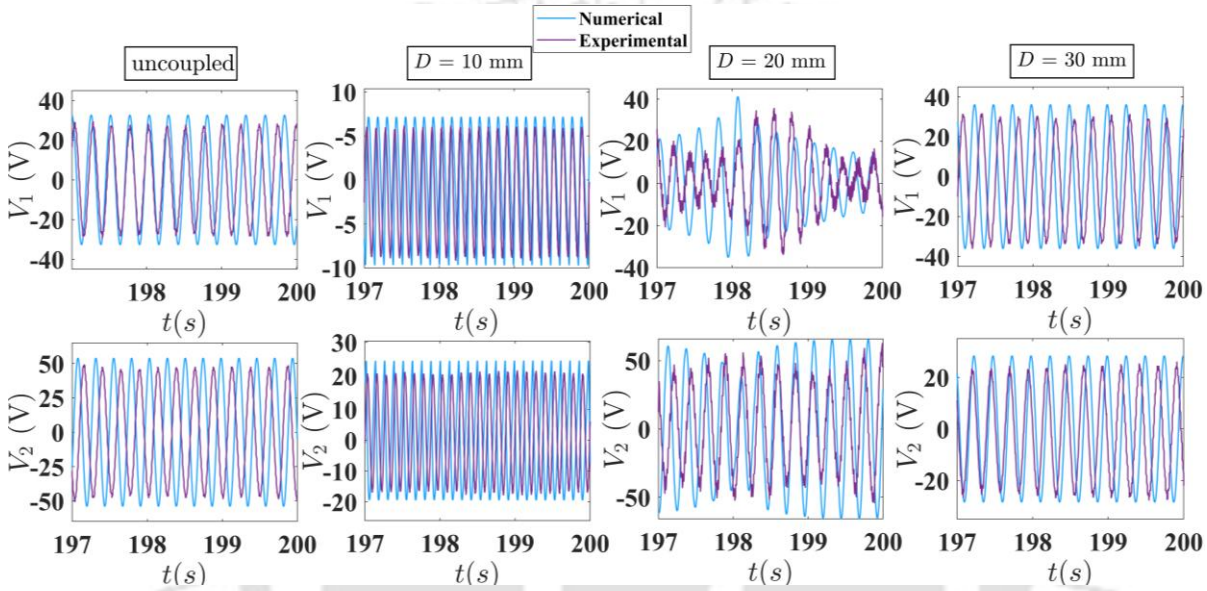

Figure 5.21: Comparison of the numerical calculated and experimentally obtained output voltage of the energy harvester for uncoupled and coupled conditions at $U_w = 3$ m/s

Table 5.7: Numerical and experimental output voltages and % error at $U_w = 3$ m/s

Output Voltage	Uncoupled			$D = 10$ mm			$D = 20$ mm			$D = 30$ mm		
	Num. (V)	Exp. (V)	% diff.	Num. (V)	Exp. (V)	% diff.	Num. (V)	Exp. (V)	% diff.	Num. (V)	Exp. (V)	% diff.
V_1	32.7	28.2	13.8	7.01	6.16	13.5	41.3	35.6	13.7	36.1	30.9	14.4
V_2	54.1	47.4	12.4	24.8	21.15	14.7	65.8	57.3	12.9	28.4	24.9	12.3

Figure 5.21 shows the comparison between the numerically (using ode45) and experimentally obtained output voltages of the uncoupled as well as coupled system at wind speed of 3 m/s. It can be observed that experimentally obtained output voltages are slightly less compared to that of the simulated results. The difference is may be due to the imperfections in the physical prototype of the energy harvester such as imperfect bonding between the MFC patches and the

beam surfaces, actual magnetic repulsive force may not be exactly the same which is considered in the numerical study, turbulence intensity of the wind tunnel, the uneven facing surface of the bluff bodies, etc. Though the experimental results show deviation from the numerically simulated ones; however, the dynamic responses observed are quite similar in both of the cases. At wind speed of 3 m/s, one can observe periodic responses which can also be verified from the bifurcation diagrams of displacements of the beams as shown in Figure 5.10. Both of the beams exhibit limit cycle oscillation in their respective intra-well. As the wind speed increases and becomes 4 m/s, the solutions jump from intra-well to inter-well and exhibit typical quasi-periodic oscillations.

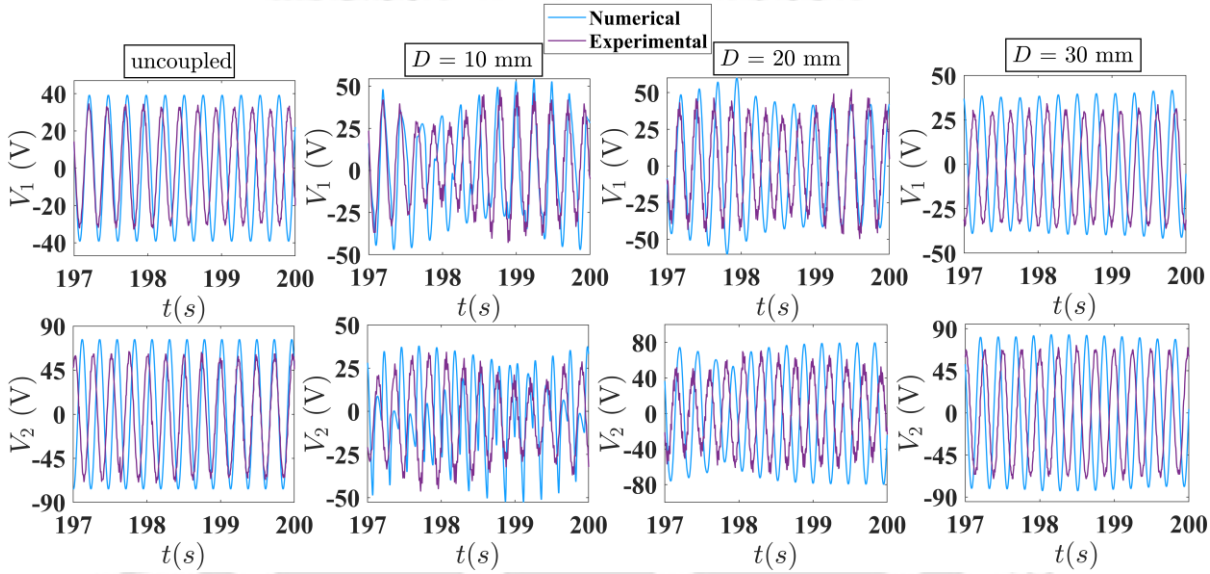

Figure 5.22: Comparison of the numerical calculated and experimentally obtained output voltage of the energy harvester for uncoupled and coupled conditions at $U_w = 4$ m/s

Table 5.8: Numerical and experimental output voltages and % error at $U_w = 4$ m/s

Output Voltage	Uncoupled			$D = 10$ mm			$D = 20$ mm			$D = 30$ mm		
	Num. (V)	Exp. (V)	% diif.	Num. (V)	Exp. (V)	% diff.	Num. (V)	Exp. (V)	% diff.	Num. (V)	Exp. (V)	% diff.
V_1	39.2	33.8	13.8	54.4	47.7	12.3	60.0	54.1	13.3	39.6	34.7	12.3
V_2	75.8	65.1	14.1	24.8	21.15	14.7	79.85	69.6	12.8	82.0	72.2	12.0

Figure 5.22 shows the time responses of numerical simulations (using ode45) and experimental results of the output voltages of the system at wind speed of 4 m/s. As the distance between the permanent magnets increases, the voltage output of the MFC patches increases. Due to less magnetic repulsive force, the responses can oscillate easily in the inter-well potential. The

experimental observations are in good agreement with the simulated results. The comparison and percentage difference between numerical and experimental values of output voltages at wind speed of 3 m/s and 4 m/s, respectively are given in Table 5.7 and Table 5.8, respectively. It is to be noted that, here the tabulated numerical and experimental data are given considering the highest peak values of the voltage responses shown in Figure 5.21 and Figure 5.22.

Table 5.9: Qualitative performance comparison between existing magnetically coupled GPEHs and the present model (Th.: Theoretical, Exp.: Experimental)

Authors' Name	**System config.**	**Th. /Exp. /Both**	**Natural Frequency**	**Critical galloping speed**	**Excitation (Wind/Base)**	**Voltage (V)**	**Power (mW)**
Alhadidi and Daqaq [248]	1 DOF	Both	N/A	1 m/s	Wind: 5.5 m/s	N/A	6 mW
Sun et al. [249]	2 DOF	Both	21.98 rad/s, 43.96 rad/s	2.2 m/s	Wind: 4 m/s	~ 80 V	N/A
Sun et al. [247]	2 DOF	Th,	125.66 rad/s, 153.9 rad/s	0.5 m/s	Wind: 10 m/s	60 V	21 mW
Chen and Zhao [251]	2 DOF	Both	N/A	1.6 m/s	Wind: 5 m/s	32.5 V	N/A
Li et al. [252]	1 DOF	Both		N/A	Wind: 3.6 m/s Base: 12 Hz	35 V	N/A
Zhou et al. [253]	2 DOF	Both	63.05 rad/s, 80.78 rad/s	N/A	Base: 10.4 Hz	~ 20 V	~ 0.16 mW
Lan et al. [254]	2 DOF	Th.	N/A	1.05 m/s	Wind: 4 m/s	~ 20 V	~ 0.4 mW
Present study	2 DOF	Both	24.34 rad/s, 26.17 rad/s	0.7 m/s	Wind: 4 m/s	~106 V	4.13 mW

Table 5.9 represents a qualitative comparison of performance between some already existing magnetically coupled GPEHs and the model considered in the present study. In the work of Sun et al. [247], one can find that operating a magnetically coupled 2 degrees of freedom galloping energy harvester with 1:1 internal resonance can enhance the performance of the system. Hence for the present model, both of the natural frequencies are chosen to be nearer to

each other which make both the beams to start oscillation at nearly the same critical galloping speed (0.7 m/s). The system starts oscillating at lesser wind speed and tends to have a wider operational wind speed range as compared to most of the magnetically coupled piezoelectric energy harvesters presented in Table 5.9. Hence at low wind speed, the system starts to harvest more power. At a wind speed of 4 m/s, the total power output of the proposed energy harvester is 4.13 mW which is quite good in parallel to the existing magnetically coupled energy harvester models compared in Table 5.9.

At present, the experimental validation is performed under controlled wind tunnel conditions. However, while implementing this galloping-based energy harvester in real world outdoor condition, the system is subjected to turbulent wind flow, which introduces stochastic fluctuations in wind speed and direction. This can lead to irregular oscillations, intermittent galloping and reduced predictability of the harvested power. Additionally, variations in angle of attack due to change in direction of the wind flow may shift the system away from optimal condition to induce galloping, thereby affecting the performance. In the work of Adhikari et al. [255], a detailed investigation of a piezoelectric energy harvester under broadband random excitation is present. The optimal design of the energy harvester is found by studying peak response characteristics. This approach is important for modelling real world turbulent wind conditions.

From structural perspective, fatigue and long-term durability of the system are critical concerns. Continuous oscillations under variable loading conditions may lead to material degradation, especially in the piezoelectric layers of the MFC patches and the mechanical joints. Environmental factors such as moisture, temperature variation, and dust accumulation may further influence the functionality of the system. To address this challenges, future work may focus in designing the system including stochastic model to simulate turbulent wind flow, incorporating self-tuning mechanism to adjust with variable wind speed and maintain galloping instability, and finally conducting a long-term field testing for performance validation.

5.5 Summary

This chapter investigates the nonlinear dynamics and energy harvesting performance of a magnetically coupled double beam piezoelectric energy harvester operating under wind-induced galloping. The proposed configuration consists of two orthogonally placed cantilever beams, one horizontally and one vertically. Square shaped bluff bodies are attached to the tip

of the beams to introduce galloping excitation. A pair of identical NdFeB magnets are mounted on the bluff bodies with same poles facing each other, which introduces a repulsive force that couples the beams. This arrangement allows the system to transition between monostable and bistable configurations depending on the gap between the magnets.

A comprehensive mathematical model is developed by formulating expressions for kinetic, elastic, gravitational and magnetic potential energies and also the work done by aerodynamic galloping, damping and the electrical moment. The galloping force is derived using the quasi-steady aerodynamic approximation, while the magnetic force is modelled using a dipole-dipole model. Considering single-mode approximation and using Lagrange's principle, a set of nonlinear differential equations of motion is obtained. These equations include geometric and inertial nonlinearity, nonlinear damping from galloping, and strongly nonlinear magnetic terms.

The numerical results reveal how the gap between the magnets influences the potential energy of the system. For small gaps, the beams exhibit bistability, while larger gaps extinguish the potential barrier, leading to monostable state. Across three wind-speed regions - light air, light breeze, and gentle breeze; the system's responses show rich dynamics including periodic, quasi-periodic, and chaotic motions. At low wind speeds, magnetic coupling often enhances the output because the beams exchange energy more effectively. However, in the light breeze, the coupled system frequently enters quasi-periodic or chaotic states, leading to fluctuating power levels which lower the performance compared to the uncoupled case. In the gentle breeze region, particularly for moderate to large magnet gaps, the coupled system again becomes advantageous, with output power surpassing the uncoupled configuration.

The study also considers the effect of mass of the bluff bodies. The natural frequencies of the system can be tuned by adjusting the masses and correspondingly, the beams can be brought close to internal resonance conditions such as 1:1 or 2:1. This tuning can increase the output power, especially at low wind speeds.

A prototype of the harvester is fabricated and tested in a wind tunnel. The experimental results match well with the numerical trends. Although the measured voltages are slightly lower due to practical imperfections; however, the comparison shows the feasibility of the proposed system. Overall, this chapter illustrates that magnetic coupling can be strategically used to enhance the performance of the galloping-based energy harvesters.

Chapter 6

Conclusions and Scope for Future Work

6.1 Introduction

In this chapter, the overall conclusions drawn from the research work carried out in this thesis is presented. The aim of this study is to explore the nonlinear dynamics and vibrational characteristics of double cantilever beam based PEHs operating under different types of excitation conditions such as parametric, magnetic, and galloping. Through mathematical modelling, numerical simulations, and experimental investigations, the research work has investigated the effectiveness of coupling mechanisms, nonlinearities, and different excitation conditions for enhancing the energy harvesting capability of such PEH systems. In the next sections, general conclusions and specific conclusions are given. The scopes of future work are also highlighted which can serve the purpose of further developments in the field of piezoelectric energy harvesting.

6.2 General conclusions

In this research work, the nonlinear dynamic analysis and performance improvement studies have been conducted on PEHs that use a double cantilever beam based configuration. The study is focused on three main systems: a spring-coupled double beam based PEH investigating the principal parametric resonance condition, a spring coupled double beam based PEH under parametric and magnetic excitation, and a magnetically coupled double beam based PEH under wind induced galloping instability. The main purpose is to understand how coupling and nonlinear effects can be used to make piezoelectric energy harvesters more efficient and capable of working over a wider range of external excitation conditions.

The first work of the research presents a spring coupled double beam energy harvester that is externally excited harmonically at the base. The excitation is given in such a way that the PEH undergoes principal parametric resonance. The system is modelled using Euler–Bernoulli beam theory and assumptions. Due to large transverse displacement and mass moment of inertia of the attached tip mass, the system exhibits geometric and inertial nonlinearities. The coupled

electromechanical equations of motion are derived using Lagrange principle and generalized Galerkin's method and are solved using the method of multiple scales (MMS) and the 4th order Runge Kutta method based ode45 solver in MATLAB. Solutions obtained using both the methods are compared and found to be in good agreement. The study showed that introducing a spring between the two beams improved the system's performance in several ways. The coupling allowed energy transfer between the beams, which increases the output voltage and power in some cases compared to a single beam. The operational frequency bandwidth over which the system can harvest energy also gets wider. Stability analysis reveals the bifurcation points i.e., the transitions between stable and unstable solutions. Interesting nonlinear phenomena such as quasiperiodicity, chaos can be observed in the time and frequency responses. Parametric studies are also conducted on parameters like tip mass, spring stiffness and load resistance. The findings confirmed that spring coupling is an effective way to improve the performance of piezoelectric energy harvesters.

In the second work, a similar PEH system is studied considering the influence of magnetic interaction. Two permanent magnets, one at the tip of the 2nd beam and another attached to the movable base, are used to introduce magnetic repulsive force into the system. This incorporates tuneable nonlinearity, which can be controlled by changing the distance between the magnets. The system can be driven to monostable or bistable state by varying this distance. The results show that magnetic interaction strongly affects the system dynamics. The beams exhibit higher amplitudes of oscillation. Responses can be periodic, quasi-periodic, and even chaotic depending on the magnetic field strength and excitation frequency. When both beams are equipped with MFC patches and magnetic force is introduced, with proper selection of load resistance the total output power can increase by more than ten times compared to the system without magnets. The study proves that controlled magnetic interaction can greatly enhance the overall efficiency and extend the operational frequency bandwidth of a piezoelectric energy harvester.

In the third work, a magnetically coupled double beam based PEH is investigated under galloping excitation. The beams are placed orthogonal to each other. Bluff bodies are attached to the beams to induce galloping based self-excited oscillation. The aerodynamic force is modelled using the quasi-steady hypothesis, and the effects of wind speed and electrical load on the harvester's output are examined. This study includes both theoretical modelling and experimental validation. A prototype of the system has been fabricated and tested in wind tunnel facility of IIT Guwahati, and the measured output voltages are compared with the

numerically obtained results. It is observed that as the wind speed increases, the output voltage and power also increase up to a certain point, beyond which complex nonlinear responses appear. Depending on the wind conditions and magnetic spacing, the system exhibits periodic, quasi-periodic, and chaotic motion. The magnetic interaction again plays an important role in tuning the response and maintaining stability. The system can effectively harvest energy even at low wind speeds, which makes it suitable for practical use in outdoor or remote environments where steady vibrations are not always available.

From all three studies, it can be concluded that the coupling between beams and the introduction of magnetic interaction are convenient ways to improve the performance of PEHs. The spring coupling helps to widen the operating frequency range, while magnetic coupling provides tuneable nonlinearity and further improved energy conversion. The galloping energy harvester shows that magnetically coupled system can also be employed to enhance energy generation from wind induced vibrations. Together, these results demonstrate that nonlinear effects, when properly controlled, can turn natural instabilities into useful mechanisms for energy harvesting. The findings of this thesis also emphasize the importance of combining analytical, numerical, and experimental approaches to understand complex dynamic systems.

6.3 Specific conclusions

6.3.1 Base Excited Spring Coupled Double Beam Piezoelectric Energy Harvester

- The spring-coupled double beam configuration exhibits much better performance compared to the uncoupled or single beam system. The coupling of spring allows energy to transfer between the two beams, which increases vibration amplitudes and improves the overall energy harvesting efficiency. The coupled system shows a significant increase in operating frequency range. When a spring stiffness of 1 N/m is used, the frequency bandwidth of the first beam increased by nearly three times and that of the second beam by about 76%. When the spring stiffness is increased to 2 N/m, the bandwidth improves more. For the 1st and 2nd beam, the frequency bandwidth enhances by 336.66% and 92.64%, respectively.
- The influence of the coupling spring is also evident in the shape and extent of the parametric instability regions. With an increase in spring stiffness, the ‘w’ shaped unstable region observed for K = 1 N/m splits into two distinct ‘v’ shaped unstable

regions, with an additional smaller region appearing in between. This verify that coupling introduces internal resonance and enhances the system's ability to extract energy over multiple frequency bands. The minimum value of base excitation amplitude required to initiate parametric resonance is around 0.002 m. Once this threshold is crossed, the system starts to oscillate.

- The tip mass of the beams plays a major role in the system's dynamic response. Increasing the tip mass reduces the natural frequencies and causes the beams to buckle beyond a certain limit. For K = 1 N/m, the buckling masses are $m_1 = 0.0104$ kg and $m_2 = 0.053$ kg. For K = 2 N/m, the buckling masses are $m_1 = 0.0109$ kg and $m_2 = 0.0561$ kg. Operating the system within the pre-buckled range results in more stable periodic motion and higher output voltage, while operating in the post-buckled state lead to irregular and less efficient voltage generation.
- The output power of the energy harvester is strongly dependent on the electrical load resistance. The power increases with resistance up to an optimal value and then starts to decrease. For coupled spring stiffness of 2 N/m, maximum output power of 0.76 mW and 3.91 mW can be obtained from the 1st and 2nd beam with load resistance of 0.35 MΩ and 2.5 MΩ, respectively.
- With coupled spring stiffness of 2 N/m, the output power of the 1st and 2nd beam are 0.76 mW and 3.91 mW, respectively; whereas that of the uncoupled 1st and 2nd beam are 0.157 mW and 0.963 mW respectively. Output enhances significantly by 3.84 and 3.06 times for the 1st and 2nd beam, respectively.

6.3.2 Base Excited Double Beam Piezoelectric Energy Harvester under Magnetic Force

- Introduction of spring coupling itself improves system output even without magnets. The maximum RMS voltage increases to 3.14 V, marking an 18.04% rise over the uncoupled configuration, while the operating frequency range gets doubled from 0.14 in uncoupled case to 0.28 in coupled case ($\Phi = 1.81$ to 1.95 and $\Phi = 2.075$ to 2.225).
- With introducing the magnetic force, the system dynamics exhibit strong nonlinearities characterized by pitchfork, hopf, and torus bifurcations. For specific magnet spacings (D = 40 – 60 mm), the responses transition from periodic to quasi-periodic and chaotic. Multiple stable attractors indicate broadband harvesting potential.

- The gap distance between the magnets critically controls the dynamic behavior. When D decreases from 60 mm to 45 mm, the system exhibits a significant increase in output voltage amplitude near the principal parametric resonance (at $\Phi = 2.15$). The RMS output voltage reaches to 5.96 V with D = 55 mm which is about 90% higher than the 3.14 V obtained without magnetic coupling.
- Comparative load resistance studies show strong nonlinear dependence. For the magnetically coupled monostable configuration, the maximum RMS voltage and power reaches to 29.06 V and 1.134 mW respectively for D = 45 mm, at load resistances of 1300 kΩ and 590 kΩ. The output power enhances by over 12-fold compared to the without magnet case (0.087 mW at 960 kΩ).
- Reducing the gap distance between the magnets below 40 mm, the static system switches to a bistable state through a pitchfork bifurcation, resulting in two non-trivial equilibrium branches. Within this bistable domain, RMS output voltage of 4.84 V and cab be achieved at $D = 35$ mm and excitation frequency of $\Phi = 2.05$, showing a 54.14% gain in output voltage relative to the without magnet configuration.
- A distinct nonlinear behavior can be observed for higher load resistance, where the harvester oscillates with quasi-periodic and chaotic responses leading to reduction in output voltage and power. This highlights the sensitive interplay between magnetic gap, load resistance, and excitation frequency.
- When both beams are equipped with bimorph MFC patches, at excitation frequency $\Phi = 2.1$ and D = 45 mm, the first and second beam generate RMS voltage of 25.34 V and 10.41 V, respectively; corresponding to voltage enhancements of 574% and 129% over the without magnet case.
- The results conclusively demonstrate that the coupled spring configuration and magnetic interaction of the PEH, not only extends the operational bandwidth but also enhances the harvester output. The optimized magnetic spacing (D = 45 – 55 mm) yield to the best choice for high output voltage, power and dynamic stability.

6.3.3 Magnetically Coupled Double Beam Piezoelectric Energy Harvester under Galloping Excitation

- The galloping instability initiates at a critical wind speed of about 0.7 m/s, enabling self-sustained oscillations at very low wind speeds. The natural frequencies of the two

beams (24.34 rad/s and 26.17 rad/s) are close enough to create an internal resonance condition, which allows strong coupling and effective energy transfer between them.

- The analysis of the magnetic potential energy and force curves show that as the magnet spacing D decreases, the system transitions from monostable to bistable state. At D = 15 – 20 mm, strong nonlinear restoring forces can be observed.
- Performance of the energy harvester is analysed for the different wind speed regions and magnet spacings. In the light air region, at $U_w = 0.8$ m/s the coupled system with D = 15 mm generates output power of 0.023 mW, which is 8.2 times higher than the uncoupled system (0.002 mW). At the wind speed of 2 m/s, the coupled configuration with D = 20 mm can generate 1.05 mW, showing an 8.24% improvement over the uncoupled harvester (0.97 mW).
- In the gentle breeze region, the magnetic coupling enhances the output. At a wind speed of 3.3 m/s, the coupled system with D = 25 mm can harvest 3.79 mW, representing a 10.8% enhancement over the uncoupled output of 3.42 mW. At 4 m/s, the same configuration can achieve a 15% higher power than the uncoupled case. These results clearly indicate that magnetic coupling improves the energy harvester efficiency.
- Time responses, phase portraits, and FFT plots show periodic, quasi-periodic, and chaotic motions at various wind speeds. For example, at $U_w = 1.4$ m/s and D = 20 mm, the harvester exhibits stable periodic oscillations, whereas at 1.5 m/s, the motion transitions into quasi-periodic and chaotic states.
- Experimental investigations of the prototype qualitatively show similar nonlinear dynamic responses to those predicted numerically, validating the reliability of the mathematical and simulation models. However, there is error estimated in between the experimental and theoretical outcomes which may be because of turbulence intensity of the wind tunnel or imperfect bonding between beams and MFC patches.

6.4 Scope for future work

In the present study, initially parametrically excited double cantilever beam based piezoelectric energy harvester is studied theoretically considering spring and magnetic coupling. Then, a magnetically coupled double beam-based energy harvester is investigated numerically and experimentally. There are many possibilities to extend the present work in order to enhance the performance and operability under different excitation environment. Some of them are given below.

- The present work can be extended by performing detailed experimental validation of the spring and magnetically coupled double beam systems under parametric excitation condition. A controlled base excitation setup with precise displacement and voltage measurements would help verify the theoretical and numerical results and identify possible deviations under real vibration conditions.
- Optimization of system parameters using modern computational techniques such as genetic algorithms, particle swarm optimization, or machine learning based approaches can be explored. These methods can help to determine the most effective combination of coupling spring stiffness, gap between the magnets, tip mass, and load resistance for maximum energy harvesting.
- Manufacturing uncertainties such as fabrication tolerances, material property variations, geometric imperfections, assembly processes, all of these can affect and deviate the performance of the energy harvester. Hence, these aspects are very important and need to be considered before real world implication of the energy harvesters.
- The shape, size and orientation of the magnets can be studied to incorporate tri-stable, quad-stable or multi-stable configurations, which may enhance the performance of such PEH systems.
- Different size and shape of the bluff bodies such as triangular, D-shaped can also be investigated. Bio-inspired shapes can be used for designing bluff bodies, which will be a novel research work.
- In real life operating condition of the galloping based PEH system; turbulence, fluctuation of wind speed, and variable direction of wind flow is common. To incorporate these uncertainties, stochastic excitation condition can be adapted.
- Energy harvesters with hybrid excitation combining parametric, direct base excitation, and various aerodynamic instabilities can be developed in future studies. Such systems may take advantage of multiple vibration sources and generate higher output with improved frequency bandwidth suitable for varying environmental conditions.
- The concept of the proposed harvester can be miniaturized for micro electromechanical systems (MEMS) or wearable energy harvesting applications. A compact design with integrated energy storage circuit can power small wireless sensors, health-monitoring devices, and autonomous systems in low-energy environments.

- Future work can also focus on the study of coupled arrays of harvesters. The interaction and synchronization among array elements may produce constructive interference, resulting in higher total output power.
- Long-term durability and fatigue testing can be conducted to assess the mechanical and electrical stability of the harvester under continuous loading cycle. These studies can help to investigate the suitability for field deployment and identify required material or structural improvements.
- Similar type of PEH systems can be utilized for harvesting energy in biomedical applications.

Appendix A

$$\alpha_{i0} = \frac{C_i}{\rho A N_{i1} + m_i + I_{m_i} N_{i5}^2} \qquad \bar{\alpha}_{i0} = \frac{\alpha_{i0}}{\varepsilon \sqrt{\alpha_{11}}}$$

$$\alpha_{i1} = \frac{EI_i N_{i6} - \rho g A N_{i9} - m_i g N_{i4} + N_{i10}}{\rho A N_{i1} + m_i + I_{m_i} N_{i5}^2} \qquad \bar{\alpha}_{i1} = \frac{\alpha_{i1}}{\alpha_{11}}$$

$$\alpha_{i2} = \frac{\rho A_i N_{i3} + m_i N_{i4}^2 + I_{m_i} N_{i5}^4}{\rho A_i N_{i1} + m_i + I_{m_i} N_{i5}^2} \qquad \bar{\alpha}_{i2} = \frac{\alpha_{i2} l_g^2}{\varepsilon}$$

$$\alpha_{i3} = \frac{2EI_i N_{i7}}{\rho A N_{i1} + m_i + I_{m_i} N_{i5}^2} \qquad \bar{\alpha}_{i3} = \frac{\alpha_{i3} l_g^2}{\varepsilon \alpha_{11}}$$

$$\alpha_{i4} = \frac{N_{i11}}{\rho A N_{i1} + m_i + I_{m_i} N_{i5}^2} \qquad \bar{\alpha}_{i4} = \frac{\alpha_{i4}}{\varepsilon \alpha_{11}}$$

$$\alpha_{i5} = \frac{\theta_i}{\rho A N_{i1} + m_i + I_{m_i} N_{i5}^2} \qquad \bar{\alpha}_{i5} = \frac{\alpha_{i5}}{\varepsilon \alpha_{11} l_g}$$

$$f_i = \frac{z_0 \omega^2 \left(\rho A N_{i2} + m_i N_{i4}\right)}{\rho A N_{i1} + m_i + I_{m_i} N_{i5}^2} \qquad r_{11} = \frac{1}{C_P R_L \sqrt{\bar{\alpha}_{11}}}$$

$$\bar{f}_i = \frac{f_i}{\varepsilon \alpha_{11}}$$

Appendix B1

$$\alpha_{10} = \frac{C_1}{\rho A N_{11} + m_1 + I_{m_1} N_{15}^2}$$

$$\alpha_{20} = \frac{C_2}{\rho A N_{21} + m_2 + I_{m_2} N_{25}^2}$$

$$\alpha_{11} = \frac{EI_1 N_{16} - \rho g A N_{18} - m_1 g N_{14} + N_{10}}{\rho A N_{11} + m_1 + I_{m_1} N_{15}^2}$$

$$\alpha_{21} = \frac{EI_2 N_{26} - \rho g A N_{28} - m_2 g N_{24} + N_{20} - \frac{3\mu}{\pi D^5}}{\rho A N_{21} + m_2 + I_{m_2} N_{25}^2}$$

$$\alpha_{12} = \frac{\rho A N_{13} + m_1 N_{14}^2 + I_{m_1} N_{15}^4}{\rho A N_{11} + m_1 + I_{m_1} N_{15}^2}$$

$$\alpha_{22} = \frac{\rho A N_{23} + m_2 N_{24}^2 + I_{m_2} N_{25}^4}{\rho A N_{21} + m_2 + I_{m_2} N_{25}^2}$$

$$\alpha_{13} = \frac{2EI_1 N_{17}}{\rho A N_{11} + m_1 + I_{m_1} N_{15}^2}$$

$$\alpha_{23} = \frac{2EI_2 N_{27} + \frac{45\mu}{4\pi D^7}}{\rho A N_{21} + m_2 + I_{m_2} N_{25}^2}$$

$$\alpha_{14} = \frac{N_{110}}{\rho A N_{11} + m_1 + I_{m_1} N_{15}^2}$$

$$\alpha_{24} = \frac{N_{210}}{\rho A N_{21} + m_2 + I_{m_2} N_{25}^2}$$

$$\alpha_{15} = \frac{\theta_1}{\rho A N_{11} + m_1 + I_{m_1} N_{15}^2}$$

$$f_2 = -\frac{z_0 \omega^2 \left(\rho A N_{22} + m_2 N_{24}\right)}{\rho A N_{21} + m_2 + I_{m_2} N_{25}^2}$$

$$f_1 = -\frac{z_0 \omega^2 \left(\rho A N_{12} + m_1 N_{14}\right)}{\rho A N_{11} + m_1 + I_{m_1} N_{15}^2}$$

$$\theta_1 = \gamma_p \psi'\left(l_1\right)$$

$$r_{11} = \frac{1}{C_p R_l \sqrt{\bar{\alpha}_{11}}}$$

$$N_{i4} = \left(\frac{\pi^2}{8}\right)\frac{1}{l_i}$$

$$N_{i1} = \left(\frac{3\pi - 8}{2\pi}\right) l_i$$

$$N_{i5} = \left(\frac{\pi}{2}\right)\frac{1}{l_i}$$

$$N_{i2} = \left(\frac{\pi^2}{16} - 0.25\right)$$

$$N_{i6} = \left(\frac{\pi^4}{32}\right)\frac{1}{l_i^3}$$

$$N_{i3} = \left(\frac{2\pi^4 - 9\pi^2}{384}\right)\frac{1}{l_i}$$

$$N_{i7} = \left(\frac{\pi^6}{512}\right)\frac{1}{l_i^5}$$

$$N_{i8} = \left(\frac{\pi^2}{16} - 0.25\right) \qquad \bar{\alpha}_{15} = \frac{\alpha_{15}\theta_1}{\varepsilon\alpha_{11}C_p}$$

$$N_{i0} = K\left(1 - \cos\left(\frac{\pi l_K}{2l_i}\right)\right)^2 \qquad \bar{f}_1 = \frac{f_1}{\varepsilon\alpha_{11}}$$

$$N_{110} = N_{210} = K\left(1 - \cos\left(\frac{\pi l_K}{2l_1}\right)\right)\left(1 - \cos\left(\frac{\pi l_K}{2l_2}\right)\right) \qquad \bar{\alpha}_{20} = \frac{\alpha_{20}}{\varepsilon\sqrt{\alpha_{11}}}$$

$$\bar{\alpha}_{10} = \frac{\alpha_{10}}{\varepsilon\sqrt{\alpha_{11}}} \qquad \bar{\alpha}_{21} = \frac{\alpha_{21}}{\alpha_{11}}$$

$$\bar{\alpha}_{11} = \frac{\alpha_{11}}{\alpha_{11}} \qquad \bar{\alpha}_{22} = \frac{l_g^2\alpha_{22}}{\varepsilon}$$

$$\bar{\alpha}_{12} = \frac{l_g^2\alpha_{12}}{\varepsilon} \qquad \bar{\alpha}_{23} = \frac{l_g^2\alpha_{23}}{\varepsilon\alpha_{11}}$$

$$\bar{\alpha}_{13} = \frac{l_g^2\alpha_{13}}{\varepsilon\alpha_{11}} \qquad \bar{\alpha}_{24} = \frac{\alpha_{24}}{\varepsilon\alpha_{11}}$$

$$\bar{\alpha}_{14} = \frac{\alpha_{14}}{\varepsilon\alpha_{11}} \qquad \bar{f}_2 = \frac{f_2}{\varepsilon\alpha_{11}}$$

Here, $i = 1, 2$ denotes the 1st and 2nd beam, respectively.

Appendix B2

$$j_{11} = \frac{\partial p_1'}{\partial p_1} = -\frac{\bar{\alpha}_{10}}{2} - \left(2\sqrt{\bar{\alpha}_{11}}\bar{\alpha}_{12} - \frac{3\bar{\alpha}_{13}}{\sqrt{\bar{\alpha}_{11}}}\right)\left(\frac{p_1 q_1}{4}\right) - \frac{\bar{\alpha}_{15} r_{11}}{2\left(\bar{\alpha}_{11} + r_{11}^2\right)} - \frac{\bar{\alpha}_{16}}{4\sqrt{\bar{\alpha}_{11}}}$$

$$j_{12} = \frac{\partial p_1'}{\partial q_1} = -\frac{\sigma_1}{2} - \left(2\sqrt{\bar{\alpha}_{11}}\bar{\alpha}_{12} - \frac{3\bar{\alpha}_{13}}{\sqrt{\bar{\alpha}_{11}}}\right)\left(\frac{p_1^2 + 3q_1^2}{8}\right) + \frac{\bar{\alpha}_{15}\sqrt{\bar{\alpha}_{11}}}{2\left(\bar{\alpha}_{11} + r_{11}^2\right)}$$

$$j_{13} = \frac{\partial p_1'}{\partial p_2} = 0$$

$$j_{13} = \frac{\partial p_1'}{\partial q_2} = -\frac{\bar{\alpha}_{14}}{2\sqrt{\bar{\alpha}_{11}}}$$

$$j_{21} = \frac{\partial q_1'}{\partial p_1} = \frac{\sigma_1}{2} + \left(2\sqrt{\bar{\alpha}_{11}}\bar{\alpha}_{12} - \frac{3\bar{\alpha}_{13}}{\sqrt{\bar{\alpha}_{11}}}\right)\left(\frac{3p_1^2 + q_1^2}{8}\right) - \frac{\bar{\alpha}_{15}\sqrt{\bar{\alpha}_{11}}}{2\left(\bar{\alpha}_{11} + r_{11}^2\right)}$$

$$j_{22} = \frac{\partial q_1'}{\partial q_1} = -\frac{\bar{\alpha}_{10}}{2} + \left(2\sqrt{\bar{\alpha}_{11}}\bar{\alpha}_{12} - \frac{3\bar{\alpha}_{13}}{\sqrt{\bar{\alpha}_{11}}}\right)\left(\frac{p_1 q_1}{4}\right) - \frac{\bar{\alpha}_{15} r_{11}}{2\left(\bar{\alpha}_{11} + r_{11}^2\right)} + \frac{\bar{\alpha}_{16}}{4\sqrt{\bar{\alpha}_{11}}}$$

$$j_{23} = \frac{\partial q_1'}{\partial p_2} = \frac{\bar{\alpha}_{14}}{2\sqrt{\bar{\alpha}_{11}}}$$

$$j_{24} = \frac{\partial q_1'}{\partial q_2} = 0$$

$$j_{31} = \frac{\partial p_2'}{\partial p_1} = 0$$

$$j_{32} = \frac{\partial p_2'}{\partial q_2} = -\frac{\bar{\alpha}_{24}}{2\sqrt{\bar{\alpha}_{21}}}$$

$$j_{33} = \frac{\partial p_2'}{\partial p_2} = -\frac{\bar{\alpha}_{20}}{2} - \left(2\sqrt{\bar{\alpha}_{21}}\bar{\alpha}_{22} - \frac{3\bar{\alpha}_{23}}{\sqrt{\bar{\alpha}_{21}}}\right)\left(\frac{p_2 q_2}{4}\right) - \frac{\bar{\alpha}_{26}}{4\sqrt{\bar{\alpha}_{21}}}$$

$$j_{34} = \frac{\partial p_2'}{\partial q_2} = -\left(\frac{\sigma_1}{2} + \sigma_2\right) - \left(2\sqrt{\bar{\alpha}_{21}}\bar{\alpha}_{22} - \frac{3\bar{\alpha}_{23}}{\sqrt{\bar{\alpha}_{21}}}\right)\left(\frac{p_2^2 + 3q_2^2}{8}\right)$$

$$j_{41} = \frac{\partial q_2'}{\partial p_1} = \frac{\bar{\alpha}_{24}}{2\sqrt{\bar{\alpha}_{21}}}$$

$$j_{42} = \frac{\partial q_2'}{\partial q_1} = 0$$

$$j_{43} = \frac{\partial q_2'}{\partial p_2} = -\left(\frac{\sigma_1}{2} + \sigma_2\right) + \left(2\sqrt{\bar{\alpha}_{21}}\bar{\alpha}_{22} - \frac{3\bar{\alpha}_{23}}{\sqrt{\bar{\alpha}_{21}}}\right)\left(\frac{3p_2^2 + q_2^2}{8}\right)$$

$$j_{44} = \frac{\partial q_2'}{\partial q_2} = -\frac{\bar{\alpha}_{20}}{2} - \left(2\sqrt{\bar{\alpha}_{21}}\bar{\alpha}_{22} - \frac{3\bar{\alpha}_{23}}{\sqrt{\bar{\alpha}_{21}}}\right)\left(\frac{p_2 q_2}{4}\right) + \frac{\bar{\alpha}_{26}}{4\sqrt{\bar{\alpha}_{21}}}$$

Appendix C

$$\alpha_{11}=\frac{C_1}{\rho A_1 N_{11}+m_{bb1}N_{12}+m_{m1}N_{13}} \qquad \alpha_{21}=\frac{C_2}{\rho A_2 N_{21}+m_{bb2}N_{22}+m_{m2}N_{23}}$$

$$\alpha_{12}=\frac{EI_1 N_{14}}{\rho A_1 N_{11}+m_{bb1}N_{12}+m_{m1}N_{13}} \qquad \alpha_{22}=\frac{EI_2 N_{24}-\rho AgN_{25}-m_{bb2}gN_{26}-m_{m2}gN_{27}}{\rho AN_{21}+m_{bb2}N_{22}+m_{m2}N_{23}}$$

$$\alpha_{12}=\frac{\rho A_1 N_{15}+m_{bb1}N_{16}+m_{m1}N_{17}}{\rho A_1 N_{11}+m_{bb1}N_{12}+m_{m1}N_{13}} \qquad \alpha_{23}=\frac{\rho A_2 N_{28}+m_{bb2}N_{29}+m_{m2}N_{210}}{\rho A_2 N_{21}+m_{bb2}N_{22}+m_{m2}N_{23}}$$

$$\alpha_{14}=\frac{2EI_1 N_{18}}{\rho A_1 N_{11}+m_{bb1}N_{12}+m_{m1}N_{13}} \qquad \alpha_{24}=\frac{2EI_2 N_{211}+\frac{1}{3}m_{bb2}g\frac{l_{bb2}}{2}N_{212}^4+\frac{1}{3}m_{m2}l_{bb2}N_{212}^4}{\rho A_2 N_{21}+m_{bb2}N_{22}+m_{m2}N_{23}}$$

$$N_{11}=\left(\frac{3\pi-8}{2\pi}\right)l_1 \qquad N_{21}=\left(\frac{3\pi-8}{2\pi}\right)l_2$$

$$N_{12}=1+\frac{\pi}{2l_1}b_{bb1}+\frac{5b_{bb1}^2}{12}\left(\frac{\pi}{2l_1}\right)^2 \qquad N_{22}=1+l_{bb2}\frac{\pi}{2l_2}+\frac{l_{bb2}^2}{4}\left(\frac{\pi}{2l_2}\right)^2+\frac{b_{bb2}^2+7l_{bb2}^2}{12}\left(\frac{\pi}{2l_2}\right)^2$$

$$N_{13}=1+b_{bb1}\frac{\pi}{2l_1}+\frac{3b_{bb1}^2}{8}\left(\frac{\pi}{2l_1}\right)^2 \qquad N_{23}=1+2l_{bb2}\frac{\pi}{2l_2}+2l_{bb2}^2\left(\frac{\pi}{2l_2}\right)^2$$

$$N_{14}=\frac{\pi^4}{32l_1^3} \qquad N_{24}=\frac{\pi^4}{32l_2^3}$$

$$N_{15}=\left\{\frac{\pi^2\left(2\pi^2-9\right)}{384}\right\}\frac{1}{l_1} \qquad N_{25}=\left(-\frac{1}{4}+\frac{\pi^2}{16}\right)$$

$$N_{16}=\frac{\pi^4}{64l_1^2}+\frac{5b_{bb1}^2}{12}\left(\frac{\pi}{2l_1}\right)^4 \qquad N_{26}=\frac{\pi^2}{8l_2}+\frac{l_{bb2}}{2}\left(\frac{\pi}{2l_2}\right)^2$$

$$N_{17} = \frac{\pi^4}{64 l_1^2} + \frac{b_{bb1}^2}{4}\left(\frac{\pi}{2l_1}\right)^4$$

$$N_{18} = \frac{\pi^6}{512 l_1^5}$$

$$N_{27} = \frac{\pi^2}{8 l_2} + l_{bb2}\left(\frac{\pi}{2l_2}\right)^2$$

$$N_{28} = \left\{\frac{\pi^2\left(2\pi^2 - 9\right)}{384}\right\}\frac{1}{l_2}$$

Bibliography

1. Meindl, J. D. (2002). Low power microelectronics: Retrospect and prospect. *Proceedings of the IEEE*, *83*(4), 619-635.
2. Priya, S., & Inman, D. J. (Eds.). (2009). *Energy harvesting technologies* (Vol. 21, p. 2). New York: Springer.
3. Mallick, D., Constantinou, P., Podder, P., & Roy, S. (2017). Multi-frequency MEMS electromagnetic energy harvesting. *Sensors and Actuators A: Physical*, *264*, 247-259.
4. Khan, F. U., & Qadir, M. U. (2016). State-of-the-art in vibration-based electrostatic energy harvesting. *Journal of Micromechanics and Microengineering*, *26*(10), 103001.
5. Ferrari, M., Ferrari, V., Guizzetti, M., Marioli, D., & Taroni, A. (2008). Piezoelectric multifrequency energy converter for power harvesting in autonomous microsystems. *Sensors and Actuators A: Physical*, *142*(1), 329-335.
6. Sunil, M., Jelmy, E. J., Vijoy, K. V., Saji, K. J., & John, H. (2023). Triboelectric smart shoes for real time position detection. *Sensors and Actuators A: Physical*, *363*, 114730.
7. Ahmad, M. M., & Khan, F. U. (2021). Review of vibration-based electromagnetic–piezoelectric hybrid energy harvesters. *International Journal of Energy Research*, *45*(4), 5058-5097.
8. Hamid, R., & Yuce, M. R. (2017). A wearable energy harvester unit using piezoelectric–electromagnetic hybrid technique. *Sensors and Actuators A: Physical*, *257*, 198-207.
9. Sharma, S. K., Kumar, S., & Kumar, R. (2023). Parametric analysis of hybrid tribo-piezoelectric energy harvester. *Mechanics Based Design of Structures and Machines*, *51*(11), 6360-6373.
10. Priya, S. (2007). Advances in energy harvesting using low profile piezoelectric transducers. *Journal of electroceramics*, *19*, 167-184.
11. Daqaq, M. F., Masana, R., Erturk, A., & Dane Quinn, D. (2014). On the role of nonlinearities in vibratory energy harvesting: a critical review and discussion. *Applied mechanics reviews*, *66*(4), 040801.
12. Thomsen, J. J., Thomsen, J. J., & Thomsen, J. J. (2003). *Vibrations and stability* (Vol. 2). Berlin: Springer-Verlag.

13. Kar, R. C., & Dwivedy, S. K. (1999). Non-linear dynamics of a slender beam carrying a lumped mass with principal parametric and internal resonances. *International journal of non-linear mechanics*, *34*(3), 515-529.
14. Nayfeh, A. H., & Mook, D. T. (2024). *Nonlinear oscillations*. John Wiley & Sons.
15. Erturk, A., & Inman, D. J. (2009). An experimentally validated bimorph cantilever model for piezoelectric energy harvesting from base excitations. *Smart materials and structures*, *18*(2), 025009.
16. Wagg, D., & Virgin, L. (Eds.). (2012). *Exploiting nonlinear behavior in structural dynamics* (Vol. 536). Springer Science & Business Media.
17. Garg, A., & Dwivedy, S. K. (2020). Piezoelectric energy harvester under parametric excitation: a theoretical and experimental investigation. *Journal of Intelligent Material Systems and Structures*, *31*(4), 612-631.
18. Lumentut, M. F., & Howard, I. M. (2014). Electromechanical finite element modelling for dynamic analysis of a cantilevered piezoelectric energy harvester with tip mass offset under base excitations. *Smart Materials and Structures*, *23*(9), 095037.
19. Xia, G., Fang, F., Zhang, M., Wang, Q., & Wang, J. (2019). Performance analysis of parametrically and directly excited nonlinear piezoelectric energy harvester. *Archive of Applied Mechanics*, *89*, 2147-2166.
20. Abdelkefi, A., Yan, Z., & Hajj, M. R. (2013). Nonlinear dynamics of galloping-based piezoaeroelastic energy harvesters. *The European Physical Journal Special Topics*, *222*(7), 1483-1501.
21. Shan, X., Li, H., Yang, Y., Feng, J., Wang, Y., & Xie, T. (2019). Enhancing the performance of an underwater piezoelectric energy harvester based on flow-induced vibration. *Energy*, *172*, 134-140.
22. Hu, Y., Yang, B., Chen, X., Wang, X., & Liu, J. (2018). Modeling and experimental study of a piezoelectric energy harvester from vortex shedding-induced vibration. *Energy conversion and management*, *162*, 145-158.
23. Dai, H. L., Abdelkefi, A., & Wang, L. (2014). Piezoelectric energy harvesting from concurrent vortex-induced vibrations and base excitations. *Nonlinear Dynamics*, *77*, 967-981.
24. Bibo, A., & Daqaq, M. F. (2013). Energy harvesting under combined aerodynamic and base excitations. *Journal of sound and vibration*, *332*(20), 5086-5102.

25. Shan, X., Tian, H., Cao, H., & Xie, T. (2020). Enhancing performance of a piezoelectric energy harvester system for concurrent flutter and vortex-induced vibration. *Energies*, *13*(12), 3101.
26. Erturk, A., Hoffmann, J., & Inman, D. J. (2009). A piezomagnetoelastic structure for broadband vibration energy harvesting. *Applied Physics Letters*, *94*(25).
27. Abdelkefi, A., Nayfeh, A. H., & Hajj, M. R. (2012). Global nonlinear distributed-parameter model of parametrically excited piezoelectric energy harvesters. *Nonlinear Dynamics*, *67*, 1147-1160.
28. Adoukatl, C., Ntamack, G. E., & Azrar, L. (2023). High order analysis of a nonlinear piezoelectric energy harvesting of a piezo patched cantilever beam under parametric and direct excitations. *Mechanics of Advanced Materials and Structures*, *30*(23), 4835-4861.
29. Xia, G., Fang, F., Zhang, M., Wang, Q., & Wang, J. (2019). Performance analysis of parametrically and directly excited nonlinear piezoelectric energy harvester. *Archive of Applied Mechanics*, *89*, 2147-2166.
30. Chen, K., Zhang, X., Xiang, X., Shen, H., Yang, Q., Wang, J., & Litak, G. (2023). High performance piezoelectric energy harvester with dual-coupling beams and bistable configurations. *Journal of Sound and Vibration*, *561*, 117822.
31. Eshtehardiha, R., Tikani, R., & Ziaei-Rad, S. (2021). Experimental and numerical investigation of energy harvesting from double cantilever beams with internal resonance. *Journal of Sound and Vibration*, *500*, 116022.
32. Wang, J., Geng, L., Yang, K., Zhao, L., Wang, F., & Yurchenko, D. (2020). Dynamics of the double-beam piezo–magneto–elastic nonlinear wind energy harvester exhibiting galloping-based vibration. *Nonlinear Dynamics*, *100*, 1963-1983.
33. Kim, P., Nguyen, M. S., Kwon, O., Kim, Y. J., & Yoon, Y. J. (2016). Phase-dependent dynamic potential of magnetically coupled two-degree-of-freedom bistable energy harvester. *Scientific reports*, *6*(1), 34411.
34. Moheimani, S. R., & Fleming, A. J. (2006). *Piezoelectric transducers for vibration control and damping*. Springer Science & Business Media.
35. Bhalla, S., Moharana, S., Talakokula, V., & Kaur, N. (2017). Piezoelectric materials: applications in SHM, energy harvesting and biomechanics.
36. Meeker, T. R. (1996). Publication and proposed revision of ANSI/IEEE standard 176-1987 ANSI/IEEE Standard on piezoelectricity. *IEEE Transactions on Ultrasonics Ferroelectrics and Frequency Control*, *43*(5), 717-772.
37. Ikeda, T. (1996). *Fundamentals of piezoelectricity*. Oxford university press.

38. Ramsay, M. J., & Clark, W. W. (2001, June). Piezoelectric energy harvesting for bio-MEMS applications. In *Smart structures and materials 2001: industrial and commercial applications of smart structures technologies* (Vol. 4332, pp. 429-438). SPIE.
39. Roundy, S., & Wright, P. K. (2004). A piezoelectric vibration based generator for wireless electronics. *Smart Materials and structures*, *13*(5), 1131.
40. Jeon, Y. B., Sood, R., Jeong, J. H., & Kim, S. G. (2005). MEMS power generator with transverse mode thin film PZT. *Sensors and Actuators A: Physical*, *122*(1), 16-22.
41. Dong, B., & Li, Z. (2005). Cement-based piezoelectric ceramic smart composites. *Composites Science and Technology*, *65*(9), 1363-1371.
42. Swallow, L. M., Luo, J. K., Siores, E., Patel, I., & Dodds, D. (2008). A piezoelectric fibre composite based energy harvesting device for potential wearable applications. *Smart Materials and Structures*, *17*(2), 025017.
43. Massaro, A., De Guido, S., Ingrosso, I., Cingolani, R., De Vittorio, M., Cori, M., ... & Passaseo, A. (2011). Freestanding piezoelectric rings for high efficiency energy harvesting at low frequency. *Applied physics letters*, *98*(5),
44. Hwang, G. T., Byun, M., Jeong, C. K., & Lee, K. J. (2015). Flexible piezoelectric thin-film energy harvesters and nanosensors for biomedical applications. *Advanced healthcare materials*, *4*(5), 646-658.
45. Soh, C. K., Tseng, K. K., Bhalla, S., & Gupta, A. (2000). Performance of smart piezoceramic patches in health monitoring of a RC bridge. *Smart materials and Structures*, *9*(4), 533.
46. Yao, S., Peralta-Braz, P., Alamdari, M. M., Ruiz, R. O., & Atroshchenko, E. (2024). Optimal design of piezoelectric energy harvesters for bridge infrastructure: Effects of location and traffic intensity on energy production. *Applied Energy*, *355*, 122285.
47. Annamdas, V. G. M., Bhalla, S., & Soh, C. K. (2017). Applications of structural health monitoring technology in Asia. *Structural Health Monitoring*, *16*(3), 324-346.
48. Yang, Z., Zhou, S., Zu, J., & Inman, D. (2018). High-performance piezoelectric energy harvesters and their applications. *Joule*, *2*(4), 642-697.
49. Zelenika, S., Hadas, Z., Bader, S., Becker, T., Gljušćić, P., Hlinka, J., Janak, L., Kamenar, E., Ksica, F., Kyratsi, T., Louca, L., Mrlik, M., Osmanović, A., Pakrashi, V., Rubes, O., Ševeček, O., Silva, J. P. B., Tofel, P., Trkulja, B., ... Vrcan, Ž. (2020). Energy Harvesting Technologies for Structural Health Monitoring of Airplane Components - A Review. *Sensors*, *20*(22), 6685.

50. Xu, T. B. (2016). Energy harvesting using piezoelectric materials in aerospace structures. In *Structural health monitoring (SHM) in aerospace structures* (pp. 175-212). Woodhead Publishing.
51. Shan, G., Wang, D., Chew, Z. J., & Zhu, M. (2023). A high-power, robust piezoelectric energy harvester for wireless sensor networks in railway applications. *Sensors and Actuators A: Physical*, *360*, 114525.
52. Qu, S., Ren, Y., Hu, G., Ding, W., Dong, L., Yang, J., ... & Zhai, W. (2024). Event-driven piezoelectric energy harvesting for railway field applications. *Applied Energy*, *364*, 123160.
53. Bowen, C. R., & Arafa, M. H. (2015). Energy harvesting technologies for tire pressure monitoring systems. *Advanced Energy Materials*, *5*(7), 1401787.
54. Zhang, L., Zhang, F., Qin, Z., Han, Q., Wang, T., & Chu, F. (2022). Piezoelectric energy harvester for rolling bearings with capability of self-powered condition monitoring. *Energy*, *238*, 121770.
55. Lynch, J. P., & Loh, K. J. (2006). A summary review of wireless sensors and sensor networks for structural health monitoring. *Shock and vibration digest*, *38*(2), 91-130.
56. Kong, N., & Ha, D. S. (2011). Low-power design of a self-powered piezoelectric energy harvesting system with maximum power point tracking. *IEEE Transactions on power electronics*, *27*(5), 2298-2308.
57. Ali, A., Iqbal, S., & Chen, X. (2024). Recent advances in piezoelectric wearable energy harvesting based on human motion: Materials, design, and applications. *Energy Strategy Reviews*, *53*, 101422.
58. Sun, C., Shang, G., & Wang, H. (2019). On piezoelectric energy harvesting from human motion. *Journal of Power and Energy Engineering*, *7*(1), 155-164.
59. Ali, A., Shaukat, H., Bibi, S., Altabey, W. A., Noori, M., & Kouritem, S. A. (2023). Recent progress in energy harvesting systems for wearable technology. *Energy Strategy Reviews*, *49*, 101124.
60. Bai, Y., Tofel, P., Hadas, Z., Smilek, J., Losak, P., Skarvada, P., & Macku, R. (2018). Investigation of a cantilever structured piezoelectric energy harvester used for wearable devices with random vibration input. *Mechanical Systems and Signal Processing*, *106*, 303-318.
61. Almarri, N., Chang, J., Song, W., Jiang, D., & Demosthenous, A. (2024). Piezoelectric energy harvesting and ultra-low-power management circuits for medical devices. *Nano Energy*, 110196.

62. Panda, S., Hajra, S., Mistewicz, K., In-na, P., Sahu, M., Rajaitha, P. M., & Kim, H. J. (2022). Piezoelectric energy harvesting systems for biomedical applications. *Nano energy*, *100*, 107514.
63. Haq, M. (2018). Application of piezo transducers in biomedical science for health monitoring and energy harvesting problems. *Materials Research Express*, *6*(2), 022002.
64. Kumar, A., Kiran, R., Chauhan, V. S., Kumar, R., & Vaish, R. (2018). Piezoelectric energy harvester for pacemaker application: a comparative study. *Materials Research Express*, *5*(7), 075701.
65. Zhang, T., Liang, H., Wang, Z., Qiu, C., Peng, Y. B., Zhu, X., ... & Zhu, B. (2022). Piezoelectric ultrasound energy–harvesting device for deep brain stimulation and analgesia applications. *Science Advances*, *8*(15).
66. Zhang, X., Jin, A., Li, S., Wang, X., Ma, X., & Yang, G. (2025). Design and optimization of a piezoelectric-electromagnetic hybrid energy harvester for sustainable smart agriculture systems. *Smart Materials and Structures*, 34, 065024.
67. Khernane, S., Bouam, S., & Arar, C. (2024). Renewable energy harvesting for wireless sensor networks in precision agriculture. *International Journal of Networked and Distributed Computing*, *12*(1), 8-16.
68. Zheng, X., Han, L., Yang, J., Li, Q., & He, L. (2024). Piezoelectric breeze energy harvester with mechanical intelligence mechanism for smart agricultural monitoring systems. *Smart Materials and Structures*, *33*(6), 065027.
69. Sathasivam, K., Garip, I., Sharif, H., Abbas, J. K., Hussein, A. A., Khaleel, S. K., & Rasol, M. A. (2023). Developing a Piezoelectric Generator for Military Equipment–A Feasibility Study. *Electric Power Components and Systems*, *51*(17), 1859-1877.
70. Othman, A. (2017, May). Modeling of piezoelectric energy harvesting system embedded in soldier's boot using Matlab/Simulink. In *2017 International Conference on Military Technologies (ICMT)* (pp. 787-792). IEEE.
71. Rastegar, J., Pereira, C., Ervin, M., & Feng, D. (2014, April). Piezoelectric-based electrical energy harvesting and storage methods and electronics for munitions. In *Industrial and Commercial Applications of Smart Structures Technologies 2014* (Vol. 9059, pp. 62-67). SPIE.
72. Anton, S. R., & Inman, D. J. (2008). Vibration energy harvesting for unmanned aerial vehicles. In *Active and passive smart structures and integrated systems 2008* (Vol. 6928, pp. 621-632). SPIE.
73. Erturk, A., & Inman, D. J. (2011). *Piezoelectric energy harvesting*. John Wiley & Sons.

74. Erturk, A., & Inman, D. J. (2008). On mechanical modeling of cantilevered piezoelectric vibration energy harvesters. *Journal of intelligent material systems and structures*, *19*(11), 1311-1325.
75. Erturk, A., & Inman, D. J. (2009). Electromechanical modeling of cantilevered piezoelectric energy harvesters for persistent base motions. In *Energy Harvesting Technologies* (pp. 41-77). Boston, MA: Springer US.
76. Roundy, S., Wright, P. K., & Rabaey, J. (2003). A study of low level vibrations as a power source for wireless sensor nodes. *Computer communications*, *26*(11), 1131-1144.
77. Friswell, M. I., Ali, S. F., Bilgen, O., Adhikari, S., Lees, A. W., & Litak, G. (2012). Non-linear piezoelectric vibration energy harvesting from a vertical cantilever beam with tip mass. *Journal of Intelligent Material Systems and Structures*, *23*(13), 1505-1521.
78. Karličić, D., Chatterjee, T., Cajić, M., & Adhikari, S. (2020). Parametrically amplified Mathieu-Duffing nonlinear energy harvesters. *Journal of Sound and Vibration*, *488*, 115677.
79. Dwivedy, S. K., & Kar, R. C. (2003). Simultaneous combination and 1: 3: 5 internal resonances in a parametrically excited beam–mass system. *International journal of non-linear mechanics*, *38*(4), 585-596.
80. Dwivedy, S. K., & Kar, R. C. (2001). Non-linear dynamics of a slender beam carrying a lumped mass under principal parametric resonance with three-mode interactions. *International journal of non-linear mechanics*, *36*(6), 927-945.
81. Garg, A., & Dwivedy, S. K. (2020). Dynamic analysis of piezoelectric energy harvester under combination parametric and internal resonance: a theoretical and experimental study. *Nonlinear Dynamics*, *101*(4), 2107-2129.
82. Xia, G., Fang, F., Zhang, M., Wang, Q., & Wang, J. (2019). Performance analysis of parametrically and directly excited nonlinear piezoelectric energy harvester. *Archive of Applied Mechanics*, *89*, 2147-2166.
83. Fossen, T., & Nijmeijer, H. (Eds.). (2011). *Parametric resonance in dynamical systems*. Springer Science & Business Media.
84. Rhoads, J. F., Miller, N. J., Shaw, S. W., & Feeny, B. F. (2008). Mechanical domain parametric amplification.
85. Sharma, M., Sarraf, E. H., Baskaran, R., & Cretu, E. (2012). Parametric resonance: Amplification and damping in MEMS gyroscopes. *Sensors and Actuators A: Physical*, *177*, 79-86.

86. Zhou, L., & Chen, F. (2020). Chaotic motion of the parametrically excited roll motion for a class of ships in regular longitudinal waves. *Ocean Engineering*, *195*, 106729.
87. Wu, T. X. (2008). Parametric excitation of wheel/track system and its effects on rail corrugation. *Wear*, *265*(9-10), 1176-1182.
88. Nordborg, A. (2002). Wheel/rail noise generation due to nonlinear effects and parametric excitation. *The Journal of the Acoustical Society of America*, *111*(4), 1772-1781.
89. Liang, F., Gao, A., Li, X. F., & Zhu, W. D. (2021). Nonlinear parametric vibration of spinning pipes conveying fluid with varying spinning speed and flow velocity. *Applied Mathematical Modelling*, *95*, 320-338.
90. Daqaq, M. F., Stabler, C., Qaroush, Y., & Seuaciuc-Osório, T. (2009). Investigation of power harvesting via parametric excitations. *Journal of Intelligent Material Systems and Structures*, *20*(5), 545-557.
91. Alevras, P., Theodossiades, S., & Rahnejat, H. (2017). Broadband energy harvesting from parametric vibrations of a class of nonlinear Mathieu systems. *Applied Physics Letters*, *110*(23).
92. Scapolan, M., Tehrani, M. G., & Bonisoli, E. (2016). Energy harvesting using parametric resonant system due to time-varying damping. *Mechanical Systems and Signal Processing*, *79*, 149-165.
93. Yildirim, T., Zhang, J., Sun, S., Alici, G., Zhang, S., & Li, W. (2017). Design of an enhanced wideband energy harvester using a parametrically excited array. *Journal of Sound and Vibration*, *410*, 416-428.
94. Jia, Y., & Seshia, A. A. (2014). An auto-parametrically excited vibration energy harvester. *Sensors and Actuators A: Physical*, *220*, 69-75.
95. Yan, Z., & Hajj, M. R. (2017). Nonlinear performances of an autoparametric vibration-based piezoelastic energy harvester. *Journal of Intelligent Material Systems and Structures*, *28*(2), 254-271.
96. Kecik, K., & Borowiec, M. (2013). An autoparametric energy harvester. *The European Physical Journal Special Topics*, *222*(7), 1597-1605.
97. Tan, T., Wang, Z., Zhang, L., Liao, W. H., & Yan, Z. (2021). Piezoelectric autoparametric vibration energy harvesting with chaos control feature. *Mechanical Systems and Signal Processing*, *161*, 107989.
98. Bobryk, R. V., & Yurchenko, D. (2016). On enhancement of vibration-based energy harvesting by a random parametric excitation. *Journal of Sound and Vibration*, *366*, 407-417.

99. Ramakrishnan, S., & Edlund, C. (2020). Stochastic stability of a piezoelectric vibration energy harvester under a parametric excitation and noise-induced stabilization. *Mechanical Systems and Signal Processing*, *140*, 106566.
100. Li, H., Qin, W., & Deng, W. (2018). Coherence resonance of a magnet-induced buckled piezoelectric energy harvester under stochastic parametric excitation. *Journal of Intelligent Material Systems and Structures*, *29*(8), 1620-1631.
101. Fan, Y., Deng, L., Zhang, Y., Niu, M. Q., & Chen, L. Q. (2024). A robust parametrically excited piezoelectric energy harvester with resonant attachment. *Journal of Sound and Vibration*, *585*, 118441.
102. Daqaq, M. F. (2010). Response of uni-modal duffing-type harvesters to random forced excitations. *Journal of sound and Vibration*, *329*(18), 3621-3631.
103. Adhikari, S., Friswell, M. A., & Inman, D. J. (2009). Piezoelectric energy harvesting from broadband random vibrations. *Smart materials and structures*, *18*(11), 115005.
104. De Paula, A. S., Inman, D. J., & Savi, M. A. (2015). Energy harvesting in a nonlinear piezomagnetoelastic beam subjected to random excitation. *Mechanical Systems and Signal Processing*, *54*, 405-416.
105. Ali, S. F., Adhikari, S., Friswell, M. I., & Narayanan, S. (2011). The analysis of piezomagnetoelastic energy harvesters under broadband random excitations. *Journal of Applied Physics*, *109*(7).
106. Khovanova, N. A., & Khovanov, I. A. (2011). The role of excitations statistic and nonlinearity in energy harvesting from random impulsive excitations. *Applied Physics Letters*, *99*(14).
107. Litak, G., Friswell, M. I., & Adhikari, S. (2010). Magnetopiezoelastic energy harvesting driven by random excitations. *Applied Physics Letters*, *96*(21).
108. Kumar, P., Narayanan, S., Adhikari, S., & Friswell, M. I. (2014). Fokker–Planck equation analysis of randomly excited nonlinear energy harvester. *Journal of Sound and Vibration*, *333*(7), 2040-2053.
109. Lan, C., Qin, W., & Deng, W. (2015). Energy harvesting by dynamic unstability and internal resonance for piezoelectric beam. *Applied Physics Letters*, *107*(9).
110. Li, P., Gao, S., & Cai, H. (2015). Modeling and analysis of hybrid piezoelectric and electromagnetic energy harvesting from random vibrations. *Microsystem Technologies*, *21*, 401-414.

111. Cottone, F., Gammaitoni, L., Vocca, H., Ferrari, M., & Ferrari, V. (2012). Piezoelectric buckled beams for random vibration energy harvesting. *Smart materials and structures*, *21*(3), 035021.
112. Ding, W. J. (2009). Self-excited vibration. *Tsing-Hua University Press: Beijing, China*.
113. Hartog, D., Pieter, J. (1985). *Mechanical vibrations*. Courier Corporation.
114. Novak, M. (1972). Galloping oscillations of prismatic structures. *Journal of the Engineering Mechanics Division*, *98*(1), 27-46.
115. Nayfeh, A. H., & Abdel-Rohman, M. (1991). Analysis of galloping responses in cantilever beams. *Journal of sound and vibration*, *144*(1), 87-93.
116. Alonso, G., Valero, E., & Meseguer, J. (2009). An analysis on the dependence on cross section geometry of galloping stability of two-dimensional bodies having either biconvex or rhomboidal cross sections. *European Journal of Mechanics-B/Fluids*, *28*(2), 328-334.
117. Mukhopadhyay, V., & Dugundji, J. (1976). Wind excited vibration of a square section cantilever beam in smooth flow. *Journal of Sound and Vibration*, *45*(3), 329-339.
118. Ewere, F., & Wang, G. (2014). Performance of galloping piezoelectric energy harvesters. *Journal of Intelligent Material Systems and Structures*, *25*(14), 1693-1704.
119. Zhao, L., & Yang, Y. (2015). Analytical solutions for galloping-based piezoelectric energy harvesters with various interfacing circuits. *Smart Materials and Structures*, *24*(7), 075023.
120. Zhao, L., Tang, L., & Yang, Y. (2012, September). Small wind energy harvesting from galloping using piezoelectric materials. In *Smart materials, adaptive structures and intelligent systems* (Vol. 45103, pp. 919-927). American Society of Mechanical Engineers.
121. Abdelkefi, A., Yan, Z., & Hajj, M. R. (2014). Performance analysis of galloping-based piezoaeroelastic energy harvesters with different cross-section geometries. *Journal of Intelligent Material Systems and Structures*, *25*(2), 246-256.
122. Barrero-Gil, A., Alonso, G., & Sanz-Andres, A. (2010). Energy harvesting from transverse galloping. *Journal of Sound and Vibration*, *329*(14), 2873-2883.
123. Sirohi, J., & Mahadik, R. (2011). Piezoelectric wind energy harvester for low-power sensors. *Journal of Intelligent Material Systems and Structures*, *22*(18), 2215-2228.
124. Truitt, A., & Mahmoodi, S. N. (2013). A review on active wind energy harvesting designs. *International Journal of Precision Engineering and Manufacturing*, *14*, 1667-1675.

125. Ewere, F., Wang, G., & Frendi, K. (2015). Galloping Piezoelectric Energy Harvester with Bio-inspired Square Bluff Body. In *23rd AIAA/AHS Adaptive Structures Conference* (p. 1257).

126. Roohi, R., Akbari, M., Karimzadeh, A., & Amiri, M. J. (2023). Investigating the Effect of an Elliptical Bluff Body on the Behavior of a Galloping Piezoelectric Energy Harvester. *Sustainability*, *15*(22), 15773.

127. Dash, R. C., Maiti, D. K., & Singh, B. N. (2020). Dynamic stability and performance analysis of a galloping-based piezoelectric energy harvester for different order representations of the aerodynamic force. *International Journal of Non-Linear Mechanics*, *121*, 103463.

128. Ibarra, D., F. Sorribes, G. Alonso, and J. Meseguer. "Transverse galloping of two-dimensional bodies having a rhombic cross-section." *Journal of Sound and Vibration* 333, no. 13 (2014): 2855-2865.

129. Javed, U., & Abdelkefi, A. (2017). Impacts of the aerodynamic force representation on the stability and performance of a galloping-based energy harvester. *Journal of Sound and Vibration*, *400*, 213-226.

130. Bibo, A., Alhadidi, A. H., & Daqaq, M. F. (2015). Exploiting a nonlinear restoring force to improve the performance of flow energy harvesters. *Journal of applied Physics*, *117*(4).

131. Yan, Z., & Abdelkefi, A. (2014). Nonlinear characterization of concurrent energy harvesting from galloping and base excitations. *Nonlinear Dynamics*, *77*(4), 1171-1189.

132. Abdel-Rohman, M. (1992). Galloping of tall prismatic structures: a two-dimensional analysis. *Journal of sound and vibration*, *153*(1), 97-111.

133. Abdel-Rohman, M. (2001). Effect of unsteady wind flow on galloping of tall prismatic structures. *Nonlinear Dynamics*, *26*, 233-254.

134. Zulli, D., & Luongo, A. (2012). Bifurcation and stability of a two-tower system under wind-induced parametric, external and self-excitation. *Journal of Sound and Vibration*, *331*(2), 365-383.

135. Luongo, A., & Zulli, D. (2011). Parametric, external and self-excitation of a tower under turbulent wind flow. *Journal of Sound and Vibration*, *330*(13), 3057-3069.

136. Kitio Kwuimy, C. A., Litak, G., Borowiec, M., & Nataraj, C. (2012). Performance of a piezoelectric energy harvester driven by air flow. *Applied Physics Letters*, *100*(2).

137. Lakshmanan, N., Gomathinayagam, S., Harikrishna, P., Abraham, A., & Ganapathi, S. C. (2009). Basic wind speed map of India with long-term hourly wind data. *Current science*, 911-922.

138. Bernitsas, M. M., Ben-Simon, Y., Raghavan, K., & Garcia, E. M. H. (2009). The VIVACE converter: model tests at high damping and reynolds number around 10 5.

139. Zhang, L. B., Abdelkefi, A., Dai, H. L., Naseer, R., & Wang, L. (2017). Design and experimental analysis of broadband energy harvesting from vortex-induced vibrations. *Journal of Sound and Vibration*, *408*, 210-219.

140. Wang, S., Liao, W., Zhang, Z., Liao, Y., Yan, M., & Kan, J. (2021). Development of a novel non-contact piezoelectric wind energy harvester excited by vortex-induced vibration. *Energy Conversion and Management*, *235*, 113980.

141. Dai, H. L., Abdelkefi, A., & Wang, L. (2014). Theoretical modeling and nonlinear analysis of piezoelectric energy harvesting from vortex-induced vibrations. *Journal of Intelligent Material Systems and Structures*, *25*(14), 1861-1874.

142. Chen, S., Wang, Y., Song, R., Gao, Y., Wang, Z., & Yang, Z. (2024). VIV array for wind energy harvesting. *Journal of Intelligent Material Systems and Structures*, *35*(7), 727-739.

143. An, X., Huang, H., Song, B., & Ma, C. (2021). Performance evaluation of a vortex induced piezoelectric energy converter (vipec) with CFD approach. *Sustainability*, *13*(5), 2971.

144. Adhikari, S., Rastogi, A., & Bhattacharya, B. (2020). Piezoelectric vortex induced vibration energy harvesting in a random flow field. *Smart Materials and Structures*, *29*(3), 035034.

145. Naseer, R., & Abdelkefi, A. (2022). Nonlinear modeling and efficacy of VIV-based energy harvesters: Monostable and bistable designs. *Mechanical Systems and Signal Processing*, *169*, 108775.

146. Su, W. J., & Lin, W. Y. (2020). Design and analysis of a vortex-induced bi-directional piezoelectric energy harvester. *International Journal of Mechanical Sciences*, *173*, 105457.

147. Wang, J., Gu, S., Abdelkefi, A., & Bose, C. (2021). Enhancing piezoelectric energy harvesting from the flow-induced vibration of a circular cylinder using dual splitters. *Smart Materials and Structures*, *30*(5), 05LT01.

148. Mehdipour, I., Madaro, F., Rizzi, F., & De Vittorio, M. (2022). Comprehensive experimental study on bluff body shapes for vortex-induced vibration piezoelectric energy harvesting mechanisms. *Energy Conversion and Management: X*, *13*, 100174.

149. Lu, D., Li, Z., Hu, G., Zhou, B., Yang, Y., & Zhang, G. (2022). Two-degree-of-freedom piezoelectric energy harvesting from vortex-induced vibration. *Micromachines*, *13*(11), 1936.

150. Franzini, G. R., & Bunzel, L. O. (2018). A numerical investigation on piezoelectric energy harvesting from Vortex-Induced Vibrations with one and two degrees of freedom. *Journal of Fluids and Structures*, *77*, 196-212.

151. Jia, J., Shan, X., Zhang, X., Xie, T., & Yang, Y. (2022). Equivalent circuit modeling and analysis of aerodynamic vortex-induced piezoelectric energy harvesting. *Smart Materials and Structures*, *31*(3), 035009.

152. McCarthy, J. M., Deivasigamani, A., John, S. J., Watkins, S., Coman, F., & Petersen, P. (2013). Downstream flow structures of a fluttering piezoelectric energy harvester. *Experimental Thermal and Fluid Science*, *51*, 279-290.

153. Bryant, M., and Garcia, E. (2011). "Modeling and Testing of a Novel Aeroelastic Flutter Energy Harvester." ASME. *Jounal of Vibration and Acoustics*, 133(1), 011010.

154. Abdelkefi, A., Nayfeh, A. H., & Hajj, M. R. (2012). Design of piezoaeroelastic energy harvesters. *Nonlinear Dynamics*, *68*, 519-530.

155. Zakaria, M. Y., Al-Haik, M. Y., & Hajj, M. R. (2015). Experimental analysis of energy harvesting from self-induced flutter of a composite beam. *Applied Physics Letters*, *107*(2).

156. Bae, J. S., & Inman, D. J. (2014). Aeroelastic characteristics of linear and nonlinear piezo-aeroelastic energy harvester. *Journal of Intelligent Material Systems and Structures*, *25*(4), 401-416.

157. Abdelkefi, A., & Nuhait, A. O. (2013). Modeling and performance analysis of cambered wing-based piezoaeroelastic energy harvesters. *Smart Materials and Structures*, *22*(9), 095029.

158. Bibo, A., & Daqaq, M. F. (2013). Energy harvesting under combined aerodynamic and base excitations. *Journal of sound and vibration*, *332*(20), 5086-5102.

159. Dai, H. L., Abdelkefi, A., & Wang, L. (2014). Piezoelectric energy harvesting from concurrent vortex-induced vibrations and base excitations. *Nonlinear Dynamics*, *77*, 967-981.

160. Stamatellou, A. M., & Kalfas, A. I. (2021). Piezoelectric energy harvesting experiments under combined aerodynamic and base excitation. *Journal of Intelligent Material Systems and Structures*, *32*(2), 169-181.

161. Zhao, L., & Yang, Y. (2018). An impact-based broadband aeroelastic energy harvester for concurrent wind and base vibration energy harvesting. *Applied Energy*, *212*, 233-243.

162. Iqbal, M., & Khan, F. U. (2018). Hybrid vibration and wind energy harvesting using combined piezoelectric and electromagnetic conversion for bridge health monitoring applications. *Energy conversion and management*, *172*, 611-618.

163. Hu, G., Lan, C., Liang, J., Tang, L., & Zhao, L. (2022). Theoretical study of a two-degree-of-freedom piezoelectric energy harvester under concurrent aeroelastic and base excitation. *Journal of Intelligent Material Systems and Structures*, *33*(15), 2000-2016.

164. Hou, C., Li, C., Shan, X., Yang, C., Song, R., & Xie, T. (2022). A broadband piezo-electromagnetic hybrid energy harvester under combined vortex-induced and base excitations. *Mechanical Systems and Signal Processing*, *171*, 108963.

165. Chen, S., Eager, D., & Zhao, L. (2022). Enhanced frequency synchronization for concurrent aeroelastic and base vibratory energy harvesting using a softening nonlinear galloping energy harvester. *Journal of Intelligent Material Systems and Structures*, *33*(5), 687-702.

166. Kuang, Z., Zhang, Z., Liao, W., Lin, S., Wang, K., Zhang, J., & Kan, J. (2024). Magnetic transfer piezoelectric wind energy harvester with dual vibration mode conversion. *Energy*, *308*, 133020.

167. Xu, C., & Zhao, L. (2022). Investigation on the characteristics of a novel internal resonance galloping oscillator for concurrent aeroelastic and base vibratory energy harvesting. *Mechanical Systems and Signal Processing*, *173*, 109022.

168. Upadrashta, D., & Yang, Y. (2015). Finite element modeling of nonlinear piezoelectric energy harvesters with magnetic interaction. *Smart Materials and Structures*, *24*(4), 045042.

169. Kuang, Y., & Zhu, M. (2017). Design study of a mechanically plucked piezoelectric energy harvester using validated finite element modelling. *Sensors and Actuators A: Physical*, *263*, 510-520.

170. Roundy, S., Wright, P. K., & Rabaey, J. (2003). A study of low level vibrations as a power source for wireless sensor nodes. *Computer communications*, *26*(11), 1131-1144.

171. Williams, C. B., & Yates, R. B. (1996). Analysis of a micro-electric generator for microsystems. *sensors and actuators A: Physical*, *52*(1-3), 8-11.

172. Wang, G., Liao, W. H., Yang, B., Wang, X., Xu, W., & Li, X. (2018). Dynamic and energetic characteristics of a bistable piezoelectric vibration energy harvester with an elastic magnifier. *Mechanical Systems and Signal Processing*, *105*, 427-446.

173. Lan, C., Tang, L., Qin, W., & Xiong, L. (2018). Magnetically coupled dual-beam energy harvester: Benefit and trade-off. *Journal of Intelligent Material Systems and Structures*, *29*(6), 1216-1235.

174. Sodano, H. A., Park, G., & Inman, D. J. (2004). Estimation of electric charge output for piezoelectric energy harvesting. *Strain*, *40*(2), 49-58.

175. Paquin, S., & St-Amant, Y. (2010). Improving the performance of a piezoelectric energy harvester using a variable thicknessbeam. *Smart Materials and Structures*, *19*(10), 105020.

176. Rami Reddy, A., Umapathy, M., Ezhilarasi, D., & Gandhi, U. (2016). Improved energy harvesting from vibration by introducing cavity in a cantilever beam. *Journal of Vibration and Control*, *22*(13), 3057-3066.

177. Aladwani, A., Aldraihem, O., & Baz, A. (2014). A distributed parameter cantilevered piezoelectric energy harvester with a dynamic magnifier. *Mechanics of Advanced Materials and Structures*, *21*(7), 566-578.

178. Anton, S. R., & Sodano, H. A. (2007). A review of power harvesting using piezoelectric materials (2003–2006). *Smart materials and Structures*, *16*(3), R1.

179. Cook-Chennault, K. A., Thambi, N., & Sastry, A. M. (2008). Powering MEMS portable devices—A review of non-regenerative and regenerativepower supply systems with special emphasis on piezoelectric energy harvestingsystems. *Smart materials and structures*, *17*(4), 043001.

180. Fan, Y., Ghayesh, M. H. and Lu, T. F. (2021). A broadband magnetically coupled bistable energy harvester via parametric excitation. *Energy Conversion and Management*, *244*, 114505.

181. Malaji, P. V., & Ali, S. F. (2018). Analysis and experiment of magneto-mechanically coupled harvesters. *Mechanical Systems and Signal Processing*, *108*, 304-316.

182. Song, J., Sun, G., Zeng, X., Li, X., Bai, Q., & Zheng, X. (2022). Piezoelectric energy harvester with double cantilever beam undergoing coupled bending-torsion vibrations by width-splitting method. *Scientific Reports*, *12*(1), 1-14.

183. Ramalingam, U., Gandhi, U., Mangalanathan, U., & Choi, S. B. (2018). A new piezoelectric energy harvester using two beams with tapered cavity for high power and wide broadband. *International Journal of Mechanical Sciences*, *142*, 224-234.

184. Machado, S. P., Febbo, M., Ramirez, J. M., & Gatti, C. D. (2020). Rotational double-beam piezoelectric energy harvester impacting against a stop. *Journal of Sound and Vibration*, *469*, 115141.

185. Lu, Z. Q., Zhang, F. Y., Fu, H. L., Ding, H., & Chen, L. Q. (2021). Rotational nonlinear double-beam energy harvesting. *Smart Materials and Structures*, *31*(2), 025020.

186. Eshtehardiha, R., Tikani, R., & Ziaei-Rad, S. (2022). Investigating the multiple scales method based on a new scaling for energy harvesting from a double cantilever beam with internal resonance. *Meccanica*, *57*(6), 1281-1306.

187. Xiang, X., Liu, S., Yang, Q., Shen, H., & Song, R. (2025). Dual-coupling beams energy harvester for random vibrations and human motions: Modeling and experimental validation. *Energy*, *322*, 135589.

188. Shao, N., Chen, Z., Wang, X., Zhang, C., Xu, J., Xu, X., & Yan, R. (2023). Modeling and analysis of magnetically coupled piezoelectric dual beam with an annular potential energy function for broadband vibration energy harvesting. *Nonlinear Dynamics*, *111*(13), 11911-11937.

189. Sodano, H. A., Inman, D. J., & Park, G. (2004). A review of power harvesting from vibration using piezoelectric materials. *Shock and Vibration Digest*, *36*(3), 197-206.

190. Dutoit, N. E., Wardle, B. L., & Kim, S. G. (2005). Design considerations for MEMS-scale piezoelectric mechanical vibration energy harvesters. *Integrated ferroelectrics*, *71*(1), 121-160.

191. Kawai, H. (1969). The piezoelectricity of poly (vinylidene fluoride). *Japanese journal of applied physics*, *8*(7), 975.

192. Wei, C., & Jing, X. (2017). A comprehensive review on vibration energy harvesting: Modelling and realization. *Renewable and Sustainable Energy Reviews*, *74*, 1-18.

193. Priya, S. (2007). Advances in energy harvesting using low profile piezoelectric transducers. *Journal of electroceramics*, *19*, 167-184.

194. Khaligh, A., Zeng, P., & Zheng, C. (2009). Kinetic energy harvesting using piezoelectric and electromagnetic technologies—State of the art. *IEEE transactions on industrial electronics*, *57*(3), 850-860.

195. Bogue, R. (2009). Energy harvesting and wireless sensors: a review of recent developments. *Sensor Review*, *29*(3), 194-199.

196. Shaikh, F. K., & Zeadally, S. (2016). Energy harvesting in wireless sensor networks: A comprehensive review. *Renewable and Sustainable Energy Reviews*, *55*, 1041-1054.

197. Kim, H. S., Kim, J. H., & Kim, J. (2011). A review of piezoelectric energy harvesting based on vibration. *International journal of precision engineering and manufacturing*, *12*, 1129-1141.

198. Dagdeviren, C., Joe, P., Tuzman, O. L., Park, K. I., Lee, K. J., Shi, Y., ... & Rogers, J. A. (2016). Recent progress in flexible and stretchable piezoelectric devices for mechanical energy harvesting, sensing and actuation. *Extreme mechanics letters*, *9*, 269-281.

199. Twiefel, J., & Westermann, H. (2013). Survey on broadband techniques for vibration energy harvesting. *Journal of Intelligent Material Systems and Structures*, *24*(11), 1291-1302.

200. Harne, R. L., & Wang, K. W. (2013). A review of the recent research on vibration energy harvesting via bistable systems. *Smart materials and structures*, *22*(2), 023001.

201. Xiao, H., & Wang, X. (2014). A review of piezoelectric vibration energy harvesting techniques. *International Review of Mechanical Engineering, 8*(3), 609-620.

202. Zhu, D., Tudor, M. J., & Beeby, S. P. (2009). Strategies for increasing the operating frequency range of vibration energy harvesters: a review. *Measurement Science and Technology*, *21*(2), 022001.

203. Yildirim, T., Ghayesh, M. H., Li, W., & Alici, G. (2017). A review on performance enhancement techniques for ambient vibration energy harvesters. *Renewable and Sustainable Energy Reviews*, *71*, 435-449.

204. Ibrahim, S. W., & Ali, W. G. (2012). A review on frequency tuning methods for piezoelectric energy harvesting systems. *Journal of renewable and sustainable energy*, *4*(6).

205. Li, H., Tian, C., & Deng, Z. D. (2014). Energy harvesting from low frequency applications using piezoelectric materials. *Applied physics reviews*, *1*(4).

206. Abdelkefi, A. (2016). Aeroelastic energy harvesting: A review. *International Journal of Engineering Science*, *100*, 112-135.

207. Tan, Y., Dong, Y., & Wang, X. (2016). Review of MEMS electromagnetic vibration energy harvester. *Journal of Microelectromechanical Systems*, *26*(1), 1-16.

208. Uchino, K. (2018). Piezoelectric energy harvesting systems—Essentials to successful developments. *Energy Technology*, *6*(5), 829-848.

209. Wong, C. H., Dahari, Z., Abd Manaf, A., & Miskam, M. A. (2015). Harvesting raindrop energy with piezoelectrics: a review. *Journal of Electronic Materials*, *44*, 13-21.

210. Sezer, N., & Koç, M. (2021). A comprehensive review on the state-of-the-art of piezoelectric energy harvesting. *Nano energy*, *80*, 105567.

211. Ramadass, Y. K., & Chandrakasan, A. P. (2009). An efficient piezoelectric energy harvesting interface circuit using a bias-flip rectifier and shared inductor. *IEEE journal of solid-state circuits*, *45*(1), 189-204.

212. Guilar, N. J., Amirtharajah, R., & Hurst, P. J. (2008, February). A full-wave rectifier for interfacing with multi-phase piezoelectric energy harvesters. In *2008 IEEE International Solid-State Circuits Conference-Digest of Technical Papers* (pp. 302-615). IEEE.

213. Hsieh, Y. C., Chen, J. J., Chen, H. S., & Wu, W. J. (2016, November). An integrated circuit design of high efficiency parallel-SSHI rectifier for piezoelectric energy harvesting. In *Journal of Physics: Conference Series* (Vol. 773, No. 1, p. 012029). IOP Publishing.

214. Sanchez, D. A., Leicht, J., Hagedorn, F., Jodka, E., Fazel, E., & Manoli, Y. (2016). A parallel-SSHI rectifier for piezoelectric energy harvesting of periodic and shock excitations. *IEEE Journal of Solid-State Circuits*, *51*(12), 2867-2879.

215. Shareef, A., Goh, W. L., Narasimalu, S., & Gao, Y. (2018). A rectifier-less AC–DC interface circuit for ambient energy harvesting from low-voltage piezoelectric transducer array. *IEEE Transactions on Power Electronics*, *34*(2), 1446-1457.

216. Brenes, A., Lefeuvre, E., Badel, A., Seok, S., & Yoo, C. S. (2018). Unipolar synchronized electric charge extraction for piezoelectric energy harvesting. *Smart Materials and Structures*, *27*(7), 075054.

217. Hu, H., Xue, H., & Hu, Y. (2007). A spiral-shaped harvester with an improved harvesting element and an adaptive storage circuit. *IEEE transactions on ultrasonics, ferroelectrics, and frequency control*, *54*(6), 1177-1187.

218. Zhao, Z., Wang, S., & You, C. (2010). Piezoelectric micro-power generation to charge supercapacitor with optimized duty cycle. *Journal of intelligent material systems and structures*, *21*(11), 1131-1140.

219. Guan, M. J., & Liao, W. H. (2008). Characteristics of energy storage devices in piezoelectric energy harvesting systems. *Journal of intelligent material systems and structures*, *19*(6), 671-680.

220. Sodano, H. A., Inman, D. J., & Park, G. (2005). Generation and storage of electricity from power harvesting devices. *Journal of intelligent material systems and structures*, *16*(1), 67-75.

221. Guan, M. J., & Liao, W. H. (2007). On the efficiencies of piezoelectric energy harvesting circuits towards storage device voltages. *Smart Materials and Structures*, *16*(2), 498.

222. Pörhönen, J., Rajala, S., Lehtimäki, S., & Tuukkanen, S. (2014). Flexible piezoelectric energy harvesting circuit with printable supercapacitor and diodes. *IEEE Transactions on Electron Devices*, *61*(9), 3303-3308.

223. Raghavendran, S., Umapathy, M., & Karlmarx, L. R. (2018). Supercapacitor charging from piezoelectric energy harvesters using multi-input buck–boost converter. *IET Circuits, Devices & Systems*, *12*(6), 746-752.

224. Sodano, H. A., Inman, D. J., & Park, G. (2005). Comparison of piezoelectric energy harvesting devices for recharging batteries. *Journal of intelligent material systems and structures*, *16*(10), 799-807.

225. Jung, H. J., Song, Y., Hong, S. K., Yang, C. H., Hwang, S. J., Jeong, S. Y., & Sung, T. H. (2015). Design and optimization of piezoelectric impact-based micro wind energy harvester for wireless sensor network. *Sensors and Actuators A: Physical*, *222*, 314-321.

226. Pillatsch, P., Yeatman, E. M., & Holmes, A. S. (2012). A scalable piezoelectric impulse-excited energy harvester for human body excitation. *Smart Materials and Structures*, *21*(11), 115018.

227. Ottman, G. K., Hofmann, H. F., Bhatt, A. C., & Lesieutre, G. A. (2002). Adaptive piezoelectric energy harvesting circuit for wireless remote power supply. *IEEE Transactions on power electronics*, *17*(5), 669-676.

228. Ottman, G. K., Hofmann, H. F., & Lesieutre, G. A. (2003). Optimized piezoelectric energy harvesting circuit using step-down converter in discontinuous conduction mode. *IEEE Transactions on power electronics*, *18*(2), 696-703.

229. Bai, Q., Zhou, T., Gan, C., Wang, Q., Zheng, X., & Wei, K. X. (2024). A triboelectric-piezoelectric hybrid nanogenerator for rotational energy harvesting based on bistable cantilever beam. *Energy Conversion and Management*, *300*, 117971.

230. Mei, X., Zhou, S., Yang, Z., Kaizuka, T., & Nakano, K. (2021). Enhancing energy harvesting in low-frequency rotational motion by a quad-stable energy harvester with time-varying potential wells. *Mechanical Systems and Signal Processing*, *148*, 107167.

231. Cao, Y., Yang, J., & Yang, D. (2023). A magnetic excitation enhanced energy harvester with combined beam for rotational motion. *Sensors and Actuators A: Physical*, *360*, 114569.

232. Crawley, E. F., & Anderson, E. H. (1990). Detailed models of piezoceramic actuation of beams. *Journal of Intelligent Material Systems and Structures*, *1*(1), 4-25.

233. Zavodney, L. D., & Nayfeh, A. H. (1989). The non-linear response of a slender beam carrying a lumped mass to a principal parametric excitation: theory and experiment. *International journal of non-linear mechanics*, *24*(2), 105-125.

234. Esmailzadeh, E., & Nakhaie-Jazar, G. (1998). Periodic behavior of a cantilever beam with end mass subjected to harmonic base excitation. *International journal of non-linear mechanics*, *33*(4), 567-577.

235. Yang, Y., Yeo, J., & Priya, S. (2012). Harvesting energy from the counterbalancing (weaving) movement in bicycle riding. *Sensors*, *12*(8), 10248-10258.

236. Yung, K. W., Landecker, P. B., & Villani, D. D. (1998). An analytic solution for the force between two magnetic dipoles. *Physical Separation in Science and Engineering*, *9*(1), 39-52.

237. Bakri, T., Kuznetsov, Y. A., & Verhulst, F. (2015). Torus bifurcations in a mechanical system. *Journal of Dynamics and Differential Equations*, *27*, 371-403.

238. Tan, T., Zuo, L., & Yan, Z. (2021). Environment coupled piezoelectric galloping wind energy harvesting. *Sensors and Actuators A: Physical*, *323*, 112641.

239. Abdelkefi, A., Yan, Z., & Hajj, M. R. (2013). Modeling and nonlinear analysis of piezoelectric energy harvesting from transverse galloping. *Smart materials and Structures*, *22*(2), 025016.

240. Sagar, A. K., Adhikari, J., Chauhan, R., & Kumar, R. (2024). Geometric modifications to bluff body for enhanced performance in a wind-induced vibration energy harvester. *Mechanics of Advanced Materials and Structures*, *31*(23), 5942-5952.

241. Abdelmoula, H., & Abdelkefi, A. (2017). Investigations on the presence of electrical frequency on the characteristics of energy harvesters under base and galloping excitations. *Nonlinear Dynamics*, *89*(4), 2461-2479.

242. Abdollahzadeh Jamalabadi, M. Y. (2019, September). Effect of tip mass length ratio on low amplitude galloping piezoelectric energy harvesting. In *Acoustics* (Vol. 1, No. 4, p. 45). MDPI.

243. Zhao, D., Hu, X., Tan, T., Yan, Z., & Zhang, W. (2020). Piezoelectric galloping energy harvesting enhanced by topological equivalent aerodynamic design. *Energy Conversion and Management*, *222*, 113260.

244. Awrejcewicz, J., & Mrozowski, J. (1989). Bifurcations and chaos of a particular van der Pol-duffing oscillator. *Journal of Sound and Vibration*, *132*(1), 89-100.

245. Cheng, C. (1991). Invariant torus bifurcation series and evolution of chaos exhibited by a forced non-linear vibration system. *International journal of non-linear mechanics*, *26*(1), 105-116.

246. Simiu, E., & Cook, G. R. (1991). Chaotic motions of self-excited forced and autonomous square prisms. *Journal of engineering mechanics*, *117*(2), 241-259.

247. Sun, W., Guo, C., Cheng, G., He, S., Yang, Z., & Ding, J. (2022). Performance enhancement of galloping-based piezoelectric energy harvesting by exploiting 1: 1 internal resonance of magnetically coupled oscillators. *Nonlinear Dynamics*, *108*(4), 3347-3366.

248. Alhadidi, A. H., & Daqaq, M. F. (2016). A broadband bi-stable flow energy harvester based on the wake-galloping phenomenon. *Applied Physics Letters*, *109*(3).

249. Sun, W., Jang, H., & Seok, J. (2021). Magnetically coupled piezoelectric galloping-based energy harvester using a tandem configuration. *Mechanical Systems and Signal Processing*, *161*, 107952.

250. Shao, N., Chen, Z., Wang, X., Zhang, C., Xu, J., Xu, X., & Yan, R. (2023). Modeling and analysis of magnetically coupled piezoelectric dual beam with an annular potential energy function for broadband vibration energy harvesting. Nonlinear Dynamics, 1-27.

251. Chen, S., & Zhao, L. (2023). A quasi-zero stiffness two degree-of-freedom nonlinear galloping oscillator for ultra-low wind speed aeroelastic energy harvesting. Applied Energy, 331, 120423.

252. Li, H., Dong, B., Cao, F., Qin, W., Ding, H., & Chen, L. (2023). Nonlinear dynamical and harvesting characteristics of bistable energy harvester under hybrid base vibration and galloping. *Communications in Nonlinear Science and Numerical Simulation*, *125*, 107400.

253. Zhou, S., Cao, J., Wang, W., Liu, S., & Lin, J. (2015). Modeling and experimental verification of doubly nonlinear magnet-coupled piezoelectric energy harvesting from ambient vibration. *Smart Materials and Structures*, *24*(5), 055008.

254. Lan, C., Tang, L., Hu, G., & Qin, W. (2019). Dynamics and performance of a two degree-of-freedom galloping-based piezoelectric energy harvester. *Smart Materials and Structures*, *28*(4), 045018.

255. Adhikari, S., Friswell, M. I., Litak, G., & Khodaparast, H. H. (2016). Design and analysis of vibration energy harvesters based on peak response statistics. *Smart Materials and Structures*, *25*(6), 065009.

भारतीय प्रौद्योगिकी संस्थान गुवाहाटी
Indian Institute of Technology Guwahati

List of Publications

Journal publications

- Roy, R. and Dwivedy, S. K. (2024). Nonlinear dynamic analysis of a spring coupled double beam based piezoelectric energy harvester under parametric base excitation. *Mechanics Based Design of Structures and Machines*, *52(12),* 10516-10538. https://doi.org/10.1080/15397734.2024.2356725
- Roy, R. and Dwivedy, S. K. (2024). Nonlinear dynamics of magnetically coupled double beam based piezoelectric energy harvester under galloping excitation. *Sensors and Actuators A: Physical*, *371*, 115288. https://doi.org/10.1016/j.sna.2024.115288
- Roy, R. and Dwivedy, S. K. (2025). Nonlinear dynamic analysis of a parametrically excited piezoelectric energy harvester under magnetic repulsive force. *Applied Mathematical Modelling, 154,* 116701. https://doi.org/10.1016/j.apm.2025.116701

Conferences

- Roy, R., Garg, A., & Dwivedy, S. K. (February 7 – 9, 2020). Dynamic analysis of parametrically excited coupled beam-based piezoelectric energy harvester. In 1st International Conference on Recent Advancement of Mechanical Engineering, ICRAME, NIT Silchar, Assam, India. https://doi.org/10.1007/978-981-15-7711-6_63
- Roy, R., Garg, A., Borgohain, A., & Dwivedy, S. K. (December 15 – 17, 2022). Fixed-Guided Beam Based Piezoelectric energy harvester (FG-PEH): An Experimental Investigation. In 17th International Conference on Vibration Engineering and Technology of Machinery, VETOMAC, The Institute of Engineering, Pulchowk Campus, Nepal.
- Roy, R., Garg, A., & Dwivedy, S. K. (December 18 – 20, 2025). Nonlinear dynamics of a double cantilever-based piezoelectric energy harvester under combiner galloping and parametric excitation. In 20th International Conference on Vibration Engineering and Technology of Machinery, VETOMAC, IIT Guwahati, Assam, India. (accepted for conference presentation)

Brief Biography of Author

Ranit Roy is a resident of West Bengal, India. In 2016, he received the B.Tech degree from the Department of Mechanical Engineering, National Institute of Technology Durgapur. He earned his M.Tech degree in 2019 from the Department of Mechanical Engineering, Indian Institute of Technology Guwahati, focusing on the mathematical modelling and nonlinear analysis of piezoelectric energy harvesters. During this period, he developed an interest of doing deeper research in nonlinear dynamics, which motivated his continued work in this field. He is currently pursuing his Ph.D. degree in the Department of Mechanical Engineering, Indian Institute of Technology Guwahati, working on the nonlinear dynamics of double beam piezoelectric energy harvesters subjected to parametric, magnetic, and galloping excitations. His research blends analytical, numerical, and experimental techniques to advance small-scale renewable energy technologies.